

CHEMICAL VAPOR DEPOSITION OF $W_N C_y$ THIN FILMS FOR DIFFUSION BARRIER
APPLICATION

By

HIRAL M. AJMERA

A DISSERTATION PRESENTED TO THE GRADUATE SCHOOL
OF THE UNIVERSITY OF FLORIDA IN PARTIAL FULFILLMENT
OF THE REQUIREMENTS FOR THE DEGREE OF
DOCTOR OF PHILOSOPHY

UNIVERSITY OF FLORIDA

2007

© 2007 Hiral M. Ajmera

To my great grandmother Jeevatiben Z. Ajmera, grandparents Chunilal and Heeraben Ajmera,
and my parents Mahesh and Neela Ajmera

ACKNOWLEDGMENTS

I thank the chair of my advisory committee, Dr. Timothy J. Anderson, for his continued support and guidance throughout the course of my study at the University of Florida. My advisory committee members, Dr. Lisa McElwee-White, Dr. David Norton and Dr. Fan Ren, also provided excellent guidance in my work. The work on the design, assembly and testing of the CVD copper reactor would not have been possible without the support of Jim Hinnant (Chemical Engineering, UF), Dennis Vince (Chemical Engineering, UF), Rob Holobof (A&N Corporation), and Chuck Rowland (MicroFabritech). The excellent facilities at Major Analytical Instrumentation Center along with its extremely helpful staff (Wayne Acree, Dr. Valentin Craciun, Kerry Siebein, and Rosabel Ruiz) were instrumental in obtaining film characterization results. I thank my co-workers Dr. Omar J. Bchir, Andrew T. Heitsch, Karthik Boinapally, Dr. Seemant Rawal and Dr. Kee-Chan Kim for their assistance. Last but not the least, I thank my parents, Neela and Mahesh Ajmera, my brother, Abhijit Ajmera and my wife, Kinjal Ajmera for their unconditional love and support throughout my education.

TABLE OF CONTENTS

	<u>page</u>
ACKNOWLEDGMENTS	4
LIST OF TABLES	9
LIST OF FIGURES	11
ABSTRACT.....	16
CHAPTER	
1 INTRODUCTION	19
1.1 Background	19
1.2 Device Scaling and Moore's Law	21
1.3 Interconnects - Challenges	22
1.3.1 Delay in Interconnects.....	22
1.3.2 Electromigration in Interconnects	23
1.3.3 Power Consumption in Interconnects	24
1.4 Transition from Al-W-SiO ₂ to Copper low- <i>k</i> Metallization Scheme.....	24
1.4.1 RC Delay in Aluminum Interconnects.....	25
1.4.2 Electromigration in Aluminum Interconnects.....	25
1.4.3 Copper Interconnects	26
1.4.4 Low- <i>k</i> Dielectrics	27
1.5 Challenges to Copper Metallization.....	28
1.5.1 Diffusion of Copper in Silicon.....	28
1.5.2 Patterning of Copper	30
1.5.3 Dielectric Integration and Reliability.....	32
1.5.4 Electromigration.....	33
1.6 Problem Statement	35
1.6.1 Limitations of PVD	35
1.6.2 Drawbacks of TaN Deposition via CVD or ALD	36
1.6.3 Desired Properties of Diffusion Barrier Film and its Deposition Process	37
1.7 Hypothesis.....	38
2 LITERATURE REVIEW	46
2.1 Diffusion in Thin Films.....	46
2.2 Refractory Carbides and Nitrides as Diffusion Barriers	48
2.3 Deposition Methods for Diffusion Barrier Films.....	50
2.3.1 Physical Vapor Deposition.....	50
2.3.2 Chemical Vapor Deposition.....	52
2.4 Characterization and Testing of Diffusion Barrier Films	57
2.4.1 Diffusion Barrier Film Characterization	57
2.4.2 Diffusion Barrier Testing	61

2.5	Titanium Nitride as Diffusion Barrier.....	64
2.5.1	Chemical Vapor Deposition of Titanium Nitride.....	64
2.5.2	Atomic Layer Deposition of Titanium Nitride.....	71
2.6	Tantalum Nitride as Diffusion Barrier.....	78
2.6.1	Chemical Vapor Deposition of Tantalum Nitride.....	78
2.6.2	Atomic Layer Deposition of Tantalum Nitride.....	85
2.7	Tungsten Nitride as Diffusion Barrier.....	91
2.7.1	Chemical Vapor Deposition of Tungsten Nitride.....	91
2.7.2	Atomic Layer Deposition of Tungsten Nitride.....	96
2.8	Tungsten Nitride Carbide as Diffusion Barrier.....	98
2.8.1	Atomic Layer Deposition of WN_xC_y	98
2.8.2	Chemical Vapor Deposition of WN_xC_y	101
3	EXPERIMENTAL TECHNIQUES FOR THIN FILM DEPOSITION AND CHARACTERIZATION.....	111
3.1	Description of the CVD Reactor.....	111
3.2	Modification of the CVD Reactor.....	111
3.2.1	Installation of H_2 and N_2 Purifiers in the H_2 and N_2 Delivery Lines.....	111
3.2.2	Reconfiguration of the Gas Lines Downstream of the Reactor.....	112
3.2.3	Modification to the Line for Delivery of NH_3 to the Reactor.....	113
3.2.4	Replace MKS Mass Flow and Pressure Programmer Display.....	113
3.3	Operating Procedure for CVD Deposition.....	114
3.4	Deposition Parameters.....	114
3.5	Dimensionless Numbers for CVD Reactor.....	114
3.5.1	Prandtl Number.....	115
3.5.2	Knudsen Number.....	116
3.5.3	Reynolds Number.....	117
3.5.4	Peclet Number.....	118
3.5.5	Grashof Number.....	118
3.5.6	Rayleigh Number.....	119
3.6	Techniques Used for Thin Film Characterization.....	119
3.6.1	X-Ray Diffraction.....	119
3.6.2	Auger Electron Spectroscopy.....	121
3.6.3	X-Ray Photoelectron Spectroscopy.....	123
3.6.4	Scanning Electron Microscopy.....	124
3.6.5	Four Point Probe.....	125
3.7	Diffusion Barrier Testing.....	125
4	WN_xC_y THIN FILM DEPOSITION from $Cl_4(RCN)W(NC_3H_5)$, NH_3 AND H_2	135
4.1	Precursor Synthesis.....	135
4.2	Film Composition.....	136
4.3	X-Ray Diffraction Measurement.....	138
4.3.1	Film Crystallinity.....	138
4.3.2	Lattice Parameter.....	140
4.3.3	Polycrystal Grain Size.....	141

4.4	Film Growth Rate.....	142
4.5	Film Resistivity	142
4.6	Comparison of Films Deposited from 3a,b and 2a,b	143
4.7	Conclusions	144
5	DEPOSITION OF $W_Nx C_y$ USING $W(N^iPr)Cl_3[{}^iPr(NMe_2)N^iPr]$ AND H_2	156
5.1	Precursor Synthesis	156
5.2	Film Growth.....	157
5.3	Film Composition	157
5.4	X-Ray Diffraction of Films.....	159
5.5	Lattice Parameter	162
5.6	Grain Size.....	163
5.7	Film Growth Rate.....	164
5.9	Atomic Bonding from XPS Measurement.....	165
5.8	Film Resistivity	167
5.9	Diffusion Barrier Testing.....	168
5-10	Conclusions.....	170
6	DEPOSITION OF $W_Nx C_y$ FROM $W(N^iPr)Cl_3[{}^iPrNC(NMe_2)N^iPr]$: EFFECT OF NH_3 CO-REACTANT ON FILM PROPERTIES	194
6.1	Film Growth Studies	194
6.2	Film Composition	194
6.3	Film Crystallinity	196
6.4	Lattice Parameter	197
6.5	Grain Size.....	198
6.6	Film Growth Rate.....	199
6.7	Atomic Bonding.....	200
6.8	Film Resistivity	203
6.9	Diffusion Barrier Testing.....	204
	6.9.1 Barrier Testing for 1A.....	204
	6.9.2 Barrier Testing for 1B	206
6-10	Film Conformality.....	207
6-11	Conclusions	208
7	DEPOSITION OF $W_Nx C_y$ FROM $(CH_3CN)Cl_4W(NNMe_2)$ FOR DIFFUSION BARRIER APPLICATION	231
7.1	Precursor Synthesis	231
7.2	Film Growth by CVD	231
7.3	Film Composition	232
7.4	Film Crystallinity	233
7.5	Lattice Parameter	234
7.6	Grain Size.....	235
7.7	Film Growth Rate.....	235
7.8	Atomic Bonding from XPS.....	236

7.9	Film Resistivity	238
7.10	Diffusion Barrier Testing	239
7-11	Conclusions	240
8	QUANTUM MECHANICAL CALCULATIONS FOR PREDICTING PRECURSOR FRAGMENTATION.....	257
8.1	Computational Methodology	257
8.2	Geometry Optimization.....	258
8.3	Acetonitrile Cleavage.....	258
8.4	Chlorine Cleavage.....	259
8.4.1	Reaction of 5a with H ₂	259
8.4.2	Reaction Pathways for Removal of a Chloride from MI-1	260
8.4.3	Reaction Pathways for Removal of Chloride from MI-2 and RI-2.....	260
8.4.4	Reaction Pathways for Removal of the Fourth Chloride from 5a	261
8.5	Conclusion	262
9	CONCLUSION AND FUTURE WORK	273
9.1	Diffusion Barrier Testing	273
9.1.1	Film Thickness Control.....	273
9.1.2	Contamination Control.....	274
9.1.3	Realistic Diffusion Barrier Testing	275
9.2	Diffusion Barrier Integration	275
	APPENDIX: DENSITY FUNCTIONAL THEORY.....	277
A.1	Exchange-Correlation Functional (E _{xc}).....	279
A.1.1	Exchange Energy Density	279
A.1.2	Correlation Energy Density	280
A.2	Density Gradient Correction	281
A.2.1	Correction to Exchange Functional:	281
A.2.2	Correction to Correlation Functional	281
A.3	Similarity Between Hartree-Fock (HF) and DFT Methodologies	282
A.4	Comparison of DFT to Molecular Orbital Theory	282
A.4.1	Computational Efficiency	282
A.4.2	Energetics.....	283
A.4.3	Geometries	283
A.5	The Future of DFT	284
	LIST OF REFERENCES	286
	BIOGRAPHICAL SKETCH	299

LIST OF TABLES

<u>Table</u>	<u>page</u>
1-1 Bulk resistivity at room temperature of the five most conductive elemental metals.....	39
1-2 Dielectric constant of materials with low- <i>k</i> value.....	39
2-2 Techniques used for characterization of diffusion barrier thin films.....	103
2-3 Precursors used for deposition of TiN _x thin films by CVD	104
2-4 Precursors used for deposition of TiN _x thin films by ALD	104
2-5 Precursors used for deposition of TaN _x thin films by CVD	105
2-6 Precursors used for deposition of TaN _x thin films by ALD.....	106
2-7 Precursors used for deposition of WN _x thin films by CVD.....	107
2-8 Precursors used for deposition of WN _x thin film by ALD.....	107
3-1 Process parameters for CVD of thin films from precursors 3a,b, 4 and 5	127
3-2 Knudsen number for precursors 3a,b, 4 and 5 with H ₂ or N ₂ carrier gas for different deposition temperature.....	127
3-3 Reynolds number for H ₂ and N ₂ carrier gas for different deposition temperature	128
3-4 Grashof number for H ₂ and N ₂ carrier gas for different deposition temperature.....	128
3-5 Reference XRD peaks and their relative intensity for Si, β-W ₂ N, β-W ₂ C, α-W ₂ C and WO ₃ from JCPDS for Cu Kα radiation.....	129
3-6 Elemental relative sensitivity factors for AES quantification along with position of peaks in dN(E)/d(E) spectra used for quantification.....	129
4-1 Bond distances (Å) and angles (degrees) for Cl ₄ (CH ₃ CN)W(NC ₃ H ₅) (3a).....	146
5-1 Selected bond distances (Å) and bond angles (°) for 4	172
5-2 Analysis results from the deconvolution of the XPS peak of W for films deposited from 4 on Si(100) substrate at 400, 500, 600 and 700 °C.....	173
5-3 Analysis results from the deconvolution of XPS peaks of C, N and O for films deposited from 4 on Si(100) substrate at 400, 500, 600 and 700 °C	174
6-1 Molar flow rates used for deposition of WN _x C _y thin film from precursor 4	209

6-2	Analysis results from deconvolution of XPS peaks of W for films deposited by procedure 1A on Si(100) substrate between 300 and 700 °C.	210
6-3	Analysis results from deconvolution of XPS peaks of C, N and O for films deposited by procedure 1A on Si(100) substrate between 300 and 700 °C	211
6-4	Analysis results from deconvolution of XPS peaks of W for films deposited by procedure 1B on Si(100) substrate between 300 and 700 °C.	212
6-5	Analysis results from deconvolution of XPS peaks of C, N and O for films deposited by procedure 1B on Si(100) substrate between 300 and 700 °C	213
6-6	Apparent sputter rate of barrier film measured by dividing barrier film thickness by the time required to sputter the film during AES depth profiling.....	214
7-1	Molar flow rates of reactants in CVD reactor for deposition from precursor 5	242
7-2	Analysis results from deconvolution of XPS peak of W for films deposited from 5 on Si(100) substrate between 300 and 700 °C.....	243
7-3	Analysis results from deconvolution of XPS peaks of C, N and O for films deposited from 5 on Si(100) substrate between 300 and 700 °C.	244
8-1	Selected bond lengths (Å) and bond angles (°) for precursor 5 obtained from X-ray crystallographic measurement and DFT calculation.....	263
8-2	Selected bond lengths (Å) and bond angles (°) for 5a obtained from DFT calculation ..	263

LIST OF FIGURES

<u>Figure</u>	<u>page</u>
1-1	Cross-sectional view of metal-oxide-semiconductor field effect transistor (MOSFET) ...40
1-2	A cross-sectional view of metallization scheme.....40
1-3	Scaling of transistors in the last 3 decades for Intel Corporation microprocessors41
1-4	The device delay as a function of different device generations.....42
1-5	Effect of feature size scaling on total capacitance..42
1-6	Damaged Al interconnect line showing the formation of hillock and void due to electromigration..43
1-7	Electromigration lifetime for aluminum interconnects at different current densities.....43
1-8	Band diagram of copper impurity in silicon. A) p-type silicon. B) n-type silicon44
1-9	Simplified steps in damascene processing for copper deposition.44
1-10	Schematic of one ALD cycle forming a monolayer of film45
2-1	Arrhenius plot for CVD showing mass transfer limited and reaction limited growth regimes. G is the film growth rate and T is the deposition temperature in K.....108
2-2	Characteristic ALD growth rate vs. T curve showing different growth regimes.....109
2-3	Characteristic ALD plot showing the exposure time required to achieve self-limiting growth110
3-1	Schematic of CVD reactor used for thin film deposition130
3-2	Line diagram of the carrier gas feed line. A) Before installation of gas purifier. B) after installation of gas purifier.....131
3-3	Flow diagram of reactor downstream. A) Before reconfiguration. B) After reconfiguration.....132
3-4	Design of new cold trap made of stainless steel133
3-5	Schematic of the old and new NH ₃ feed port.....134
4-1	Thermal ellipsoids diagram of the molecular structure of Cl ₄ (CH ₃ CN)W(NC ₃ H ₅) (3a). Thermal ellipsoids are plotted at 50% probability146

4-2	Composition of films deposited from 3a,b (with and without ammonia) and 2a,b with NH ₃ at different deposition temperature as determined by AES on Si (100) substrate.	147
4-3	X-ray photoelectron spectroscopy patterns of films deposited at 450, 600 and 750 °C from 3a,b and ammonia on Si (100) substrate.....	148
4-4	X-ray diffraction spectra of films deposited on Si (100) substrate from 3a,b and ammonia.....	149
4-5	Grazing incidence XRD spectra of films deposited on Si (100) substrate from 3a,b and ammonia	150
4-6	Thickness of film (obtained from X-SEM) at different deposition temperature for films deposited with 3a,b and ammonia on Si(100) substrate.....	151
4-7	Lattice parameters for films grown from 3a,b on Si (100) substrate with and without ammonia.....	152
4-8	Average grain size at different deposition temperature for films grown from 3a,b with and without ammonia on Si (100) substrate.	153
4-9	Scanning electron microscope images for films grown from 3a,b with ammonia. A) Film deposited at 450 °C. B) Film deposited at 650 °C	153
4-10	Arrhenius plot of log of film growth rate vs. inverse temperature for deposition from 3a,b (with and without ammonia ¹⁵⁷) and 2a,b with ammonia.....	154
4-11	Change in film resistivity with deposition temperature for films grown on Si (100) from 3a,b (with and without ammonia) and 2a,b with ammonia.....	155
5-1	Thermal ellipsoids diagram of the molecular structure of W(N ⁱ Pr)Cl ₃ [ⁱ Pr(NMe ₂)N ⁱ Pr].	175
5-2	Composition of films deposited from 4 and 2a,b on Si (100) substrate at different deposition temperature as determined by AES after 0.5 min of sputtering.....	176
5-3	N/W and C/W atomic ratios for films deposited from 4 and 2a,b on Si (100) substrate at different deposition temperature as determined by AES after 0.5 min of sputtering.....	177
5-4	X-ray photoelectron spectroscopy patterns for films deposited from 4 at 400, 500, 600 and 700 °C on Si(100) surface.....	178
5-5	X-ray diffraction patterns for films deposited from 4 on Si (100) substrate	179
5-6	Deconvolution of XRD peaks for films deposited from 4 at 700 °C on a Si (100) substrate.	180

5-7	Deconvolution of XRD peaks for films deposited from 4 at 750 °C on a Si (100) substrate.	181
5-8	Grazing incidence X-ray diffraction spectra for films deposited from 4 on Si (100) substrate	182
5-9	Lattice parameters for films grown from 4 and 2a,b on Si (100) substrate.....	183
5-10	Average grain size at different deposition temperature for films grown from 4 and 2a,b on Si (100) substrate	184
5-11	Scanning electron microscope images for films grown from 4 on Si (100) substrate between 400 and 750 °C in 50 °C increments	185
5-12	Arrhenius plot of log of film growth rate vs. inverse temperature for deposition from 4 and 2a,b on a Si(100) substrate.....	186
5-13	Deconvolution of the XPS peaks of W, N, C and O for film deposited from 4 at 400, 500, 600 and 700 °C on Si (100) substrate	187
5-14	Change in film resistivity with deposition temperature for films grown on Si (100) from 4 and 2a,b	188
5-15	Pre-anneal AES depth profile of Cu (100 nm)/ WN _x C _y (45 nm)/Si (substrate) stack for WN _x C _y film deposited at 450 °C (using precursor 4).	189
5-16	Auger electron spectroscopy profiles of Cu/WN _x C _y /Si stack for WN _x C _y deposited at 450 °C using 4 and annealed at A) 200 °C B) 400 °C C) 500 °C D) 600 °C.	190
5-17	X-ray diffraction plots for Cu/WN _x C _y /Si stack (WN _x C _y films deposited from 4 at 450 °C) before annealing and after annealing at 200, 400, 500 and 600 °C.....	191
5-18	Auger electron spectroscopy depth profiles of Cu (100 nm)/WN _x C _y (55 nm)/Si (100) stack for WN _x C _y film deposited at 500 °C (using precursor 4) and annealed in vacuum for 30 min at A) 200 °C B) 400 °C C) 500 °C D) 600 °C.....	192
5-19	X-ray diffraction plots for Cu/WN _x C _y /Si stack (WN _x C _y films deposited with 4 at 500 °C) before annealing and after annealing at 200, 400, 500 and 600 °C.....	193
6-1	Composition of films deposited by procedures 1A, 1B and 1C on Si (100) substrate at different deposition temperature as determined by AES after 0.5 min of sputtering ..	215
6-2	X-ray diffraction patterns for films deposited on Si (100) substrate by procedure 1A ...	216
6-3	X-ray diffraction patterns for films deposited on Si (100) substrate by procedure 1B....	217
6-4	Lattice parameters for films grown by procedures 1A and 1C on Si (100) substrate. ...	218

6-5	Average grain size at different deposition temperature for films grown by procedures 1A and 1B on Si (100) substrate.	219
6-6	Scanning electron microscope images for films grown by procedure 1A at different deposition temperature on Si (100) substrate.....	220
6-7	Scanning electron microscope images for films grown by procedure 1B at different deposition temperature on Si (100) substrate.....	221
6-8	Arrhenius plot for growth using procedures 1A, 1B and 1C for growth on a Si(100) substrate	222
6-9	X-ray photoelectron spectroscopy measurements for films deposited by procedure 1A between 300 and 700 °C on Si (100) substrate	223
6-10	X-ray photoelectron spectroscopy measurements for films deposited for between 300 and 700 °C by procedure 1B on Si (100) substrate.....	224
6-11	Change in film resistivity with deposition temperature for films deposited by procedures 1A, 1B and 1C on Si (100) substrate.....	225
6-12	Pre- and post-anneal AES depth profiles of Cu (100 nm)/ WN_xC_y /Si (substrate) stacks for WN_xC_y films deposited by procedure 1A.	226
6-13	Pre- and post-anneal XRD measurements of Cu (100 nm)/ WN_xC_y /Si (substrate) stacks for WN_xC_y film deposited by procedure 1A at 300, 350 and 400 °C	227
6-14	Pre- and post-anneal AES depth profiles of Cu (100 nm)/ WN_xC_y /Si (substrate) stacks for WN_xC_y film deposited by procedure 1B.	228
6-15	Pre- and post-anneal XRD measurements of Cu (100 nm)/ WN_xC_y /Si (substrate) stack for WN_xC_y film deposited by procedure 1B at 300, 350 and 400 °C	229
6-16	Scanning electron microscope images of WN_xC_y thin films deposited on FSG dielectric. The feature size is 0.2 μ m with aspect ratio of 2:1	230
7-1	Composition of films deposited from 5 on Si (100) substrate at different deposition temperature as determined by AES after 0.5 min of sputtering.....	245
7-2	X-ray photoelectron spectroscopy measurements for films deposited from 5 on Si (100) substrate at different deposition temperature	246
7-3	X-ray diffraction patterns for films deposited from 5 between 300 and 700 °C on Si (100) substrate.....	247
7-4	Lattice parameters for films grown from 5 on Si (100) substrate. Error bars indicate uncertainty in determination of peak position for lattice parameter calculation.	248

7-5	Average grain size for films grown from 5 at different deposition temperature on Si (100) substrate.....	249
7-6	Scanning electron microscope images for films deposited from 5 between 300 and 700 °C on Si (100) substrate	250
7-7	Arrhenius plot for deposition from 5 on a Si(100) substrate	252
7-8	X-ray photoelectron spectroscopy measurements for films deposited from 5 between 300 and 700 °C on Si (100) substrate	253
7-9	Change in film resistivity with deposition temperature for films deposited from 5 on Si (100) substrate	254
7-10	Pre- and post-anneal AES depth profile of Cu/WN _x C _y /Si (substrate) stack for WN _x C _y film deposited from 5	255
7-11	Pre- and post-anneal XRD measurement of Cu (100 nm)/ WN _x C _y /Si (substrate) stack for WN _x C _y film deposited from 5 at 350 and 400 °C	256
8-1	Geometry of 5 . A) X-ray crystallographic determination. B) Geometry optimization by DFT calculation	264
8-2	Cleavage of acetonitrile ligand from precursor 5 . The figure shows optimized geometries for 5a and CH ₃ CN	264
8-3	Calculated transition state and products for reductive elimination and σ-bond metathesis from 5a	265
8-4	Possible reaction pathways for chloride cleavage by reductive elimination and σ-bond metathesis from MI-1 intermediate.	266
8-5	Possible reaction pathways for reductive elimination and σ-bond metathesis from MI-2 (<i>cis</i> and <i>trans</i>).	267
8-6	Possible reaction pathway for reductive elimination from RI-2. R = reductive elimination, T = transition state and I = reaction intermediate	268
8-7	Possible reaction pathways for reductive elimination and/or σ-bond metathesis from MI-3 and RI-3.	269
8-8	The ΔH values with respect to the ΔH (5a) for reaction pathway through intermediate MI2- <i>cis</i>	270
8-9	The ΔH values with respect to the ΔH (5a) for reaction pathway through intermediate MI2- <i>trans</i>	271
8-10	The ΔH values with respect to the ΔH (5a) for reaction pathway through intermediate RI2.	272

Abstract of Dissertation Presented to the Graduate School
of the University of Florida in Partial Fulfillment of the
Requirements for the Degree of Doctor of Philosophy

CHEMICAL VAPOR DEPOSITION OF $W_Nx C_y$ THIN FILMS FOR DIFFUSION BARRIER
APPLICATION

By

Hiral M. Ajmera

August 2007

Chair: Timothy J. Anderson
Major: Chemical Engineering

The speed and reliability of integrated circuits has been improved significantly by replacing the Al/SiO₂ based metallization scheme with a Cu/low-*k* based one. This study focused on chemical vapor deposition (CVD) of ultra-thin $W_Nx C_y$ diffusion barrier films using novel tungsten metal organic precursors. The precursors used for deposition of $W_Nx C_y$ thin film were Cl₄(RCN)W(NC₃H₅) (**3a**, R = CH₃; **3b**, R = Ph), W(N^{*i*}Pr)Cl₃[^{*i*}PrNC(NMe₂)N^{*i*}Pr] (**4**) and (CH₃CN)Cl₄W(NNMe₂) (**5**). The thin films deposited in a aerosol assisted, vertical CVD reactor were evaluated for their material properties and diffusion barrier efficacy.

Successful thin film deposition of $W_Nx C_y$ by MOCVD utilizing **3a,b**, H₂ and NH₃ was achieved in the temperature range of 450 to 750 °C. The lowest temperature for film growth was 450 °C. The $W_Nx C_y$ films consisted of W, N, C and O as determined by AES. The Cl content of the film was below the detection limit of XPS (ca. 1 at. %). As compared to films deposited with **3a,b** in H₂, those deposited with **3a,b**, H₂ and NH₃ had a higher N content. The higher nitrogen content in films deposited with NH₃ resulted in higher film resistivity with the lowest measured resistivity of 1690 μΩ-cm for the film grown at 550 °C. The apparent activation energy for the film growth from **3a,b**, H₂ and NH₃ in the kinetically controlled growth regime was 0.34 eV,

which is significantly higher than the activation energy of 0.15 eV observed for film growth from **3a,b** in H₂.

Successful WN_xC_y thin film deposition could be achieved for **4** with coreactant(s) NH₃ + H₂, only NH₃, and only H₂. The lowest temperature for which film growth occurred was 300 °C with either NH₃ + H₂ or only NH₃ coreactant(s). Comparison of films deposited with coreactant(s) NH₃ + H₂, only NH₃, and only H₂ shows that the best films, in terms composition, resistivity, and microstructure, are deposited using only NH₃ as a coreactant. The films deposited with NH₃ at 400 °C had a high N content of 28 at. % and were X-ray amorphous. The films also showed very good conformality in a 0.2 μm wide, 2:1 aspect ratio feature. Diffusion barrier testing showed that films deposited at 400 °C with only NH₃ coreactant were able to prevent Cu diffusion after annealing at 500 °C for 30 min in vacuum.

Chemical vapor deposition of WN_xC_y was achieved using **5** with H₂ as a coreactant. It was determined that H₂ coreactant is essential for deposition of WN_xC_y films from **5**. The lowest growth temperature for **5** was 300 °C. Films consisted of W, N, C, and O as determined by AES and no Cl impurity was detected by XPS. The film N content was significantly higher for films deposited from **5** as compared to those deposited from **3a,b** or **4**. An Amorphous film microstructure was observed for deposition below 550 °C. The apparent activation energy for the film growth in the kinetically controlled growth regime was 0.52 eV. The films showed a high resistivity compared to the bulk resistivity of pure W₂N and W₂C. Diffusion barrier testing showed that films deposited at 350 and 400 °C were able to prevent bulk Cu diffusion after annealing at 500 °C in vacuum for 30 min.

CVD thin film deposition from **3a,b**, **4**, and **5** highlights the importance of precursor selection and deposition parameters (e.g., coreactant selection, deposition temperature) on the

film properties and diffusion barrier performance. Detailed film characterization and preliminary diffusion barrier testing revealed that films deposited with **3a,b** and NH_3 exhibited the most promise for diffusion barrier applications.

To aid the precursor screening process and help understand the mechanism of precursor fragmentation prior to the growth studies, quantum mechanical (QM) calculations using density functional theory were carried out. Statistical mechanics along with QM calculations were employed to determine the energy barrier of potential reaction pathways which would lead to the deposition of WN_xC_y thin film. QM calculations for fragmentation of precursor **5** showed that the first step of precursor fragmentation was dissociation of the CH_3CN ligand, followed by removal of the Cl ligands by either sigma-bond metathesis or reductive elimination.

CHAPTER 1 INTRODUCTION

1.1 Background

In the last few decades, electronic devices have become an integral part of our day-to-day life. From personal computers to laptops, cell phones to PDAs, almost all the electronic devices contain integrated circuits (ICs). The exponential growth in functionality of these ICs is the result of continued miniaturization of the devices in circuits, leading to an increase in chip functionality and decrease in cost.

Semiconductor devices can be built on various substrates, which include the elemental semiconductors silicon and germanium, and compound semiconductors such as GaN and GaAs. While compound semiconductors are used for specialized applications such as communication ICs, most of the ICs today use silicon as the substrate. The abundance of silicon ICs is primarily because SiO_2 can be grown easily on silicon substrate. SiO_2 is also an excellent insulator that can easily passivate the silicon surface.

The manufacturing of ICs can be divided in two phases: front-end-of-line (FEOL) processing and back-end-of-line (BEOL) processing. FEOL is the initial processing on semiconductor substrate to build devices such as transistors and resistors. Major FEOL processes include epitaxial silicon film deposition, dopant implantation, diffusion, oxidation and deposition, and associated patterning steps. BEOL processing includes all the steps involved in connecting the active components of the circuitry via metal wiring. BEOL processing includes deposition of contacts, insulators, metal lines and vias, dielectric and associated patterning steps. The deposition of bonding sites for chip to package connection and wafer dicing are included in BEOL processing.

The basic structures deposited during FEOL processing of ICs are resistors, capacitors, diodes, transistors, fuses, and conductors.¹ Transistors are the building block of an IC. They act as a switch or an amplifier in an IC. There are many different types of transistors, the most prominent being field effect transistor (FET) and bipolar junction transistor (BJT). Figure 1-1 shows a metal gate metal-oxide-semiconductor field effect transistor (MOSFET). In a MOSFET, when a sufficient voltage is applied to the gate metal, current flows between the source and drain through the channel region. By controlling the gate voltage, the transistor can be turned on or off. MOS devices are voltage amplifiers, whereas BJTs are current amplifiers. MOS transistor circuits have the advantage of small area requirement and higher yield in processing. Unlike BJTs, the MOS transistor is normally in “off” mode and hence it is ideal for low power application. Moreover, lower power requirement results in low heat generation in MOS transistors. MOS transistor circuits require fewer processing steps resulting in lower cost per transistor. Because of these advantages, the majority of devices used in ICs today employ MOSFETs. The CMOS (complimentary metal-oxide-semiconductor) FET is formed in both p-channel and n-channel MOS transistor. CMOS uses lower power than similar circuits and is most popular in low power application.

Various devices deposited during FEOL processing are connected to each other via a three dimensional network of metal lines known as interconnects. The application of metals in ICs is known as metallization. The metal lines are separated from each other by dielectric materials. Figure 1-2 shows a cross-section of a three-level metallization scheme.

Interconnects can be ‘local’ interconnects or ‘global’ interconnects. Local interconnects primarily refer to interconnects that connect the gate, source, and drain in MOSFET. Typical local interconnects are doped polysilicon and refractory metal silicide. Local interconnects can

have higher resistivity because the current in them travels for very short distances. But local interconnects need to be able to withstand higher processing temperature. Global interconnects, on the other hand, travel long distances and need to have lower resistivity. Typical global interconnect metals are aluminum and copper.

1.2 Device Scaling and Moore's Law

Moore's Law is an empirical observation that the number of components per chip (or chip functionality) doubles every 24 months. The law is attributed to Gordon Moore, co-founder of Intel Corporation. Figure 1-3 shows how the number of transistors per microprocessor has roughly doubled every 24 months over the last three decades.

The scaling of transistors in the earlier years was achieved primarily through the improvements in the FEOL processes. Between 1970 and 1990, the speed of IC was primarily determined by the speed of the transistors. Much of the speed increase achieved in transistors was by scaling the transistor dimensions such as oxide film thickness and channel length and width. Scaling of the device resulted in a higher transistors density per chip for a given chip area, lower the cost per transistor and increasing speed. The disadvantage of scaling is the higher current density in the transistors. Figure 1-4 shows how overall device performance varies with the scaling of the device.² For earlier generation devices with large feature size, the gate delay dictated the overall device performance. With the shrinking of device dimensions, interconnect delay becomes much more important. In fact, interconnect delay is the dominant factor in determining the device speed for sub-100 nm devices.

1.3 Interconnects - Challenges

1.3.1 Delay in Interconnects

The time delay in an interconnect circuit depends on two factors: resistance of the conductor and the capacitance of the dielectric material. For a MOS circuit, the RC delay is defined in terms of the circuit response.³

$$V_{\text{out}}(t) = V_{\text{out}}(\text{max}) \left[1 - \exp\left(\frac{-t}{RC}\right) \right] \quad (1-1)$$

The output voltage of the circuit at time t is $V_{\text{out}}(t)$, maximum output voltage is $V_{\text{out}}(\text{max})$, the resistance of the metal line is R , and the total capacitance of the circuit is C . The resistance of interconnect line is defined in terms of its length L , width W , thickness t_M , and resistivity ρ .

$$R = \rho \frac{L}{W t_M} \quad (1-2)$$

The capacitance between silicon substrate and metal line (metal to ground), C_{M-G} , is given by Equation 1-3.

$$C_{M-G} = \epsilon \epsilon_0 \frac{WL}{t_D} \quad (1-3)$$

ϵ and t_D are the dielectric constant of the dielectric material and thickness of the dielectric line respectively, and ϵ_0 is the permittivity of free space. The capacitance between two metal lines (C_{M-M}) separated by distance D is given by Equation 1-4.⁴

$$C_{M-M} = \epsilon \epsilon_0 \frac{t_M L}{D} \quad (1-4)$$

The total capacitance, C , can then be calculated from Equations 1-3 and 1-4.

$$C = K_I (C_{M-G} + C_{M-M}) = K_I \epsilon \epsilon_0 L \left(\frac{W}{t_D} + \frac{t_M}{D} \right) \quad (1-5)$$

K_I is a constant that depends on the fringing field effect. The RC delay is calculated from Equations 1-2 and 1-5.

$$RC = \frac{K_I \epsilon \epsilon_0 \rho L^2}{W t_M} \left(\frac{W}{t_D} + \frac{t_M}{D} \right) \quad (1-6)$$

As the critical device dimension shrinks, C_{M-M} dominates the overall capacitance C (Figure 1-5).⁵

The RC delay can then be written as Equation 1-7.

$$RC \approx \frac{K_I \epsilon \epsilon_0 \rho L^2}{WD} \quad (1-7)$$

For local interconnects the shrinking of the transistor leads to a corresponding decrease in L , W and D . Therefore, the actual delay in the local interconnect does not increase with device scaling. However, the chip area increases with each successive technology node. This leads to an increase in the length of global interconnects and a corresponding increase in the RC time delay.

1.3.2 Electromigration in Interconnects

Electromigration is the phenomenon by which high current density in the interconnect lines leads to the movement of the metal atoms in the direction of the electron flow. Most present day microprocessors operate at high temperature (ca. 100 °C). At high temperature, the metal atoms in the interconnect have higher mobility. When high energy electrons transfer their momentum to these mobile metal atoms, there is a movement of metal atoms in the direction of electron flow. This atom movement leads to formation of voids at the cathode and hillocks at the anode (Figure 1-6)

Electromigration, which causes failure of the circuit, is one of the most important concerns for interconnect reliability. As the interconnect dimensions shrink with each successive generation, the current density in the interconnects also increases. The scaling of interconnects

requires higher electromigration resistance in interconnect materials. Electromigration becomes a major concern for aluminum-based metallization scheme. Figure 1-7 shows that the mean time to failure for aluminum interconnect sharply decreases if the current density in the interconnect exceeds 3 MA/cm^2 .

1.3.3 Power Consumption in Interconnects

The power consumption in an interconnect operating at frequency f and voltage V is given by Equation 1-8.

$$P = CV^2f \quad (1-8)$$

The shrinking of interconnect dimensions causes an increase in parasitic capacitance, thereby increasing the power required to operate the IC. The power requirement in ICs is increasingly becoming an important issue because of the popularity of battery operated mobile devices. Since the improvements in power storage capacity of batteries has not increased as fast as the power requirement of ICs, there is an increased focus on developing lower power ICs. To reduce the power requirement of interconnects, it becomes important to decrease the capacitance of the inter-metal dielectric.

1.4 Transition from Al-W-SiO₂ to Copper low- k Metallization Scheme

Until the 1990's, aluminum had been the preferred metal for interconnect lines and SiO₂ was the preferred dielectric. Tungsten was deposited in the vias to connect different levels of aluminum lines. The Al-W-SiO₂ based metallization scheme has many advantages.⁶ Aluminum can be easily deposited with evaporation or sputtering techniques with film resistivity close to the bulk resistivity of $2.7 \mu\Omega\text{-cm}$. Aluminum is easy to pattern as it can be readily etched by dry or reactive ion etching. Aluminum also has good adhesion to the SiO₂ surface. Addition of 0.5 at. % copper to aluminum increases the electromigration resistance of aluminum interconnects.

1.4.1 RC Delay in Aluminum Interconnects

One of the major problems with the Al-W-SiO₂ based interconnect scheme is that RC delay in these interconnects, which is a significant factor in determining the speed of an IC. The interconnect delay surpassed the transistor delay below 0.25 μm minimum feature size (Figure 1-4). To leverage the gains made in transistor speeds and density, a reduction in interconnect delay is required. Increase in signal noise and higher power requirement for narrower global interconnect lines necessitated use of new dielectric material with dielectric constant lower than that of SiO₂ (dielectric constant $k = 3.9$).

1.4.2 Electromigration in Aluminum Interconnects

Another major problem with the aluminum-based interconnect scheme is reliability. In 1960s, it was discovered that electromigration can damage the aluminum lines and compromise the interconnect reliability.⁷ Electromigration of aluminum atoms at the Al-W interface results in movement of aluminum atoms away from the interface by grain boundary diffusion. The vacancies created by aluminum atoms due to electromigration accumulate to form a void. If the size of the void becomes larger than the diameter of the via, an opening in the circuit is created. This phenomenon, which leads to the failure of the interconnect, is referred to as “wear-out” mode of failure. The “wear-out mode” in Al-W-SiO₂ metallization scheme results in a decrease in lifetime of multilevel metallization by a factor of 50 as compared to single level aluminum interconnect.⁸ A short-term solution to electromigration problem in Al-W-SiO₂ metallization was to use small amount of solute (1 - 4 at. % copper) in aluminum lines. Ames et al.⁹ found that the addition of 4 at. % copper in aluminum strips increased the electromigration resistance by a factor of 70 as compared to pure aluminum strips under similar testing conditions of 175 °C temperature and 4 MA/cm² current density. Copper in aluminum forms Al₂Cu precipitates along the grain boundaries of aluminum crystallites. While the exact mechanism behind the increase in

electromigration resistance of aluminum by addition of copper is not completely understood, it is believed that copper may either decrease the concentration of vacancies in grain boundaries or increase the activation energy of aluminum diffusion through grain boundaries.

The use of copper as solute extended the use of aluminum as the preferred material for interconnects. However, with further increase in current density in interconnects, even the aluminum doped with copper could not provide sufficient electromigration resistance. Sakimoto et al.¹⁰ studied the mean time to failure (MTTF) of aluminum (0.5 at. % copper) at 200 °C. The MTTF showed a dramatic decrease at current densities of 3 MA/cm² and higher. Higher current densities in interconnects demand a new interconnect material that has a higher resistance to electromigration than aluminum doped with copper.

1.4.3 Copper Interconnects

One way to reduce the RC delay in interconnects is to use a material with higher electrical conductivity as interconnect. Table 1 shows the conductivity of the 5 most conductive metals. The metal with lowest bulk resistivity is silver. But silver shows low resistance to electromigration. Gold also has a lower bulk resistivity compared to aluminum, but gold is much more expensive and the performance gain in terms of resistivity is minimal. Copper with bulk resistivity close to silver is a much better conductor than aluminum. Moreover, copper has a melting temperature (1083 °C), which is much higher than that of aluminum (660 °C). Atomic diffusion is slower in copper owing to its high melting temperature, and hence is expected to have a better electromigration resistance as compared to aluminum. The semiconductor industry has gradually moved towards copper metallization for global interconnects because of lower resistivity and superior electromigration resistance of copper. IBM was the first major chip manufacturer to announce successful implementation of copper interconnects in 1997.

1.4.4 Low-*k* Dielectrics

Another way of reducing the RC time delay is to use dielectric material with a lower dielectric constant. The dielectric constant of a material depends on the polarizability of its constituent atoms or molecules; the higher the polarizability, the higher the dielectric constant. SiO₂ has a dielectric constant of 3.9. For SiO₂ based materials, low dielectric constant film can be obtained by replacing the Si-O bonds in the film with Si-C or Si-F bonds, which have a much lower polarizability as compared to Si-O bonds. The C and F atoms are incorporated in the film by introducing an organic precursor or a fluorinated silicon precursor source during the plasma enhanced chemical vapor deposition (PECVD) of SiO₂.

Another important class of materials that has been investigated for dielectric application includes silsesquioxane (SSQ) group based materials. Since the cubic SSQ cells occupy a much larger volume than tetrahedral SiO₂, the *k*-value of SSQ is lower than that of SiO₂. Silsesquioxane unit cell contains Si-O bonds in a cubic arrangement. In hydrogen terminated SSQ (HSSQ), unit cells are connected to each other via oxygen atoms, whereas the cube corners are terminated by hydrogen. In methyl terminated SSQ (MSSQ), the cubes are connected by –CH₂ group, while cube corners are terminated by –CH₃ group.

Non-polar organic compounds have also been investigated for dielectric application. Aliphatic compounds have the lowest *k*-value but they are thermally unstable at temperature higher than 300 °C.¹¹ Aromatic compounds and cross-linked polymers have a higher thermal stability. Table 1-2 lists the important polymeric materials that have been studied for their potential application as dielectric material in ICs.

Decreasing the density of polarizable molecules is an effective way of reducing the *k*-value, however, it often comes at the expense of mechanical strength. Density can be decreased by introducing micro/meso pores in the dielectric film. Most materials have some inherent

porosity, though the pore size might be very small. This inherent porosity is referred to as constitutive porosity. To increase the k -value of dielectric film, intentional doping of thermally unstable molecules is used. Once these unstable molecules are evaporated or decomposed by thermal treatment, they leave behind a matrix of void spaces or pores resulting in a decrease in k -value of the film. These void causing agents are referred to as porogens and are very effective in lowering the k -value of dielectric film. The porosity that is increased after the growth of the film, by agents such as porogen or by selective etching of the film, is referred to as subtractive porosity. For silica based films deposited by PECVD, CH_x is used as porogen. Xerogels and aerogels both have ultra low- k values primarily due to their subtractive porosity.

Presently, many IC manufacturers have successfully integrated PECVD deposited carbon doped oxide (CDO or SiOC) into their metallization schemes in 90 nm devices with effective k -value of 2.7 - 2.9. While acceptance of copper as the metal of choice for interconnects has been ubiquitous, the semiconductor industry has not yet singled out a single dielectric material for 45 nm devices. Carbon doped oxides have been preferred over other low- k materials for 65 nm devices, however, industry is still evaluating different materials and processes for a suitable low- k dielectric (< 2.5) at the 45 nm technology node.

1.5 Challenges to Copper Metallization

The introduction of new materials has led to new challenges in fabrication of ICs. These challenges are related to the processing of the new material or the integration of new material with other components of the IC. Copper metallization has introduced many processing and integration related challenges and this section highlights the most important challenges.

1.5.1 Diffusion of Copper in Silicon

In a transistor, interstitial impurities such as Cu, Ni, Fe, and Li can be incorporated during various processing steps. The tolerance level of these impurities in the device depends on the

energy level of the impurity in band structure of the device, device dimension, diffusivity, and interaction of the impurity with silicon and dopants. If an impurity has an energy level lying deep in the band gap of the semiconductor, such impurities can be detrimental to the device performance. These ‘deep impurities’ can act as alternate recombination centers and hence decrease diffusion length, increase junction leakage, and decrease minority carrier life time.³ Moreover, the tolerable amount of defects in silicon decreases as the device dimension shrinks.

Copper is an extremely fast diffuser in silicon. The diffusion coefficient of copper in silicon at 500 °C is $2.0 \times 10^{-5} \text{ cm}^2/\text{sec}$.¹⁴ Furthermore, copper is mobile in silicon even after annealing. Copper can travel significant distances within the silicon wafer even at room temperature. The interaction of copper in silicon depends on the doping of the silicon substrate. In n-type silicon, copper primarily forms neutral or negatively charged precipitates. Since interstitial copper is positively charged in silicon¹⁵, there is either no barrier or electrostatic attraction between interstitial copper and copper precipitates. Hence, in n-type silicon, copper readily forms Cu_3Si precipitates. These copper precipitates can act as recombination centers for minority carriers and significantly lower minority carrier lifetime.¹⁶ In p-type silicon, copper precipitates are positively charged species.¹⁷ There is electrostatic repulsion between the positively charged copper in precipitates and positively charged interstitial copper, which acts as a barrier in nucleation and precipitation of copper in p-type silicon. The out diffusion of copper to the silicon surface is also dependent on the type of doping of silicon. If the surface of a p-type Si wafer is free of native oxide, copper diffuses from the bulk to the surface of the wafer. Since surface segregated copper can easily be etched by a H_2O_2 and HF mixture, it is inferred that the copper does not form Cu_3Si precipitates. For n-type silicon wafer, out diffusion occurs only when the wafer is heated to 400 °C.

The primary reason why copper is extremely undesirable in silicon is that it forms deep levels in the band gap of silicon (Figure 1-8). If copper exists in the triplet state, it forms three acceptor levels in the silicon band gap at 0.24, 0.37 and 0.52 eV.³ Once copper has diffused in silicon, the high diffusivity of copper in silicon ensures that the detrimental effects of copper spreads throughout the device. Copper is also detrimental if it diffuses into the dielectric film. Copper in dielectrics decrease the breakdown voltage of the dielectric and also increases the parasitic capacitance, thus negating the benefits achieved from low-*k* dielectric film.

To prevent diffusion of copper into dielectric films, researchers have investigated various thin films that can act as diffusion barrier between copper and the dielectric. Industry presently employs a TaN/Ta bilayer as diffusion barrier/adhesion promoter. TaN has good diffusion barrier properties and has good adhesion to SiO₂. Ta, on other hand, shows good adhesion to copper and TaN films. Ta also promotes the growth of copper (111) crystals during physical vapor deposition (PVD) copper seed deposition. It is well known that copper (111) has higher electromigration resistance as compared to other crystal orientations. With the scaling of interconnects, the barrier film also has to shrink. This is a major challenge in copper metallization because the PVD process currently employed to deposit the barrier film can not be extended for future generations of interconnects. The challenges in barrier deposition are discussed in detail in section 1.6.

1.5.2 Patterning of Copper

One of the main challenges in initial adoption of copper interconnects in ICs was its patterning scheme. Since copper does not form any volatile by-products at low temperature, reactive ion etching (RIE) can not be employed for patterning copper.¹⁸ This problem was addressed by a radical change in patterning scheme for interconnect layers. For aluminum metallization, aluminum is deposited first, followed by patterning via lithography and etching

steps. The SiO₂ dielectric was then deposited into the aluminum pattern. To implement copper metallization, the scheme of deposition is reversed. The dielectric film is deposited first, and then the lines and vias for the metals are patterned in the dielectric via lithography and etching steps, followed by deposition of copper in the lines and vias. The film stack is then subjected to chemical-mechanical polishing step (CMP) to planarize the copper layer and remove the barrier layer on the dielectric surface. This approach of deposition is often referred to as the ‘dual-damascene’ patterning scheme. Figure 1-9 shows the basic steps in the dual-damascene processing scheme. It should be noted that since the purpose of the figure is to highlight the main steps in dual damascene processing, deposition of other layers such as diffusion barrier, dielectric etch-stop layers and capping layers during the dual damascene processing are not included in the figure.

In the dual damascene scheme, either the trench can be formed first followed by the via, or the via can be patterned first followed by the trench. In ‘trench first approach’, patterning of the via results in ‘pooling’ of the photoresist in the trenches. The ‘pooling’ increases the thickness of dielectric in the trenches, making it difficult to etch the vias through the thicker dielectric layer. Hence, industry has adopted the ‘via first approach’ for patterning the dielectric layer for devices with minimum feature size of 0.25 μm or lower.

The detailed description of steps involved in copper interconnects are as follows:

- The copper line is coated with the first etch-stop layer (usually SiN or SiCN). Dielectric film (layer 1) is deposited on the etch-stop layer, followed by deposition of the second etch-stop layer. Another dielectric film (layer 2) is deposited on the second etch-stop layer followed by the deposition of the third etch-stop layer.
- Mask is applied to pattern the vias (for ‘via first approach’). Anisotropic etch cuts through the top etch-stop and dielectric layers to form the vias. This process is optimized to stop at the etch-stop layer at the bottom of via. The photoresist is then removed.
- Mask is applied to pattern the trenches. Anisotropic etch cuts through the third etch-stop and second dielectric layer to form the trenches. The photoresist deposited at the bottom of the

via prevents over etching of the via during the trench etch process. Low energy etching step removes the mask from bottom of the via. The mask layer is then removed.

- Diffusion barrier and adhesion promoter thin films are deposited by PVD process (TaN/Ta bilayer).
- Copper thin film, which acts as ‘seed’ layer for subsequent electrochemical plating process, is deposited by PVD. The trenches and vias are filled with bulk copper by electrochemical plating.
- Excess copper over the barrier film is removed by CMP that stops at the first etch-stop layer.

As the feature size shrinks further, new processes and/or materials are expected to be introduced in the dual damascene patterning scheme. For instance, the integration of ultra low- k dielectric films in the interconnects would require additional steps such as pore sealing to close the meso pores in the dielectric film prior to barrier film deposition.¹¹

1.5.3 Dielectric Integration and Reliability

Presently, industry has successfully integrated CDOs in the interconnect stack. These dielectric films have k -value in the range of 2.7 to 2.9. But as device dimension shrinks further, films with lower k -value will be required to decrease the parasitic capacitance and power requirements. Introduction of highly porous films lowers the dielectric constant of films but it comes at the cost of mechanical stability.¹⁹ Moreover, future interconnects will need processes such as CVD or ALD to deposit conformal diffusion barrier films. Gaseous reactants used in CVD or ALD process can easily diffuse through the interconnected pores in the dielectric film, thereby increasing the parasitic capacitance of the dielectric film. An ideal dielectric film should have uniformly distributed pores that are not interconnected to one another. These isolated pores prevent the diffusion of precursor molecules used in CVD and ALD process through the dielectric film and aid uniform deposition of barrier film. But as the porosity of dielectric film is increased to lower the k -value of dielectric film, these pores become more interconnected to one another. These interconnected pores act as pathways for diffusion of precursor molecules

through the dielectric film. Interconnected pores also make it difficult to deposit uniform barrier film that can prevent copper diffusion into the dielectric. Various processes such as plasma exposure have been proposed to plug or block the open pores on the surface of the dielectric film.

Adhesion of the dielectric film to the diffusion barrier is also of concern for new dielectric films that are being investigated for future interconnects. Failure modes such as time-dependent dielectric breakdown (TDDB) that were not previously observed for SiO₂ based interconnects, have become reliability issues for low-*k* dielectrics because of film adhesion problems.²⁰

In summary, lowering of the *k*-value comes at the expense of mechanical stability, ease of integration with barrier film deposition process, and adhesion and interconnect reliability. Extensive research is ongoing to find suitable processes and materials for deposition low-*k* dielectric film and its integration in the dual damascene processing scheme.

1.5.4 Electromigration

Numerous studies have shown that copper has better electromigration resistance as compared to aluminum. However, as the dimensions of the interconnect shrink, electromigration in copper can result in poor reliability of interconnects. Moreover, the electromigration mechanism in aluminum interconnect is very different from that in copper. While electromigration in aluminum interconnect occurs via the ‘wear-out’ mode of failure (*vide supra*), electromigration in copper interconnects is primarily a surface migration mode. Surface migration has lower activation energy as compared to grain boundary diffusion. Copper electromigration occurs via surface diffusion because copper does not adhere well with dielectric films such as SiO₂.²¹ The top surface of trench is in direct contact with the dielectric and the surface diffusion of copper atoms occurs at this interface.

One of the approaches that has found success in limiting electromigration in copper is alloying of copper metal. The solute atoms in the copper alloy block the kink sites on the surface of the dielectric forming the copper line, thereby hindering the surface diffusion of copper and increasing the electromigration resistance. Solutes such as Sn and Zr have shown significant improvements in electromigration resistance when added to copper.²² The downside of alloying copper is that the RC time delay increases as the resistance of copper alloy is higher than that of pure copper metal. Moreover, current copper bulk deposition in vias and trenches is done via an electrochemical plating process. Addition of solute in copper by the electrochemical plating process would require significant modifications to the existing process and further research needs to be done in order to adopt this approach.

Another approach that has found wide acceptance in increasing electromigration resistance of copper is the use of cap layer to separate the copper-dielectric interface. An ideal cap layer would have good adhesion to both the copper and dielectric films. Good adhesion between copper and cap layer can significantly reduce electromigration failure in interconnect lines. Recent studies have investigated various cap layers such as Ta, Ta/TaN, Pd, SiN_x, SiC_xN_yH_z and CoWP.²³⁻²⁶ The disadvantage of using a cap layer is that it increases the effective *k*-value of the dielectric film as the cap layer reduces the area of dielectric film.

Industry is believed to introduce copper alloy for improving electromigration resistance of copper because this approach is considered fairly low risk. In the long term, it is believed that capping layers can alleviate electromigration in copper interconnects for several generations.²⁰ Moreover, capping layers such as CoWP can be selectively deposited on copper line by electroless plating and hence the deposition of capping layer will not require patterning or etching steps. The primary reason why implementation of capping layer is pushed to future

generations is because there is skepticism of introducing additional layer to the interconnect stack. Additional layers in interconnect stack introduce new processes, material(s) and integration related challenges that need to be addressed.

1.6 Problem Statement

1.6.1 Limitations of PVD

Of all the future challenges to the scaling of copper metallization discussed in the previous section, one of the most important challenges is the scaling of the diffusion barrier film. With the shrinking dimensions of interconnect lines, the thickness of diffusion barrier needs to be reduced. In fact, according to the roadmap for future interconnects published by ‘International Technology Roadmap of Semiconductors’ (ITRS), a consortium of industry and academic institutions, the thickness of barrier layer needs to be scaled down from 72 to 37 Å by year 2007 and to 24 Å by year 2013.²⁷ The scaling of barrier film is required for two reasons. First, as copper line and via dimensions shrink, the relative volume that the barrier film occupies in the line or via increases resulting in decrease in available area for copper. This could increase both the RC time delay of the interconnect and the current density in the copper lines and vias. Secondly, the barrier forms a part of electrical circuit where a via contacts the line. The thinner the barrier, the lower is the resistance to electron transport between via and line. Extensive research is being done to find a suitable process along with new material for deposition of low resistivity ultra-thin barrier film with good conformality and adhesion to copper and dielectric layers.

Physical vapor deposition, which is presently employed to deposit diffusion barrier film, is believed to be incapable of depositing ultra-thin films with conformal coverage. The PVD process is a ‘line of sight’ process and the directional nature of the deposition process results in excess deposition at the edges and poor sidewall coverage inside the trenches and vias. Ionized

PVD (I-PVD), a variant of PVD, employs a high density plasma to ionize the metal ions during deposition. These ions are then directed perpendicular to the wafer surface via magnets to obtain better sidewall coverage.²⁸ While I-PVD has helped in extending the usefulness of PVD for deposition of diffusion barrier film, future generations of diffusion barrier films would require deposition techniques that have a significantly better step coverage than I-PVD.

Chemical vapor deposition (CVD) is a technique that employs gaseous reactants to deposit thin films. Films deposited by CVD have much better step coverage than the best variant PVD process. Atomic layer deposition (ALD), a variant of CVD process, also has excellent step coverage and precise control over film thickness. Similar to CVD, ALD employs gaseous reactants but the delivery of the reactants is done in a sequential manner. One ALD cycle consists of 4 steps (Figure 1-10). In the first step, the substrate is exposed to reactant A, which adsorbs the first layer on the substrate surface by chemisorption and subsequent layers by physisorption. In the next step, excess reactant A is purged from the reactor and the reactant molecules that are physisorbed on the chemisorbed layer are removed from the reactor. In the third step, a co-reactant B is introduced into the reactor. Co-reactant B reacts with the chemisorbed A to form a monolayer thick film. In the last step, excess B is purged from the reactor. If chemisorption occurs in a self-limiting mode, one ALD cycle should ideally be able to deposit a monolayer film. Atomic layer deposition is believed to be capable of extremely uniform film deposition in very high aspect ratio features.

1.6.2 Drawbacks of TaN Deposition via CVD or ALD

Another challenge to scaling of the diffusion barrier is the material. While PVD TaN has been very successful so far as a diffusion barrier, future interconnects require films deposited with CVD or ALD. Many investigators have attempted the growth of TaN thin films via CVD and ALD. But the growth of the resistive Ta₃N₅ phase during attempts to grow TaN by CVD

results in an increase in resistivity of the film.²⁹ Presently, many new materials are being investigated for diffusion barrier application, the details of which are included in the next chapter.

1.6.3 Desired Properties of Diffusion Barrier Film and its Deposition Process

The following are the main requirements of a diffusion barrier film:

- Prevent copper diffusion under device operating conditions
- Good adhesion with copper, dielectric, and etch-stop layers
- Low resistivity ($< 400 \mu\Omega\text{-cm}$)
- Good mechanical and thermal stability
- CMP removal rate of the barrier film similar to that of copper

Together with the material, there are certain process requirements for deposition of the diffusion barrier film:

- Capable of ultra-thin film deposition (few nm thick)
- Excellent conformality
- Low deposition temperature ($< 500 \text{ }^\circ\text{C}$)
- No pin-holes in the barrier film

Film properties that are considered beneficial for diffusion barrier film include:

- 1 Amorphous microstructure: Diffusion through the barrier film primarily occurs via grain boundary diffusion. One of the ways of hindering the diffusion of copper through the barrier film is to deposit a single crystal barrier film. However, thermal requirements and lattice mismatch make deposition of a single crystal film impractical. The next best option is to deposit an amorphous barrier film.³⁰
- 2 Sufficient N content: Transition metal nitrides have been found to have good diffusion barrier properties. The primary reason, it is believed, is the presence of excess N at the grain boundaries of the film. Since N does not form a stable compound with copper, the presence of N hinders the diffusion of copper through the grain boundaries. So, an effective diffusion barrier should have sufficient N to “stuff” the grain boundaries to prevent copper diffusion.
- 3 Low impurities incorporation: Oxygen impurities form oxides that have a high resistivity. So, incorporation of O has to be minimal in the diffusion barrier film. In addition, impurities such as Cl and F are also undesirable because they increase the film resistivity and adversely affect the adhesion of barrier film with copper.

1.7 Hypothesis

Thin film WN_xC_y deposited by metal-organic chemical vapor deposition (MOCVD) would be capable of meeting the material and process requirements expected from a good diffusion barrier film. WN_xC_y , a ternary transition metal compound, is expected to be able to be grown with an amorphous microstructure because the presence of a third element in the binary transition metal nitride matrix disrupts the crystal lattice to favor the growth of amorphous film. Carbon in the film is expected to lower the film resistivity of WN_xC_y because WC_x is more conductive than WN_x .

An important focus of the present work is deposition of WN_xC_y thin films using metal organic precursors. Films deposited by single-source metal organic precursors should help to lower the deposition temperature. Low deposition temperature from these films should also aid the deposition of amorphous films. Precursors used for MOCVD should help in preventing incorporation of halides in the film. Previous studies have shown that WN_x films have excellent diffusion barrier properties.^{31,32,33} It is anticipated that WN_xC_y films deposited with the metal organic precursors used in the present work would also have excellent diffusion barrier properties. The WN_xC_y films deposited by MOCVD are expected to have good thermal and mechanical stability, good adhesion to dielectric and copper films, and a CMP removal rate similar to that of copper.

Since the deposition technique used in the present work is CVD, it is expected that the process would yield films with excellent conformality. As discussed earlier, films deposited by CVD have a much better conformality than those deposited by PVD. Film thickness control of CVD is expected to be similar to that of PVD. The precursors that are successful in CVD deposition of WN_xC_y films can then be used to attempt film growth by ALD to get even better conformality and precise thickness control.

Table 1-1. Bulk resistivity at room temperature of the five most conductive elemental metals

Metal	Bulk Resistivity ($\mu\Omega\text{-cm}$)
Silver (Ag)	1.6
Copper (Cu)	1.7
Gold (Au)	2.4
Aluminum (Al)	2.6
Molybdenum (Mo)	5.2

Table 1-2. Dielectric constant of materials with low- k value

Material	Dielectric Constant (k)	Reference
Silicon-based		
SiF	3.2 – 3.4	11
Si-C	2.7 – 2.8	11
Silsequioxane (SSQ) based		
HSSQ	2.8 – 3.0	12
MSSQ	2.7 – 2.9	13
Polymer based		
Polyimides	3.0 – 4.0	12
Parylene-N	2.6	12
Parylene-F	2.2	12
Teflon (PTFE)	1.9 – 2.1	12
Highly porous oxides		
Xerogels/Aerogels	< 2.5	12

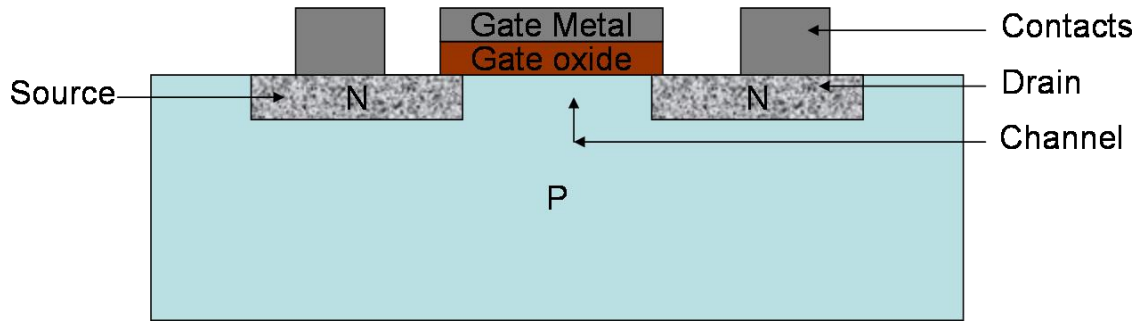


Figure 1-1. Cross-sectional view of metal-oxide-semiconductor field effect transistor (MOSFET)

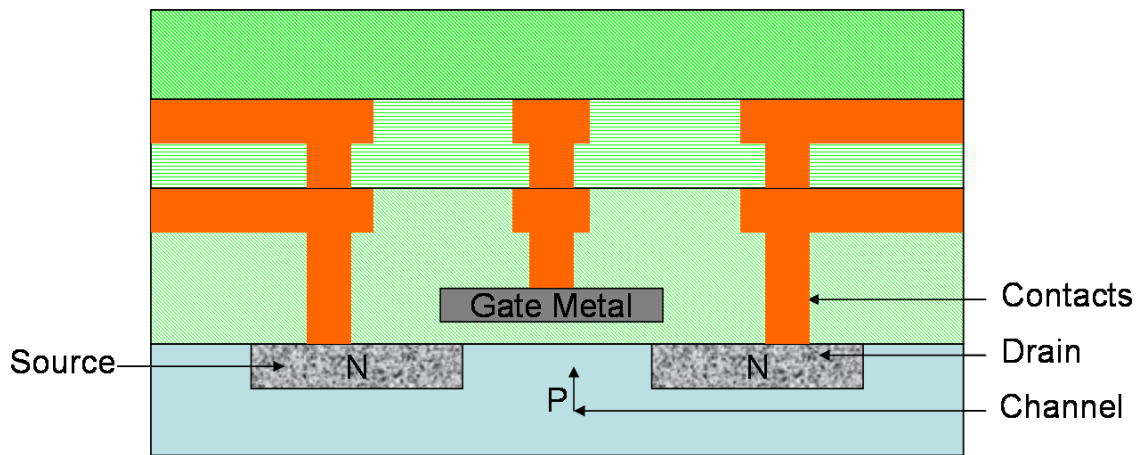


Figure 1-2. A cross-sectional view of metallization scheme

Moore's Law

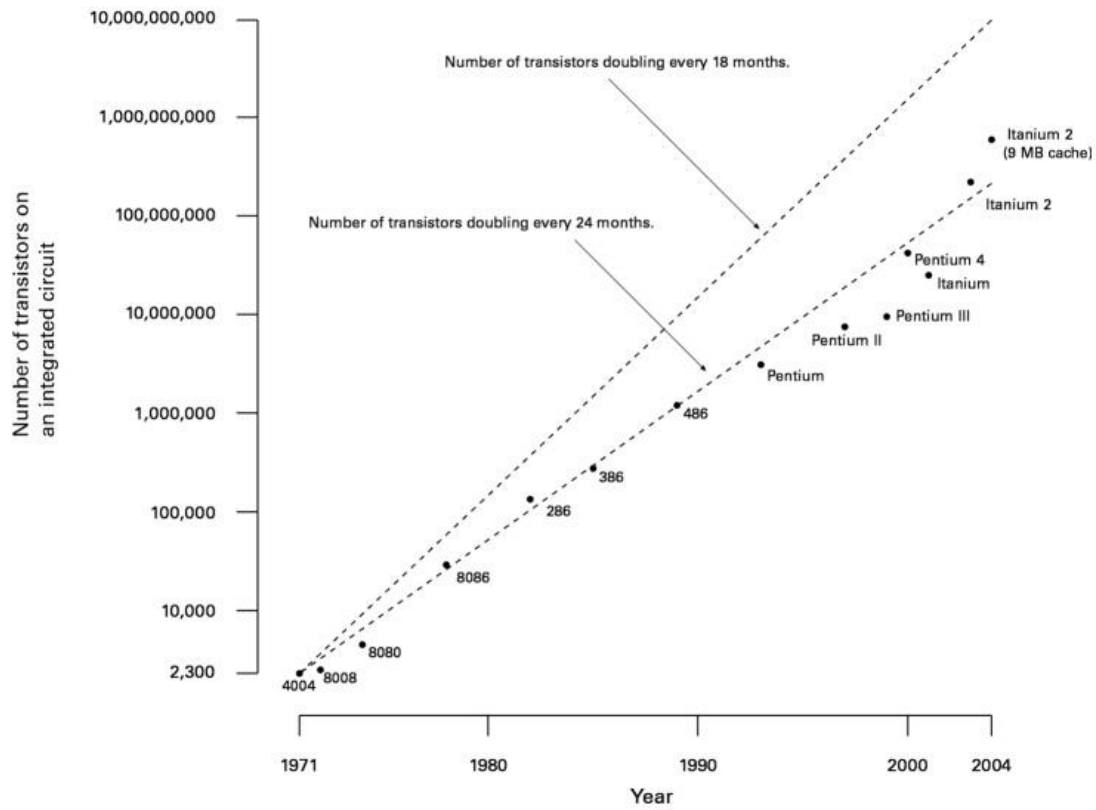


Figure 1-3. Scaling of transistors in the last 3 decades for Intel Corporation microprocessors (Wikipedia, http://en.wikipedia.org/wiki/Moores_law, May, 2007)

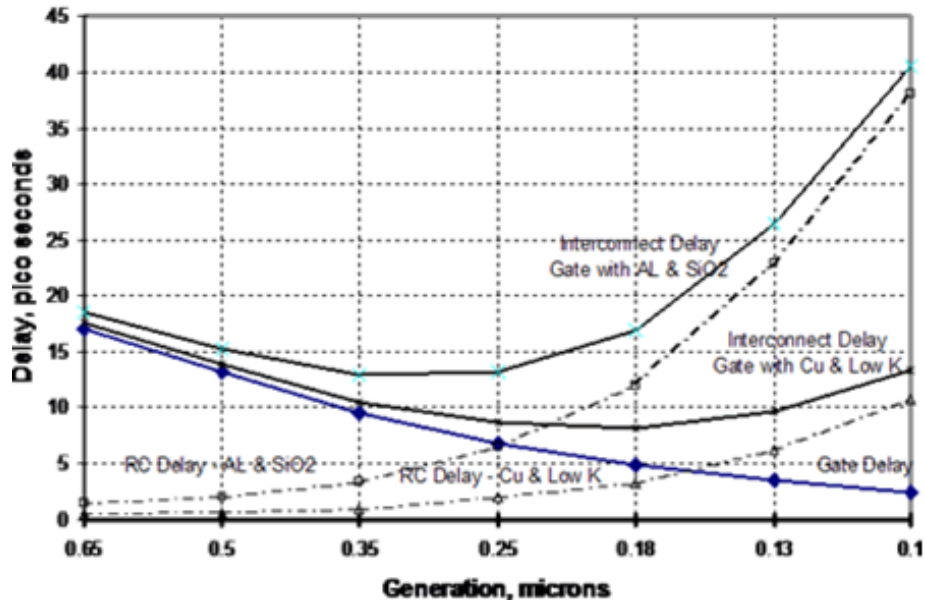


Figure 1-4. The device delay as a function of different device generations.² Adopted from M. T. Bohr, "Interconnect scaling - the real limiter to high performance ULSI," Proceedings of IEEE International Electron Devices Meeting, 241 (1995). ©1995 IEEE. Reproduced with permission.

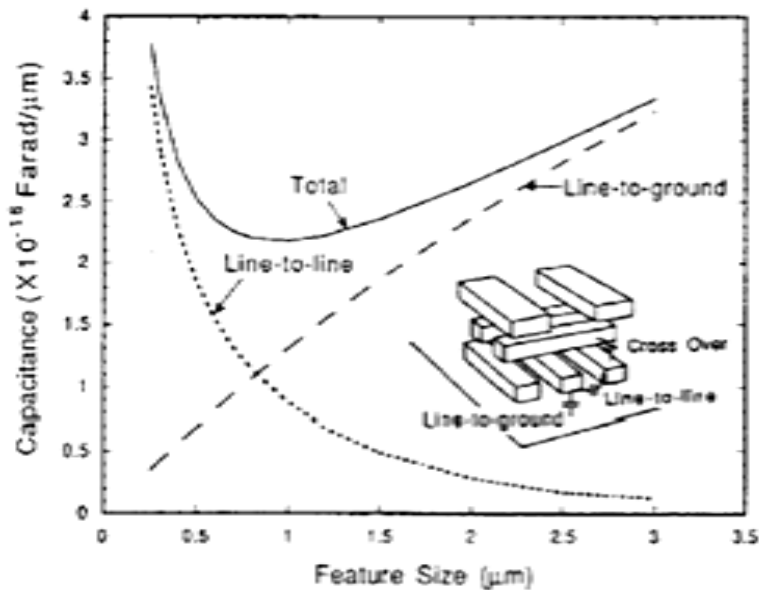


Figure 1-5. Effect of feature size scaling on total capacitance.⁵ Adopted from S. P. Jeng, R. H. Havemann, and M. C. Chang, "Process integration and manufacturability issues for high performance multilevel interconnect", Mat. Res. Soc. Symp. Proc. **337**, 24 (1994). © 1994, Materials Research Society, Pittsburgh, PA. Reproduced with permission.

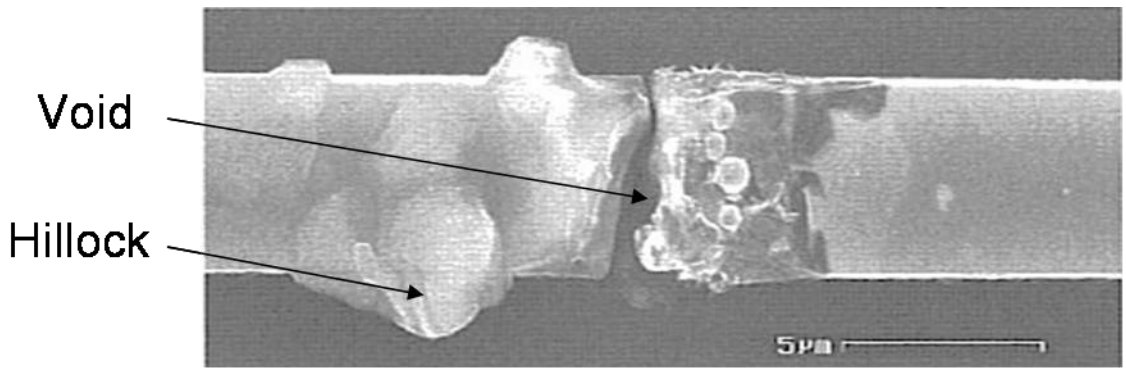


Figure 1-6. Damaged Al interconnect line showing the formation of hillock and void due to electromigration. Adopted from K. Wetzig and C. M. Schneider, *Metal Based Thin Films for Electronics*, 2nd Edition, 231 (Wiley-VCH, 2006), © Wiley-VCH Verlag GmbH & Co. KGaA. Reproduced with permission.

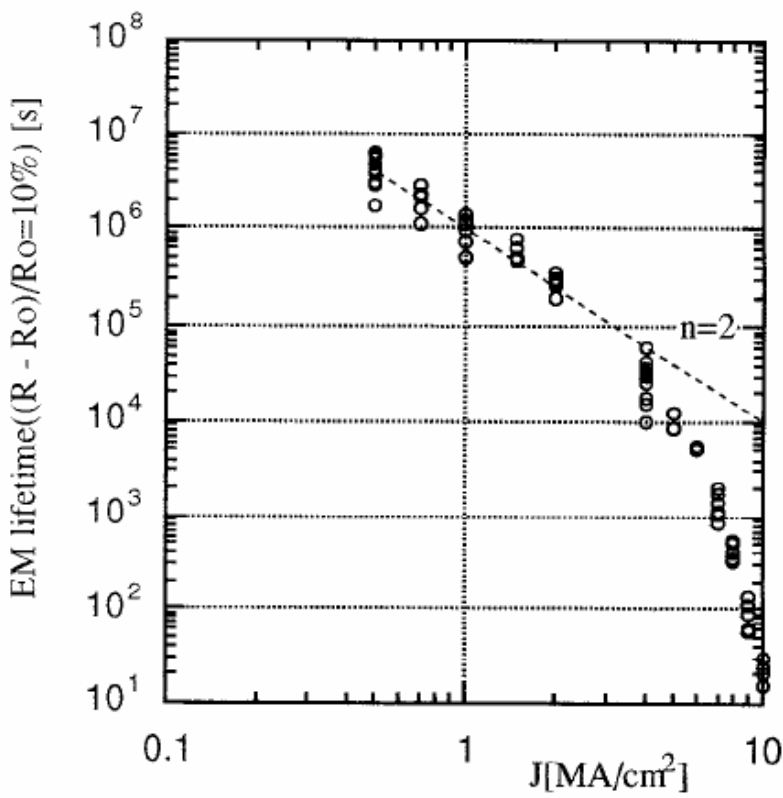


Figure 1-7. Electromigration lifetime for aluminum interconnects at different current densities.¹⁰ Adopted from M. Sakimoto, T. Fujii, H. Yamaguchi, and K. Eguchi, "Temperature measurement of Al metallization and the study of Black's model in high current density", Proceedings of the IEEE Reliability Physics Symposium, Las Vegas, NV, 333 (1995). © 1995 IEEE. Reproduced with permission.

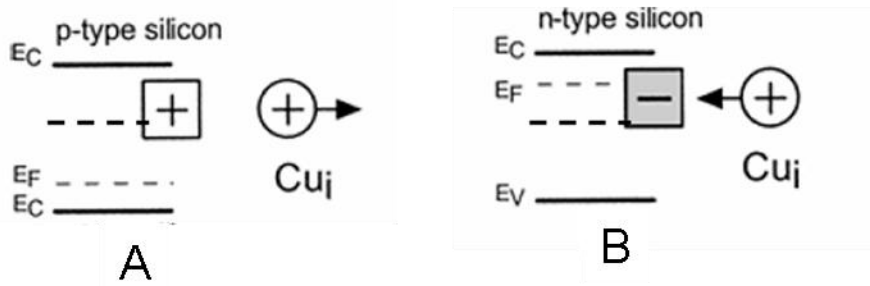


Figure 1-8. Band diagram of copper impurity in silicon. A) p-type silicon. B) n-type silicon¹³
 Adopted from A. A. Istratov, C. Flink, and E. R. Weber, "Impact of the unique physical properties of copper in silicon on characterization of copper diffusion barriers", *Physica Status Solidi B: Basic Research* 222, 261 (2000). © Wiley-VCH Verlag GmbH & Co. KGaA. Reproduced with permission.

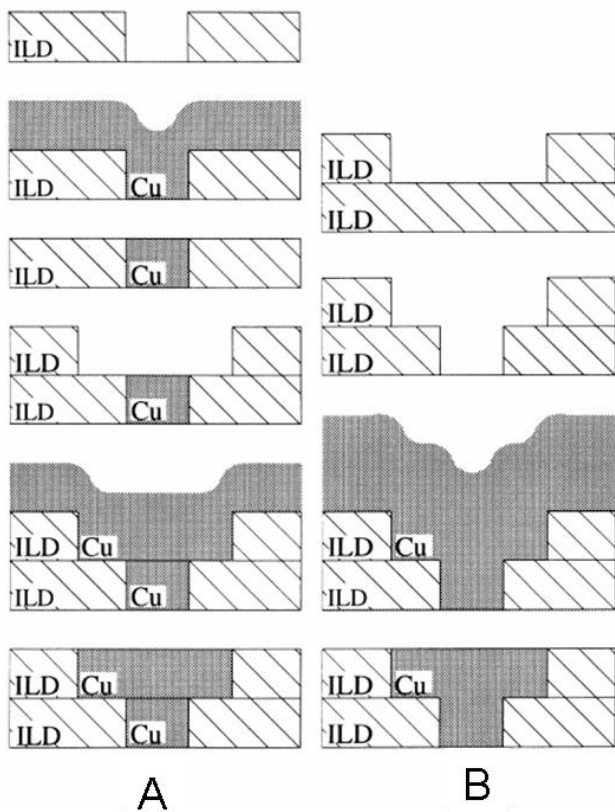
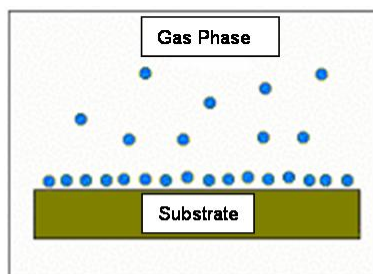
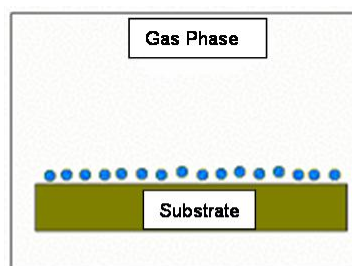


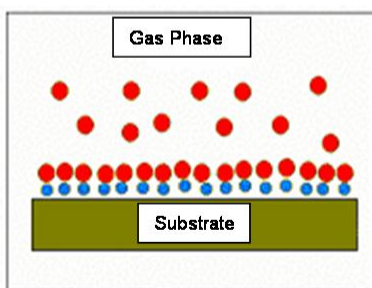
Figure 1-9. Simplified steps in damascene processing for copper deposition. A) Single damascene copper deposition. B) Dual-damascene copper deposition.³⁵ Adopted from D. T. Price, R. J. Gutmann, and S. P. Murarka, "Damascene copper interconnects with polymer ILDs", *Thin Solid Films* 308–309, 525 (1997). © Elsevier. Reproduced with permission.



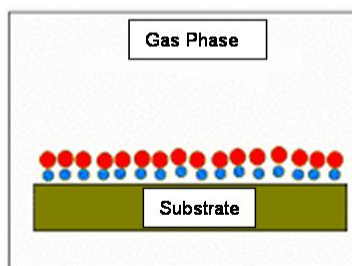
1. Adsorption of reactant A on substrate



2. Chemisorption of A on substrate and purging of excess A in gas phase



3. Introduction of reactant B.
 $A + B \rightarrow$ barrier film



4. Purging of reactant B

Figure 1-10. Schematic of one ALD cycle forming a monolayer of film

CHAPTER 2 LITERATURE REVIEW

2.1 Diffusion in Thin Films

To prevent diffusion of copper into silicon by depositing a barrier film between the two materials, it is important to understand the fundamental mechanism of diffusion through thin films. When two dissimilar materials are put in contact with one another, atoms from one material diffuse into the other and vice versa because of the difference in concentration gradient. Fick's law (Eq. 2-1 for 1D diffusion) gives a relation between the atomic flux at position x and the local concentration gradient of diffusing species.

$$J = -D \left(\frac{dC}{dx} \right) \quad (2-1)$$

The atomic concentration is C and atomic flux in direction x is J . For solids the diffusion coefficient, D , is most often expressed by Equation 2-2.

$$D = D_0 e^{\frac{-E_a}{RT}} \quad (2-2)$$

Where, D_0 is a constant which is independent of temperature. It depends on the thermodynamic and kinetic properties of interaction between the two materials. E_a is the activation energy for diffusion, R is the universal gas constant, and T is the temperature in K. The activation energy for diffusion depends on the mechanism of diffusion. Diffusion can occur for example by lattice diffusion, surface diffusion, grain boundary diffusion or dislocation diffusion. There is a hierarchy of diffusion rates for these mechanisms of diffusion. Experimental observations for diffusion reveal that the activation energy for diffusion through a material depends on its absolute melting temperature (Eq. 2-3).

$$E_a \propto A T_m \quad (2-3)$$

The proportionality constant, A , depends on many factors such as lattice structure and material interactions. The melting temperature (in Kelvin) of the film through which the material is diffusing is T_m . The values of A for surface, grain boundary, dislocation and lattice diffusion are 13, 17, 25 and 34 J/(gmol.K), respectively and the corresponding values of pre-exponential term D_0 are 0.014, 0.3, 2.1 and 0.5 cm²/sec, respectively.³⁶ Since the diffusion of material across surfaces is being considered, the surface diffusion can be ignored in the discussion. It is quite evident that the activation energy for diffusion is lower for grain boundary diffusion as compared to lattice diffusion. Since the diffusion coefficient varies exponentially with activation energy, the diffusion coefficient for grain boundary diffusion is several orders of magnitude higher than that for lattice diffusion.

Since both lattice and grain boundary diffusion depend on temperature, a cross over occurs where the mechanism of diffusion changes from one to the other. The temperature at which this crossover occurs is known as the Tammann temperature. It is widely believed that the Tammann temperature is between one-half or two-thirds of the melting temperature T_m of the solid.³⁷ Since almost all the potential diffusion barrier films have high melting temperature, grain boundary diffusion is the predominant mechanism by which diffusion occurs in these films. The problem becomes severe for thin film diffusion barriers because the grain boundaries in thin films are of the order of thickness of the film for polycrystalline films.

The discussion on various diffusion mechanisms reveals two important properties of a good diffusion barrier film: high melting temperature and defect-free microstructure. A high melting temperature material is expected to have a higher activation energy for diffusion. The primary reason why diffusion barrier research has focused on transition metal compounds is because of the high melting temperature of transition metals along with their compounds such as

nitrides and carbides. The melting temperature of some transition metals and their compounds are listed in Table 2-1.

A perfect diffusion barrier would have no grain boundaries or micro-structural defects. A defect-free single crystal would be the best diffusion barrier because of the absence of grain boundaries. However, lattice mismatch and thermal budget limitations make the growth of single crystal diffusion barriers difficult.³⁸ The next best solution is amorphous films as these films have no long range order. Hence, one of the primary structural requirements for diffusion barrier is to have amorphous microstructure. It should be noted that the material has to be perfectly amorphous. Nano-crystalline film, which has grain boundaries of the order of few nanometers, is worse than polycrystalline film as it provides a network of pathways through which copper could diffuse.

2.2 Refractory Carbides and Nitrides as Diffusion Barriers

The majority of research towards finding diffusion barrier materials for copper metallization has focused on transition metals and their compounds. In particular, transition metal nitrides and carbides have been extensively researched as diffusion barrier to copper. To understand what makes these refractory carbides and nitrides good candidates for diffusion barrier application in copper metallization, a brief survey of the general properties of these compounds is presented.

Transition metal carbides and nitrides can have a significant concentration of vacancies. These compounds can have significantly varying C or N content with appreciable vacancy concentration. Therefore, these compounds generally deviate from stoichiometric formulations. Carbon and nitrogen are interstitially located in the transition metal sublattice. Two kinds of bonding exist in these compounds, metal-to-metal and metal-to-nonmetal (C or N). The metal-

to-metal bonding is 'metallic' whereas the metal-to-nonmetal bonding is covalent. The metal-to-oxygen bonding is presumed to be ionic.

Transition metals and their compounds have many properties that make them good candidates for diffusion barrier application. Carbides and nitrides of transition metals have extremely high melting temperatures (2000 - 4000 °C) and are therefore referred to as 'refractory carbides and nitrides'. For instance, TaC has a melting temperature of 3983 °C, which is the highest melting temperature of any known material.³⁹ Since the activation energy for diffusion depends on the melting temperature of the compound (*vide supra*), refractory carbides and nitrides can be expected to be good barriers against copper diffusion.

Diffusion barrier films should show good mechanical stability because thin films deposited by vacuum processes are almost always under stress.⁴⁰ The processes subsequent to deposition of barrier films also involve thermal cycling and contribute to the stress levels in the barrier film. Poor mechanical strength could cause fracture of the film and lead to diffusion of copper through macroscopic gaps in the barrier film. Refractory carbides and nitrides are also known for their excellent mechanical stability. These compounds, such as TiN and WC, are extremely hard and have found application as wear-resistant coatings. While the exact reason for the extreme hardness of these materials is not known, it is believed that the presence of either C or N in transition metal stiffens the metal matrix resulting in increased hardness of refractory carbides and nitrides as compared to corresponding transition metals.³⁹ Refractory nitrides and carbides are brittle and they undergo minimal plastic deformation at low temperature (< 800 °C). However, these compounds become plastic at higher temperature.

Another important property of the barrier film is its electrical resistivity. In dual damascene processing, one trench and via feature is separated from the other by the barrier film.

The barrier film forms part of the interconnect stack and hence low resistivity of barrier film is desired. Most refractory carbides and nitrides are metallic in nature and have low resistivity. Moreover, the resistivity of these compounds shows little temperature dependence. The resistivity of refractory carbide or nitride thin film depends on factors such as porosity, non-metal to metal ratio and impurity concentration. Oxygen impurity is always present in refractory carbides and nitrides due to the high affinity of these compounds for oxygen. Oxygen in the lattice can scatter electrons and increase the resistivity of the film. It should be noted that even though refractory carbides have low resistivity in general, a large variation in resistivity values for the same refractory carbide or nitride is observed because of factors discussed above.

2.3 Deposition Methods for Diffusion Barrier Films

Thin films can be prepared by various techniques such as evaporation, PVD, CVD and ALD. Films for diffusion barrier applications have been predominantly deposited by PVD and CVD or one of their variants. The deposition technique is an important consideration for diffusion barrier film because many film properties depend strongly on the deposition process. Properties such as adhesion, microstructure, impurity concentration, within wafer uniformity, and conformality depend on the deposition process. This section details the advantages and limitations of most common deposition techniques for diffusion barrier film deposition. Important processing parameters for these deposition techniques and their general implications on film properties are also discussed.

2.3.1 Physical Vapor Deposition

In general, PVD includes deposition processes such as evaporation, sputtering, pulsed laser deposition, and high velocity oxygen fuel. For diffusion barrier film deposition, the most prominent PVD technique used is sputtering. In sputtering, ions generated by a plasma are accelerated towards the target (substrate). The sputtered target atoms deposit on the substrate

resulting in the formation of thin film. Plasma generation can be done either by radio frequency (RF) or direct current (DC). Radio frequency sputtering is used for a non-conducting target, whereas DC sputtering is used for conducting targets. When a magnetron is used to trap the electrons in the plasma closer to the target for low pressure plasma sustainability, the process is referred to as magnetron sputtering. For deposition of a metallic substance, pure metal is used as the target. To deposit alloys such as WN_x , a reactive gas (e.g., N_2) is used along with an inert gas to incorporate nitrogen into the metal. This process is often referred to as reactive ion sputtering.

Important processing parameters for PVD are deposition pressure, applied voltage, target to substrate distance, partial pressure of reactive gas (for reactive ion sputtering), substrate temperature, and bias voltage on the substrate. The most important factor affecting the film properties is the energy of sputtered particles at the substrate surface. Applied voltage, target-to-substrate distance, chamber pressure and bias voltage on the substrate determine the energy of the sputtered particles impacting the surface of the substrate. Applied voltage determines the energy of the sputtered particles ejected from the target surface. The deposition pressure determines the mean free path of the sputtered particles. The higher the mean free path, the higher the kinetic energy of the particles deposited on the substrate. The target-to-substrate distance, chamber pressure, and the bias on the substrate determine how much of the energy of the sputtered particle is lost due to collisions prior to reaching the substrate surface. All these factors can influence the film adhesion, porosity, crystallinity, texture, and substrate damage. The substrate temperature can also influence the crystallinity and texture of the deposited film.⁴¹ The partial pressure of reactive gas used in reactive ion sputtering can influence the incorporation of reactant atoms in the deposited films.⁴²

The advantages of sputtering are good film adhesion, uniform film deposition, low contamination and ease of deposition. The stoichiometry of alloys deposited by reactive ion etching can also be altered easily by changing the partial pressure of reactant gas. The major disadvantage of this technique is that it has poor conformality for ultra-thin barrier film deposition. While I-PVD can extend the use of PVD technique by improving the conformality of films deposited by PVD^{28,43}, new deposition techniques will be required in the future to deposit highly conformal films in high aspect ratio features. Another disadvantage of PVD is the columnar microstructure of films deposited by PVD. Columnar microstructure provides short pathways for copper to diffuse along grain boundaries.

Although it is well acknowledged that PVD cannot be extended to deposition of ultra thin barrier films, researchers have used the technique extensively because PVD is one of the easiest techniques to test new materials for diffusion barrier application. Unlike CVD which requires suitable precursors for deposition of thin films, PVD only needs a suitable target of good purity for deposition. A review of PVD films is not included in this section because PVD process is not capable of depositing ultra thin barrier films for future interconnects. Moreover, films of a particular material deposited by PVD films can have markedly different properties than the same material deposited by CVD because of the differences in deposition mechanism.

2.3.2 Chemical Vapor Deposition

In CVD, gaseous reactants or precursors are used to deposit thin films onto the substrate. For deposition of diffusion barrier film, the different variants of CVD that have been predominantly used are plasma enhanced CVD (PECVD), low pressure CVD (LPCVD), metal-organic CVD (MOCVD), aerosol assisted CVD (AACVD), atomic layer CVD (ALCVD or ALD) and plasma assisted ALD (PAALD).

The important processing parameters for a CVD reactor are reactor pressure, precursor(s) selection and their carrier gas flow rates, substrate temperature, and for PECVD and PAALD, power of plasma. The reactor pressure determines the number of collisions that involve the precursor molecules in the gas phase, which is important for determining the rate of homogenous gas phase reactions. The reactor pressure together with carrier gas flow rates and substrate temperature determine the flow dynamics inside the reactor. The thermal energy supplied to the substrate aids the precursor decomposition on the substrate surface and is important to determining the rate of heterogeneous reactions.

A characteristic growth curve for thermal CVD is shown in Figure 2-1. Two distinct growth rate regimes are visible in the curve. At low deposition temperature, there is an exponential increase in film growth rate with deposition temperature. This behavior is observed when the rate determining step for the film growth is thermally activated, most commonly by surface reaction, hence this growth rate regime is often termed ‘reaction limited’ or ‘kinetically controlled’. The growth rate in this growth regime, G , is given by Equation 2-4.

$$G = Ae^{\frac{-E_a}{RT}} \quad (2-4)$$

The activation energy for the film growth is E_a , proportionality constant is A , the universal gas constant is R and the absolute temperature of deposition is T . The slope of the plot of $\ln(G)$ vs. $1/T$ gives the value of E_a .

At higher deposition temperature, the film growth rate is proportional to T^m , where m has a value of approximately 1.5. In this growth regime, the rate determining step is the mass transfer of the precursor to the substrate surface and hence it is often termed ‘mass transfer controlled’ growth regime. This growth regime is sensitive to the reactor pressure and flow dynamics of the reactor. By reducing the reactor pressure, the growth rate increases because the boundary layer

thickness decreases with decrease in pressure. A decrease in boundary layer thickness increases the mass transfer of the reactants to the substrate surface and increases the film growth rate.

A CVD process uses a heated substrate to aid the decomposition of the precursor(s) on the substrate. In PECVD, a plasma is used to aid the decomposition of the precursor(s). The primary advantage of PECVD is that the plasma facilitates the deposition of films at low temperature as compared to thermal CVD. This is particularly important when halides such as WF_6 or WCl_6 are used as precursors because halide precursors usually require very high temperature for decomposition. The disadvantage of PECVD is that plasma gives directionality to the atoms, molecules and/or ions and this has an adverse effect on the conformality of deposited film. Another disadvantage of PECVD is that excessive fragmentation of the precursor leads to incorporation of impurities such as halides into the film. Halide impurities are undesirable in diffusion barrier films since they can increase the resistivity of the film. Moreover, halides present at the interface are known to create adhesion problems between the barrier and copper.⁴⁴ Excessive fragmentation can also lead to deposition of undesirable compounds. For instance, PECVD of WN_x has W also present in the film. Precise control of the precursor fragmentation due to the plasma is difficult. The plasma can also result in damage to the substrate surface.

In LPCVD, the deposition of thin films is carried out at sub-atmospheric pressures. Low pressure increases the mean free path of the precursor(s), which in turn decreases the collision rate of precursor molecules and carrier gas in the gas phase prior to reaching the substrate surface. Low pressure also improves the within wafer uniformity of the film. Most CVD processes used in the semiconductor industry are LPCVD processes.

In MOCVD, a metal-organic precursor is used for deposition of thin film. As compared to CVD, which uses inorganic precursors, MOCVD has many advantages. Inorganic precursors predominantly use halogen containing precursors such as WCl_6 , which are corrosive. Moreover, the byproducts of the halogen containing precursors are HCl or HF, which are also very corrosive and can etch the underlying substrate. Films deposited by halogen containing precursors have shown pitting because of the etching action of precursor or byproducts (*vide infra*). In general, halogen containing precursors are hazardous and need special handling. In MOCVD, the precursor is mostly non-corrosive. The metal organic precursor may or may not have halide containing ligands. Most of the by-products of metal-organic precursors that do not contain halides are non-corrosive and hence do not cause pitting of the substrate. Even for halogen containing metal-organic precursors, the likelihood of pitting is less because of the presence of non-corrosive organic byproducts. A limitation of MOCVD is that sometimes carbon containing ligands can also incorporate into the film. The C impurity can be either beneficial or not depending on application of the thin film. For diffusion barrier application, particularly for WN_x , a small amount of C is beneficial because it can increase the recrystallization temperature of the film. But greater amounts of C deposition can lead to significant increase in film resistivity and hence is not desirable for diffusion barrier film. Overall, MOCVD is a very good technique for diffusion barrier film deposition because of its low deposition temperature, non-corrosive precursor, minimal halide contamination, and minimal substrate damage.

AACVD is a variant of CVD where solid precursor is dissolved in a solvent and delivered to the reactor by aerosol generation. The aerosol generation is achieved by a nebulizer and the aerosol is transferred to the reactor by carrier gas. The advantage of using AACVD is that solid

precursors with low vapor pressure can be delivered to the CVD reactor. The disadvantage of AACVD is that the solvent could participate in the homogenous or heterogeneous reactions, thereby altering the film properties.

ALD (or ALCVD) is a limiting case of CVD in which the substrate is exposed to the precursors in a sequential manner to achieve self-limiting growth (*vide supra*). The major advantage of the ALD process is the precise thickness control and excellent conformality. Since the growth of film occurs layer by layer, an ALD process can give very good thickness control and the conformality is also excellent. In fact, researchers have shown that even in features with 200:1 aspect ratio, the ALD process achieves excellent conformality.⁴⁵ Another important advantage of ALD is that since the precursors are introduced in the reactor alternately, there is no homogenous reaction of precursors.

The two plots that are characteristic of an ALD process are growth rate versus temperature and growth rate versus precursor exposure time (Figures 2-2 and 2-3). In Figure 2-2, the growth rate increases linearly with temperature at lower temperature. Since the precursor adsorption and reaction between precursor and surface are thermally activated processes, the thermal energy available for precursor reaction at low deposition temperature is insufficient to achieve complete saturation or reaction.⁴⁶ The second growth regime is characterized by film growth rate independent of temperature. This region is often referred to as the 'process window' of ALD because the film growth rate is insensitive to substrate temperature. The third growth regime is characterized by decomposition of the precursor resulting in a 'CVD-like' growth. Figure 2-3 shows how the growth rate of film varies with exposure time. Initially when complete saturation of the surface is not achieved, film growth rate increases with an increase in the exposure time. Once complete saturation is achieved, the growth rate is independent of precursor exposure time,

unless sufficient time is given for chemical reaction between the chemisorb layer and any gas phase species, including impurities.

2.4 Characterization and Testing of Diffusion Barrier Films

Diffusion barrier films need to be characterized to understand the factors that affect the diffusion barrier performance of the film. The barrier film also needs to be tested for its ability to prevent copper diffusion. This section summarizes various techniques that have been used for diffusion barrier film characterization and testing.

2.4.1 Diffusion Barrier Film Characterization

There are a number of properties of the deposited film that are very important. These include microstructure, composition, density, resistivity, thickness, surface roughness, bonding between different atoms and adhesion of barrier film to copper and dielectric (low- k or SiO_2). Various techniques used to analyze these film properties are listed in Table 2-2. This section details the efficacy of each technique in analyzing various film properties without discussing the guiding principles of each technique. Detailed explanation of principles of analysis techniques used in the present work are given in the Chapter 3.

X-ray diffraction (XRD) is the most common technique used to determine the crystallinity and microstructure of thin films. For ultra thin films, grazing incidence XRD (GIXD) is used because it has a small depth of resolution. These techniques can also determine the texture of the films. Electron diffraction is another highly sensitive technique that can determine the crystallinity in thin films. Imaging techniques such as SEM and TEM can provide information on grain structure of the films. High resolution images have been used by many researchers to determine whether the films have equiaxed or columnar microstructure.

Film composition can be determined by Auger electron spectroscopy (AES), X-ray photoelectron spectroscopy (XPS), secondary ion mass spectroscopy (SIMS), energy dispersive

X-ray spectroscopy (EDS), Rutherford back scattering (RBS) and elastic recoil detection analysis (ERDA). Auger electron spectroscopy and XPS are very effective techniques in determining the elements present in the deposited film. All the elements in the periodic table, except H and He, can be detected by using AES and XPS. However, film composition determination requires the calibration to identify the relative sensitivity factors needed for quantification in both AES and XPS. Pure elemental sensitivity factors can be used for quantification to obtain an estimate of film composition but elemental sensitivity factors do not account for the matrix effect. Both techniques have a detection limit of approx. 1 at. %. Both AES and XPS are surface sensitive techniques with sampling depth of few tens of nanometers. Both these techniques have been widely used for film composition determination and depth profiling of diffusion barrier films. Secondary ion mass spectroscopy can be used for determination of film content, but this technique is not used for determination of film composition. Its main use is in determination of trace impurities in the film. The technique can detect impurity concentrations of ppm or even ppb levels. The technique can also detect presence of H and He in the film. Energy dispersive spectroscopy is another technique that has been used to determine elements present in the film, however it can determine film composition only semi-quantitatively. This technique can detect elements with atomic number greater or equal to 6. Since EDS has poorer sensitivity to lighter elements in a heavy element matrix, this technique is not commonly used for transition metal nitrides and carbides. The sensitivity of this technique is 1 at. %. Rutherford back scattering (RBS) has been widely used for film composition determination of barrier films. This technique has the advantage of not requiring standards for film composition determination. The detection limit of RBS is about 4 at. % and hence this technique is not suitable for trace impurity detection. Elastic recoil detection analysis is a complimentary technique to RBS and it can detect lighter

elements such as H in heavier element matrix. This technique has been widely used to determine H element composition in deposited films. This technique has a detection limit of 0.1 at. % and a depth of resolution of few tens of nanometers.

The common techniques used to determine film thickness are cross sectional scanning electron microscopy (X-SEM) and transmission electron microscopy (TEM) imaging. Both these techniques provide an accurate measure of film thickness. Film thickness from profilometer measurements requires depositing film on a section of the substrate and profiling the step created by the film on the substrate. The accuracy of this technique depends on the resolution of the profilometer, which is usually few tens of angstroms. Rutherford back scattering and XRR can also provide measurement of film thickness, but these techniques are indirect techniques. The accuracy of the measurement by RBS and XRR depends on the accuracy of the variables used in simulation.

Two techniques that have been prominently used to determine film density are RBS and XRR. Both these techniques are indirect techniques for density measurement. Rutherford back scattering uses atomic density and the thickness obtained from either SEM or TEM analysis to simulate the value of film density. Film density can be obtained from XRR by simulating the fringes in the spectrum. Simulation of XRR pattern requires accurate values of film thickness and roughness. Accuracy of both XRR and RBS in determining film density depends on the accuracy of parameters used in the simulation.

The most common technique for determination of diffusion barrier resistivity is four point probe. Four point probe determines the value of sheet resistance and this value when multiplied with the film thickness (from SEM or TEM) gives the resistivity of the film. Bonding between elements present in the film can be determined by XPS analysis. The change in bonding state of

an atom results in a shift in the binding energy observed in XPS spectra. This shift in binding energy can be used to determine the atomic bonding of a particular element in the film. X-ray photoelectron spectroscopy is the only technique that can give the bonding information of atoms in thin films.

Surface roughness of the film can be determined by various techniques such as AFM, stylus profilometer, scanning tunneling microscopy (STM), optical profilometer, SEM, TEM and X-ray reflectivity (XRR). Of these techniques, AFM and stylus profilometer are contact techniques because the probe used for roughness measurement is in contact with the surface. Non-contact techniques used for surface roughness measurement include STM, optical profilometer, SEM, TEM and XRR.

Among the contact measurement techniques, AFM provides the best surface resolution of a fraction of an Ångstrom. Atomic force microscopy can give 3-dimensional images of the scanned surface and provide values of root-mean squared (RMS) surface roughness and average grain size. The probe used in AFM is a cantilever that scans across the surface. A stylus profilometer uses a diamond stylus to scan across a surface and provide 2-dimensional image of the surface. The resolution of a stylus profilometer is few tens of nanometer. Stylus profilometer is commonly used to measure uniformity of film in trenches or vias, whereas AFM is commonly used to measure surface roughness of a blanket film. Since both AFM and stylus profilometer are contact measurement techniques, they can damage the surface because of scratching by the probe.

Non-contact techniques include imaging techniques such as SEM and TEM. These techniques are good for qualitative determination of surface roughness but not suitable to obtain RMS roughness. An optical profilometer uses light scattering to probe the surface roughness.

This technique has a good spatial resolution of few nanometers and can provide 3-dimensional images as well as RMS roughness of the film. The disadvantage of this technique is that the surface has to be reflective. Since most of the diffusion barrier films are metallic in nature, this technique can be used to measure surface roughness of diffusion barrier films. X-ray reflectivity is an indirect method for surface roughness measurement and it requires accurate values of film thickness and density to simulate fringes in the XRR spectra. X-ray reflectivity is not commonly used for surface roughness measurement. Scanning tunneling microscopy uses a very sharp probe which tunnels current through the sample surface to obtain images of the surface with atomic scale resolution. This technique requires very careful sample preparation and the imaging area is very small. Hence this technique is not commonly used to measure surface roughness of diffusion barrier films.

The best method to determine the adhesion strength of a barrier to copper and dielectric is the four point bend test. This test measures the adhesion energies of interfaces in a multilayer thin film stack. Another method that is commonly used to determine the adhesion of barrier film qualitatively is the Scotch tape test. This test uses an adhesive tape that is applied to the thin film and the tape is pulled to determine if the thin film adheres to the substrate. The Scotch tape test is primarily used for preliminary evaluation of barrier film adhesion to copper and dielectric.

2.4.2 Diffusion Barrier Testing

Various direct and indirect methods are used to test the effectiveness of diffusion barrier film in preventing copper diffusion. There are numerous techniques that can detect copper diffusion through the barrier into silicon and the most effective technique to detect trace amount of copper in silicon is electrical characterization. For a MOS test structure, electrical characterization techniques that are used to detect trace amount of copper in silicon or SiO₂ are flat band voltage shift in CV measurement, I-V measurement and triangular voltage sweep

(TVS).⁴⁷ For a Schottky contact test structure, the transient ion drift (TID) method can be used to detect and quantify the amount of copper that has diffused into silicon through the barrier after the film has been subjected to thermal stress or bias temperature stress.

Ideally, a diffusion barrier test should involve integration of the barrier in actual chip followed by electrical characterization to determine the barrier performance. However, preliminary diffusion barrier testing is often done on test structures such as a MOS capacitor to check for diffusion of copper through the barrier film. In a MOS test structure, copper metal dots are deposited on barrier/ SiO₂/ Si stack. The test structure is then stressed at high temperature (150 – 300 °C) under a bias of few MV/cm. This accelerated diffusion test is often referred to as bias temperature stress (BTS). Electrical characterization is then done to detect any diffusion of copper through the barrier into the oxide and silicon. In CV measurement, the flat band voltage is measured before and after BTS. If copper has diffused through the barrier film, the flat band voltage shifts indicating that the barrier film has failed. The I-V measurement can also be done on a MOS capacitor after BTS. In an I-V measurement, if the leakage current density of the capacitor is higher than 10⁻⁶ A/cm² for the applied electric field of 1.2 MV/cm, then the capacitor is considered a failed capacitor.⁴⁸ A leaked capacitor would mean that copper has diffused through the barrier film. In TVS measurement, a positive voltage is applied to the copper electrode and is slowly made negative at a constant rate. If copper has diffused through the barrier, the mobile copper ions are injected back into the oxide from the Si-SiO₂ interface. This results in a jump in the measured current and copper diffusion through the barrier can be detected. Among the three techniques, i.e. flat band voltage shift in CV measurement, I-V measurement and TVS, the TVS technique is the most sensitive in detecting the presence of copper in silicon.⁴⁸

In the TID technique, a Schottky barrier test structure is made by depositing barrier film on p-type Si. Copper metal dots are then deposited on the barrier and encapsulated by a protection layer.⁴⁹ If the Schottky test structure is quenched after thermal stressing, most of the copper in silicon remains as an interstitial for a few hours.⁵⁰ The interstitial copper ions in silicon tend to drift out when high electric field is applied. The resulting change in electric charge distribution induces a transient capacitance signal, which can be correlated to the copper ion concentration in silicon. This method has a detection limit of 10^{12} at/cm³.

For preliminary evaluation of diffusion barrier efficacy, researchers have used other simpler techniques that do not require fabrication of a device. In one such test, a Cu/barrier/Si (or SiO₂) structure is thermally stressed by annealing at temperatures between 200 and 800 °C. The higher the temperature at which the barrier shows copper diffusion into silicon, the better is the diffusion barrier performance. The diffusion of copper through the barrier is then detected by various techniques such as four point probe, depth profiling (by AES, XPS or SIMS) and XRD. Four point probe measurement gives the sheet resistance of the Cu/barrier/Si(SiO₂) stack. When copper diffuses through barrier film, there is a sharp increase in sheet resistance. Depth profiling by AES, XPS or SIMS uses Ar⁺ sputtering to sample through the Cu/barrier/Si(SiO₂) stack and detect if copper has diffused through the barrier into silicon. The disadvantage of depth profiling is that copper can be knocked forward the barrier film during the Ar⁺ sputtering and the resulting artifact could give a false positive. A solution to the ‘knock-on’ problem with sputtering is to etch the copper layer after thermal stressing and prior to depth profiling. Since bulk copper has been etched, the ‘knock-on’ effect due to sputtering can be avoided. The detection limit for copper by depth profiling depends on the technique used for elemental detection. Secondary ion mass spectroscopy provides the best resolution in detecting the presence of copper (detection

limit ca. 10^{15} atoms/cm³). Both AES and XPS can detect copper if its concentration in silicon is ca. 1 at. %. Pre- and post anneal XRD measurements can provide information on diffusion of copper through the barrier and into the silicon. Copper forms Cu₃Si in silicon at a relatively low temperature of 150 °C. The annealing temperature at which Cu₃Si peaks appear in the XRD spectra indicates the lowest temperature at which the barrier film has failed. All these techniques, i.e. sheet resistance measurement, XRD, four point probe measurement and depth profiling, have poorer resolution in detecting copper in silicon than electrical characterization. However, these techniques can be very helpful in preliminary screening of diffusion barrier films as these techniques are much simpler than electrical characterization.

Most of the research on diffusion barriers has been focused on refractory nitrides and carbonitrides of Ti, Ta and W (*vide supra*). The following sections review the work done on refractory nitrides and carbonitride thin films of Ti, Ta and W deposited by CVD and ALD techniques with primary focus on the suitability of these films for diffusion barrier application.

2.5 Titanium Nitride as Diffusion Barrier

2.5.1 Chemical Vapor Deposition of Titanium Nitride

Table 2-3 shows the inorganic and metal organic precursors that have been used to deposit TiN_x thin films by CVD. TiN_x has been deposited using the inorganic precursors TiCl₄ and TiI₄ as Ti source and NH₃ or N₂ plasma as N source. Thermodynamically, the reaction between TiCl₄ and NH₃ is feasible at temperature as low as 300 °C, but appreciable film growth rate is observed only at 400 °C by thermal CVD.⁵¹ Two different processes, LPCVD and APCVD (atmospheric pressure chemical vapor deposition) have been used for thermal reaction of TiCl₄ and NH₃. Both APCVD and LPCVD deposit nearly stoichiometric TiN films with N:Ti ratio close to 1. Deposition by APCVD gives more uniform growth but the film contains a large amount of Cl impurity. At 400 °C, the films contain as high as 50±20 at. % Cl impurity. Increasing the

deposition temperature leads to decrease in Cl content and films deposited at 620 °C have Cl content of 5 ± 2 at. %.⁵¹ Film resistivity has a direct correlation with the Cl content of film. The resistivity of film decreases from 6000 $\mu\Omega$ -cm for films grown at 400 °C to 200 $\mu\Omega$ -cm for films grown at 620 °C. When LPCVD is used to deposit TiN films from TiCl₄ and NH₃, the film impurity content and resistivity are better than those deposited by APCVD. Films deposited by LPCVD show 3 - 4 at. % Cl impurity for deposition at 450 °C and high quality films with impurity content below the detection limit of AES and RBS are deposited at 650 °C.⁵² However, O and H content in the film increases with increasing deposition temperature. Because of low Cl content, films deposited with LPCVD have a lower resistivity. Resistivity of the film decreases from 290 $\mu\Omega$ -cm for films grown at 450 °C to 110 $\mu\Omega$ -cm for films grown at 700 °C. The XRD spectra of films deposited below 600 °C show that TiN films are textured with (200) preferred orientation. However, the films deposited at 700 °C show a preferred orientation of (111).⁵³ Diffusion barrier testing by leakage current testing on p⁺n junction of TiN/TiSi₂ bilayer deposited with CVD showed that the bilayer was able to prevent copper diffusion after annealing at 550 °C for 30 min in N₂ environment.⁵⁴ Annealing above 550 °C caused an increase in leakage current suggesting that copper had diffused through the barrier film.

The main challenge for the LPCVD TiN process from TiCl₄ and NH₃ is the high Cl content of film for low temperature deposition. It is believed that Cl impurities in the film have high diffusivity. If these impurities diffuse to the interface, corrosion and adhesion problems can result. Increasing deposition temperature does reduce Cl content, but higher temperature processing is not desirable because of the thermal instability of low-*k* dielectrics above 450 °C. Yokoyama et al.⁵³ tried to use high temperature anneal in H₂ environment to remove Cl impurity from the film. The process did reduce the Cl content of film from 5.7 at. % to 2.7 at. % after

annealing at 1000 °C for 30 min., but the complete Cl elimination from the film was not achieved. The N:Ti ratio of the film also decreased from 1.02 to 0.97 after the annealing process, suggesting that the Cl and N are lost from the film as NH₄Cl. Chlorine remains in the film after annealing due to the low volatility of TiN_xCl_y even at 1000 °C. Besides the Cl problem, LPCVD from TiCl₄ deposits polycrystalline films that have columnar microstructure. As discussed earlier, columnar microstructure provides short diffusion pathways for copper diffusion and is highly undesirable. The process has problems with particulates because NH₃ reacts with TiCl₄ to form NH₄Cl, a white solid. TiCl₄ also reacts with NH₃ at room temperature to form TiCl₄.2NH₃, which is also a solid.⁵⁵ This problem cannot be solved without changing the precursor chemistry of deposition.

To address the Cl impurity concern, two different approaches have been attempted. One is the use of an alternate halide source such as TiI₄ and the other is the use of N₂ plasma as N source. TiI₄ approach is believed to lower the halide content of film because the Ti-I bond is weaker than the Ti-Cl bond. The heat of formation of Ti-I at 298 K is -92 kcal/mol whereas the heat of formation of Ti-Cl is -192 kcal/mol at 298 K.⁵⁶ Moreover, since I is a larger element compared to Cl, it would require much higher activation energy as compared to Cl to diffuse out of TiN_x and into the Si. TiN_x deposition by LPCVD from TiI₄ and NH₃ shows that the films deposited are nearly stoichiometric with N:Ti ratio of 1.06:1 at 430 °C deposition temperature.^{56,57} The I and O impurities in films are less than 2 and 1 at. %, respectively. The density of the film is also higher by approx. 10 % as compared to the density of PVD TiN_x film. The film has resistivity as low as 100 μΩ-cm and the step coverage in a 0.5 μm 3:1 AR feature is 90%. The TiI₄ process does yield better films as compared to films deposited using TiCl₄.

However, the films are still polycrystalline and amorphous film growth could not be realized.

Diffusion barrier testing for copper metallization was not reported for films deposited with TiI_4 .

PECVD has been used to deposit TiN_x using TiCl_4 and $\text{H}_2 + \text{N}_2$ plasma.^{58,59} When RF $\text{H}_2 + \text{N}_2$ plasma is used, violet colored films were deposited below $300\text{ }^\circ\text{C}$.⁵⁹ The authors argued that the films were probably TiCl_3 . A minimum temperature of $300\text{ }^\circ\text{C}$ was required to deposit TiN_x films. The films deposited at and above $300\text{ }^\circ\text{C}$ were TiN_x . The films were slightly Ti-rich and the lowest Cl content was 3 at. % at $500\text{ }^\circ\text{C}$ deposition temperature. Increasing the H_2 flow resulted in an increase in Cl content, whereas an increase in the N_2 flow decreased the Cl content of the film. Other properties of the film deposited with plasma assistance were similar to those for film deposited by LPCVD process. While the use of plasma did allow deposition to occur at lower deposition temperature, higher temperature close to $500\text{ }^\circ\text{C}$ was still needed to deposit films with minimal Cl impurity and low resistivity. So, the plasma process did not show any significant advantage over the LPCVD process.

Tetrakis (dimethylamido) titanium (TDMAT) has been used as a precursor for TiN deposition. When TDMAT is used in an inert atmosphere as a single source precursor, TiN_xC_y films are deposited.⁶⁰ Films can be deposited at temperature as low as $250\text{ }^\circ\text{C}$.⁶¹ Film deposited at $300\text{ }^\circ\text{C}$ has 27 at. % Ti, 17 at. % N, 11 at. % O and 35.2 at. % of C. X-ray photoelectron spectroscopy analysis of the film shows that the C in the film exists in both carbidic form (bonded to Ti) and amorphous or organic form.⁶² Films are also resistive, with the resistivity varying from 1500 to 5000 $\mu\Omega\text{-cm}$. The films showed an ‘aging’ effect as evidenced by the post growth increase in resistivity with time due to oxygen and moisture incorporation in the film. Diffusion barrier testing of the film shows that the barrier fails after vacuum annealing at $500\text{ }^\circ\text{C}$. The poor performance of the barrier films was attributed to the porous nature of the film.⁶³

When TDMAT is used with H_2 and NH_3 , films were nearly stoichiometric with N:Ti ratio of 1.⁶⁴ Since TDMAT undergoes transamination reaction in solution, NH_3 was used as co-reactant to aid the transamination reaction in gas phase. The transamination reaction also lowers the C incorporation in the films.⁶⁵ The films have a low C content of less than 3 at. % and the O content of the film varied between 4 and 9 at. %. The use of NH_3 has a significant effect on the lowest deposition temperature for film growth. Films could be deposited at temperatures as low as 30 °C. The films also showed an ‘aging’ effect as the resistivity of the film increased by 20 % within 24 hours of exposure to the ambient. The films were quite conductive and the resistivity varied between 400 to 1500 $\mu\Omega$ -cm for as deposited films. However, the films were polycrystalline and showed columnar microstructure.⁶⁴ Moreover, films deposited with NH_3 showed poor step coverage and the films were less conformal at higher deposition temperature.⁶⁶ The conformality of the film was 30 % at 450 °C deposition temperature. So, the process with NH_3 is not suitable for diffusion barrier application.

Hydrazine (N_2H_4) has been used as a co-reactant with and without NH_3 to deposit TiN_x thin films using TDMAT.⁶⁷ N_2H_4 has a higher N:H ratio and lower dissociation temperature (140 °C) as compared to NH_3 . When N_2H_4 is used with TDMAT to deposit thin films, the N:Ti ratio of film can be modulated by changing the N_2H_4 :TDMAT ratio. The films contain very high O content (ca. 36 at. % at 100 °C deposition temperature). The films also show the ‘aging’ effect and the film resistivity more than doubles after 150 min exposure to ambient. The resistivity of the as deposited film is 3000 $\mu\Omega$ -cm for deposition at 200 °C. The ‘aging’ effect is attributed to the diffusion and subsequent reaction of oxygen with the unsaturated Ti atoms. To improve the film properties, a mixture of N_2H_4 and NH_3 was used to deposit thin films. The films deposited with N_2H_4 and NH_3 were polycrystalline and nearly stoichiometric TiN with O content below the

detection limit of RBS. The authors argued that while N_2H_4 was a better reducing agent, NH_3 was a better transamination reagent. So, the films deposited with N_2H_4 and NH_3 had the best film properties. The resistivity of the film was ca. $1000 \mu\Omega\text{-cm}$ so the use of NH_3 with N_2H_4 couldn't lower the film resistivity. No diffusion barrier testing on these films has been reported so far.

Plasma has been used both during growth and post-growth to improve the properties of film deposited with TDMAT. When the N_2 plasma treatment is used post-growth, films show an increase in N:Ti ratio.^{68,69} The C content of the film decreases from 23 at. % to 3 at. % upon exposure to N_2 plasma. The films also show a low resistivity of $720 \mu\Omega\text{-cm}$ and no 'aging' effect is observed for plasma exposed films. The decrease in resistivity due to plasma exposure is believed to be because of a decrease in (N+C+O):Ti ratio because N, C and O act as scattering centers for electrons.⁶⁹ The plasma treatment is helpful only if done *in situ*. Once the films are exposed to the ambient, subsequent plasma exposure does not cause a dramatic improvement in film properties. Plasma exposure also increases the film density. The plasma exposure, however, does not have any effect on diffusion barrier performance of the film. Films that are exposed to N_2 plasma after deposition fail at the same temperature of $550 \text{ }^\circ\text{C}$ as the films that are not exposed to plasma.

Tetrakis(ethylmethylamido) titanium (TDEAT) has been used as a Ti precursor to deposit TiN_x films with and without co-reactant NH_3 . When the precursor is used without NH_3 , a minimum temperature of $350 \text{ }^\circ\text{C}$ is required for thin film deposition.⁷⁰ For films deposited at $450 \text{ }^\circ\text{C}$, the film has a N:Ti ratio of 1. The films have significant C content (20 at. %) suggesting that the films are actually TiN_xC_y . The films have a high O contamination of 18 at. % possibly because of the post growth diffusion of O in porous TiN_xC_y films. The film density has a value

of 3.0 g/cc, which is low as compared to the bulk TiN density of 5.4 g/cc. The film shows an ‘aging effect’, whereby the film resistivity increases with exposure time to the ambient because of the adsorption of O in the film. The resistivity of film deposited at 420 °C increases from 1500 $\mu\Omega$ -cm to ca. 8000 $\mu\Omega$ -cm after exposure to air for 24 hr.⁶⁸ To improve the film resistivity, *in situ* N₂ plasma exposure was employed. The plasma process densifies the films and incorporates N into the film as evidenced by the increase in N content from 23 to 44 at. % after plasma exposure. The C content of the film also shows a small decrease from 30 to 23 at. % after plasma exposure. The O in the film is decreased to below 3 at. % by plasma exposure resulting in a decrease in film resistivity to below 1000 $\mu\Omega$ -cm. The film does not show an ‘aging effect’ as the film resistivity increases by only 4 % after air exposure for 24 hr. Since Wang et al.⁶⁸ deposited TiN_x for application as a barrier for W in plugs, no copper diffusion testing was performed.

To improve the properties of films deposited with TDEAT, NH₃ has been used as a co-reactant. With NH₃, TDEAT shows an increase in growth rate by a factor of 2 - 3 as compared to deposition without NH₃.⁷⁰ It is believed that this increase in growth rate is because of transamination. The films are slightly N-rich with N:Ti ratio of 1.2:1 for deposition at 425 °C. The C and O contamination in the film is ca. 0.5 at. %. The films deposited with NH₃ have a higher density of 4.2 g/cc (at 425°C) as compared to that for films deposited without NH₃. Increasing deposition temperature, pressure or NH₃ flow rate results in a decrease in film density and resistivity. However, increase in TDEAT flow results in a decrease in film density and resistivity.⁷¹ The lowest resistivity of 200 $\mu\Omega$ -cm was observed for deposition at 425 °C. The drawbacks of using NH₃ as co-reactant are the poor conformality and particle generation due to high precursor reactivity. Poor conformality is observed with NH₃ because NH₃ addition

increases the growth rate of film and the growth mechanism changes from surface reaction limited to mass transfer limited. A process operated in the mass transfer limited growth regime is expected to give poor conformality.⁶⁴ Increase in deposition temperature further increases the reactive sticking coefficient and worsens the conformality.⁷¹ The conformality of film deposited with NH₃ at 425 °C in a 0.45 μm 3 AR contact hole is only 30 %. So, the process with NH₃ is not suitable for deposition of highly conformal diffusion barrier film.

To improve the property of film deposited with TDEAT, Yun et al.⁷² used N₂ and H₂ plasma to deposit thin films via PECVD. When N₂ plasma is used to deposit TiN_x, the films were C-rich (45 at. %) and the Ti and N content of the film was 25 and 13 at. %, respectively. The films had a resistivity of 1500 – 1700 μΩ-cm. When H₂ plasma was used instead of N₂ plasma, the films show low C content (17 at. %), but the film N content was also reduced (6 at. %). The film resistivity was between 1200 and 1500 μΩ-cm. Overall, the use of plasma with TDEAT does not result in deposition of good quality films with low resistivity and favorable composition.

2.5.2 Atomic Layer Deposition of Titanium Nitride

Table 2-4 shows the precursors that have been employed for deposition of TiN_x thin films by ALD. Two main inorganic Ti sources used to deposit TiN_x are TiCl₄ and TiI₄. Since Ti in these precursors is in the +4 oxidation state, reducing agents are needed to reduce Ti to the +3 oxidation state in TiN. The reducing agents that have been used are NH₃, Zn, dimethylhydrazine, *tert*-butylamine and allylamine.

The deposition using TiCl₄ and NH₃ has been attempted between 350 and 500 °C. The growth by ALD mode is nonlinear for first 50 cycles because of the initial nucleation and growth on the SiO₂ substrate.^{72,172} The temperature process window, which is characteristic of an ALD process, is not observed for TiCl₄ and NH₃ chemistry. The growth rate per cycle increases with

increase in deposition temperature. Films deposited were polycrystalline and showed dense columnar structure.^{73,74} The ratio of Ti:N was ca. 1:1, but the films contained Cl contamination. Similar to CVD deposition, ALD showed a decrease in Cl contamination with an increase in deposition temperature.⁷⁵ The resistivity of film decreased from 250 to 50 $\mu\Omega\text{-cm}$ as the deposition temperature was increased from 350 to 500 °C. There is a direct correlation between Cl contamination in the film and the resistivity of the film. Increase in the Cl contamination increases film resistivity.⁷⁵ At least 100 nm thick barrier film was required for complete surface coverage of TiN_x on SiO_2 as determined by low energy ion scattering spectroscopy (LEISS). The adhesion of TiN film with copper and SiO_2 was excellent. The adhesion energy values for TiN on SiO_2 and copper were 60 and 25 J/m^2 , respectively as determined by the four point bend test.⁷⁶ In BTS testing of 5 nm thick TiN film, the barrier film did not fail after stressing at 2 MV/cm at 200 °C for various times.

There are 3 critical drawbacks of TiN_x films deposited with TiCl_4 and NH_3 . First, the films are polycrystalline and have columnar microstructure. As discussed earlier, polycrystalline films can act as fast diffusion pathways for copper and hence are undesirable. The films also had columnar microstructure, which provides shorter pathways for copper diffusion. Second, the deposition temperature to obtain good quality TiN_x films with minimal Cl contamination is close to 500 °C, which is relatively high since the low- k dielectrics are thermally unstable at this temperature. Higher deposition temperature for TiCl_4 is needed because the Ti-Cl bond is very strong (bond energy of 429 kJ/mol). Moreover, higher temperature is also needed because at low temperature, NH_3 reacts with Cl adsorbed on surface to form NH_4Cl and temperature above 370 °C is required to sublime NH_4Cl .⁷⁴ Third, HCl formed as a byproduct of the reaction can

severely etch the substrate and cause pitting. Severe copper pitting has been observed when TiN_x is grown on copper.^{73,74,77}

One of the ways to reduce deposition temperature is to use PAALD. Plasma assisted ALD using TiCl_4 and NH_3 has been investigated by Elers and coworkers.⁷⁸ Similar to thermal ALD, PAALD also did not show the characteristic ALD process window for growth temperature. The growth rate of films deposited with PAALD was significantly higher than that for thermal ALD process. Film deposited by PAALD had lower Cl contamination as compared to films deposited with ALD and the lowest Cl contamination of 1.2 at. % was observed at 400 °C deposition temperature. The change of plasma power in PAALD resulted in a change in N:Ti ratio in the film. The N:Ti ratio increased with an increase in plasma power. Such modulation of composition is not possible for thermal ALD, where composition is determined only by growth temperature. While PAALD did have some advantage over thermal ALD, the process still was not able to deposit Cl-free films. Moreover, the films were polycrystalline with columnar microstructure. Furthermore, the use of halide chemistry also meant that the process would cause pitting on the substrate surface.

To overcome the problems related to corrosive byproducts of the reaction, additional reducing agent such as Zn has been used in the ALD process.^{75,79} When Zn is used as a reducing agent, there is no difference in growth rate per cycle. However, the Zn does influence the film texture. When Zn is used as reducing agent along with NH_3 , the films have (111) preferential orientation, whereas without Zn the preferred orientation of the film is (100). No Zn impurity is found in the TiN_x films.⁷⁵ The film composition with or without Zn is similar except Cl content, which is higher for films deposited without Zn. Films deposited with Zn also had about 5 times lower resistivity than those deposited without Zn. Even though very good film qualities are

obtained with Zn pulses in TiN_x ALD, this process is not suitable for diffusion barrier deposition because Zn is an electrically active impurity in silicon and its incorporation in active areas of a transistor can severely affect the device performance.

Since 1,1-dimethylhydrazine (DmHy) is a much stronger reducing agent than NH₃, ALD TiN_x using TiCl₄ and DmHy has been investigated.⁸⁰ The films deposited had a very high Cl content, up to 23 at. % at 200 °C deposition temperature. The films were also more resistive because of the increased Cl and C content in the film. The lowest resistivity obtained was 500 μΩ-cm at 350 °C deposition temperature. The films were weakly polycrystalline. The use of DmHy did not show any significant improvements over NH₃ as co-reactant. In fact, the resistivity and impurity content of films deposited was worse when DmHy was used.

tert-Butylamine and allylamine have also been investigated as reductive N sources to lower the deposition temperature of TiN_x ALD using TiCl₄.⁸¹ Depositions were done between 400 and 500 °C. Films deposited with *tert*-butylamine had a low growth rate of 0.03 Å/cycle. Addition of NH₃ to *tert*-butylamine increased the growth rate to 0.15 Å/cycle. Film resistivity was similar to those deposited with NH₃ only and the contamination level of C and H was also below 1 at. %. By using *tert*-butylamine, the deposition temperature could be lowered from 500 to 400 °C to obtain low resistivity TiN_x films with minimal Cl contamination (1.4 at. %). However, the process could not deposit amorphous TiN_x films.

When allylamine was used as the reducing agent, the films had higher C and Cl contamination of 7 and 6 at. %, respectively.⁸¹ This resulted in an increase in film resistivity to 360 μΩ-cm. Addition of NH₃ to allylamine did not have any significant effect, although the Cl contamination decreased to 4 at. % and C contamination increased to 9 at. %. As with *tert*-butylamine, films deposited with allylamine were weakly polycrystalline. Additional diffusion

barrier testing of TiN_x films deposited with either *tert*-butylamine or allylamine has not been reported yet.

TiN_x ALD has been attempted using TiI₄ and NH₃.^{79,82,83} The ALD process did not show the characteristic temperature process window as the film growth rate increased with increase in deposition temperature.⁸³ The films were Ti-rich and the N content of film increased from 20 at. % at 350 °C to 45 at. % at 500 °C. Impurity content of the film, as measured by RBS, showed that the films had low I content (2 at. % at 350 °C and 0 at. % at 400 °C). The films were heavily contaminated with O and the film O content decreased with increase in deposition temperature. Films deposited at 350 °C showed O content of 40 at. %, while those deposited at 500 °C showed O content of 10 at. %. The TiN_x films were polycrystalline and the preferred orientation was dependent on deposition temperature. Films deposited below 425 °C showed preferred orientation of (100), whereas films deposited above 450 °C showed preferred orientation of (111). The film resistivity for deposition at 400 °C was 380 μΩ-cm. Overall, high porosity and the presence of impurities such as I and O made the films deposited by this process unsuitable for diffusion barrier deposition.

To overcome the issues related to halogen impurities in films deposited using inorganic precursors, organometallic Ti precursors have been investigated for deposition of ALD TiN_x thin films. Tetrakis(ethylmethanido) titanium (TEMAT), or Ti[N(C₂H₅)(CH₃)]₄, has been used with NH₃ to deposit ALD TiN_x thin films. Self-limiting growth of TiN_x has been reported using TEMAT.^{84,85} Unlike ALD from halide precursors, ALD from TEMAT showed the characteristic ALD process window. While one report established the ALD process window for TEMAT between 150 and 220 °C,⁸⁵ another report located the ALD process window between 170 and 210 °C.⁸⁴ The deposition temperature for TEMAT is considerably lower than that for inorganic

Ti precursors. The growth rate per cycle is 5 Å/cycle, which is about 1.6 ML/cycle for TiN_x film. It has been argued that the film growth of more than 1 ML/cycle is possible if NH₃ can react with TEMAT adsorbed on the surface and TEMAT can react with chemisorbed NH₃. Film growth during the individual pulses of both TEMAT and NH₃ would result in film growth rate greater than 1 ML/cycle.⁸⁴ Unlike films grown with inorganic Ti precursors, films grown with TEMAT had amorphous microstructure. While films deposited with inorganic Ti precursors had a N:Ti ratio close to 1:1, films deposited with TEMAT had N:Ti ratio of 0.55 suggesting that the film deposited is actually Ti₂N. C and H contamination in the film was 4 and 6 at. %, respectively for films deposited at 200 °C. The film resistivity varied between 230 μΩ-cm for films grown at 160 °C to 8000 μΩ-cm for films grown at 200 °C. Diffusion barrier testing for Ti₂N films showed that the barrier was able to prevent bulk copper diffusion after annealing at 600 °C in vacuum (as determined by XRD of film post-anneal). After annealing at 650 °C, Cu₃Si peaks appeared in XRD suggesting that copper had penetrated through the barrier film. Ti₂N films deposited by TEMAT showed many properties expected from a good diffusion barrier film. To evaluate if Ti₂N is effective in preventing trace copper diffusion, additional electrical testing of barrier film is required.

TDMAT has also been used with NH₃ to deposit TiN_x films via ALD. Unlike TEMAT, TDMAT did not show the characteristic temperature process window for ALD. The reaction of TDMAT and NH₃ is not self limiting. Precursor decomposition study by FTIR indicated weak dependence of growth rate on TDMAT exposure time because of incomplete desorption of residual Ti(N(CH₃)₂)_x species.⁸⁶ Mechanistic study by FTIR also indicated that the film growth occurs via transamination between TDMAT and NH₃. Similar to TEMAT, TDMAT was also able to deposit TiN_x thin films at relatively low deposition temperature. At 180 °C deposition

temperature, the growth rate of TiN_x was $2 \text{ \AA}/\text{cycle}$.⁸⁷ Films were Ti-rich and the N:Ti ratio of ca. 0.5 indicated the presence of Ti_2N . The C contamination in the film was less than 10 at. % but the films had a very high O contamination which decreased with increase in deposition temperature.⁸⁶ The films were highly porous ($> 35\%$ porosity) which explained the low density of Ti_2N film. The highest film density was 3 g/cc while the bulk density of stoichiometric TiN is 5.2 g/cc . High porosity results in an increase in O diffusion through the barrier film and a corresponding increase in film resistivity. The lowest resistivity of $1.4 \times 10^4 \mu\Omega\text{-cm}$ was observed at $240 \text{ }^\circ\text{C}$ deposition temperature. High porosity and extremely high resistivity of Ti_2N films deposited by TDMAT makes this process unsuitable for diffusion barrier application.

To improve the Ti_2N film quality, post-growth rapid thermal nitriding and plasma exposure have been explored.⁸⁷ Rapid thermal nitriding at $500 \text{ }^\circ\text{C}$ resulted in a net decrease in organic C in the film (ca. 5 at. %) and the films were amorphous even after nitriding. Increasing the nitriding temperature to $700 \text{ }^\circ\text{C}$ resulted in formation of macroscopic cracks in the barrier film. Post-growth plasma exposure decreases the film C content below the detection limit of XPS. Since higher N content was observed on the surface of Ti_2N than in bulk, N most likely gets incorporated in the film during plasma exposure. The plasma exposure lowered the film resistivity from 2×10^4 to $3000 \mu\Omega\text{-cm}$ due to lowering of C content and minimal O incorporation. The plasma exposure also resulted in the densification of the Ti_2N surface. The only disadvantage of the plasma process was that it changed the film microstructure from amorphous to weakly polycrystalline as indicated by the Ti_2N peak in the XRD spectrum.

TiN_x film growth by PAALD using TDMAT with remote N_2 , $\text{N}_2 + \text{H}_2$ and H_2 plasma has been investigated.^{88,89} The use of plasma was aimed at reducing the film C content. Since the plasma is generated *ex situ*, the likelihood of surface damage by plasma is also minimized.

Unlike thermal ALD of TiN_x using TDMAT and NH_3 , the PAALD process did show a characteristic ALD temperature window of 200 - 300 °C where the film growth rate did not change with deposition temperature. Plasma also resulted in dense films which produced low levels of O impurities (ca. 10 at. %). The C content of the film was also < 10 at. %. The film resistivity was between 300 and 500 $\mu\Omega\text{-cm}$. Film resistivity was lowest for films deposited using the N_2 plasma process, followed by those deposited using $\text{H}_2 + \text{N}_2$ plasma. The highest resistivity was observed for films deposited with H_2 plasma. The C impurities also showed a similar trend for different plasma exposures with the lowest C content observed for films deposited with N_2 plasma. While thermal ALD affords 100% conformal coverage in high aspect ratio features, the step coverage for PAALD process was 95 % in 1:10 aspect ratio feature. Diffusion barrier testing of 19 nm TiN_x films deposited with different plasma exposures showed that copper was able to diffuse through the film after annealing at 500 °C as witnessed by the emergence of Cu_3Si peaks in XRD spectra. The failure temperature of barrier film was same irrespective of whether N_2 , $\text{H}_2 + \text{N}_2$ or N_2 plasma was used for film deposition.⁸⁹ Even though the PAALD film was able to decrease the film resistivity as compared to thermal ALD, the copper diffusion barrier performance of the film was not satisfactory.

2.6 Tantalum Nitride as Diffusion Barrier

2.6.1 Chemical Vapor Deposition of Tantalum Nitride

CVD of TaN_x has employed both inorganic and metal organic precursors as the Ta source (Table 2-5). The three main inorganic precursors that have been employed to deposit TaN_x thin films are TaCl_5 , TaF_5 and TaBr_5 . TaI_5 has not been employed for CVD because it requires very high temperature to obtain sufficient vapor pressure for delivery in a CVD reactor.⁹⁰ TaCl_5 , TaF_5 and TaBr_5 are polycrystalline solids at room temperature with sufficient vapor pressure at

elevated temperature for delivery in a CVD reactor. The N sources employed with these Ta precursors have been either NH_3 alone or NH_3 with H_2 .

Chemical vapor deposition of TaN_x from TaCl_5 and NH_3 at the low deposition temperature of $350\text{ }^\circ\text{C}$ is not suitable for diffusion barrier application because the films had very high resistivity ($> 10,000\text{ }\mu\Omega\text{-cm}$) and high Cl contamination (4.5 at. %).⁹⁰ Since the Ta-Cl bond is very strong, higher energy is required to cleave the bond. When TaN_x films are deposited using TaF_5 and NH_3 at $350\text{ }^\circ\text{C}$, films have a relatively low resistivity of $1650\text{ }\mu\Omega\text{-cm}$. However, considerable F contamination (4.0 at. % F) was observed and the step coverage of the film was poor (75%).⁹⁰ The poor step coverage for TaN_x films deposited by TaF_5 can be explained by considering the high growth rate of deposition. Films deposited with TaF_5 had a growth rate of 1.5 nm/sec , which is high for a typical CVD process.⁹⁰ TaN_x deposition from thermal CVD using TaCl_4 and TaF_5 has not been pursued further, possibly because of the high temperature required to deposit TaN_x films with low resistivity and acceptable halogen contamination.

TaBr_5 has been studied as a precursor for CVD of TaN_x using H_2 and NH_3 co-reactants. It has been argued that since Br is a larger atom than Cl and F, impurity incorporated in the film would have lower diffusivity in TaN_x film and the impurity would not influence the diffusion barrier property of the film. Moreover, since the bond energy of Ta-Br in TaBr_5 is lower than that for Ta-Cl in TaCl_5 , lower deposition temperature would be required for the TaBr_5 and NH_3 reaction. Chen et al.⁹¹ reported deposition of TaN_x films between 350 and $500\text{ }^\circ\text{C}$ using TaBr_5 , H_2 and NH_3 . The films were N-rich with N:Ta ratio varying between 1.75:1 and 1.87:1 for deposition between 350 and $500\text{ }^\circ\text{C}$, indicating that the N:Ta ratio was not very sensitive to the reaction temperature. The N-rich film deposited with TaBr_5 indicates that film is possibly Ta_3N_5 and not TaN . The O and C contamination in the film was below the detection limit of AES.

Films contained Br as an impurity and the Br content in the film decreased with increase in deposition temperature. The highest Br content of 5 at. % was observed for deposition at 350 °C while the Br content in film was below the detection limit of AES for deposition at 500 °C. The film crystallinity was strongly dependent on deposition temperature. Films deposited at 350 and 425 °C were amorphous whereas films deposited at 500 °C were polycrystalline with the peak positions in XRD spectrum indicating the presence of tetragonal Ta₃N₅ and hexagonal TaN phases. Film resistivity also showed a strong dependence on deposition temperature with the lowest resistivity of 5040 μΩ-cm observed at 500 °C. The resistivity of the films decreased with increase in deposition temperature. To ascertain the diffusion barrier efficacy of TaN_x films, Kaloyeros et al.⁹² performed extensive barrier testing on TaN_x films deposited at 425 °C. The Cu/TaN_x/Si stack was annealed between 450 and 650 °C to determine the temperature at which barrier film failed. From post-anneal XRD analysis, it was confirmed that the barrier film was able to prevent bulk diffusion of copper up to 650 °C annealing as no Cu₃Si peaks were observed in the XRD spectrum. X-ray photoelectron spectroscopy depth profile also confirmed that copper had not diffused through the barrier film. However, when the Seeco etch pit test was performed to identify trace copper diffusion through the barrier, films annealed at 600 and 650 °C showed etch pits, suggesting that a trace amount of copper had actually diffused through the barrier film. To compare diffusion barrier efficacy of films deposited by PVD and CVD, the authors also deposited PVD TaN_x films with the same N:Ta ratio. TaN_x films deposited by PVD did not fail the Seeco etch pit test after annealing at 650 °C. The difference in diffusion barrier efficacy of CVD TaN_x and PVD TaN_x was attributed to the polycrystalline phase difference between CVD and PVD films. The PVD TaN_x films exhibited hexagonal TaN phase, which has a N:Ta ratio of 1:1. Since the PVD films had a 1.78:1 N:Ta ratio, the excess N in PVD films

might ‘stuff’ the grain boundaries thereby preventing copper diffusion. For CVD films, the predominant phase is believed to be Ta_3N_5 . The emergence of Ta_3N_5 peaks in XRD spectra when CVD TaN_x film is annealed at 650 °C further supports this assumption.⁹² In Ta_3N_5 , the N:Ta ratio is 1.67:1, which means that there is very little excess N to ‘stuff’ the grain boundaries in CVD TaN_x films. This difference is believed to be responsible for the difference in diffusion barrier efficacy of CVD and PVD TaN_x films with similar N:Ta ratio. Overall, the primary concerns for TaN_x films deposited from $TaBr_5$ are their higher resistivity at acceptable deposition temperature, lower recrystallization temperature and deposition of Ta_3N_5 phase instead of the desired TaN phase. A possible approach that might result in lowering recrystallization temperature, decrease in resistivity and also possibly disrupt the growth of Ta_3N_5 would be to grow a ternary compound such as TaN_xC_y using $TaBr_5$, NH_3 and a C source. The ternary compound could lower the recrystallization temperature and C in the film could disrupt the growth of Ta_3N_5 phase.

PECVD of TaN_x has been attempted with $TaCl_5$ ^{90,93}, TaF_5 ⁹³ and $TaBr_5$.^{93,94} Hillman et al.⁹⁰ used N_2 plasma to deposit TaN_x thin films. The films had a low halogen contamination with the lowest halogen content of 1 at. % observed for film deposited with $TaCl_5$. The resistivity of film deposited with $TaCl_5$, TaF_5 and $TaBr_5$ was 395, 615 and 710 $\mu\Omega$ -cm, respectively for deposition at 350 °C. The film composition and texture were not reported. The diffusion barrier testing of films deposited by these three precursors was done by depositing 20 nm barrier film and annealing the Cu (160 nm)/ TaN_x (20 nm)/ Si stack at 550 °C for 30 min in N_2 environment. Films deposited from $TaCl_5$, $TaBr_5$ and TaF_5 failed after anneal and copper in silicon was detected by SIMS depth profiling. Hence, PECVD process using halide precursors was not able to deposit good quality diffusion barrier films.

Metal organic sources have also been explored as Ta source for CVD of TaN_x. The metal organic sources that have been explored so far include tert-butylimido tris(diethylamido) tantalum (TBTDET), pentakis(dimethylamido) tantalum (PDMAT), pentakis(diethylamido) tantalum (PDEAT), ethylimidoethyl(C,N) tris(diethylimido) tantalum, and tertiaryamylimidotris(dimethylamido)tantalum (TAIMATA). Tsai et al.⁹⁵⁻⁹⁷ have extensively studied deposition of CVD TaN_x films from TBTDET. The precursor was used as a single-source precursor between 450 - 650 °C deposition temperature. Films deposited were polycrystalline with the N:Ta ratio close to 1. The C and O impurities in the film were less than 10 and 5 at. %, respectively at 600 °C deposition temperature. X-ray photoelectron spectroscopy analysis indicated that C present in the film was in carbide phase. The resistivity of film decreased from 10,000 μΩ-cm at 500 °C deposition temperature to 600 μΩ-cm at 650 °C deposition temperature. Diffusion barrier testing on 120 nm TaN_x films deposited at 650 °C revealed that trace amount of Cu could diffuse through the barrier film after the Cu/TaN_x/Si (p⁺n diode) structure was annealed at 550 °C and bulk copper diffusion occurred at 600 °C as evidenced by the formation of Cu₃Si.⁹⁷ The authors also deposited 120 nm PVD TaN_x film to compare the diffusion barrier performance of CVD TaN_x films vis-à-vis PVD TaN_x films. The PVD barrier film showed trace copper diffusion at 600 °C and bulk copper diffusion at 650 °C. The authors argued that the PVD TaN_x showed better diffusion barrier performance than CVD TaN_x primarily because PVD TaN_x films had a preferred orientation of (111), which has a higher thermal stability than the (200) orientation observed for CVD TaN_x films. However, the film texture should not play such a significant role in diffusion barrier performance because the CVD films are polycrystalline and show both (111) and (200) reflections in XRD spectra.⁹⁵ A more plausible explanation for poorer barrier performance of CVD films is the columnar

microstructure of the films deposited by CVD at higher temperature. Overall, CVD TaN_x films deposited using TBTDET without any co-reactant had several limitations including high deposition temperature, polycrystalline microstructure with columnar grains, high resistivity and poor barrier performance. The use of NH₃ or H₂ co-reactants might decrease the deposition temperature and improve film properties of TaN_x, but such an approach has not been explored yet.

Fix et al.⁹⁸ used PDMAT with NH₃ to deposit TaN_x films between 200 and 400 °C deposition temperature. The films deposited with PDMAT had amorphous microstructure. Charging effects were observed when TaN_x films were observed under electron microscope suggesting that the films were non-conducting. The films were N-rich with a N:Ta ratio of 1.7:1. The film had significant H content as measured by hydrogen forward recoil spectroscopy. The O and C contamination in the film was less than the detection limit of RBS (typically 3 - 4 at. %). The resistivity of the film was greater than 10⁶ μΩ-cm and is indicative of the growth of the non-conducting Ta₃N₅ phase. The growth of highly resistive Ta₃N₅ makes the PDMAT precursor unsuitable for diffusion barrier deposition.

PDEAT has been used with and without ammonia to deposit TaN_x films. When PDEAT was used without NH₃, the films deposited between 275 and 400 °C were Ta-rich films with significant C content (> 20 at. %) indicating that the films were actually TaN_xC_y.⁹⁹ X-ray diffraction spectra indicated that the films deposited above 275 °C were polycrystalline with peak positions corresponding to TaN(111) phase. The films deposited at low deposition temperature were very resistive ($\rho > 10^4$ μΩ-cm) and the lowest resistivity of 6000 μΩ-cm was observed for film deposited at 400 °C. Cho et al.¹⁰⁰ investigated the use of NH₃ as a co-reactant to deposit TaN_x films. The film deposited at 325 °C was polycrystalline with TaN(111) as the

dominant phase. The addition of NH_3 dramatically increased the film N content and the N:Ta ratio for films deposited with NH_3 was 1.75:1. The addition of NH_3 also decreased the C content of the film to below 10 at. %. The Seeco etch pit test on 50 nm thick barrier film showed that the barrier film was able to prevent copper diffusion after annealing at 600 °C. The comparison between films deposited with and without NH_3 indicated that films deposited with NH_3 were better at preventing copper diffusion. It was argued that finer grain structure together with dense microstructure of films deposited with NH_3 was responsible for enhancing the diffusion barrier quality. The major drawbacks of films deposited with PDEAT and NH_3 were the high resistivity (6000 $\mu\Omega\text{-cm}$) and poor conformality of the films.

When a mixture of $\text{EtN}=\text{Ta}[\text{NEt}_2]_3$ and $\text{Ta}[\text{N}(\text{Et}_2)]_5$ was used with H_2 to deposit thin films between 375 and 500 °C, the resulting films were C-rich and the N content of the film was less than 1 at. %.¹⁰¹ However, when a mixture of $\text{EtN}=\text{Ta}[\text{NEt}_2]_3$ and $(\text{Et}_2\text{N})_3\text{Ta}[\text{NEt-CMeH}]$ was used without any co-reactant to deposit thin films between 500 and 600 °C, the films had a significant N and C with the Ta:C:N ratio of 1:1:1 at 600 °C.¹⁰² The XRD measurement of films showed peaks corresponding to polycrystalline cubic TaN even though the film had significant C content. The report did not mention film resistivity and no diffusion barrier testing was done on the films.

TAIMATA has been used with NH_3 to deposit barrier films at 250 °C.¹⁰³ The report focused on the barrier efficacy and its integration with SiOC:H dielectric. Film characterization was not discussed in detail. Bias temperature stress testing at 0.75 MV/cm and 350 °C on 10 and 15 Å thick barrier film showed that the TaN_x film was able to prevent copper diffusion. The precursor shows promise as a diffusion barrier but a detailed analysis of films deposited from TAIMATA is yet to be reported.

Overall, the biggest challenge for CVD TaN_x deposition is the growth of insulating Ta₃N₅ phase. Since Ta is in the +5 oxidation state in both the precursor and the deposited film, the use of a stronger reducing agent such as dimethylhydrazine might help in reduction of Ta to the +3 oxidation state to form conducting TaN films.

2.6.2 Atomic Layer Deposition of Tantalum Nitride

The precursors utilized for ALD TaN_x have been the same as those used for CVD TaN_x (Table 2-6). TaCl₅ has been used with NH₃ to deposit TaN_x thin films by thermal ALD.^{104,105} The films deposited with the TaCl₅ and NH₃ are N-rich and polycrystalline. The XRD spectrum for films deposited at 400 °C show the presence of the tetragonal Ta₃N₅ phase. The film growth rate is 0.22 - 0.24 Å/cycle and the temperature window for the ALD process is 300 – 500 °C. The films contain less than 5 at. % Cl and less than 2.5 at. % H impurity. Similar to CVD, ALD using TaCl₅ and NH₃ shows that the Cl impurity in TaN_x films decreases with increasing deposition temperature. The resistivity of the film varies from $0.5 \times 10^6 - 200 \times 10^6 \mu\Omega\text{-cm}$. The film is highly resistive because of the presence of the non-conducting Ta₃N₅ phase. Similar to CVD, ALD from TaCl₅ also shows that the reducing power of NH₃ is not sufficient to reduce Ta from the +5 oxidation state in TaCl₅ to the + 3 oxidation state in TaN.

To aid the reduction of Ta, Zn has been utilized as an additional reducing agent in the ALD process for deposition using TaCl₅.¹⁰⁵ When a Zn pulse is used between the TaCl₅ and NH₃ pulses in the ALD process, the film growth rate is 0.2 Å/cycle at 400 °C and 0.15 Å/cycle at 500 °C. The characteristic temperature window of ALD could not be established because the growth rate was not constant between 400 and 500 °C. The films deposited were cubic TaN and impurity content in the film was lower than that for films deposited without a Zn pulse. The impurity content of film was 0.1 – 4.0 at. % Cl, 3.0 - 4.0 at. % O, less than 0.5 at. % H and less than 0.5 at. % Zn. The films were quite conductive and the lowest resistivity of the film was 900

$\mu\Omega\text{-cm}$. The main challenges for deposition with Zn as a reducing agent are the polycrystalline films deposited with the ALD process, incorporation of electrically active Zn impurity in the films and higher deposition temperature. As discussed earlier, Zn is an electrically active impurity and its diffusion in the device can cause severe degradation of device performance. Deposition below $400\text{ }^\circ\text{C}$ is not possible with Zn because Zn has a low volatility and its delivery below $400\text{ }^\circ\text{C}$ is not possible.

There are a number of other reducing agents that have been used with and without NH_3 to deposit TaN_x from TaCl_5 and TaBr_5 . These reducing agents include DmHy⁸⁰, *tert*-butyl amine (with and without NH_3) and allylamine (with and without NH_3).¹⁰⁶ When DmHy was used as a reducing agent, no significant improvement in film properties was achieved as compared to NH_3 based ALD. The film deposited from TaCl_5 and DmHy was insulating Ta_3N_5 and the resistivity of the film was too high to be measured by the standard four point probe technique.

tert-Butyl amine has been used with and without NH_3 to deposit TaN_x films from TaCl_5 and TaBr_5 .¹⁰⁶ When *tert*-butyl amine is used without NH_3 , deposition with TaCl_5 has a higher growth rate and yields films with lower resistivity as compared to TaBr_5 . Films deposited with TaCl_5 are amorphous at $350\text{ }^\circ\text{C}$ deposition temperature but polycrystalline TaN films are deposited above $400\text{ }^\circ\text{C}$. The films with TaCl_5 and *tert*-butyl amine show Cl impurity between 3 and 8 at. %. Film impurity content and resistivity decreases with increase in deposition temperature. Similar to CVD, low temperature ALD utilizing halide precursors gives highly resistive films with high impurity content. Good quality films with resistivity below $2700\ \mu\Omega\text{-cm}$ are obtained at $500\text{ }^\circ\text{C}$ deposition temperature but such high temperature is not suitable for barrier film deposition. To improve the film quality, NH_3 is used along with *tert*-butyl amine as

a reducing agent. The process does show improvement with respect to impurity content in the film and resistivity. However, amorphous film deposition could not be obtained for this process.

When allylamine is used with and without NH_3 to deposit TaN_x films from TaCl_5 , the films deposited were polycrystalline TaN .¹⁰⁶ The films were highly resistive with lowest resistivity of 18000 $\mu\Omega\text{-cm}$. Thus, the process with allylamine did not show any significant improvement over the *tert*-butyl amine process.

Plasma assisted ALD of TaN_x films using TaCl_5 and $\text{H}_2 + \text{N}_2$ plasma has been reported.¹⁰⁷ Depending on the partial pressure of N_2 in plasma, the film N content could be varied to deposit Ta-rich Ta_2N films, stoichiometric TaN films or N-rich Ta_3N_5 films. The growth rate increased with deposition temperature indicating that no characteristic ALD process window was observed for PAALD process. The TaN films deposited were quite conductive with resistivity varying between 350 and 400 $\mu\Omega\text{-cm}$. Films had a high H impurity of about 11 at. % and low Cl content of less than 3 at. %. Similar to thermal ALD, PAALD also showed decrease in Cl impurity with increase in deposition temperature. Overall, PAALD was able to deposit good quality films that might be suitable for the diffusion barrier application. However, the process could not yield amorphous films.

Metal organic precursors such as TBTDET, TDMAT and TAIMATA have been used to deposit TaN_x films by ALD. Chemical vapor deposition using these precursors deposited films that had high C and O impurities and high resistivity. The ALD process, if used with the same CVD precursors, is expected to yield films with low C content and dense microstructure at lower deposition temperature.

When TBTDET is used with NH_3 to deposit TaN_x films in ALD mode, amorphous TaN_x films are deposited between 150 and 300 °C. The films deposited are Ta-rich and the N:Ta ratio

is 0.73:1. The films contained low C contamination (< 5 at. %) but had a higher level of O impurity (ca. 17 at. %). The films were highly resistive ($> 10^6 \mu\Omega\text{-cm}$ at 260 °C) despite high Ta content in the film. High resistivity could possibly result from the formation of Ta_3N_5 , high O contamination and/or low density of the film (3.6 g/cc). The resistivity of the film decreases to 15000 $\mu\Omega\text{-cm}$ when the deposition temperature is increased to 450 °C.¹⁰⁸ Choi et al.¹⁰⁹ reported that the temperature window for the ALD process is between 200 and 250 °C, but the growth rate versus temperature curve shows that no saturation region can be conclusively determined. The growth rates of 1.1 and 0.4 Å/cycle have been reported for ALD using TBTDET and NH_3 .^{109,110} If deposition is done in the ALD process window and the growth occurs through the ALD mode, the growth rate per cycle should be independent of all other reactor conditions such as reactor pressure. The discrepancy in the growth rates reported by Choi et al.¹⁰⁹ and Park et al.¹¹⁰ suggests that the film growth from TBTDET might actually not be in ‘ALD mode’. Overall, TBTDET is not a suitable precursor for diffusion barrier deposition because of the deposition of highly insulating films.

PAALD of TaN_x films from TBTDET and H radical has been reported.¹¹⁰ This ALD process is unique in that it employs TBTDET as a single source precursor as H radicals are used for reduction of TBTDET. The intent behind using H radicals is that all the N atoms attached to Ta atoms via single bonds are cleaved by H radical while the N atom attached to Ta via a double bond survives the H radical exposure, leading to the formation of stoichiometric TaN film. The PAALD process showed a growth rate of 0.8 Å/cycle. The resulting TaN_x films are Ta-rich with N:Ta ratio of 3:5. The films deposited had high C content (20 at. %) and it could be argued that the films were actually TaN_xC_y instead of TaN_x . The films were polycrystalline and had low resistivity of 1000 $\mu\Omega\text{-cm}$. The films were considerably denser than those deposited with

thermal ALD. Overall, the plasma process improved the film property of films deposited using TBTDET. The process, however, deposited polycrystalline films. No diffusion barrier testing was reported for films deposited via this process.

Thermal ALD from PDMAT and NH_3 has been used to deposit TaN_x films.¹¹¹⁻¹¹⁴ The process shows that the growth rate is constant at $0.3 \text{ \AA}/\text{cycle}$ between 225 and $300 \text{ }^\circ\text{C}$, indicating that the growth in this temperature window is truly in ALD mode.¹¹⁴ The film composition and microstructure strongly depends on the substrate used for deposition.¹¹³ The films deposited on Si, SiO_2 and Cu are N-rich, with N:Ta ratio of 2:1 for deposition at $275 \text{ }^\circ\text{C}$.^{111,113} However, when the same process is used to deposit TaN_x films on Ta, the films are Ta-rich with N:Ta ratio of 1:2. The films have a high level of H impurity that can be removed by annealing the film at $600 \text{ }^\circ\text{C}$ for 1 hr. The C and O impurity in the film is 2 and 5 at. %, respectively. Even though the films have high N content, the microstructure analysis indicates the presence of cubic TaN phase. The excess N is believed to reside in Ta vacancies in the Ta sublattice.¹¹¹ The films deposited are nanocrystalline with average grain size of 4 nm. 10 nm thick TaN_x film was able to prevent Cu diffusion after annealing at $750 \text{ }^\circ\text{C}$ for 30 min in vacuum. The biggest drawback of the film was its extremely high resistivity, which could not be measured by standard four point probe technique. Overall, the TaN_x films deposited with PDMAT and NH_3 in ALD mode not suitable for barrier application primarily because of its extremely high resistivity.

To deposit more conductive films using PDMAT, PAALD has been investigated.^{112,114,115} Kim et al.¹¹⁵ investigated the effect of plasma on the deposition of TaN_x films. When H_2 plasma is used, the film growth rate saturates between 225 and $300 \text{ }^\circ\text{C}$, indicating that ALD growth mode is achieved with PDMAT and H_2 plasma. The deposited film is Ta-rich, with N:Ta ratio between 0.7 and 0.8. The film C and O content is ca. 15 and 15 at. %, respectively. The films

are conductive with resistivity of 350 $\mu\Omega$ -cm observed for deposition at 250 °C. The microstructure analysis by TEM reveals that the film contains 2 -3 nm cubic TaN crystallites in an amorphous matrix. Diffusion barrier testing of the film shows that 3 nm TaN_x film is able to prevent copper diffusion after annealing at 750 °C in vacuum. This process could be a potential candidate for deposition of diffusion barrier film. When N₂ + H₂ plasma is used with PDMAT, the film N:Ta ratio varies between 1.2 and 1.6, depending on the partial pressure of N₂ in the plasma. A sharp decrease in C and O content is also observed, with the impurity content decreasing with increasing N₂ partial pressure. But the additional N in the film results in an increase in film resistivity and the lowest resistivity of ca. 800 $\mu\Omega$ -cm was observed at low N₂ partial pressure. Diffusion barrier testing for TaN_x film shows that 0.6 nm barrier film is able to prevent copper diffusion after annealing at 800 °C. From the diffusion barrier standpoint, N₂ + H₂ plasma yields better films than films deposited with H₂ plasma. Overall, PAALD from PDMAT provides various options to modify film composition and further investigation on integration of TaN_x films could provide additional information on suitability of the film for diffusion barrier application. The effect of plasma exposure on underlying layers along with conformality of the film also needs to be investigated.

Metal organic precursor TAIMATA has also been investigated with NH₃ co-reactant for deposition of TaN_x thin films by ALD.¹⁰⁹ Films deposited by thermal ALD between 150 and 175 °C exhibit a growth rate that is constant at 0.2 Å/cycle implying that the growth is self-limiting in this temperature window. The films deposited are N-rich with N:Ta ratio of 1.31. The films had minimal C contamination (< 5 at. %) but the O contamination was high (ca. 20 at. %). The XRD spectra indicate the presence of the insulating Ta₃N₅ phase. The films deposited with thermal ALD had extremely high resistivity and hence are not suitable for diffusion barrier

application. When H₂ plasma is used instead of NH₃ to deposit TaN_x films by PAALD, conductive films with low resistivity of 366 μΩ-cm were deposited for growth at 250 °C.¹¹⁶ The low resistivity of PAALD TaN_x films is probably because of a more favorable N:Ta ratio of 0.71 and the absence of insulating Ta₃N₅ phase. The films also had a high C content of about 15 at. %. The growth rate per cycle is 1.2 Å/cycle. Films deposited by PAALD are polycrystalline with the XRD peak position indicating the presence of cubic TaN phase. The conformality of the films deposited with PAALD was 94% achieved in a 10:1 aspect ratio 0.25 μm via. The major drawback of PAALD using TAIMATA is that the process could not deposit amorphous TaN_x films.

To summarize, both inorganic and metal-organic precursors have been used to deposit TaN_x films by ALD. The biggest challenge for inorganic precursors such as TaCl₅ is the formation of the insulating Ta₃N₅ phase instead of the conductive TaN phase. Moreover, the films deposited with halide precursors contain halogen impurities and the use of stronger reducing agents or plasma could not completely eliminate the halogen incorporation in the film for low deposition temperature. The use of metal-organic precursors was also more likely to deposit Ta₃N₅ phase at low temperature and the use of plasma was essential to obtain conducting TaN_x thin films with a favorable N:Ta ratio. Further investigation needs to be done on PAALD to achieve the deposition of TaN_x films on different substrates and determine if plasma has any adverse effects on the substrate.

2.7 Tungsten Nitride as Diffusion Barrier

2.7.1 Chemical Vapor Deposition of Tungsten Nitride

Table 2-7 shows the precursors that have been used to deposit WN_x thin films by CVD. WCl₆ has been used with NH₃ and H₂ to deposit WN_x thin films for application in catalysis.^{117,118} However, the lowest deposition temperature for this precursor is 500 °C, so this precursor has

not been explored for diffusion barrier application. Another inorganic precursor, WF_6 , has been explored for deposition of WN_x films. This precursor, when used with NH_3 as co-reactant, results in the formation of $WF_6:NH_3$ adduct even at temperature as high as $600\text{ }^\circ\text{C}$.¹¹⁹ The films are highly resistive and the lowest resistivity of $3000\text{ }\mu\Omega\text{-cm}$ is observed for films deposited at $350\text{ }^\circ\text{C}$.¹²⁰ To prevent the adduct formation, H_2 is used as an additional reducing agent. The resulting process deposits polycrystalline WN_x films and the lowest deposition temperature is $450\text{ }^\circ\text{C}$. Because of F impurity in the films, relatively high deposition temperature and high film resistivity, this process also has not been further investigated for diffusion barrier film deposition. A modification to the process is the use of SiH_4 as a reducing agent.¹²⁰ The lowest deposition temperature for this process is $385\text{ }^\circ\text{C}$. The resulting films are W-rich and the N:W ratio decreases with an increase in SiH_4 partial pressure. X-ray diffraction measurement indicates that the films are polycrystalline and the peaks in XRD spectra indicate the presence of $\beta\text{-}W_2N$. Addition of SiH_4 as co-reactant also decreases the film resistivity to below $600\text{ }\mu\Omega\text{-cm}$ and film resistivity decreases with an increase in SiH_4 partial pressure. Diffusion barrier testing revealed that 6 nm thick barrier film can prevent Cu diffusion after annealing at $450\text{ }^\circ\text{C}$ for 4 hours. However, the study by Gonohe found that adhesion of the WN_x film to low- k dielectric film was extremely poor.¹²⁰ X-ray photoelectron spectroscopy analysis showed that the presence of F at the WN_x / low- k interface caused the delamination of the WN_x film. The presence of F at the interface was due to the reaction of WF_6 with the dielectric surface. Chemical pretreatment of the dielectric film prevented the reaction of WF_6 with the dielectric film and no F impurity was detected at the barrier-dielectric interface. Details of the chemical pretreatment process were not discussed in the paper.

PECVD using WF_6 as tungsten source has been used to deposit WN_x thin films. NH_3 plasma, $NH_3 + H_2$ plasma and $N_2 + H_2$ plasma have been used as the N source. When deposition is done with NH_3 plasma¹²¹⁻¹²³, the resulting WN_x films are N-rich. The film composition can be varied by changing the $NH_3:WF_6$ feed ratio, deposition temperature and plasma power. X-ray diffraction measurement reveals that the films are polycrystalline with peak positions indicating the presence of $\beta-W_2N$. Gas phase reaction between reactants can cause particle formation during deposition and optimization of the $NH_3:WF_6$ flow ratio is necessary to avoid this problem. Films can be deposited at temperature as low as 250 °C, however the films have a high F contamination at low deposition temperature. The lowest F contamination of 0.1 at. % is obtained for deposition at 625 °C.¹²¹ The major problem of using this chemistry to deposit WN_x thin film is the formation of an interfacial W layer about 5 nm thick due to the high reactivity of WF_6 and Si. This can also result in etching of the substrate.¹²² On SiO_2 surface, a WO_3 layer is first formed prior to the deposition of WN_x film. Another issue with the PECVD process is the poor conformality. Film conformality of only 33% is obtained for deposition in a 0.14 μm 9:1 aspect ratio feature.¹²³ Hence this process is not suitable for diffusion barrier deposition.

PECVD of WN_x using WF_6 has also been done using both NH_3 and H_2 plasma instead of just NH_3 plasma as discussed previously.¹²⁴⁻¹³⁰ The advantage of PECVD is that by altering the $NH_3:WF_6$ ratio and the plasma power, the resulting WN_x films could be deposited as stoichiometric W_2N , W-rich WN_x or N-rich WN_x .¹³⁰ Films can be deposited at temperature as low as 150 °C.¹²⁹ An increase in the $NH_3:WF_6$ ratio results in a decrease in growth rate, increase in crystallinity and better film adhesion to the substrate. The films have low resistivity and the resistivity of the film depends, among other factors, on the film N content and deposition temperature. Due to higher F incorporation at low deposition temperature, the film resistivity

decreases with increase in deposition temperature. Film resistivity as low as $90 \mu\Omega\text{-cm}$ has been reported for WN_x films deposited by this process.¹²⁵ Particle formation during deposition has also been reported and the $\text{NH}_3:\text{WF}_6$ flow ratio has to be optimized to avoid this problem.¹²⁹ The main drawback of this process is that pitting of the Si surface is observed due to the reaction of WF_6 with the underlying Si substrate.¹²⁸

WF_6 has been used with $\text{N}_2 + \text{H}_2$ plasma to deposit WN_x thin films.¹²⁴⁻¹³⁰ N_2 is used as the N source to prevent particle problems associated with the use of NH_3 . By changing the plasma power, N_2/H_2 ratio and deposition temperature, films with varying N:W ratio can be deposited by PECVD. As compared to the NH_3 plasma process, the N_2 plasma process requires higher deposition temperature to deposit WN_x films. The film resistivity depends strongly on the N:W ratio and resistivity for stoichiometric W_2N and W-rich WN_x films varies between 200 and $400 \mu\Omega\text{-cm}$.¹³¹ The stoichiometric W_2N and W-rich WN_x films are amorphous while N-rich WN_x films are polycrystalline. Similar to the NH_3 plasma process, the N_2 plasma process also resulted in the presence of F at the barrier substrate interface. The F contamination at the interface was more severe for SiO_2 substrate than Si substrate.³² The F contamination resulted in poor adhesion of the barrier film with Si and SiO_2 . The use of N_2 plasma could not prevent the deposition of highly undesirable F impurity at the barrier substrate interface.

The three main metal organic precursors that have been used to deposit WN_x thin films are bis(*tert*-butylimido)bis(*tert*-butylamido) tungsten (TBTBW), tungsten hexacarbonyl and pentacarbonyl tungsten(1-methylbutylisonitrile). Depositions with TBTBW precursor have been attempted using inert gas argon and co-reactant NH_3 .^{31,132,133} Films deposited with NH_3 have a lower C content and higher N content as compared to those deposited without NH_3 .¹³² The lowest deposition temperature for this precursor is 450°C . When the deposition is done with Ar

carrier gas at 600 °C, the film contains ca. 70 at. % W, 10 - 15 at. % N, 10 - 15 at. % C and 5 at. % O as measured by AES. The apparent activation energy for film growth in the kinetically controlled growth regime is 0.9 eV.³¹ Films were polycrystalline and the XRD spectra indicated the presence of β -W₂N in the film.¹³³ The film was highly resistive at low deposition temperature and the resistivity of film decreased with increase in deposition temperature. The lowest resistivity of film was 620 $\mu\Omega$ -cm for deposition at 600 °C. The possible reaction pathways for this precursor have also been investigated by Crane and coworkers.¹³⁴ Because of the relatively high deposition temperature, high resistivity of the film and polycrystalline microstructure, TBTBW is not a good precursor candidate for deposition of diffusion barrier thin films.

Tungsten hexacarbonyl has been successfully used to deposit WN_x thin films with NH₃ as co-reactant.¹³⁵⁻¹³⁷ Films can be deposited at temperature as low as 200 °C. Kelsey et al.¹³⁵ reported that the films were amorphous for deposition below 275 °C as measured by XRD and TEM. However, Lee et al.¹³⁶ reported that the films deposited at 250 °C were weakly polycrystalline with the peak position indicating the presence of β -W₂N. This discrepancy could result from the different deposition conditions used for the deposition of WN_x films. The apparent activation energy for film growth is 1 eV for growth in the kinetically controlled growth regime. The N:W ratio for the film was 1:1, however the presence of the W₂N polycrystalline phase in XRD spectra suggests that the films were actually W₂N polycrystals embedded in a N-rich amorphous WN_x matrix. The films had C and N impurities of less than 10 at. % and the impurity content of the film decreased with increase in deposition temperature. Low C impurity in the film was possibly due to weak coordinate covalent bonds between CO and W in the precursor. Kelsey et al.¹³⁵ reported that the films were also highly conductive and had their

lowest resistivity of 123 $\mu\Omega\text{-cm}$ for deposition at 400 °C, while Lee et al.¹³⁶ reported film resistivity of ca. 900 $\mu\Omega\text{-cm}$ for the same deposition temperature. This discrepancy in resistivity could be due to the different film thicknesses used by Kelsey et al. and Lee et al. While Kelsey et al. measured resistivity for relatively thick WN_x film (50 nm), Lee et al. measured resistivity for a much thinner film (15 nm). As discussed earlier, resistivity could increase for thinner films because of the increase in electron scattering due to surface and grain boundary scattering. The process deposited highly conformal films with conformality of 90 % observed for deposition of 50 nm thick films in a 0.25 μm via with an aspect ratio of 4:1.¹³⁵ To determine the diffusion barrier effectiveness, a Cu/WN_x (15nm)/Si stack was annealed in Ar environment for 1 hour.¹³⁶ The post-anneal XRD and sheet resistance measurements indicated that the film was able to prevent copper diffusion after 600 °C annealing. After annealing at 620 °C, the XRD spectra showed the emergence of Cu_3Si peaks indicating bulk diffusion of copper through the barrier film. Tungsten carbonyl is hence a good candidate for diffusion barrier deposition. Further tests are needed to evaluate the effectiveness of the WN_x film in preventing trace copper diffusion.

Another precursor, pentacarbonyl tungsten (1-methylbutylisonitrile), has also been used with NH_3 to deposit WN_x thin films.¹³⁸ The films were stoichiometric W_2N with amorphous microstructure. Detailed film characterization or diffusion barrier testing for this precursor has not been reported.

2.7.2 Atomic Layer Deposition of Tungsten Nitride

Table 2-8 shows the precursors that have been used to deposit WN_x films by ALD. George and coworkers^{139,140} first reported the deposition of WN_x thin films by ALD using WF_6 and NH_3 as precursors. The films were deposited between 327 and 527 °C. Minimum growth temperature for ALD growth was 327 °C because below this temperature, $\text{WF}_x:\text{NH}_3$ adduct formation was observed by FTIR due to incomplete reduction of WF_6 by NH_3 . X-ray

photoelectron spectroscopy analysis showed that the films had a N:W ratio of 1:3. The films had low C and O contaminations of ca. 5 and 3 at. %, respectively. No F contamination was detected by XPS. The ALD process had a deposition rate of 2.5 Å/cycle. The characteristic ALD process window was observed between 325 and 525 °C.¹⁴⁰ X-ray diffraction measurement showed that the films deposited were polycrystalline with the peak positions indicating the presence of β -W₂N. The average grain size of crystallites calculated from the peak broadening of β -W₂N peaks in XRD spectra was 110 Å. The films deposited have high resistivity of 4500 μΩ-cm. To deposit WN_x films with lower film resistivity, Kim et al.¹⁴¹ used diborane (B₂H₆) as an additional reducing agent along with NH₃. The use of B₂H₆ resulted in films with significantly lower resistivity (< 450 μΩ-cm). The growth rate of the film was 2.8 Å/cycle and the N:W ratio was 0.82. The XRD measurement revealed that the film contained a two phase mixture of β -W₂N and δ -WN. The density of the film was 15 g/cc, which is close to the bulk density of both β -W₂N and δ -WN. X-ray photoelectron spectroscopy measurement indicated that in addition to WN_x, the film also contained the oxynitride phase WN_xO_y. The source of oxygen in the film was not discussed. No diffusion barrier testing was reported for these films.

As discussed earlier, a major drawback of the process using WF₆ is that it can react with the underlying Si substrate to form a thin pure tungsten film before the deposition of WN_x. This could increase the total thickness of the barrier film and is not desirable. To prevent or minimize the reaction of WF₆ with the underlying Si substrate, Sim et al.^{142,143} used pulsed plasma enhanced ALD (PP-ALD). Plasma was used during the NH₃ pulse only because if plasma is applied during the WF₆ pulse, W particles could be generated and subsequently incorporated into the film. The process was able to deposit WN_x film on a Si substrate without the formation of

pure W interface. However, the films also contained F as an impurity though the F content was not quantified by the authors.

The only metal-organic precursor that has been used to deposit WN_x films by ALD is bis(*tert*-butylimido)-bis(dimethylamido)tungsten.^{45,144} The precursor, when used with NH_3 in ALD mode, deposits WN_x thin films. No ALD process window was observed between the deposition temperature of 250 and 300 °C. The N:W ratio was 1:1 and films did not contain C impurity as indicated by AES and XPS measurements. X-ray diffraction and HRTEM measurements indicated that the films were amorphous. The films were stable after annealing at 700 °C. Subsequent heating at 725 °C resulted in decomposition of film into pure W and N_2 gas. The growth rate was 1 Å/cycle. The films were very smooth with a RMS roughness of 3.3 Å. The ALD process also demonstrated 100 % step coverage in a 200:1 aspect ratio feature. WN film as thin as 1.5 nm was able to prevent copper diffusion after annealing at 600 °C. The only drawback of this film was its high resistivity (1500 – 4000 $\mu\Omega$ -cm). The resistivity of the film could be reduced by annealing the film at 700 °C in forming gas, but annealing at such high temperature is not desirable for diffusion barrier application.

2.8 Tungsten Nitride Carbide as Diffusion Barrier

2.8.1 Atomic Layer Deposition of WN_xC_y

Numerous studies on ALD WN_xC_y growth have been reported. Most of the reports of WN_xC_y by ALD have used ASM microchemistry's PulsarTM ALD deposition tool. Almost all of the reports on ALD WN_xC_y have employed halide chemistry with WF_6 as the tungsten source, NH_3 as the nitrogen source and triethyl boron (TEB) as the carbon source. The composition of films deposited was W:N:C = 55:15:30.¹⁴⁵ The concentration of impurities such as O, F and B in the film was low (< 0.5 at. % O, < 0.5 at. % F and < 0.5 at. % B).¹⁴⁶ However, F was detected at the interface of Si and WN_xC_y .⁸⁹ This is undesirable since halogens present at the interface can

severely affect adhesion of the films. In fact, the adhesion energy of WN_xC_y with SiO_2 is $1.5 J/m^2$ as measured by the four point bend test.⁷⁷ The low adhesion strength, however, did not cause delamination of the film during the CMP process.⁷⁶ Despite the use of a halide precursor, the deposition of WN_xC_y did not show any pitting on copper and WN_xC_y had good adhesion with copper.¹⁴⁵ The WN_xC_y film was nanocrystalline with the peak position indicating the presence of WN_x and WC_x or a single WN_xC_y phase. The average crystallite size was between 3 and 7 nm.¹⁴⁷ Unlike TiN films deposited by ALD, WN_xC_y films did not exhibit a columnar grain structure, which is desirable because a columnar structure could provide short diffusion paths for copper to diffuse. The density of the film was 15.37 g/cc, which is close to the bulk value. The dense microstructure of WN_xC_y was believed to be responsible for minimal O diffusion through the film after exposure to air. The film was stable after annealing at 700 °C. After annealing at 800 °C, a multiphase mixture containing metallic W, WC and WC_x emerges as evidenced by the corresponding peaks in the XRD spectrum. The N from the film is lost as N_2 gas after annealing at 800 °C. While WC_x reacts with Si to form W_5Si_3 at 700 °C¹⁴⁸, no silicide formation is observed for WN_xC_y films even after annealing at 800 °C.⁸⁹ The growth rate of the film was 0.8 - 0.9 Å/cycle. The resistivity of the film was 300 – 400 $\mu\Omega$ -cm for films deposited between 300 and 400 °C.

Growth of ALD WN_xC_y film was sensitive to the surface on which the films were deposited.¹⁴⁹ This is particularly important because in dual damascene structures, the diffusion barrier film is deposited simultaneously on three different surfaces, (i.e. copper, dielectric (SiO_2 or low-*k* dielectric) and the etch stop layer (SiC or Si_3N_4)). A transient growth regime is observed up to film thickness of 5 nm for growth on SiO_2 and SiC , however deposition on Si_3N_4 shows a much shorter transient regime. Surface treatment has been proposed to speed up the

nucleation and growth of ALD films.¹⁵⁰ WN_xC_y film deposited on PECVD SiO_2 pretreated with NH_3 plasma showed complete surface coverage after 40 ALD cycles whereas WN_xC_y deposited on untreated PECVD SiO_2 required 50 cycles to achieve complete surface coverage.

The WN_xC_y film was compatible with dielectric films such as SiO_2 and SilKTM and etch stop layers such as SiC and Si_3N_4 .¹⁴⁵ However, for ultra low- k films, the precursor diffuses through the pores of the dielectric. Diffusion of the precursor through both HSQ and MSQ dielectric films with pore size of 4 - 5 nm has been reported.⁷³ Nitrogen plasma was able to seal the pores of these dielectric films and prevent the diffusion of the precursor(s) into the dielectric film. Surface treatment of SilKTM dielectric by O_2 inductively coupled plasma (ICP) in an oxygen rich environment and reactive ion etch (RIE) done in a nitrogen rich environment have been investigated to seal the pores of the dielectric film.¹⁵¹ Hydrophilic groups created on the dielectric surface during surface treatment are expected to enhance ALD growth. N_2 RIE was able to densify the dielectric surface and close the pores of the dielectric film. However, since the O_2 ICP does not have any ion bombardment, the dielectric films remained semi-permeable after surface treatment. WN_xC_y films on plasma treated polymer were smoother, more so for film deposited on an N_2 RIE treated surface than film grown on O_2 ICP treated surface. Films deposited by ALD were continuous after 10 nm for untreated polymer, 3.5 nm for the O_2 ICP treated surface and 1.4 - 2.3 nm for the N_2 RIE treated surface.

The thermal stability of ALD WN_xC_y as measured by XRD showed that the film failed after annealing at 700 °C as evidenced by the formation of Cu_3Si .¹⁴⁷ However, the etch pit test, which can detect trace diffusion of copper through the barrier film, showed that the diffusion of copper through the WN_xC_y film occurs after annealing at 600 °C for 30 min.⁸⁹ Electromigration resistance of copper deposited on WN_xC_y has been compared with copper deposited on PVD Ta,

which is the liner material currently used in industry.⁷⁶ For the electromigration test performed at 325 °C and 2 mAmp current, copper film deposited on WN_xC_y has better electromigration resistance than copper film deposited on PVD Ta. The dominant failure mechanism of copper deposited on WN_xC_y in dual damascene structure was voiding in M2 trench starting at the via and propagating along the capping layer. Bias temperature stress tests done at 300 °C and 0.7 MV/cm bias showed that 2.7 nm WN_xC_y film failed after 30 min stress, while 5 nm WN_xC_y barrier did not fail. These reports confirm that WN_xC_y can prevent copper diffusion under normal operating conditions and has good electromigration resistance.

A major integration problem of WN_xC_y barrier film was its galvanic corrosion by the H_2O_2 based slurry used in CMP of copper. The large potential difference between Cu and WN_xC_y in H_2O_2 causes the corrosion of WN_xC_y by H_2O_2 . The corrosion occurs by dissolution of W as tungsten oxide. To overcome this problem, a CMP slurry based on HNO_3 has been proposed.¹⁵² The use of HNO_3 based slurry can reduce the WN_xC_y corrosion. Additives such as monosaccharides or organic acids can be used to slow the excessive loss of copper by HNO_3 .

2.8.2 Chemical Vapor Deposition of WN_xC_y

WN_xC_y is a very promising material for diffusion barrier application as discussed above. However, the use of WF_6 leads to F deposition at the barrier-substrate interface⁸⁹ leading to poor adhesion of the barrier film to the substrate. Moreover, WF_6 has problems related to its handling and storage. An alternate method for the deposition of WN_xC_y is thus desirable. Three different metal organic precursors have been used to deposit WN_xC_y thin films [$Cl_4(RCN)W(NPh)$ (**1a**, R = CH_3 and **1b**, R = Ph), $Cl_4(RCN)W(NC^iPr)$ (**2a**, R = CH_3 and **2b**, R = Ph) and $Cl_4(RCN)W(NC_3H_5)$ (**3a**, R = CH_3 and **3b**, R = Ph)].¹⁵³⁻¹⁵⁷ From the study of films deposited using these precursors, it was evident that the N-C imido bond strength has a significant effect on the N content of the deposited film. Films deposited with **1a,b** were W-rich and poor in N

because the strong N-C imido bond results in the cleavage of W-N bond. Films deposited with **2a,b** and **3a,b** have a higher N content due to relatively weaker N-C bond strength, even though the N content was below the desirable levels for diffusion barrier application.

Previous studies on WN_xC_y deposition by MOCVD using **1a,b**, **2a,b** and **3a,b** have shown that the films have low N content. As discussed earlier, excess N in diffusion barrier films is desirable because it improves the diffusion barrier performance by ‘stuffing’ the grain boundaries. Another concern for deposition using precursors **1a,b**, **2a,b** and **3a,b** was that the lowest temperature at which films could be deposited was 450 °C or higher. It is desirable to deposit WN_xC_y films at even lower temperature as low- k dielectrics are thermally unstable above 450 °C. In the present work, further investigation is done to deposit WN_xC_y thin films with alternate chemistries to deposit films with higher N content at temperature below 450 °C. To improve film N content, two different approaches have been used. One is the use of precursors with higher N:W ratio such as $W(N^iPr)Cl_3[{}^iPrNC(NMe_2)N^iPr]$ (**4**) and $(CH_3CN)Cl_4W(NNMe_2)$ (**5**). The other approach is to use co-reactant NH_3 to increase film N content.

Chapter 4 investigates the use of NH_3 with **3a,b** to increase the film N content. Chapter 5 discusses the results for film deposition using **4** and H_2 . Chapter 6 discusses the results obtained from thin film deposition using **4** and NH_3 (with and without H_2). The results obtained from thin films deposited with **5** and H_2 are discussed in Chapter 7. To facilitate the understanding of the gas phase reactions of **5**, Chapter 8 discusses results from quantum mechanical calculations using density functional theory. Chapter 9 provides a summary of work reported in this manuscript and discusses future work that would enhance our understanding of WN_xC_y thin film deposition using MOCVD.

Table 2-1. Melting temperature of Ti, Ta, and W and their nitrides and carbides³⁹

Transition Metal	T _m (°C)
Titanium	1677
Tantalum	2997
Tungsten	3380
Titanium Nitride	2949
Tantalum Nitride	3093
Tungsten Nitride	< 800 for WN
Titanium Carbide	3067
Tantalum Carbide	3983
Tungsten Carbide	2776

Table 2-2. Techniques used for characterization of diffusion barrier thin films

Film Property	Characterization Technique	Acronym(s)
Microstructure	X-ray diffraction	XRD
	Grazing Incidence XRD	GIXD, GIXRD
	Scanning electron microscopy	SEM
	Electron diffraction in transmission electron microscopy	TEM
Composition	Auger electron spectroscopy	AES
	X-ray photoelectron spectroscopy	XPS, ESCA
	Electron dispersive X-ray spectroscopy	EDS, EDX
	Secondary ion mass spectroscopy	SIMS
	Rutherford back scattering	RBS
	Elastic recoil detection analysis	ERDA
Film Thickness	Scanning electron microscopy	SEM
	Transmission electron microscopy	TEM
	Profilometer	
	Rutherford backscattering	RBS
	X-ray reflectivity	XRR
Density	X-ray reflectivity	XRR
	Rutherford backscattering	RBS
Resistivity	Four point probe	
Surface roughness	Atomic force microscopy	AFM
	Optical profilometer	
	Stylus profilometer	
	X-ray reflectivity	XRR
Atomic Bonding	X-ray photoelectron spectroscopy	XPS
Film Adhesion	Four point bend test, Scotch tape test	

Table 2-3. Precursors used for deposition of TiN_x thin films by CVD

Technique		Ti source	N source	Reference	
CVD	Inorganic Precursor	TiCl ₄	NH ₃	51-55, 158-160	
		TiI ₄		56, 57	
	Metal-organic Precursor	tetrakis (dimethylamido) titanium (TDMAT)			60-62, 68, 69, 72, 161
		tetrakis (dimethylamido) titanium	H ₂ or N ₂ + post-growth plasma exposure		68, 69, 162-164
		tetrakis (dimethylamido) titanium	NH ₃		60, 64-66, 165
		tetrakis (dimethylamido) titanium	hydrazine		67
		tetrakis (diethylamido) titanium (TDEAT)	inert gas		70, 64, 68, 166
		tetrakis (diethylamido) titanium	NH ₃		64, 66, 70, 71
PECVD	Inorganic Precursor	TiCl ₄	H ₂ , N ₂ plasma	58, 59	
	Metal-organic Precursor	tetrakis (diethylamido) titanium	H ₂ or N ₂ plasma	72	

Table 2-4. Precursors used for deposition of TiN_x thin films by ALD

Technique		Ti source	N source	Reference
ALD	Inorganic Precursor	TiCl ₄	NH ₃	73, 74, 77, 83, 86, 172
		TiCl ₄	Zn + NH ₃	75, 79
		TiCl ₄	dimethylhydrazine	80
		TiCl ₄	<i>tert</i> -butylamine	81
		TiCl ₄	allylamine	81
		TiI ₄	NH ₃	79, 81, 83
	Metal-organic Precursor	TDMAT	NH ₃	86, 87, 167, 168
		TEMAT	NH ₃	84, 85, 167
PAALD	Inorganic Precursor	TiCl ₄	NH ₃	78
	Metal-organic Precursor	TDMAT	remote N ₂ /H ₂ plasma	88, 89

Table 2-5. Precursors used for deposition of TaN_x thin films by CVD

Technique		Ti source	N source	Reference	
CVD	Inorganic Precursor	TaCl ₅	NH ₃	90, 169	
		TaF ₅	NH ₃	90	
		TaBr ₅	NH ₃	90	
		TaBr ₅	H ₂ + NH ₃	91, 92	
	Metal-organic Precursor	<i>tert</i> -butylimido tris(diethylamido) tantalum (TBTDET)			95-97
		pentakis(dimethylamido) tantalum (PDMAT)		NH ₃	98, 170
		pentakis(diethylamido) tantalum (PDEAT)		NH ₃	99, 100
		<i>tert</i> -amylimidotris(dimethylamido) tantalum (TAIMATA)		NH ₃	103
		ethylimidoethyl(C,N) tris(diethylimido) tantalum		H ₂	91
	PECVD	Inorganic Precursor	TaCl ₅	N ₂	90, 93
TaF ₅			N ₂	90	
TaBr ₅			N ₂	90	
TaBr ₅			N ₂ + H ₂	94	
TaBr ₅			N ₂	90	

Table 2-6. Precursors used for deposition of TaN_x thin films by ALD

Technique		Ta source	N source	Reference	
ALD	Inorganic Precursor	TaCl ₅	NH ₃	104, 105	
		TaCl ₅	Zn + NH ₃	105	
		TaCl ₅	1,1 dimethyl hydrazine	80	
		TaCl ₅	<i>tert</i> -butylamine (+NH ₃) or allylamine (+ NH ₃)	106	
		TaBr ₅	<i>tert</i> -butylamine (+NH ₃)	106	
	Metal-organic Precursor	<i>tert</i> -butylimido tris(diethylamido) tantalum (TBTDET)	NH ₃	108-110	
		pentakis(dimethylamido) tantalum (PDMAT)	NH ₃	111-114	
		tertiaryamylimidotris (dimethylamido) tantalum (TAIMATA)	NH ₃	109, 116	
	PAALD	Inorganic Precursor	TaCl ₅	N ₂ /H ₂ plasma	107
		Metal-organic Precursor	<i>tert</i> -butylimido tris(diethylamido) tantalum (TBTDET)	H radicals	110, 171
pentakis(dimethylamido) tantalum (PDMAT)			H ₂ /N ₂ plasma	112, 114, 115	
tertiaryamylimidotris (dimethylamido) tantalum (TAIMATA)			H ₂ plasma	116	

Table 2-7. Precursors used for deposition of WN_x thin films by CVD

Technique		W source	N source	Reference
CVD	Inorganic Precursor	WCl_6	$NH_3 + H_2$	117, 118
		WF_6	$NH_3 + H_2$	119
		WF_6	$NH_3 +$ $SiH_4 + H_2$	120
	Metal organic Precursor	<i>tert</i> -butylimino <i>tert</i> - butylamido tungsten	NH_3 or Ar	31, 132-134
		tungsten hexacarbonyl	NH_3	135-137
		tungsten pentacarbonyl 1-methylbutylisonitrile	NH_3	138
PECVD	Inorganic Precursor	WF_6	NH_3 plasma	121-123
		WF_6	$H_2 + NH_3$ plasma	124-130
		WF_6	$H_2 + N_2$ plasma	32, 131

Table 2-8. Precursors used for deposition of WN_x thin film by ALD

Technique		W source	N source	Reference
ALD	Inorganic Precursor	WF_6	NH_3	139, 140
		WF_6	NH_3 and B_2H_6	141
PAALD	Metal organic Precursor	bis(<i>tert</i> -butylimido) bis(dimethylamido) tungsten	NH_3	45, 144
		Inorganic Precursor	WF_6	NH_3 plasma

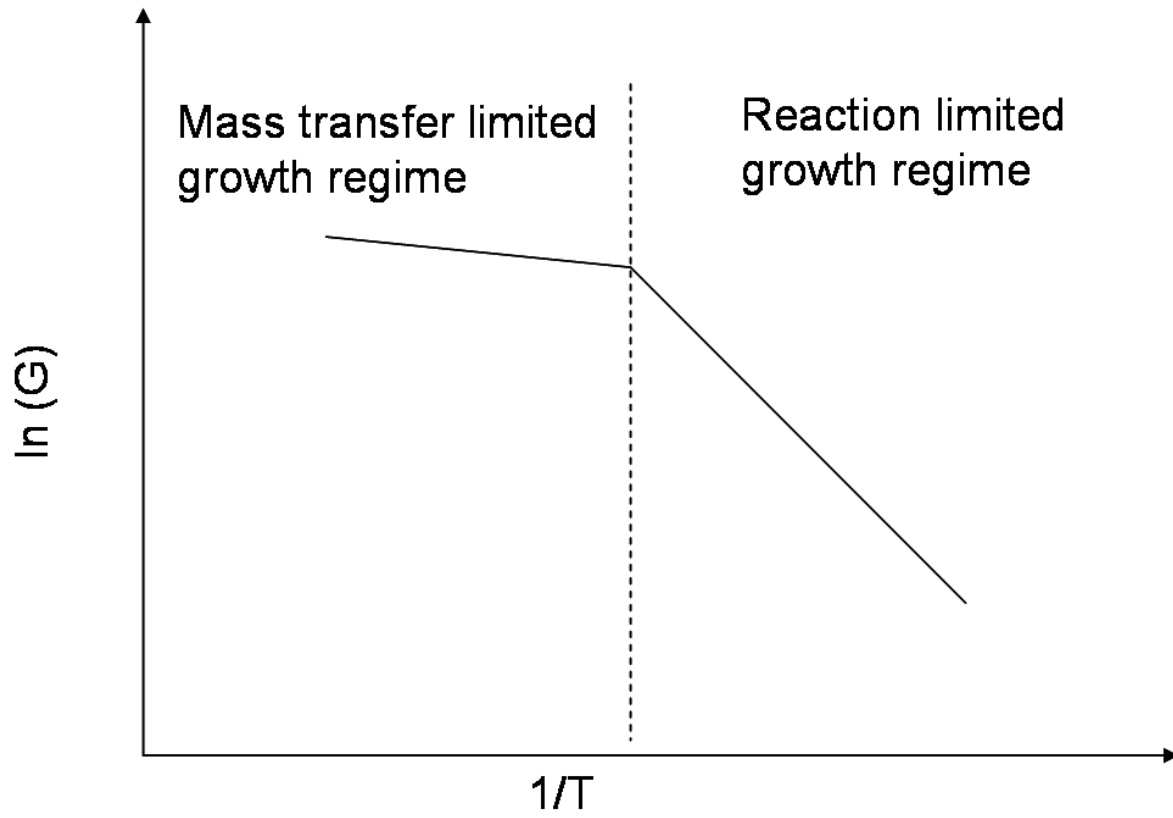


Figure 2-1. Arrhenius plot for CVD showing mass transfer limited and reaction limited growth regimes. G is the film growth rate and T is the deposition temperature in K

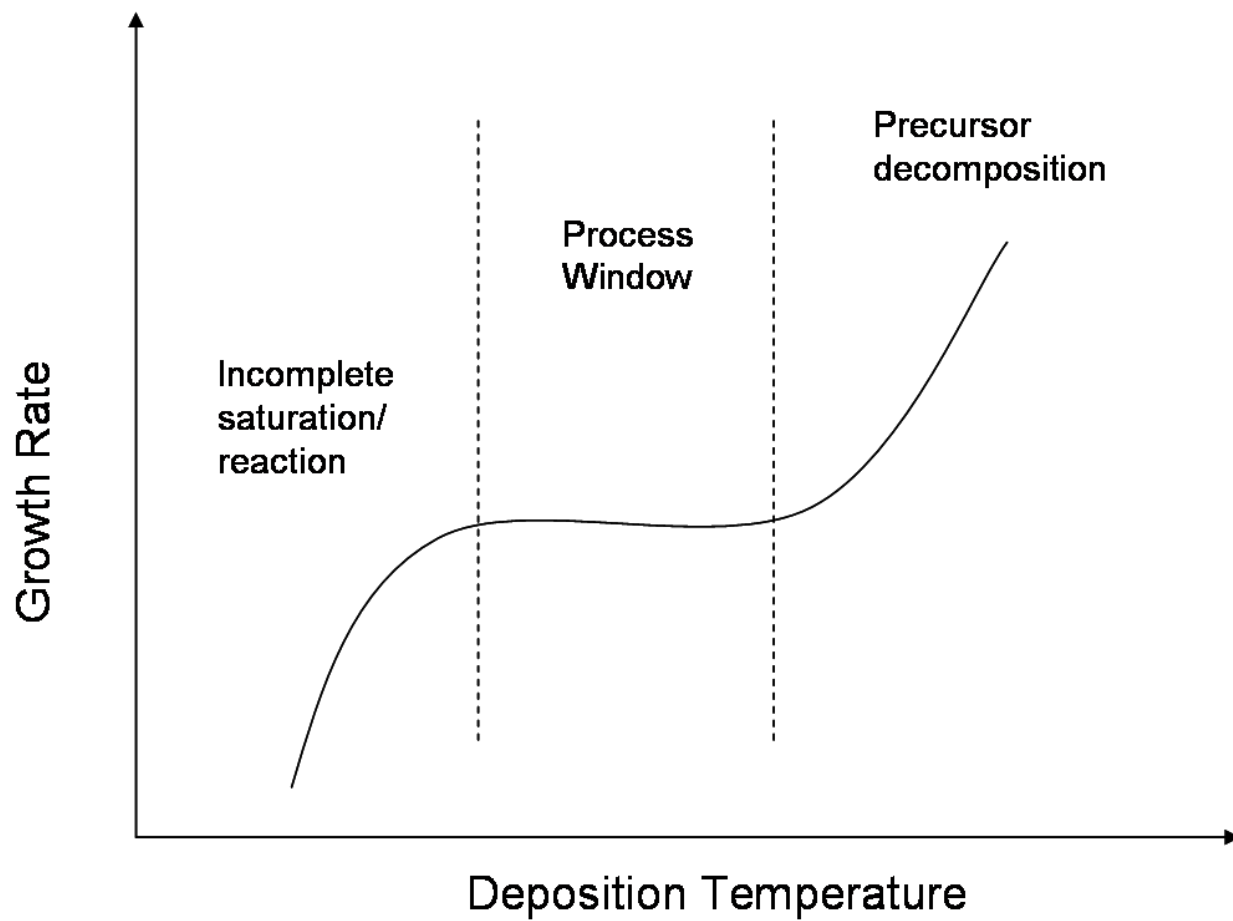


Figure 2-2. Characteristic ALD growth rate vs. T curve showing different growth regimes

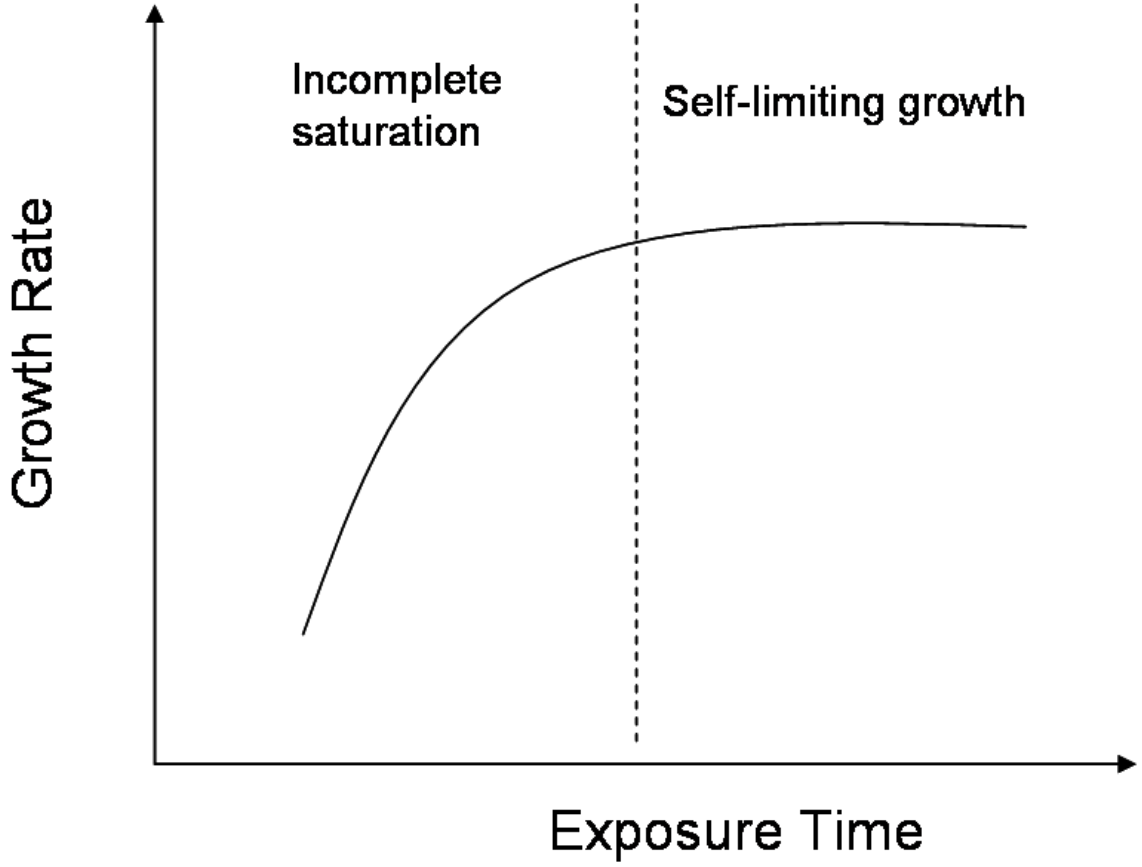


Figure 2-3. Characteristic ALD plot showing the exposure time required to achieve self-limiting growth

CHAPTER 3
EXPERIMENTAL TECHNIQUES FOR THIN FILM DEPOSITION AND
CHARACTERIZATION

3.1 Description of the CVD Reactor

All the depositions of WN_xC_y were done in a custom CVD reactor (Figure 3-1). Metal organic precursor used for CVD deposition was dissolved in benzonitrile solvent and loaded into a syringe. The solution was delivered into a nebulizer at a constant flow rate of 4 mL/hr. The nebulizer contains a quartz plate that converts the precursor-solvent mixture into aerosol and the aerosol is carried to the reactor via carrier gas (H_2 , $H_2 + NH_3$ or $N_2 + NH_3$). The aerosol/ carrier gas mixture was delivered to the reactor through heated delivery tube. The delivery tube was heated to prevent condensation and accumulation of condensates on the tube wall. The substrate was heated by RF generator and the RF power was adjusted to change the temperature of the substrate. A detailed description of the system has been reported previously.¹⁷³

3.2 Modification of the CVD Reactor

There were 4 major changes made in the experimental setup:

- Installation of H_2 and N_2 purifiers in the H_2 and N_2 delivery lines
- Reconfiguration of the gas lines downstream of the reactor
- Modification to the line for delivery of NH_3
- Replacement of MKS mass flow and pressure programmer/ display

3.2.1 Installation of H_2 and N_2 Purifiers in the H_2 and N_2 Delivery Lines

The precursors used for CVD deposition are oxygen sensitive. Hence, the CVD reactor should contain a minimal amount of oxygen during film growth. Ultra high purity gases (H_2 and N_2) obtained from Praxair contain a few ppm of oxygen and water vapor. The intent behind installing purifiers was to reduce the impurity levels of carrier gas from ppm level to ppb level. Figure 3-2 shows the change in feed line configuration before and after the installation of gas purifiers. The purifiers were made by Saes Corporation (model # PS11-MC1N for N_2

purification and PS11-MC1H for H₂ purification). The purifier uses activated catalyst to adsorb gases such as O₂, H₂O, CO and CO₂. The installation of the purifier requires that they be installed vertically with the gas inlet from the top. The gas lines were purged prior to installation of purifier since exposure to atmosphere can poison the catalyst in the purifier. The purifier also contained a particle filter that removes particles with size larger than 0.003 μm in diameter. The purifier was connected to the lines by VCR fittings. The purifier is designed to operate at a maximum flow of 5000 sccm with nominal flow of 500 sccm.

3.2.2 Reconfiguration of the Gas Lines Downstream of the Reactor

One of the major operational problems for the CVD system was the failure of the throttle valve. The throttle valve uses a small disc with an o-ring inside a cylindrical bore to modulate the conductance through the valve. To control the reactor pressure, a throttle valve controller adjusts the disc position in the valve based on the difference between pressure input from the Baratron pressure gauge and the set point for the reactor pressure. The main problem with the throttle valve was the swelling of the o-ring on the disc due to absorption of benzonitrile solvent. Since the cold trap, intended to remove condensables such as solvent vapor, was installed downstream of the throttle valve, the disc was exposed to the benzonitrile solvent. The swelling of the disc's o-ring due to benzonitrile absorption resulted in rupture of the o-ring. Consequently, the throttle valve was not able to control the reactor pressure. The frequency of throttle valve failure was once every four to six experiments.

To alleviate the problem of throttle valve failure, the downstream of the reactor was reconfigured (Figure 3-3). A cold trap was installed between the reactor and throttle valve so that benzonitrile could be condensed and removed from effluent gas to minimize the exposure of throttle valve o-ring to benzonitrile. As a result of this modification, the frequency of throttle valve failure was reduced to once every 50 experiments.

The glass cold trap was replaced by a new stainless steel cold trap (Figure 3-4). The stainless steel cold trap was designed such that its total internal volume was same as that of the glass cold trap. The glass cold trap had no port for removing the condensate collected at the bottom of cold trap. The stainless steel cold trap had an inclined bottom to collect the benzonitrile and other condensables near the purge port. After every experiment, about 1 - 2 ml of solvent (primarily benzonitrile) condensed in the cold trap. Before starting new experiment, the solvent collected in the cold trap was removed by opening the purge valve at the bottom of the cold trap.

3.2.3 Modification to the Line for Delivery of NH₃ to the Reactor

When NH₃ was used as a co-reactant, the gas was delivered using a secondary NH₃ line labeled as 'Old NH₃ feed port' in Figure 3.5. Films deposited when NH₃ was used as co-reactant were quite non-uniform in thickness. The primary reason for this non-uniformity was the inhomogeneous distribution of NH₃ because of the proximity of the NH₃ feed port to the substrate surface. To alleviate this problem, a modification was made in the system near the H₂ inlet line at the nebulizer. The line was split to allow for the introduction of NH₃ along with the H₂. The new port from which NH₃ was introduced is labeled 'new NH₃ feed port' in Figure 3-5. This modification allowed the NH₃ gas to mix properly with the H₂ carrier gas prior to the exposure of the gas mixture on the substrate. Films deposited after this modification had uniform film thickness as measured by SEM.

3.2.4 Replace MKS Mass Flow and Pressure Programmer Display

The old MKS mass flow and pressure programmer (MKS 147) failed to control the flow rate of NH₃ and had to be replaced. The manufacturing of MKS 147 pressure and flow controller has been discontinued by MKS Inc. So, a new MKS mass flow and pressure programmer display (MKS 647B) was installed in the system. The MKS 647B mass flow and pressure

programmer/display has a LCD display while the old MKS 147 had a CRT display. Most of the other features of MKS 647 B are similar to that of MKS 147. However, the new controller required rewiring of the transducer input into the controller.

3.3 Operating Procedure for CVD Deposition

The operating procedure for CVD deposition has been described previously.¹⁷³ The only change made to the procedure was that after the growth, the substrates were taken out of the CVD chamber only after the substrate temperature reached room temperature. The old procedure allowed for the substrates to be unloaded from the reactor once the substrate temperature was below 75 °C. The procedure was modified primarily to minimize the diffusion of oxygen into the deposited film.

3.4 Deposition Parameters

Table 3-1 shows the flow rates of precursor, solvent and carrier gas used for CVD growth. For a particular set of experiments, all the deposition parameters except substrate temperature were held constant. Depositions at different growth temperature were done to understand the effect of substrate temperature on film properties such as growth rate, crystallinity, resistivity, atomic bonding and efficacy as a diffusion barrier.

3.5 Dimensionless Numbers for CVD Reactor

Dimensionless numbers can provide valuable insight into the effect of various process parameters such as temperature and pressure on reactor flow pattern. This section discusses the calculation results for important dimensionless numbers for the CVD film growth for the reactor and deposition conditions discussed previously. The calculation of dimensionless numbers has been done by using the thermophysical properties of carrier gas alone unless specified otherwise.

3.5.1 Prandtl Number

The Prandtl number, Pr, is the ratio of momentum diffusivity to thermal diffusivity.

$$\text{Pr} = \frac{\nu}{\alpha} = \frac{\mu}{k/c_p} \quad (3-1)$$

The kinematic viscosity is ν , thermal diffusivity is α , viscosity is μ , thermal conductivity is k and specific heat at constant pressure is c_p . Chapman-Enskog theory can be used to estimate the Newtonian viscosity.¹⁷⁴

$$\mu = (2.669 \times 10^{-6}) \frac{(MT)^{0.5}}{\sigma^2 \Omega_\mu} \quad (3-2)$$

The molecular weight is M (kg/kgmol), temperature is T (K), collision diameter is σ (Å) and dimensionless collision integral is Ω_μ . Ω_μ is a function of dimensionless temperature, $k_B T/\epsilon$. For H_2 and N_2 carrier gases used for CVD deposition, the value of ϵ/k_B are 38.0 and 91.5 respectively. Since the depositions were done between 300 and 750 °C, the value of dimensionless temperature is greater than 6.0. For dimensionless temperature greater than 6.0, Ω_μ is given by Equation 3-3.¹⁷⁵

$$\Omega_\mu = 1.1615 \left(\frac{k_B T}{\epsilon} \right)^{-0.1487} \quad (3-3)$$

For N_2 and H_2 , the value of σ is 3.681 and 2.915 respectively.¹⁷⁶ Substituting these values in Equation 3-2, the value of μ for H_2 and N_2 carrier gases be calculated.

$$\mu_{H_2} = 4.5864 \times T^{0.6487} \quad (3-4)$$

$$\mu_{N_2} = 4.5864 \times T^{0.6487} \quad (3-5)$$

The thermal conductivity for a polyatomic gas is given by modified Eucken correlation (Eq. 3-6).¹⁷⁴

$$k = \frac{\mu R}{M} \left[1.32 \left(\frac{c_p M}{R} - 1 \right) + 1.77 \right] \quad (3-6)$$

The Universal gas constant (8314 J/mol-K) is R. Since depositions in CVD reactor were done at high temperature and low pressure, the ideal gas assumption is valid. For an ideal polyatomic gas, c_p is given by Equation 3-7.

$$c_p = \frac{7R}{2M} \quad (3-7)$$

Substituting the values of c_p , μ , R and M in Equation 3-6, the value of k can be calculated (Eq. 3-8 and 3-9).

$$k_{H_2} = 4.6742 \times 10^{-3} T^{0.6487} \quad (3-8)$$

$$k_{N_2} = 6.8995 \times 10^{-3} T^{0.6487} \quad (3-9)$$

From Equations 3-4, 3-5, 3-7, 3-8 and 3-9, the value calculated for Pr is 0.690 for both H₂ and N₂ carrier gases. The value of Pr indicates that the thermal boundary layer and the velocity boundary layer for both H₂ and N₂ carrier gases are important for thermal diffusion consideration.

3.5.2 Knudsen Number

Knudsen number (Kn) determines if the continuum approach can be used for the fluid flow in CVD reactor. For a dilute gas mixture in which species B is the predominant gas, Knudsen number is given by Equation 3-10.¹⁷⁷

$$Kn = 1.758 \times 10^{-3} \left[\left(\frac{M_A + M_B}{M_B} \right)^{-0.5} \frac{1}{(\sigma_A + \sigma_B)^2} \right] \frac{1}{L} \left(\frac{T}{x_B P} \right) \quad (3-10)$$

The characteristic length of the reactor is L, molecular weight of dilute species A (precursor **3a,b, 4** or **5**) is M_A , molecular weight of species B (H₂ or N₂) is M_B , the collision diameter of species A is σ_A and the mole fraction of species B is x_B . For the CVD reactor used for film

growth, the diameter of the reactor (0.0597 m) was used as the characteristic length of the reactor. The present work used 3 different precursors, **3a,b**, **4** and **5a,b** with N₂ and/or H₂ carrier gases. The approximate values of σ_A used for **3a,b**, **4** and **5a,b** were obtained from X-ray crystallography. The distance between furthest atoms in the X-ray crystallographic structure of all three precursor molecules was ca. 10 Å and this value was used as an approximation of σ_A . It should be noted that the X-ray crystallographic structure does not account for the substitution of acetonitrile ligand by benzonitrile when the solid precursor is dissolved in benzonitrile solvent. T is calculated by averaging the temperature of the heated impinging jet (50 °C) and the temperature of the substrate (between 300 and 750 °C). Table 3-2 shows the values of Knudsen number for precursors **3a,b**, **4** and **5** at different deposition temperature. For Kn < 0.01, continuum approach is valid for analyzing the system. Since for all the different precursors and carrier gases the Kn number is of the order of 10⁻⁷, continuum approach is valid.

3.5.3 Reynolds Number

The Reynolds number (Re) is the ratio of inertial to viscous force. Reynolds number for a CVD system is given by Equation 3-11.¹⁷⁷

$$\text{Re} = 3.747 \times 10^5 \left(\frac{\sigma^2 \Omega_\mu}{M^{0.5}} \right) \left(\frac{L}{A_{cs}} \right) \left(\frac{\dot{m}}{T^{0.5}} \right) \quad (3-11)$$

The cross-sectional area of the reactor is A_{cs} (m²) and the mass flow rate of the carrier gas is \dot{m} (kg/s). Reynolds number is calculated using carrier gas only because the molar flow rate of carrier gas is at least 3 orders of magnitude higher than that of the precursor. A_{cs} for the reactor is 2.8 × 10⁻³ m² and mass flow rate for H₂ and N₂ are 3.41 × 10⁻⁷ kg/s and 4.77 × 10⁻⁶ kg/s respectively. Table 3-3 shows the value of Re for H₂ and N₂ at different deposition temperature. Since the value of Re is less than 2000, the flow through the reactor is laminar.

3.5.4 Peclet Number

The Peclet number (Pe) is a dimensionless number related to the rate of advection of flow to its thermal diffusion. It is calculated by multiplying Reynolds number with Prandtl number. Forced convective heat transfer can be neglected if $Pe^{0.5} \ll 1$. Table 3-3 shows the values of Pe and $Pe^{0.5}$ calculated for H₂ and N₂ carrier gases at different deposition temperature. Since $(Re \cdot Pr)^{0.5}$ for H₂ and N₂ is not $\ll 1$, forced convective heat transfer through the reactor can not be neglected.

3.5.5 Grashof Number

The Grashof number (Gr) is the ratio of buoyancy force to viscous force on a fluid. This dimensionless number is helpful in determining the occurrence of turbulence for free convection. If the Grashof number is less than 10^5 , no turbulence effects are expected for free convection. Grashof number for the CVD reactor is given by Equation 3-12.¹⁷⁷

$$Gr = 1.9903 \times 10^4 (M \sigma^4 \Omega_\mu^2) (L^3) \left(\frac{\Delta T P^2}{T^4} \right) \quad (3-12)$$

The characteristic temperature difference, ΔT , is calculated by subtracting the impinging jet temperature from the temperature of the substrate. Table 3-4 summarizes the Grashof number calculated for H₂ and N₂ at different deposition temperature. For H₂, the value of Gr is less than 10^5 indicating that turbulence is not expected for free convection. However, Gr for N₂ is significantly higher than 10^5 suggesting that turbulence is expected for free convection when N₂ is used as carrier gas. Experimentally, when N₂ is used as carrier gas, condensates of benzonitrile are observed in the view port. Since the view port is located above the shower head, benzonitrile condensation on view port is possible only if longitudinal convective rolls are present in the reactor. However, when H₂ is used as carrier gas, no such condensation is

observed on the view port. This observation along with the value of Grashof number for N₂ confirms that buoyancy effects are important when N₂ is used as a carrier gas.

3.5.6 Rayleigh Number

The Rayleigh number (Ra) is the ratio of thermal flux by free convection to that by diffusion. Rayleigh number is defined as the product of Grashof number and Prandtl number. Table 3-4 summarizes the Rayleigh number calculated for H₂ and N₂ carrier gas for different deposition temperature. Natural convective heat transfer can be neglected if $(Ra*Pr)^{0.25} \ll 1$. Since the value of $(Ra*Pr)^{0.25}$ is not $\ll 1$ for both H₂ and N₂ carrier gas throughout the deposition temperature, natural convective heat transfer cannot be neglected. Longitudinal convective rolls have been observed in horizontal CVD reactor for $Ra > 1708$.¹⁷⁷ For both H₂ and N₂, the value of Ra is greater than 1708 indicating that convective rolls are present in the reactor. Furthermore, the convective rolls are expected to be more severe for N₂ carrier gas because the Ra value for N₂ is two orders of magnitude higher than 1708. Experimentally, the condensation of benzonitrile on the view port confirms that the problem of recirculation is more severe for N₂ as compared to H₂ carrier gas.

3.6 Techniques Used for Thin Film Characterization

3.6.1 X-Ray Diffraction

The film crystallinity was examined by Philips APD 3720, operating from 5 - 85 2θ degrees with Cu Kα radiation. X-rays were generated at 40 kV voltage and 20 mA current. Monochromatic Cu Kα radiation was obtained by filtering out the Cu Kβ radiation using a Ni filter. When the films were extremely thin (few nm thick), film crystallinity was measured by GIXD technique using Phillips MRD X'Pert system. Cu Kα radiation, generated at 45 kV and 40 mA (1.8 kW), was used for the GIXD analysis. The angle of incidence for measurements was 2° and the step size was 0.02° per step. The peaks obtained from the XRD and GIXD spectra

were compared with reference spectra in the JCPDS database¹⁷⁸ to determine the crystalline phase(s) present in the film. Table 3-5 lists the reference peak positions and their relative intensities for β -W₂N, β -W₂C, α -W₂C, WO₃ and Si.¹⁷⁸

The broadening of peak in XRD spectra can be used to calculate the grain size of the crystallites by Scherrer's equation (Eq. 3-13).¹⁷⁹

$$t = 0.9\lambda / (B \cos \theta) \quad (3-13)$$

The wavelength of X-rays used for measurement is λ , the angle of incidence is θ , and the broadening of the diffraction line measured as full width at half maximum (FWHM) is B. For β -W₂N or β -W₂C peaks, the most intense (111) diffraction peak was used to determine FWHM.

The peak position in an XRD spectrum can also be used to calculate the lattice parameter of the unit cell. The inter-planar spacing, d, is obtained from Bragg's Law.

$$d = \frac{\lambda}{2\sin\theta} \quad (3-14)$$

The value of λ for Cu K α 1 radiation is 1.5405 Å. The lattice parameter, a, for a cubic cell is given by Equation 3-15.

$$\frac{1}{d^2} = \frac{1}{a^2} (h^2 + k^2 + l^2) \quad (3-15)$$

The Miller Indices are h, k and l. For a hexagonal crystal, the lattice parameter is given by Equation 3-16.

$$\frac{1}{d^2} = \frac{4}{3a^2} (h^2 + hk + k^2) + \frac{1}{c^2} (l^2) \quad (3-16)$$

For hexagonal crystal, two different peak positions are required to solve for lattice parameters a and c.

3.6.2 Auger Electron Spectroscopy

Film composition was determined by AES. In AES, energetic electrons are used to knock out core electron of atoms close to the surface of the thin film. The excited atom relaxes to lower energy state by either Auger emission or X-ray fluorescence. In Auger emission, the excited atom relaxes to lower energy state by transitions of an electron from higher energy level to the inner shell. The excess energy from the transition causes another electron from higher energy level to eject from the atom. The kinetic energy of the ejected Auger electron can be used to identify the energy levels for that particular transition. Determination of the energy levels can then be used for elemental identification. In AES spectra, the number of electrons ejected is plotted versus the kinetic energy and the data are differentiated for better resolution. Elemental identification is then done by comparing the peak positions in the AES spectrum to reference spectral lines of different elements.

Auger electron spectroscopy measurements were done using a Perkin-Elmer PHI 660 Scanning Auger Multiprobe. A 5 kV acceleration voltage and 50 nA beam current was used for the Auger analysis. The beam diameter was 1 μm and the angle of incidence was 45° . The AES spectra were obtained between 50 and 2050 eV with a step size of 1 eV. Prior to AES measurement, the sample surface was cleaned by sputter etching for 30 sec using Ar^+ ions. The etch rate for the sputtering was calibrated at $100 \text{ \AA}/\text{min}$ using a Ta_2O_3 standard. The ion gun for sputtering was operated at 15 mA current at Ar pressure of $1.5 \times 10^{-3} \text{ Pa}$. The beam voltage of the ion gun was 5 keV.

A general expression for determination of quantification of atomic concentration is given by Equation 3-17.

$$X_a = \frac{N_a}{\sum N_i} = \frac{I_a/S_a}{\sum I_i/S_i} \quad (3-17)$$

where,

X_a = concentration of any constituent a in the sample

N_a = number of atoms per unit volume of constituent a

$\sum N_i$ = sum of number of atoms per unit volume of all the constituents of the film

I_a = Auger intensity of a particular transition for constituent a

$\sum I_i$ = sum of Auger intensities of all the constituents of the film

S_a = relative sensitivity factor for constituent a

S_i = relative sensitivity factor of constituent i

Auger intensity is calculated from peak-to-peak height in the numerically differentiated $\text{EdN(E)}/\text{dE}$ spectrum. The spectrum is numerically differentiated according to the Savitzky-Golay differentiation algorithm using five differentiation points. The relative sensitivity factor is calculated by comparing the peak intensity of a pure element with that of a reference standard (typically the Cu LMM transition obtained at 10 keV). Table 3-6 lists the relative sensitivity factors of C, N, O and W used for quantification in AES.¹⁸⁰ The table also lists the position of peaks used for quantification of different elements. It should be noted that the calculation of atomic concentration using Equation 3-17 does not take the matrix effect into account. If an element is present in a matrix of other elements, its properties such as Auger transition probability, secondary ionization by scattered electrons and inelastic mean free path are different from that of pure element. This change in sensitivity factor is often referred to as the matrix effect. The elemental composition obtained by using pure elemental sensitivity factors can have significant error because of the matrix effect. While the absolute value of film composition might not be accurate, the film composition values can be helpful in comparing films deposited

at different process conditions. Accurate calculation of film composition requires the calibration of the sensitivity factors using a WN_xC_y standard of known composition.

The change in elemental composition of the film with depth was measured by AES depth profile. In this technique, the sample surface is sputtered and then analyzed to identify the intensity of peaks of elements present in the film. This process is repeated to obtain the depth profile for different elements. An AES depth profile can be obtained in two different ways: 3-point depth profiling and survey depth profiling. The main difference between these two techniques is the manner in which peak intensity is calculated. In survey depth profiling, an entire survey of a particular peak is taken to determine the peak intensity. In 3-point depth profiling, a peak is identified by measuring the peak at 3 points. Two of the three points correspond to the baseline of the peak and the third point corresponds to the highest point of the peak. From these three points, the peak intensity is calculated. The advantage of 3-point depth profiling over survey profiling is that since only 3 points of a peak are measured, the measurement is much faster and a better depth resolution can be achieved. The disadvantage of this technique is that precise elemental composition can not be determined. In the present work, 3-point technique was used for depth profiling.

3.6.3 X-Ray Photoelectron Spectroscopy

XPS analysis was done to obtain bonding information of atoms in thin films. Surface analysis by XPS is done by irradiating the sample surface with monoenergetic soft X-rays and measuring the energy of the electrons ejected from sample by photoemission process. The kinetic energy of an emitted electron, KE, is given by Equation 3-18.

$$KE = hv - BE - \phi_s \quad (3-18)$$

The energy of the photon is hv , the binding energy of atomic orbital from which the electron is generated is BE and the work function of the spectrometer is ϕ_s . Since each element has a

unique binding energy, XPS can be used to determine the elements present in the sample. Depending on the bonding of a particular atom in the sample, the binding energy of that atom shifts. This shift can be used to obtain the bonding information of an element in the sample. Table 3-7 lists the binding energies of atoms in different compounds of W, C, N and O along with pure elemental binding energies of polymeric and graphitic carbon.

X-ray photoelectron spectroscopy measurements were taken using a Perkin Elmer PHI 5600 system. X-ray photoelectron spectroscopy spectra were taken using monochromatic Mg $K\alpha$ radiation with the X-ray source operating at 300 W (15 kV voltage and 20 mA current). The sample surface was sputter etched for 15 min using Ar^+ ions to remove surface contaminants. The etch rate for the XPS system was calibrated at 10 Å/min using Ta_2O_3 standard. The ion gun for sputtering was operated at 15 mA current at a Ar pressure of 1.5×10^{-3} Pa. The beam voltage of the ion gun was 5 keV.

3.6.4 Scanning Electron Microscopy

Film thickness measurement was done using SEM. In SEM, an electron beam is attracted towards substrate by a positive bias on the substrate. Secondary electrons are generated from the interaction of electron beam with the substrate surface. Secondary electrons have low energy (2 – 5 eV) and are generated very close to the surface. By mapping the coordinates with the intensity of the secondary electron, an image is constructed. For the present study, JEOL JSM 6400 and JEOL JSM 6335F scanning electron microscopes were used for measuring film thickness. To generate electron beam, JEOL JSM 6400 microscope uses thermionic emission whereas the JEOL JSM 6335F uses field emission technique. In thermionic emission, a tungsten filament was heated to 2400 °C to generate electrons. In field emission, electrons were generated by applying high bias of 15 kV on a single crystal tungsten tip. For measurements of

less than 40,000x magnification, SEM JEOL 6400 was used. To obtain resolution higher than 40,000x, a field emission SEM JEOL JSM 6335F was used. To measure film thickness, the substrate was cleaved and the cross-section of the substrate was viewed under the SEM.

3.6.5 Four Point Probe

Film sheet resistance was measured by using a four point probe. A four point probe consists of four sharp metallic probes lined with one another. Current is passed through the outer probes and the voltage is measured by the inner probes. Based on the V and I measured, the sheet resistance is calculated using Equation 3-19.

$$R_s = 4.53 \times \frac{V}{I} \quad (3-19)$$

The sheet resistance of deposited films was measured using an Alessi Industries four-point probe. The resistivity of the film, ρ , is then calculated by Equation 3-20.

$$\rho = R_s \times t \quad (3-20)$$

The thickness of the film, t, is obtained from SEM imaging.

3.7 Diffusion Barrier Testing

For diffusion barrier testing, copper film was deposited on the WN_xC_y thin film using Kurt J. Lesker CMS-18 multi-target sputter system. Prior to the deposition of copper on the barrier film, the film was exposed to air for 1 - 2 hr. The base pressure of the sputter system was 10^{-6} Torr and deposition was done at 5 mTorr with Ar used as sputter deposition gas. The forward sputtering power for Cu target was 250 W and the film growth rate was 240 Å/min. The thickness of copper deposited on the barrier film was 100 Å. After the copper deposition, the Cu/ WN_xC_y /Si stack was annealed in the same sputter chamber with the chamber pressure of ca. 10^{-6} Torr. The annealing temperature was varied between 200 and 600 °C.

To check for diffusion of copper through the barrier film, two different procedures were used. Pre- and post-anneal XRD measurement were done to check for bulk diffusion of copper through the silicon. X-ray diffraction was done using the same procedure described earlier. If the copper diffuses through the silicon, copper forms a stable compound Cu_3Si . A Cu_3Si peak in the post-anneal XRD spectrum would indicate the diffusion of copper into the silicon and the failure of the barrier film. Another method used to detect diffusion of copper in silicon was 3-point AES depth profile. An AES depth profile can indicate the presence of copper in the barrier as well as silicon. The advantage of this technique over XRD is that it has higher sensitivity (1 at. %). The disadvantage of 3-point AES depth profile is that during sputtering, the Ar^+ ion can knock copper atoms into the barrier film and also into silicon if the barrier film is very thin. This effect of sputtering is commonly referred as the 'knock-on' effect. The 'knock-on' effect can lead to artifacts in the depth profile. To avoid this problem especially for ultra thin diffusion barrier films, the copper film was etched off after annealing. The copper etching was done by dipping the $\text{Cu}/\text{WN}_x\text{C}_y/\text{Si}$ stack in 50 % HNO_3 solution for 3 seconds. The 3-point depth profile was done following the etching of the copper layer.

Table 3-1. Process parameters for CVD of thin films from precursors **3a,b**, **4** and **5**

Process Parameter	Precursor and Carrier Gas				
	3a,b +NH ₃ +H ₂ (Ch. 4)	4 + H ₂ (Ch.5)	4 +NH ₃ +H ₂ (Ch.6)	4 +NH ₃ +N ₂ (Ch.6)	5 + H ₂ (Ch.7)
Temperature (°C)	450 - 750	400-750	300 - 750	300 - 750	300 - 750
Pressure (Torr)	350	350	350	350	350
H ₂ Flow Rate (sccm)	1000	1000	1000	0	1000
N ₂ Flow Rate (sccm)	0	0	0	1000	0
NH ₃ Flow Rate (sccm)	25	0	30	30	0
Precursor conc. (mg/mL benzonitrile)	11.2	9.0	9.0	9.0	7.4

Table 3-2. Knudsen number for precursors **3a,b**, **4** and **5** with H₂ or N₂ carrier gas for different deposition temperature

Deposition Temperature (°C)	Knudsen Number					
	Precursor 3a,b		Precursor 4		Precursor 5	
	H ₂	N ₂	H ₂	N ₂	H ₂	N ₂
300	1.83×10 ⁻⁷	3.77×10 ⁻⁷	1.05×10 ⁻⁷	3.42×10 ⁻⁷	1.16×10 ⁻⁷	3.76×10 ⁻⁷
350	1.94×10 ⁻⁷	3.98×10 ⁻⁷	1.11×10 ⁻⁷	3.61×10 ⁻⁷	1.23×10 ⁻⁷	3.97×10 ⁻⁷
400	2.04×10 ⁻⁷	4.19×10 ⁻⁷	1.17×10 ⁻⁷	3.8×10 ⁻⁷	1.29×10 ⁻⁷	4.18×10 ⁻⁷
450	2.14×10 ⁻⁷	4.4×10 ⁻⁷	1.23×10 ⁻⁷	4×10 ⁻⁷	1.35×10 ⁻⁷	4.39×10 ⁻⁷
500	2.24×10 ⁻⁷	4.61×10 ⁻⁷	1.29×10 ⁻⁷	4.19×10 ⁻⁷	1.42×10 ⁻⁷	4.6×10 ⁻⁷
550	2.34×10 ⁻⁷	4.82×10 ⁻⁷	1.35×10 ⁻⁷	4.38×10 ⁻⁷	1.48×10 ⁻⁷	4.8×10 ⁻⁷
600	2.45×10 ⁻⁷	5.03×10 ⁻⁷	1.4×10 ⁻⁷	4.57×10 ⁻⁷	1.55×10 ⁻⁷	5.01×10 ⁻⁷
650	2.55×10 ⁻⁷	5.24×10 ⁻⁷	1.46×10 ⁻⁷	4.76×10 ⁻⁷	1.61×10 ⁻⁷	5.22×10 ⁻⁷
700	2.65×10 ⁻⁷	5.45×10 ⁻⁷	1.52×10 ⁻⁷	4.95×10 ⁻⁷	1.68×10 ⁻⁷	5.43×10 ⁻⁷
750	2.75×10 ⁻⁷	5.66×10 ⁻⁷	1.58×10 ⁻⁷	5.14×10 ⁻⁷	1.74×10 ⁻⁷	5.64×10 ⁻⁷

Table 3-3. Reynolds number for H₂ and N₂ carrier gas for different deposition temperature

Deposition Temperature (°C)	Reynolds Number		Peclet Number		(Re*Pr) ^{0.5} = (Pe) ^{0.5}	
	H ₂	N ₂	H ₂	N ₂	H ₂	N ₂
300	0.62	4.23	0.43	2.92	0.66	1.71
350	0.60	4.08	0.41	2.82	0.64	1.68
400	0.58	3.95	0.40	2.72	0.63	1.65
450	0.56	3.82	0.39	2.64	0.62	1.62
500	0.55	3.71	0.38	2.56	0.61	1.60
550	0.53	3.60	0.37	2.49	0.61	1.58
600	0.52	3.51	0.36	2.42	0.60	1.56
650	0.50	3.41	0.35	2.36	0.59	1.53
700	0.49	3.33	0.34	2.30	0.58	1.52
750	0.48	3.25	0.33	2.24	0.57	1.50

Table 3-4. Grashof number for H₂ and N₂ carrier gas for different deposition temperature

Deposition Temperature (°C)	Grashof Number		Rayleigh Number		(Ra*Pr) ^{0.25}	
	H ₂	N ₂	H ₂	N ₂	H ₂	N ₂
300	5388	247106	3718	170503	7	19
350	5120	234829	3533	162032	7	18
400	4788	219585	3304	151514	7	18
450	4433	203332	3059	140299	7	18
500	4081	187170	2816	129147	7	17
550	3744	171695	2583	118470	6	17
600	3428	157206	2365	108472	6	17
650	3136	143827	2164	99240	6	16
700	2869	131580	1980	90790	6	16
750	2626	120432	1812	83098	6	15

Table 3-5. Reference XRD peaks and their relative intensity for Si, β -W₂N, β -W₂C, α -W₂C and WO₃ from JCPDS¹⁷⁸ for Cu K α radiation

Si		β -W ₂ N		β -W ₂ C		α -W ₂ C		WO ₃	
2 θ	Intensity	2 θ	Intensity	2 θ	Intensity	2 θ	Intensity	2 θ	Intensity
28.44	100	37.73	100	36.98	40	34.52	25	23.64	100
47.30	55	43.85	47	42.89	100	38.03	22	33.64	69
56.11	30	63.73	33	62.03	30	39.57	100	41.46	20
69.13	6	76.52	44	74.20	50	52.30	17	48.43	16
76.38	11	80.59	13	78.23	10	61.86	14	54.57	36
						69.79	14	60.25	22
						72.84	2	70.75	6
						74.98	12	75.81	11
						75.98	10	78.06	2
						81.33	2	80.87	3

Table 3-6. Elemental relative sensitivity factors for AES quantification along with position of peaks in dN(E)/d(E) spectra used for quantification¹⁸⁰

Element	Relative sensitivity factor	Position of peak used for quantification (eV)
C	0.14	272
N	0.23	381
O	0.4	510
W	0.08	1736

Table 3-7. Binding energy of C, N, O and W in different compounds

Compound	Binding Energy (eV)				Reference
	C1s	N1s	O1s	W4f _{7/2}	
W ₂ N	--	397	--	32.8-33	122, 181, 182
W ₂ C	283.4-283.6	--	--	31.4-31.7	183-185
WC	282.7-283.5	--	--	31.8-32.4	183-186
WO ₂	--	--	530.2	32.8-33.0	183-186
W ₂ O ₅	--	--	--	34.4-34.7	186, 187
WO ₃	--	--	530.3-531.0	35.5-36.0	186-190
Pure W	--	--	--	31.2- 31.8	186, 188, 189, 191, 194
Amorphous C	284.5-285.2	--	--	--	183
Graphitic C	284.4-284.5	--	--	--	192, 193
Diamond-like C	285.3	--	--	--	192, 193

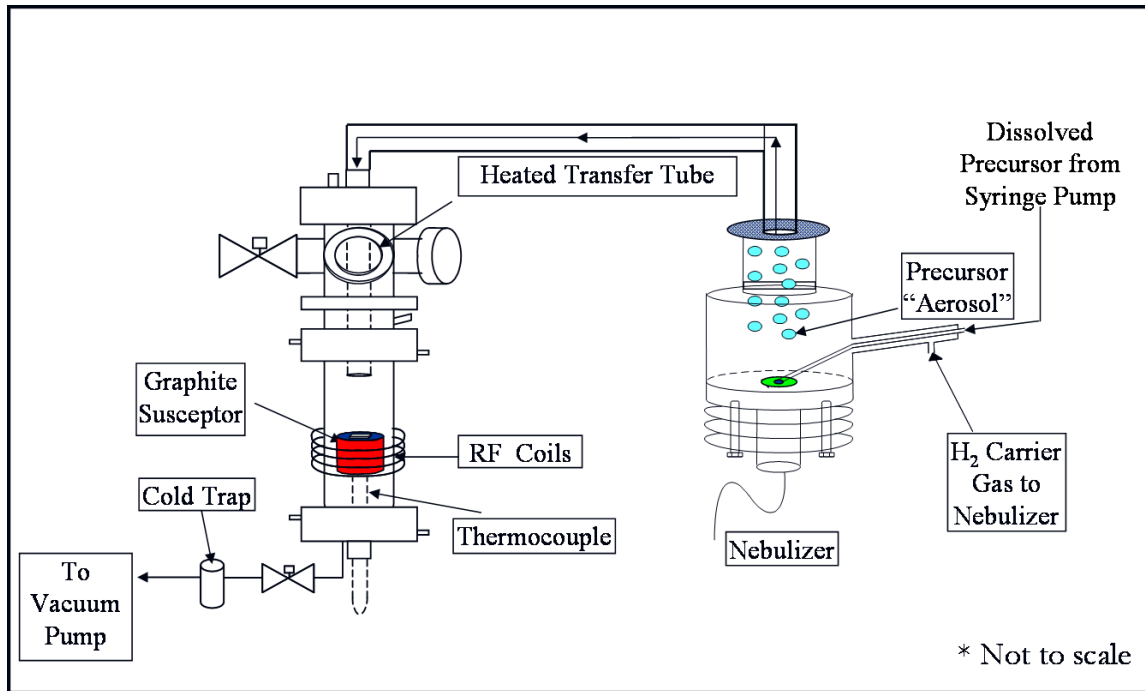


Figure 3-1. Schematic of CVD reactor used for thin film deposition

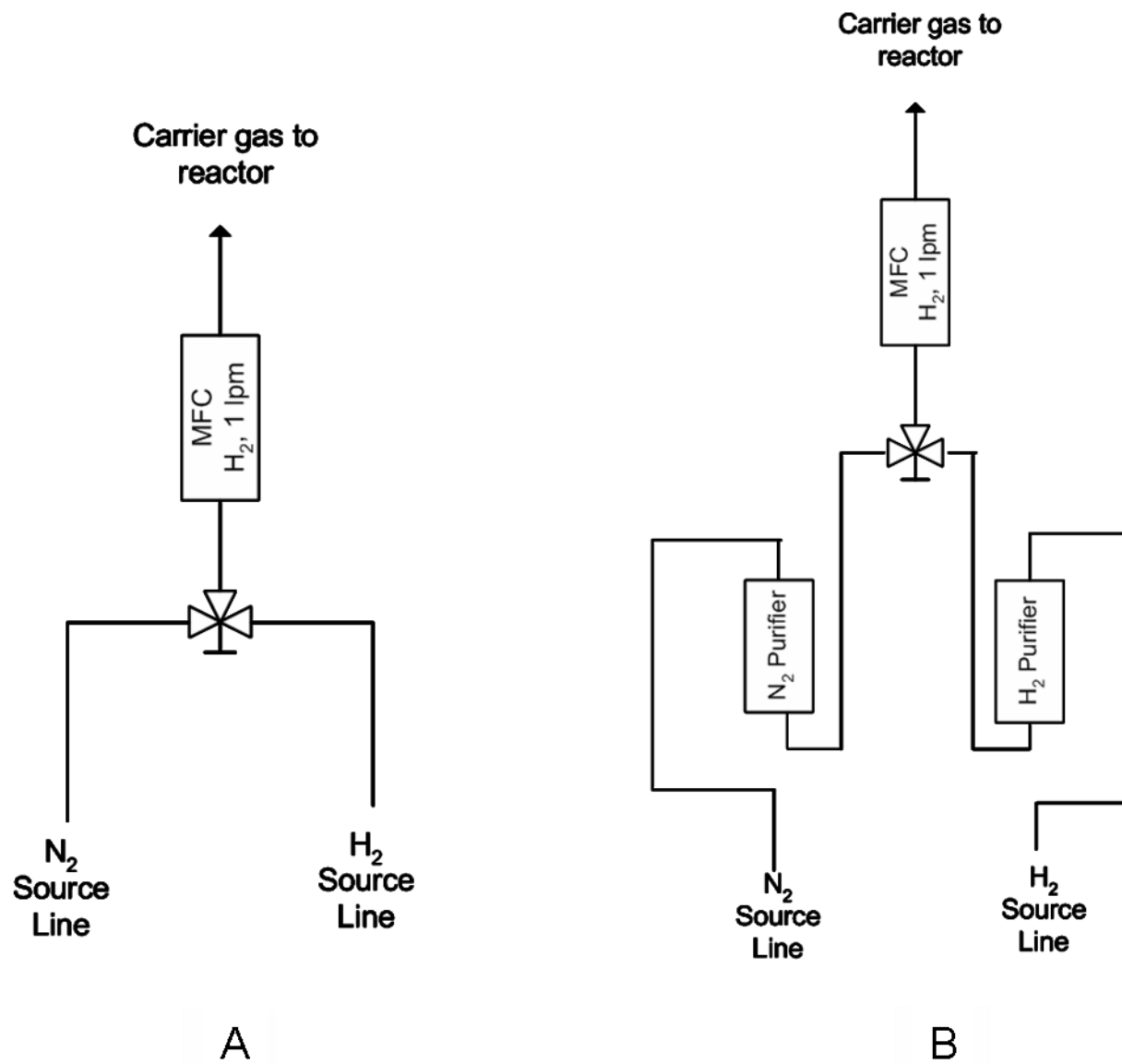


Figure 3-2. Line diagram of the carrier gas feed line. A) Before installation of gas purifier. B) after installation of gas purifier

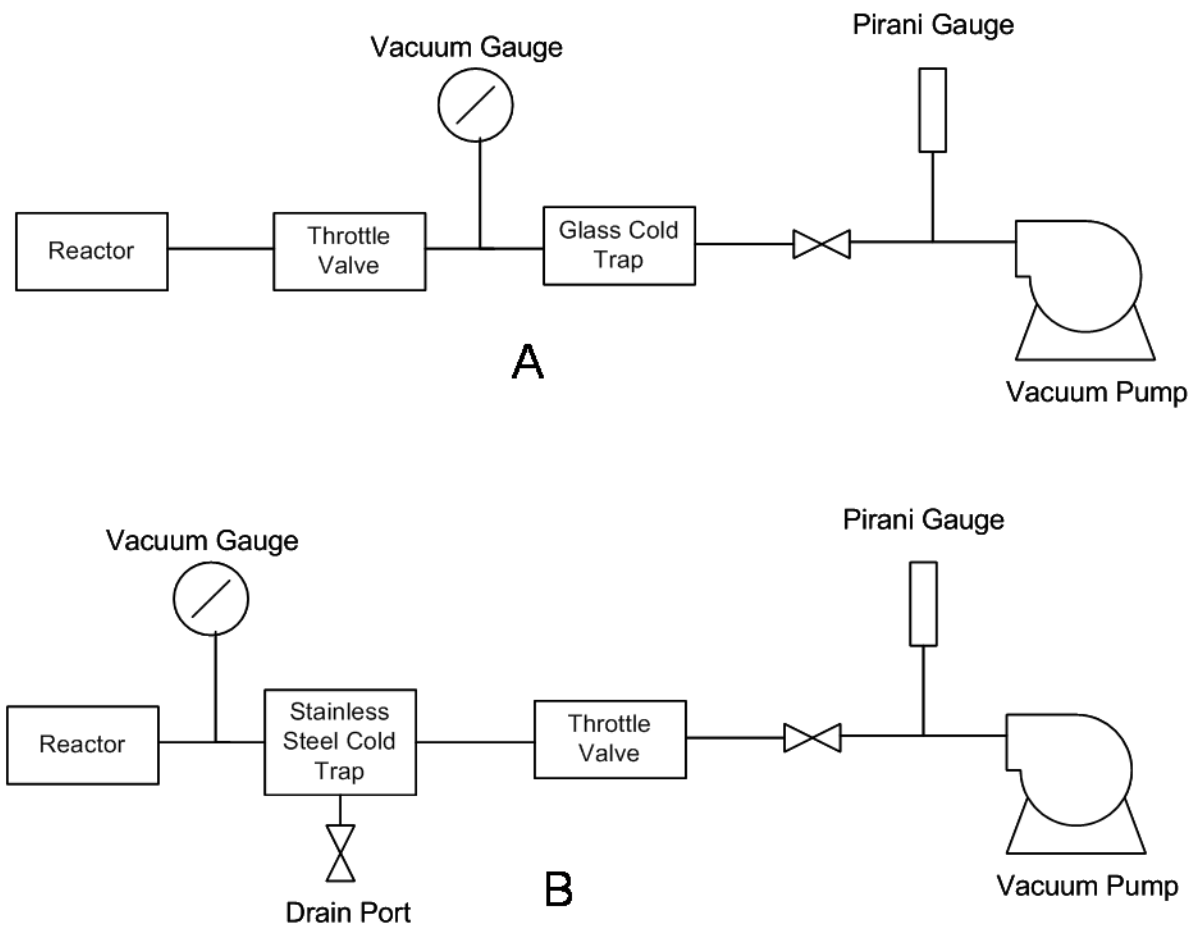


Figure 3-3. Flow diagram of reactor downstream. A) Before reconfiguration. B) After reconfiguration

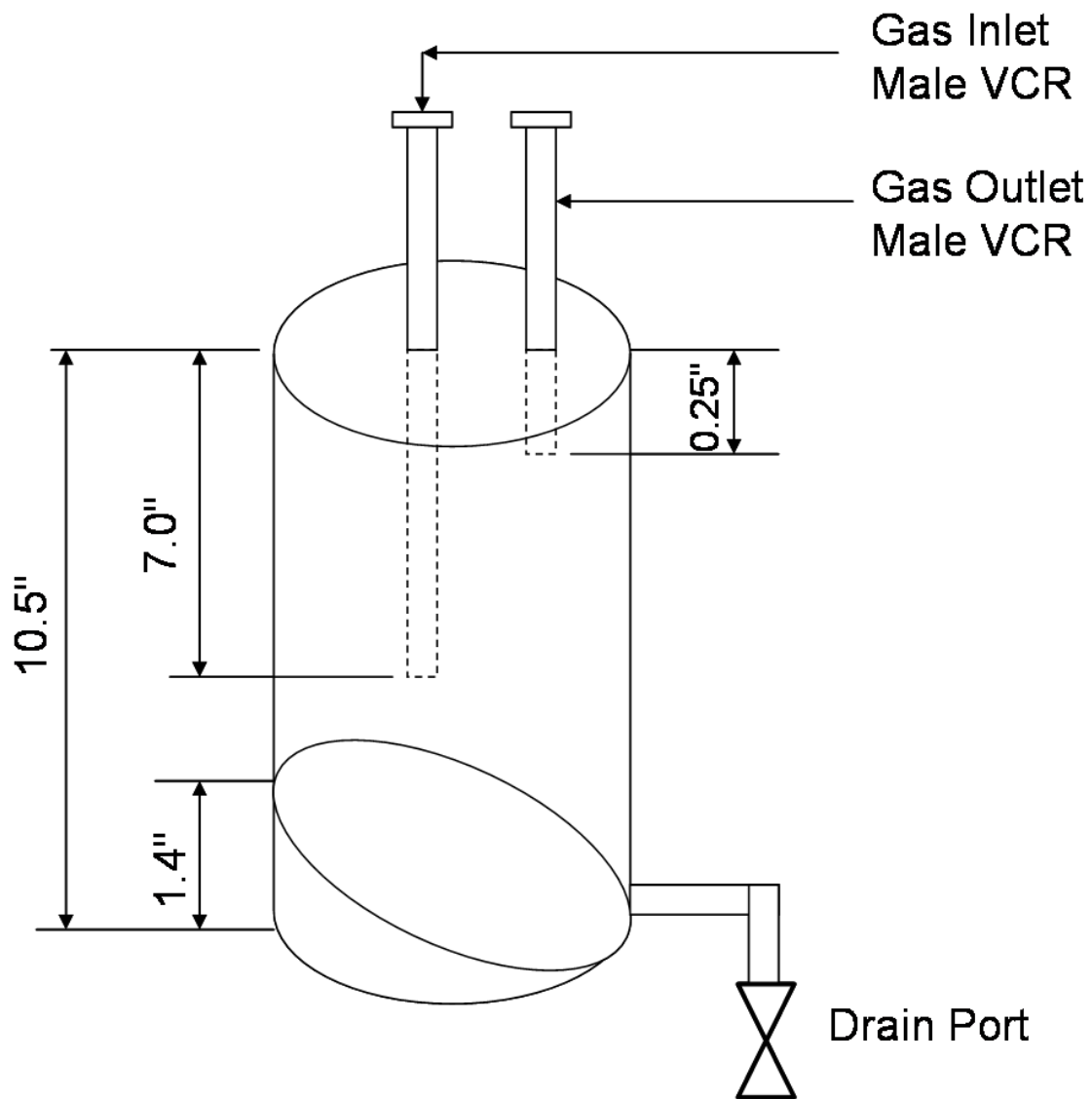


Figure 3-4. Design of new cold trap made of stainless steel

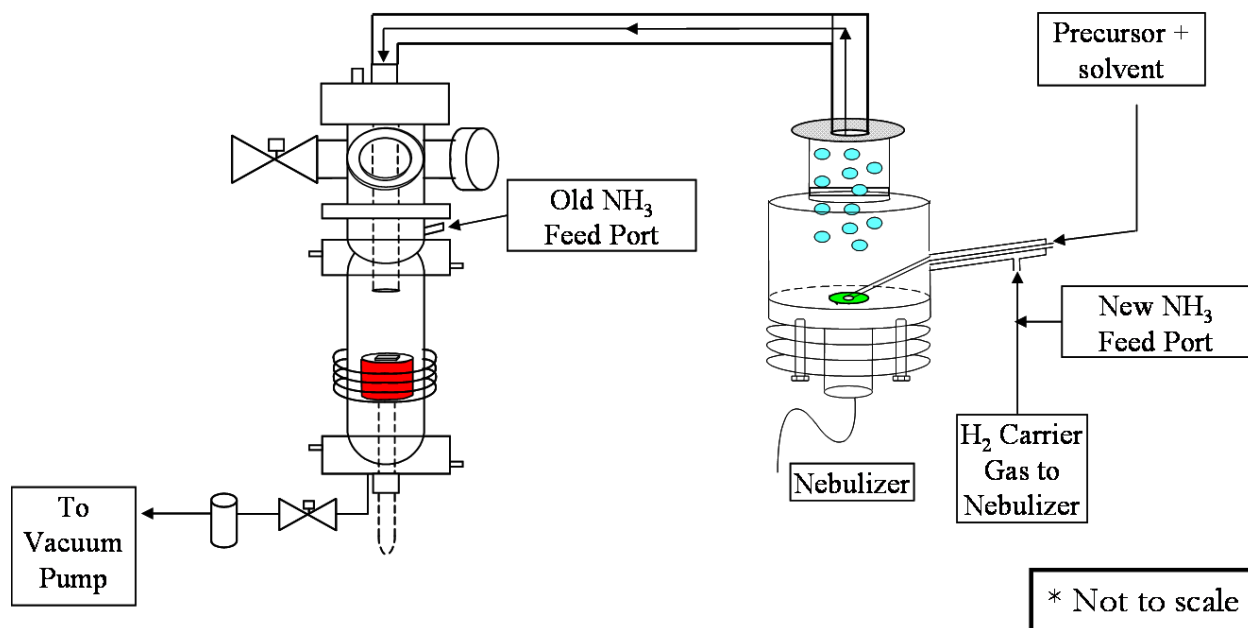


Figure 3-5. Schematic of the old and new NH₃ feed port

CHAPTER 4

WN_xC_y THIN FILM DEPOSITION FROM Cl₄(RCN)W(NC₃H₅), NH₃ AND H₂

Our group has previously reported growth of WN_xC_y thin films from **3a,b**.¹⁵⁷ Films grown from **3a,b** below 550 °C were amorphous and had a low resistivity at lower deposition temperature (287 μΩ-cm at 450 °C). However, films had low N content even though the low N-C imido bond dissociation energy for **3a,b** is expected to result in higher N content in the film. Film deposited with **3a,b** at 450 °C had only 4 at. % N and the highest N concentration of 11 at. % was for film deposited at 550 °C. A nitrogen deficient diffusion barrier film is not desirable because such films can easily form grain boundaries that can act as pathways for copper diffusion. In addition to having low N content, films deposited with **3a,b** had high O content (16 at. % at 450 °C and 11 at. % at 525 °C). When ammonia was used as a co-reactant for deposition from precursor **2a,b**, the WN_xC_y films had higher N content and lower O content.¹⁵⁵ In this chapter, deposition of WN_xC_y thin films from **3a,b** and ammonia is discussed with primary focus on diffusion barrier application. The intent of using ammonia as co-reactant is to increase the N content and decrease the O content so that films deposited with **3a,b** are more suitable for diffusion barrier application. The data for films deposited with **3a,b** and H₂ (without ammonia) previously reported¹⁵⁷ have been included to evaluate the effect of ammonia addition on film properties. The films deposited with **3a,b** and ammonia are also compared with those deposited with **2a,b** and ammonia to evaluate the effect of C₃H₅ and ⁱPr substituents in tungsten imido precursors on film properties.

4.1 Precursor Synthesis

Standard Schlenk and glovebox techniques were employed in the synthesis of **3a**. Tungsten oxychloride was prepared by a slightly modified literature method.¹⁹⁵ Tungsten oxychloride (1.229 g, 3.60 mmol) was added to a solution of allyl isocyanate (0.366 g, 4.41

mmol) in heptane (60 mL) in a sealed pressure vessel and the resulting mixture was heated at 110 °C for 36 h. After the solvent was removed *in vacuo*, the reddish brown residue was dissolved in ca. 10 mL of CH₃CN. The resulting solution was stirred for two hours and the solvent was removed under reduced pressure. Brown residue from the mixture was washed with 5 x 10 mL of toluene and the extracts concentrated to approximately 5 mL. The product was precipitated by adding hexane. The orange-brown solid was filtered and washed with hexane to afford 0.974 g (64 % yield) of the imido complex. The benzonitrile complex Cl₄(PhCN)W(NC₃H₅) (**3b**) was produced *in situ* by substitution of the acetonitrile ligand of **3a** with benzonitrile, which was utilized as the solvent for the deposition experiments. Figure 4-1 shows the X-ray crystallographic structure of **3a**.¹⁵⁷ Table 4-1 lists important bond distances and bond angles for **3a**.

4.2 Film Composition

Figure 4-2 shows the AES results for films deposited in the presence and absence of NH₃ at temperature ranging from 450 to 750 °C. The Auger spectra for films deposited with ammonia indicate the presence of W, N, C, and O in the films. Note that the AES measurements for films deposited with ammonia were done after sputtering for 30 sec whereas those for films deposited without ammonia were measured after 2 min of sputtering. Sputter etching can change the near surface composition of compounds due to preferential sputtering.¹⁹⁶ In fact, tungsten nitride has been reported to undergo preferential erosion of nitrogen during sputter etching.¹⁸⁹ Despite preferential sputtering, the film composition obtained from Auger measurements can be very useful in comparative analysis of films deposited at different temperature.

For films deposited with ammonia at 450 °C, the W concentration was 51 at. %, which increases to 61 at. % for growth at 475 °C. This is accompanied by a decrease in N

concentration from 23 at. % to 17 at. %. Above 450 °C, the W concentration gradually decreases, accompanied by an increase in C content in the films.

The film deposited with ammonia at 450 °C shows the highest N concentration of 23 at. %. As the deposition temperature is increased, the N concentration in the film decreases. The lowest N concentration of 8 at. % is observed for films grown at 750 °C.

The carbon concentration remains relatively steady at ca. 20 at. % for growth between 450 and 500 °C. Between 500 and 600 °C, the C concentration increases twofold and continues to rise with growth temperature. Increased incorporation of C from decomposition of the precursor ligands and the benzonitrile solvent is consistent with such an increase in C concentration.

Oxygen incorporation in the film remains below 6 at. % throughout the deposition temperature range. While the O concentrations at the lower end (450 – 500 °C) and higher end (650 – 750 °C) of the temperature range are slightly higher than that at the center (525 – 600 °C), the O concentration remains fairly constant over the range of deposition temperature. Oxygen is incorporated into the films either from residual gas in the reactor during growth or from exposure of film to atmosphere after growth.¹⁵⁶

In comparison to films grown in the absence of ammonia, deposition with ammonia as co-reactant resulted in a decrease in W concentration, increase in N concentration, and a marked decrease in O concentration (Figure 4-2). The increase in N concentration for depositions with ammonia is quite dramatic in the low temperature range, as exemplified by the effect for growth at 450 °C, where the addition of ammonia increases the N concentration from 4 at. % to 23 at. %. The increase in N concentration suggests that the ammonia molecule reacts with **3a,b** either in the gas phase (homogeneous reaction) or on the substrate (heterogeneous reaction), resulting in higher N incorporation in the film. Below 650 °C, C incorporation for depositions with

ammonia was higher than that for depositions without ammonia. Even at low temperature, when C deposition from the solvent is low¹⁵⁶, the C content of films deposited with ammonia is higher than for films deposited without ammonia.

Due to the presence of chlorine in the precursor complex **3a**, the possible presence of chlorine in the films was of interest. This analysis could not be carried out by Auger spectroscopy because the W NNN peak overlaps with the Cl LMM peak at 180 eV. Thus, XPS data were collected for films deposited at 450, 600 and 750 °C (Figure 4-3) to ascertain if the films contained chlorine. No chlorine peaks were observed for either the Cl 2s or Cl 2p_{3/2} at 270 eV and 199 eV, respectively, confirming that the chlorine content in the films was lower than the detection limit of XPS (ca. 1 at. %). Fe 2p peaks at 723 eV and 711 eV in the XPS spectra are artifacts that arise from the sample holder (which contains Fe) due to small sample sizes.

4.3 X-Ray Diffraction Measurement

4.3.1 Film Crystallinity

Figure 4-4 shows the XRD spectra for films deposited using **3a,b** and ammonia. The three prominent peaks in the spectra at 33.05, 61.70 and 69.15 degrees 2 θ correspond to standard reference peaks of Si(200) K α , Si(400) K β and Si(400) K α respectively. The XRD spectrum at 650 °C showed a small peak at 38.45 degrees 2 θ indicating the presence of crystalline phase of β -W₂N or β -W₂C. The deposition at all other temperature except 650 °C showed no peaks corresponding to β -W₂N or β -W₂C, indicating that the films were X-ray amorphous.

If films are very thin, the XRD measurements cannot detect a crystalline phase because of the low intensity of the diffracted X-ray beam. For very thin polycrystalline films, the XRD measurements done in the Bragg-Bretano geometry (θ -2 θ scans) do not show diffraction peaks because of low intensity signal from the film and the XRD spectrum is dominated by the high intensity substrate peak. In GIXD, the scan is done at grazing incidence; hence most of the

signal from the diffraction is generated from the top 1 - 2 nm of the thin film. The substrate peak, if present, do not dominate the GIXD spectrum. The depth of penetration of X-rays can be increased by increasing the angle of incidence in the GIXD measurement. Grazing incidence XRD measurements were done for films deposited with **3a,b** and ammonia to determine if the films were amorphous as indicated from the XRD measurements by Bragg-Bretano geometry. Figure 4-5 shows the grazing incidence XRD spectra for films deposited between 450 and 700 °C. Figure 4-6 shows the thickness of films for which grazing incidence XRD spectra were taken. The XRD spectrum of the film deposited at 450 °C indicates that it is X-ray amorphous. At 500 °C, there are three peaks that emerge at 37.47, 43.49 and 63.71 2θ degrees. All three peaks lie between the standard diffraction peaks for β -W₂N and β -W₂C, suggesting the existence of separate β -W₂N and β -W₂C phases or the presence of a single WN_xC_y phase. As the deposition temperature is increased from 500 to 550 °C, the same three peaks appear, though the intensity of these peaks is lower than that for films deposited at 500 °C. In the same temperature range, the tungsten concentration changes from 59 at. % to 49 at. %. A lower tungsten concentration would lead to decrease in the W₂N phase, W₂C phase or both, resulting in a decrease in the film crystallinity. The XRD spectrum for film deposited at 600 °C shows the highest level of crystallinity. As the deposition temperature is increased from 550 to 600 °C, the nitrogen concentration decreases while the carbon concentration increases. An increase in crystallinity would suggest an increase in the β -W₂C phase. The films deposited at 650, 700 and 750 °C show a decrease in crystallinity, evidenced by decrease in peak intensity. At higher temperature, an increase in amorphous C deposition would hinder the formation of crystallites, which is consistent with the decrease in film crystallinity at higher deposition temperature.

Peaks at 650, 700 and 750 °C are much broader possibly due to increased film strain at high temperature.

We have previously reported XRD spectra for films deposited with **3a,b** without ammonia.¹⁵⁷ The films deposited without ammonia are amorphous below 550 °C. At and above 550 °C, the film crystallinity increases with deposition temperature. Films deposited with ammonia do not show this consistent increase in crystallinity with deposition temperature. In fact, for higher temperature depositions with ammonia, the film crystallinity actually decreases. This observation reinforces the assertion that the ammonia co-reactant alters the mechanism of film deposition.

4.3.2 Lattice Parameter

Figure 4-7 shows the change in lattice parameter with deposition temperature for growth with and without ammonia. The β - WN_xC_y (111) peak position from XRD spectra was used to calculate the lattice parameter. All the films deposited with ammonia between 500 and 750 °C have a lattice parameter between the standard lattice parameters for β - W_2N (111) and β - W_2C (111). The changes in lattice parameter with deposition temperature could result from either uniform strain or compositional variation. Since the WN_xC_y films are not highly ordered, compositional variation rather than uniform strain is believed to be the primary factor affecting lattice parameter. The lattice parameter decreases with an increase in deposition temperature for depositions with ammonia between 500 and 700 °C, whereas it increases with an increase in deposition temperature for depositions without ammonia. A decrease in lattice parameter could result from a decrease in N and/or C in interstitial sublattice and an increase in the vacancy concentration. For films deposited with ammonia, the N concentration decreases with deposition temperature whereas the C concentration increases. One possible explanation for the decrease in

lattice parameter with increase in deposition temperature is that the variation in N concentration in the films is primarily responsible for the lattice parameter variation and the additional carbon deposited at higher temperature incorporates outside the WN_xC_y polycrystals.

4.3.3 Polycrystal Grain Size.

The grain size (t) was calculated using the Scherrer equation (*vide supra*). The most intense (111) diffraction peak was used to determine FWHM. Figure 4-8 shows the change in grain size with temperature for films deposited with and without ammonia. The average grain size calculation shows that films deposited with **3a,b** and ammonia are nanocrystalline between 500 and 750 °C deposition temperature, with the average grain size ranging from 37 to 60 Å. A previous study has reported the growth of nanocrystalline WN_xC_y between deposition temperature of 225 and 400 °C.¹⁹⁷ In the present work, we found that the films deposited with **3a,b** and ammonia were amorphous at 450 °C deposition temperature and nanocrystalline growth is observed at deposition temperature of 500 °C and higher. At a deposition temperature of 500 °C, the average grain size of crystallites for film deposited with ammonia is 56 Å. The average grain size remains almost unchanged at 550 °C. Between 550 °C and 700 °C, the average grain size gradually decreases from 58 Å to 39 Å. As the deposition temperature increases, the excess C deposited from the solvent/precursor fragmentation could hinder the growth of polycrystals, resulting in a decrease in grain size.

The comparison of grain size for experiments with and without ammonia shows that for deposition at temperature 600 °C and below, the average grain size is higher for films deposited with ammonia than for those deposited without ammonia. At 600 °C, the grain size for film grown with ammonia is similar to that for film grown without ammonia within the margin of

error. At 650 °C, the grain size for film deposited with ammonia is slightly lower than the grain size for films deposited without ammonia.

4.4 Film Growth Rate

Growth rates were estimated by dividing film thickness (measured from X-SEM) by deposition time. Figure 4-9 shows X-SEM images for films grown at 450 and 650 °C. The growth rate for **3a,b** with ammonia ranged from ca. 4 Å/min at 450 °C to ca. 17 Å/min at 750 °C. It should be noted that for growth using **3a,b** without ammonia, the concentration of **3a,b** in benzonitrile was 7.5 mg/mL (1.7×10^{-2} moles/L) whereas for growth using **3a,b** with ammonia, the **3a,b** concentration in benzonitrile was 11.2 mg/mL (2.66×10^{-2} moles/L). Because the introduction of ammonia as co-reactant decreases the film growth rate, a higher concentration of **3a,b** was necessary to obtain films that were sufficiently thick for materials characterization. This trend is different from that previously observed for growth from **2a,b**, where the use of ammonia as co-reactant resulted in an increase in growth rate at lower temperature and a decrease at higher temperature.¹⁵⁵ Figure 4-10 shows Arrhenius plots of growth rate for experiments with and without ammonia. The apparent activation energy (E_a) for film growth from **3a,b** and ammonia was 0.34 eV, which is significantly higher than the 0.15 eV activation energy reported for depositions with **3a,b** precursor without ammonia.

4.5 Film Resistivity

Figure 4-11 shows film resistivity at different deposition temperature for films grown with and without ammonia. For depositions with ammonia, the resistivity is 5820 $\mu\Omega\text{-cm}$ for 450 °C deposition temperature and increases to 7190 $\mu\Omega\text{-cm}$ for 500 °C. Interestingly, the film resistivity has the lowest value of 1690 $\mu\Omega\text{-cm}$ for growth at 550 °C, even though the film deposited at that temperature has lower W content and higher N content. Resistivity increases to

12650 $\mu\Omega\text{-cm}$ at 600 °C and continues to increase with an increase in deposition temperature until it reaches its highest value of 24178 $\mu\Omega\text{-cm}$ at 700 °C. The decrease in W concentration and concomitant increase in C concentration between 550 and 700 °C is believed to be the reason for the increase in film resistivity. If the C in films exists as WC_x , it would decrease the film resistivity. But an increase in resistivity with increase in C content of film could possibly result from the incorporation of additional C at the grain boundary (outside the WN_xC_y polycrystal) at higher deposition temperature. The film resistivity was considerably higher for films deposited with ammonia compared to films deposited without ammonia. This behavior is expected since ammonia tends to increase N content in the films and higher N content leads to higher film resistivity.

4.6 Comparison of Films Deposited from **3a,b** and **2a,b**

The comparison of films deposited from **3a,b** and ammonia with those deposited from **2a,b** and ammonia¹⁵⁵ can provide insight into the effect of different ligands (C_3H_5 and $i\text{Pr}$) on film properties. Films deposited at 450 °C from **3a,b** and ammonia have similar W and N content, higher C content and lower O content as compared to films deposited with **2a,b** and ammonia at same temperature (Figure 4-2). At 500 and 600 °C deposition temperature, films from **2a,b** exhibit higher N content and lower C content as compared to films deposited with **3a,b** and ammonia at the same temperature. The comparison of film crystallinity for films deposited with **3a,b** and ammonia with those deposited with **2a,b** and ammonia shows that while **3a,b** results in crystalline films at and above 500 °C, films deposited with **2a,b** do not show crystallinity until 600 °C and higher. This trend in crystallinity can be explained by considering that the film growth rate for films deposited with **2a,b** and ammonia is considerably higher (17 - 23 Å/min) than that for films deposited with **3a,b** and ammonia (4 - 17 Å/min), especially at lower

deposition temperature. Higher growth rate could shorten the time for crystallites to grow via surface diffusion, resulting in amorphous film growth.

The comparison of film resistivity (Figure 4-11) shows that at 450 and 500 °C deposition temperature, films grown with **3a,b** and ammonia have a significantly lower resistivity than those grown with **2a,b** and ammonia. Interestingly, films deposited with both precursors have the lowest resistivity for deposition at 550 °C. Above 550 °C, there is a dramatic increase in resistivity of films deposited with **3a,b** and ammonia while the resistivity of films grown with **2a,b** and ammonia levels off.

Evaluation of all films grown from **3a,b** or **2a,b** and ammonia shows that film deposited with **3a,b** and ammonia at 450 °C is the best candidate for diffusion barrier application because of its high N content, low O content, low deposition temperature, amorphous microstructure and lowest resistivity among the amorphous films grown from **3a,b** or **2a,b** with ammonia. Diffusion barrier testing is required to ascertain if this film is suitable for diffusion barrier application.

4.7 Conclusions

Successful thin film deposition of WN_xC_y by MOCVD utilizing **3a,b**, H_2 and ammonia has been achieved. When used as a co-reactant with the allylimido complexes **3a,b**, ammonia significantly alters the composition, crystallinity, and resistivity of the resulting films as compared to films grown without ammonia. Films deposited with ammonia had significantly higher carbon and nitrogen content and substantially lower oxygen content. No chlorine was detected in the XPS spectra of films grown over the entire deposition temperature range. While films grown without ammonia showed an increase in film crystallinity with increasing deposition temperature, those grown with ammonia exhibited more complex behavior, with crystallinity peaking for growth at 600 °C. The activation energy for the film growth from **3a,b** and ammonia

is estimated to be 0.34 eV, which is significantly higher than the activation energy of 0.15 eV reported for film growth from **3a,b** without ammonia. Films deposited with ammonia have higher resistivity as compared to films deposited without ammonia because of a higher N and C concentration coupled with a lower W concentration. The lowest resistivity for films deposited with ammonia was the value of 1690 $\mu\Omega$ -cm obtained from growth at 550 °C.

Films deposited with **3a,b** and ammonia have higher C content and lower O content than those grown from **2a,b** and ammonia. The N content of film grown with **3a,b** and ammonia is similar to that for film grown with **2a,b** and ammonia at 450 and 700 °C. Films grown with **2a,b** and ammonia below 600 °C were amorphous, whereas deposition from **3a,b** and ammonia resulted in amorphous film below 500 °C. At temperature below 550 °C, films deposited with **3a,b** and ammonia had a significantly lower resistivity as compared to films deposited with **2a,b** and ammonia. But above 550 °C, films deposited with **3a,b** and ammonia had a much higher resistivity as compared to those deposited with **2a,b** and ammonia.

From a diffusion barrier application standpoint, it has been demonstrated that ammonia can be used with **3a,b** to increase the N content of WN_xC_y films. A corresponding increase in film resistivity is also seen and some optimization may be needed to strike a balance between higher N content and lower film resistivity.

Table 4-1. Bond distances (Å) and angles (degrees) for Cl₄(CH₃CN)W(NC₃H₅) (**3a**)

Bond	Distance/angle	Bond	Distance/angle
W-N(1)	1.687(9)	W-Cl(4)	2.351(9)
W-N(2)	2.308(8)	N(1)-C(1)	1.508(17)
W-Cl(1)	2.339(10)	C(1)-C(2)'	1.51(2)
W-Cl(2)	2.317(8)	C(2)'-C(3)'	1.36(3)
W-Cl(3)	2.324(9)	N(2)-C(4)	1.130(12)
C(1)-N(1)-W	167(2)	N(1)-W-N(2)	175.8(15)
N(1)-W-Cl(2)	90.6(8)	N(2)-W-Cl(2)	86.0(7)
N(1)-W-Cl(3)	93.6(7)	N(2)-W-Cl(3)	84.0(6)
Cl(2)-W-Cl(3)	88.7(4)	C(4)-N(2)-W	175(3)
N(1)-W-Cl(1)	102.4(8)	N(2)-W-Cl(1)	81.1(7)
C(2)'-C(1)-N(1)	114.2(21)	C(3)'-C(2)'-C(1)	120(2)
Cl(3)-W-Cl(1)	90.18(13)	N(2)-C(4)-C(5)	178(2)

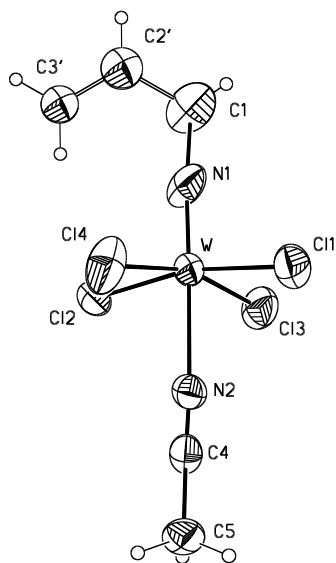


Figure 4-1. Thermal ellipsoids diagram of the molecular structure of Cl₄(CH₃CN)W(NC₃H₅) (**3a**). Thermal ellipsoids are plotted at 50% probability¹⁵⁷

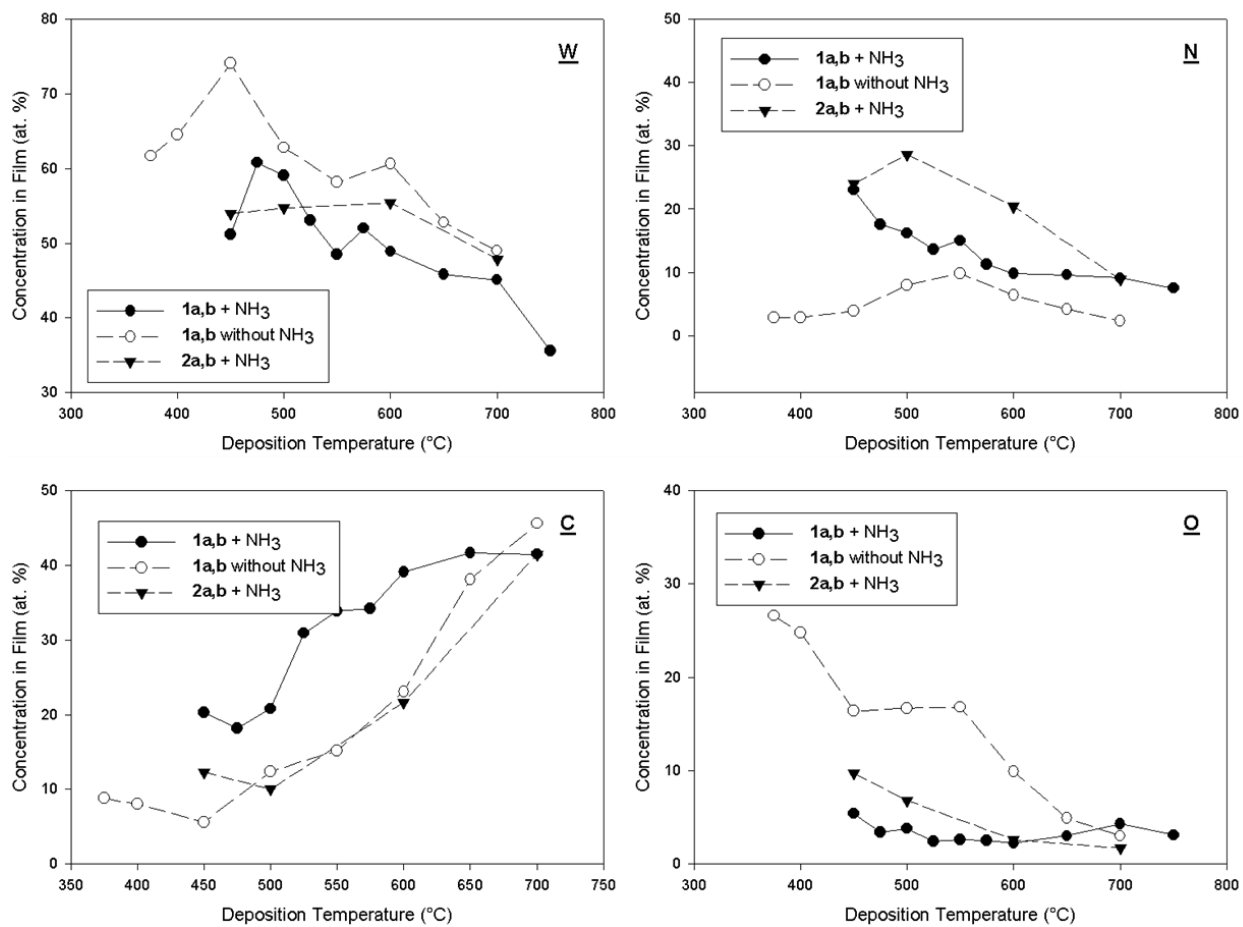


Figure 4-2. Composition of films deposited from **3a,b** (with and without ammonia¹⁵⁷) and **2a,b** with ammonia¹⁵⁵ at different deposition temperature as determined by AES on Si (100) substrate.

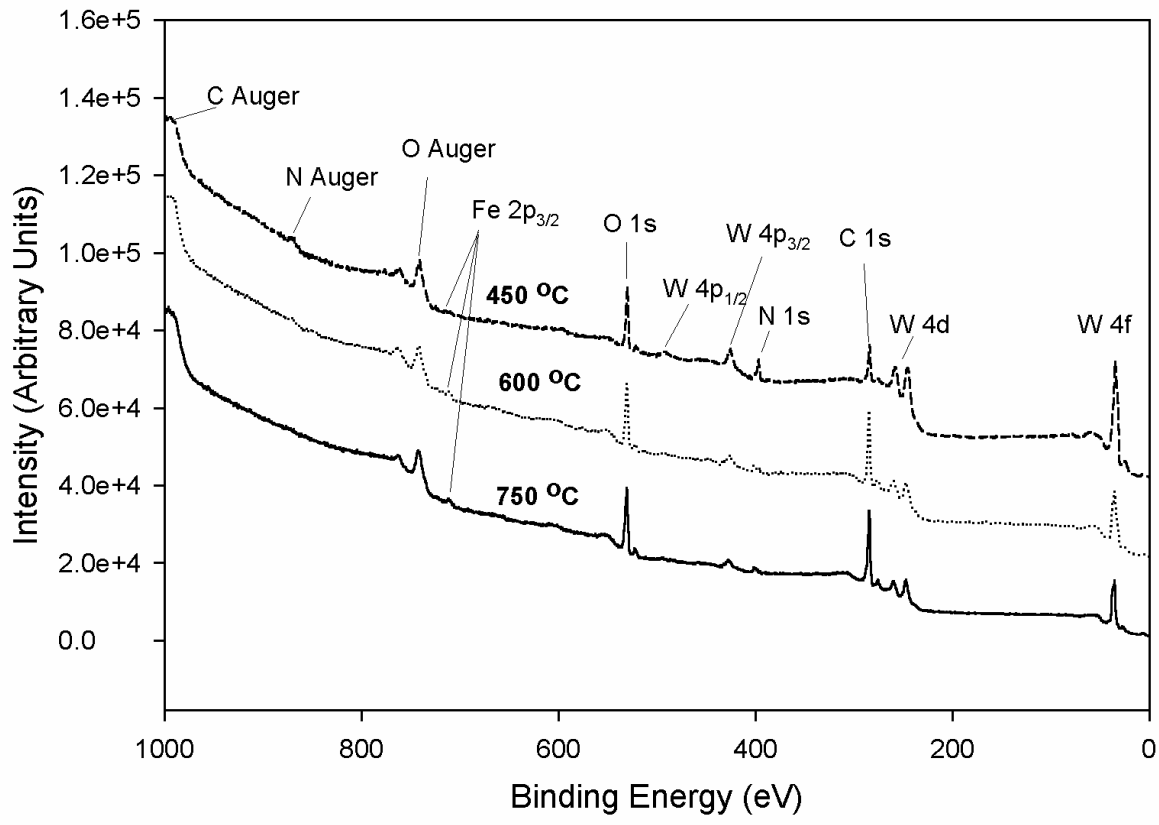


Figure 4-3. X-ray photoelectron spectroscopy patterns of films deposited at 450, 600 and 750 °C from **3a,b** and ammonia on Si (100) substrate.

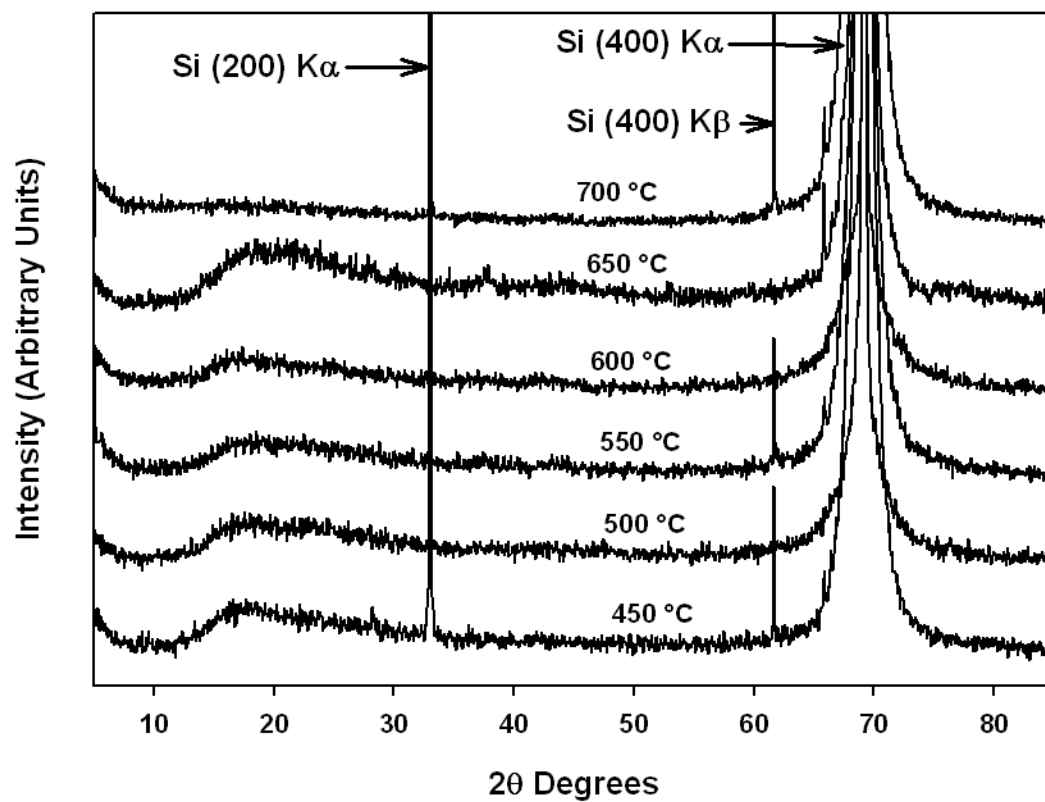


Figure 4-4. X-ray diffraction spectra of films deposited on Si (100) substrate from **3a,b** and ammonia

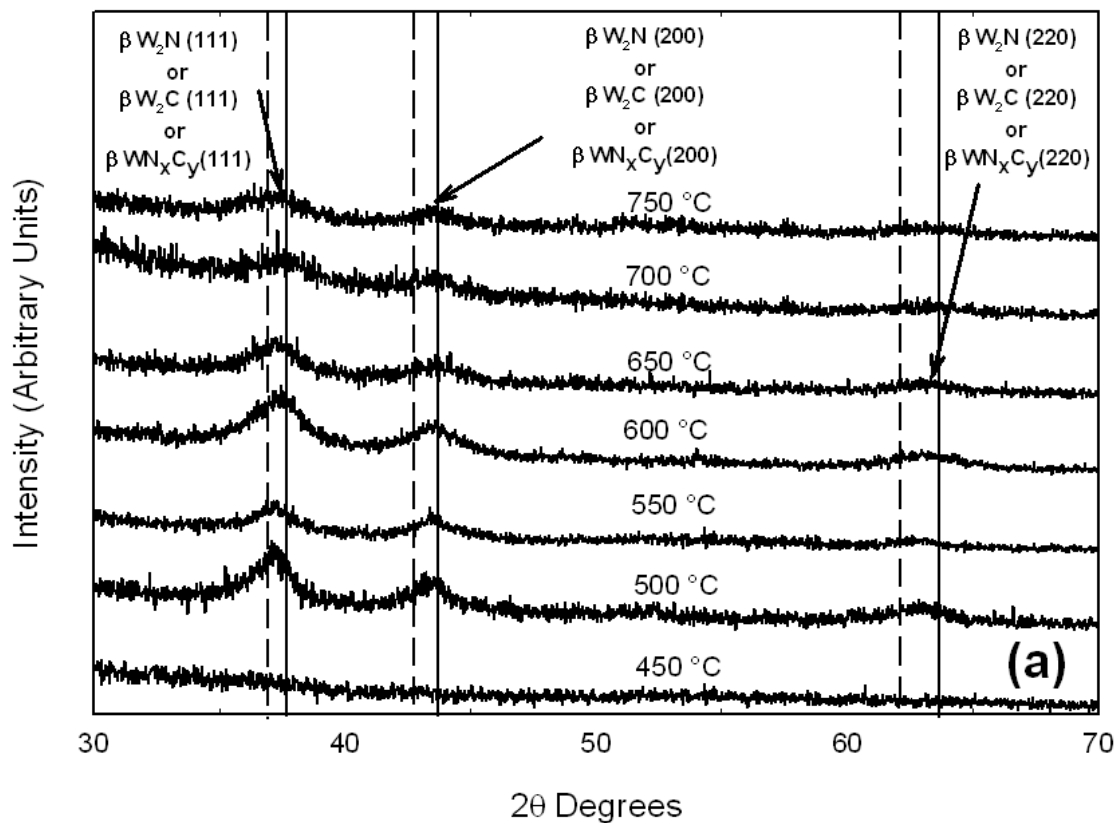


Figure 4-5. Grazing incidence XRD spectra of films deposited on Si (100) substrate from **3a,b** and ammonia. The solid and dashed vertical lines indicate the location of reference peaks for standard powder diffraction of β - W_2N and β - W_2C respectively

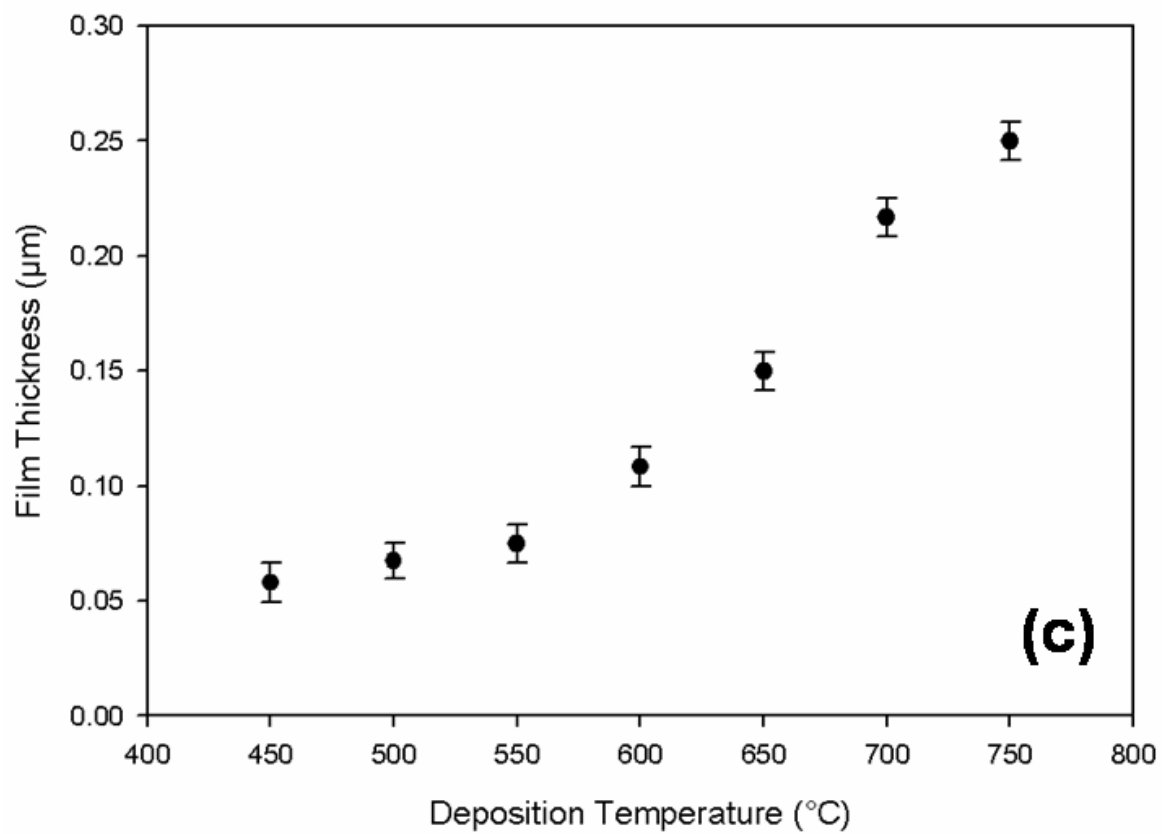


Figure 4-6. Thickness of film (obtained from X-SEM) at different deposition temperature for films deposited with **3a,b** and ammonia on Si(100) substrate

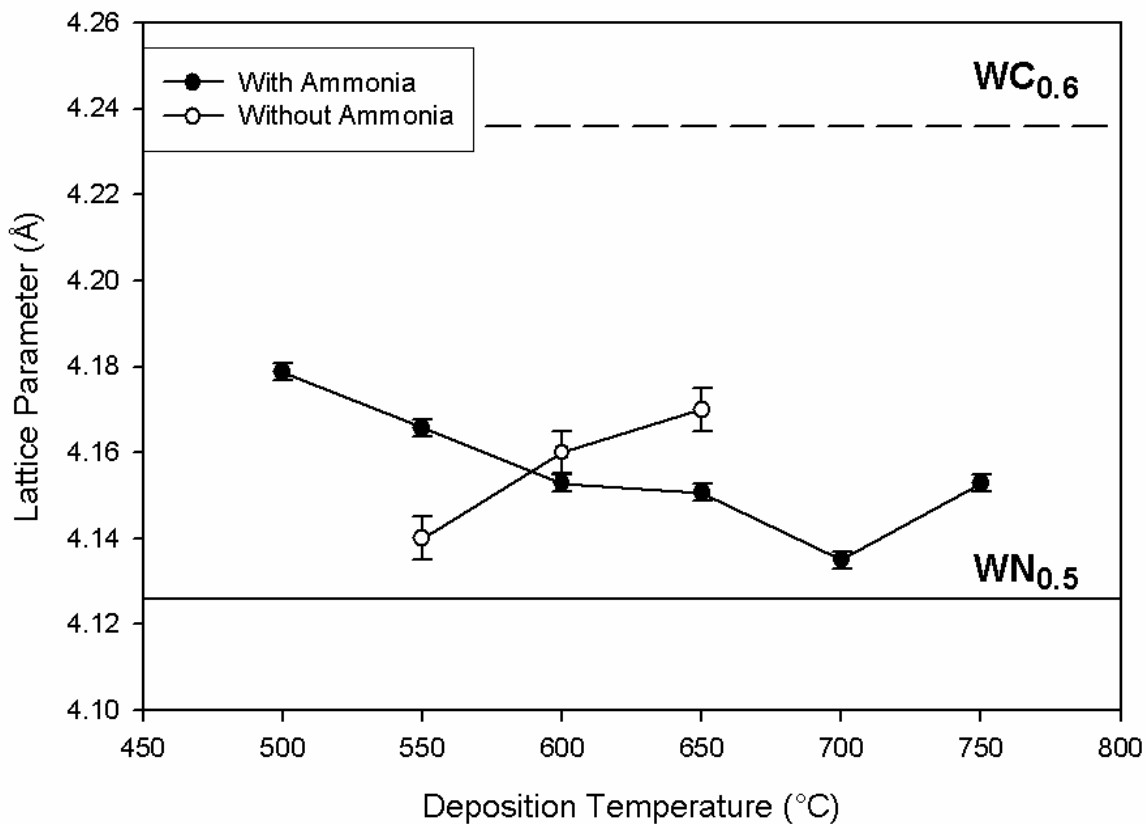


Figure 4-7. Lattice parameters for films grown from **3a,b** on Si (100) substrate with and without ammonia. The solid line at 4.126 Å corresponds to the standard lattice parameter for β -W₂N. The dashed line at 4.236 Å corresponds to standard lattice parameter for β -W₂C (111). Error bars indicate uncertainty in determination of peak position for lattice parameter calculation.

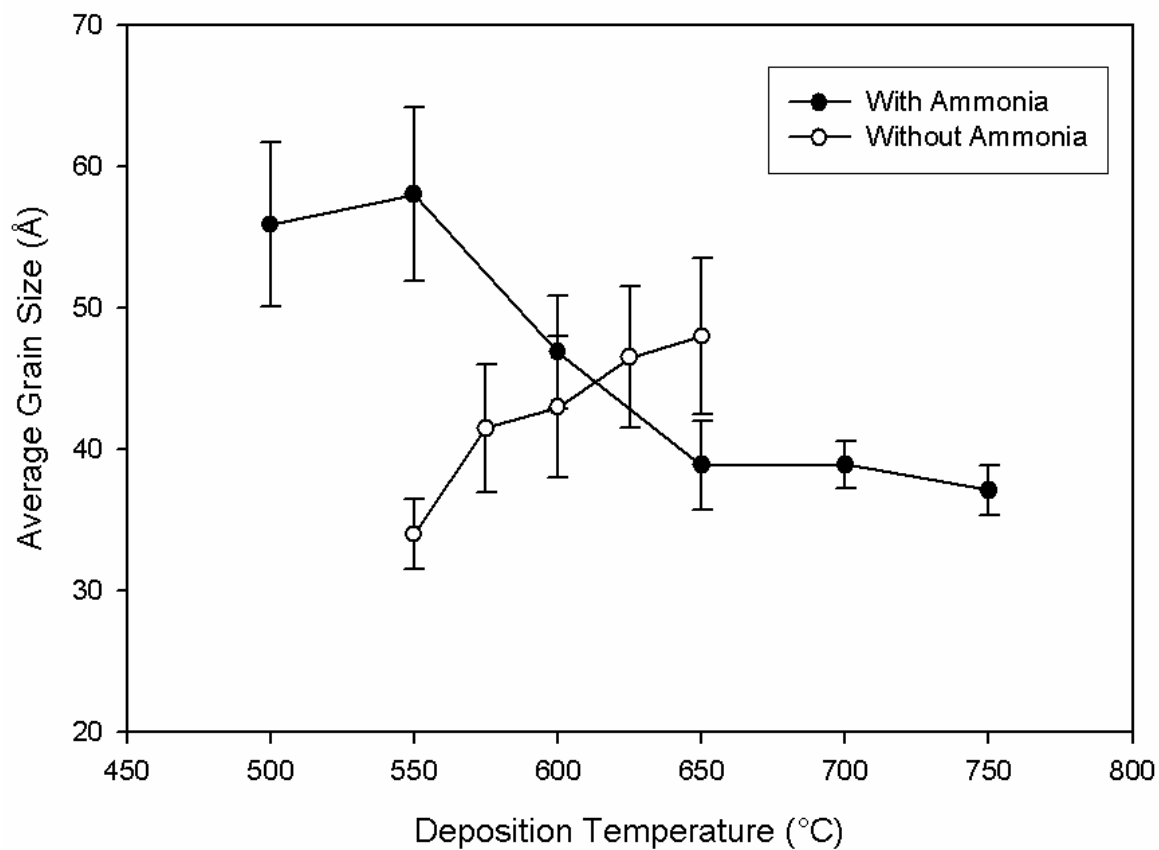


Figure 4-8. Average grain size at different deposition temperature for films grown from **3a,b** with and without ammonia¹⁵⁷ on Si (100) substrate.

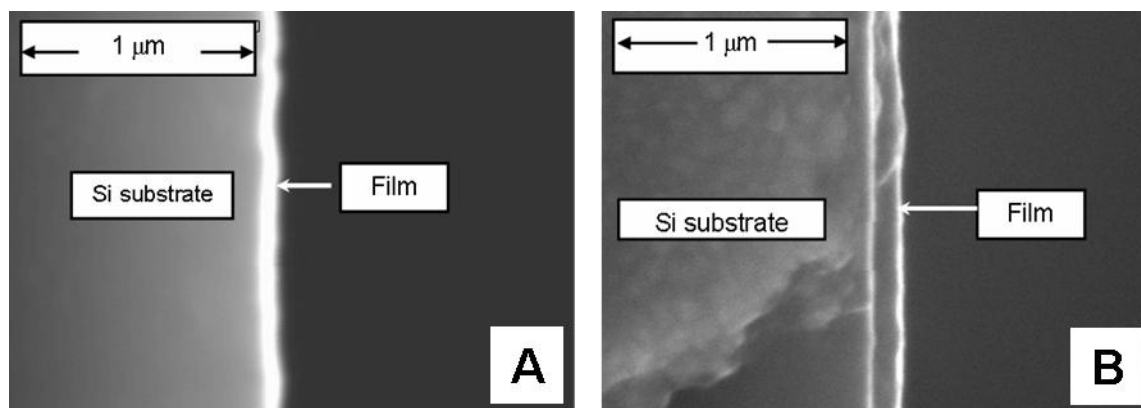


Figure 4-9. Scanning electron microscope images for films grown from **3a,b** with ammonia. A) Film deposited at 450 °C. B) Film deposited at 650 °C

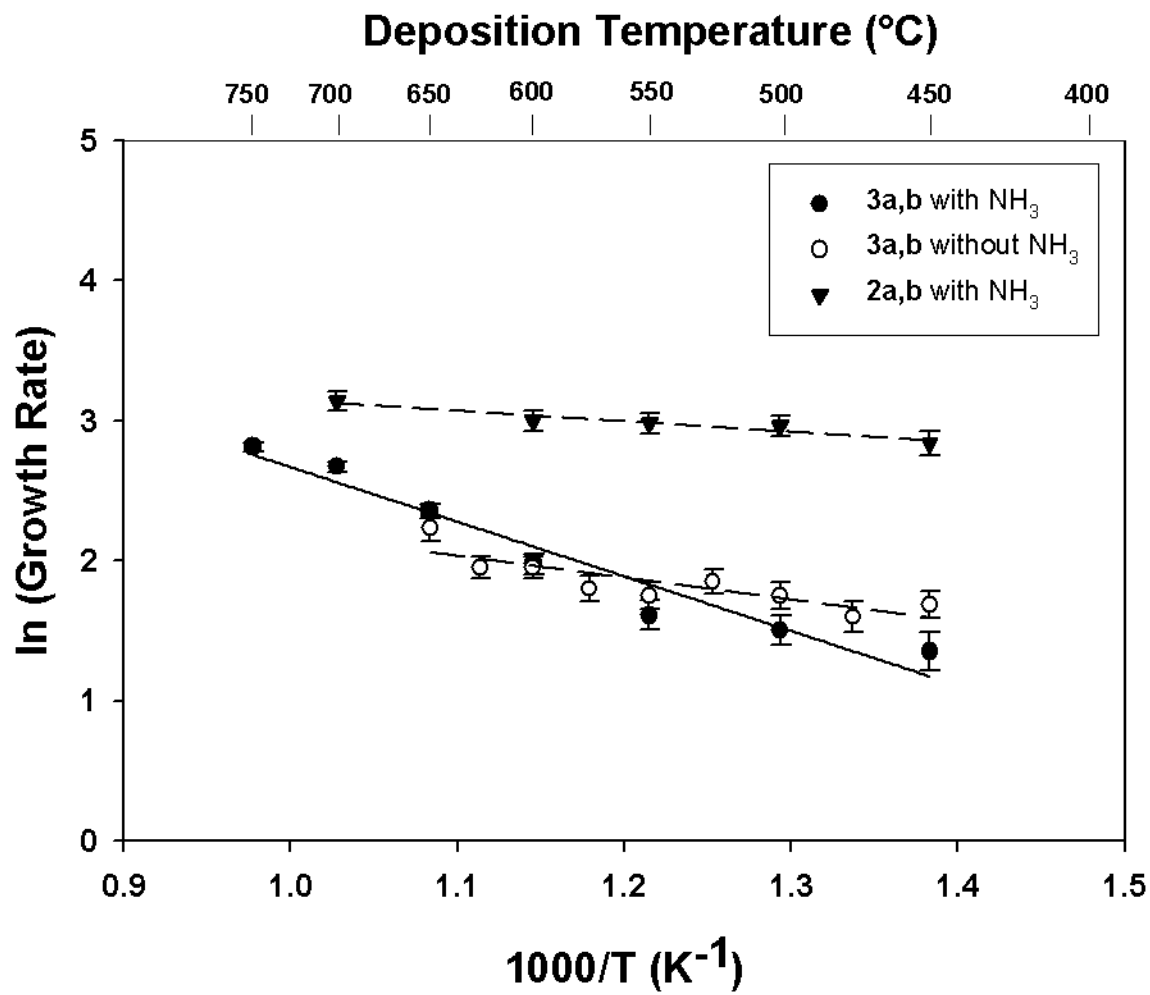


Figure 4-10. Arrhenius plot of log of film growth rate vs. inverse temperature for deposition from **3a,b** (with and without ammonia¹⁵⁷) and **2a,b** with ammonia¹⁵⁵

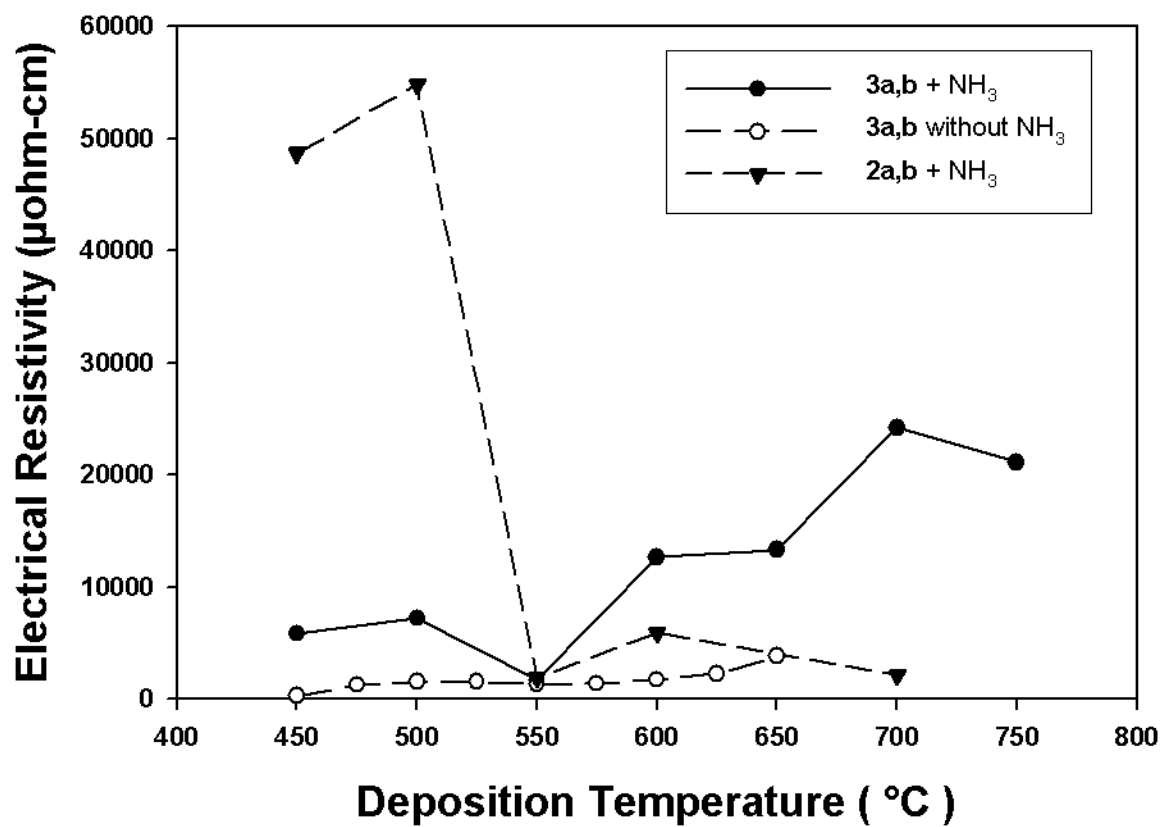


Figure 4-11. Change in film resistivity with deposition temperature for films grown on Si (100) from **3a,b** (with and without ammonia¹⁵⁷) and **2a,b** with ammonia¹⁵⁵

CHAPTER 5 DEPOSITION OF WN_xC_y USING $W(N^iPr)Cl_3[{}^iPr(NMe_2)N^iPr]$ AND H_2

Transition metal guanidinate and amidinate complexes have been used to deposit a variety of materials including TiC_xN_y , Fe, Co, Ni, Cu, and $TaN^{198-201}$ by CVD and/or ALD. The success with these complexes suggested preparation of guanidinato derivatives of **2a,b** as precursor candidates. This chapter discusses the deposition of WN_xC_y thin films using $W(N^iPr)Cl_3[{}^iPrNC(NMe_2)N^iPr]$ (**4**), a guanidinato derivative of **2a,b**, and evaluates its potential for deposition of diffusion barrier films. The film properties obtained from **4** are compared to those from **2a,b** to assess the effect of the guanidinato ligand. The WN_xC_y films were also evaluated as diffusion barriers by coating them with PVD Cu and annealing the Cu/ WN_xC_y /Si stack in vacuum at different temperature.

5.1 Precursor Synthesis²⁰²

A 250 mL Schlenk tube was charged with $LiNMe_2$ (0.223 g, 4.38 mmol) and 100 mL of Et_2O . The resulting colorless suspension was cooled to 0 °C. 1,3-diisopropylcarbodiimide (0.69 mL, 4.4 mmol) was added drop wise to the suspension at 0 °C. After warming the reaction mixture to room temperature over 2 h, the resulting cloudy solution of lithium guanidinate reagent was cannula-transferred into a 250 mL Schlenk tube containing a solution of $W(NCH(CH_3)_2)Cl_4(OEt_2)$ (2.00 g, 4.38 mmol) in Et_2O (100 mL) at -78 °C. The reaction mixture was stirred for 20 min at -78 °C and then warmed to room temperature overnight in the absence of light. The solvent was removed from the reaction mixture *in vacuo* and extraction into Et_2O (200 mL) followed by filtration yielded a dark amber solution. Et_2O was removed *in vacuo* to give crude **4** as a dark amber powder. Pure **4** crystals (1.27 g, 56%) were obtained by recrystallization from a toluene solution layered with hexane at -20 °C. Figure 5-1 shows the X-

ray crystallographic structure of precursor **4** and Table 5-1 lists important bond distances and bond angles for **4** obtained from the X-ray structure.

5.2 Film Growth

The concentration of **4** in benzonitrile was 9.0 mg/mL and the flow rate of precursor solution was 4 mL/hr. The H₂ flow rate was held constant 1000 sccm and reactor pressure was 350 Torr. Detailed description of reaction conditions is provided in Chapter 3. The lowest temperature at which appreciable film growth was observed from precursor **4** was 400 °C. Films were generally smooth and had a shiny metallic surface with film color varying from golden (deposition below 500 °C) to shiny black (deposition at and above 400 °C).

5.3 Film Composition

Figure 5-2 shows AES results for films deposited with precursors **4** and **2a,b** using H₂ as co-reactant and carrier gas. The AES spectra indicated the presence of W, N, C, and O in films deposited with precursor **4**. For films deposited with **4** at 400 °C, the W concentration is 53 at. %. As the deposition temperature is increased to 450 °C, the W content reaches its highest value of 66 at. %, then gradually decreases to 37 at. % for deposition at 700 °C, reflecting an increase in C content as the deposition temperature rises. The N content of films deposited with precursor **4** has its highest value of 12 at. % for deposition at 400 °C. The N content of the film decreases as deposition temperature is increased from 400 to 650 °C, then remains almost unchanged between 650 and 750 °C. The variation in the final film N content with growth temperature is likely influenced by several factors, including N volatilization, competition between C and O for bonding with W sites, and precursor decomposition pathways and rates.

Both C and O were detected in significant amounts in all films. The C content of film deposited with precursor **4** decreases from 20 at. % at 400 °C deposition temperature to 14 at. % at 450 °C. At growth temperatures between 450 and 700 °C, the C content of film continuously

increases and reaches its highest value of 57 at. % at 700 °C. Figure 5-3 shows a monotonic increase in C/W ratio with deposition temperature between 450 and 700 °C. In a previous study using precursor **2a,b**, it has been demonstrated that the extent of C incorporation depended upon the solvent (1,2-dichlorobenzene or benzonitrile).¹⁵⁵ It is possible, of course, that the precursor is also involved in the C incorporation mechanism directly through its decomposition pathway or indirectly by reaction with the solvent or one its decomposition products. The O content of film deposited with **4** at 400 °C is 15 at. % and it gradually decreases to 3.0 at. % at 600 °C. Between 600 and 750 °C deposition temperature, the O content of film is ca. 3.0 at. %. Oxygen is believed to be incorporated into the films either from residual gas (oxygen or water vapor) in the reactor during growth or from atmospheric oxygen exposure post-growth.¹⁵⁵

It is desirable for barrier application to deposit the film at the lowest temperature that gives suitable properties, which includes amorphous microstructure, a high value of N/W atomic ratio and low oxygen content. The comparison of films deposited from **4** and **2a,b** reveals that the observed lowest deposition temperature for **4** is one experimental increment (50 °C) lower than the lowest growth temperature of 450 °C for **2a,b**. No film deposition was observed for **4** at 350 °C as measured by AES. The comparison of film composition at 450 °C shows that film deposited from **4** has higher W and N content, similar C content and significantly lower O content as compared to film deposited with **2a,b** using the same solvent. For deposition at and above 500 °C, the N and O content of films deposited with **4** and **2a,b** are quite similar. Since the number of N atoms per W atom in **4** is double that in **2a,b**, it might be expected that films deposited with **4** would have a higher N/W ratio as compared to those deposited with **2a,b**. The highest N/W ratio for films deposited with **4** is 0.24 at 400 °C, which is considerably higher than the highest N/W ratio of 0.16 observed for films deposited with **2a,b** at the higher temperature

450 °C. This difference in N/W ratio is significant and larger than other values observed for **1a,b** and **3a,b**. Since the difference in O content between films deposited from **4** and **2a,b** is significant only at temperature below 500 °C, it is believed that films deposited below 500 °C by **4** are more dense than those deposited from **2a,b**. Higher density in the film would hinder O diffusion and decrease subsequent O incorporation. Films deposited with **4** have a significantly lower W content and a higher C content as compared to films deposited with **2a,b** for deposition temperature above 500 °C. At higher deposition temperature, decomposition of C containing ligands and the benzonitrile solvent results in C incorporation in the film.

As discussed earlier, Cl impurity is highly undesirable in the diffusion barrier film. Since the precursor **4** has three Cl atoms per molecule, there is a possibility of Cl incorporation into the film. X-ray photoelectron spectroscopy measurements were done to detect Cl in the thin film because AES was not capable of detecting Cl impurity in W containing film (*vide supra*). The detection limit of XPS technique is ca. 1 at. %. Figure 5-4 shows the XPS profiles of films deposited at 400, 500, 600 and 700 °C. The sample surface was sputter cleaned with Ar⁺ ions for 5 min prior to the measurement. The spectra do not show any Cl peak indicating that the Cl content of the film was below the detection limit of the XPS.

5.4 X-Ray Diffraction of Films

Figure 5-5 shows the XRD patterns for films deposited with **4** between 400 and 750 °C. X-ray diffraction spectra for films deposited at 400 and 450 °C show no peaks attributable to the film, but only peaks associated with the substrate (Si(200) K α , Si(400) K β , and Si(400) K α reflections at 33.10, 61.75 and 69.20° 2 θ , respectively). The absence of other peaks in these two spectra suggests that films deposited at 400 and 450 °C are X-ray amorphous. The XRD pattern for the film deposited at 500 °C shows the emergence of crystallinity as evidenced by the two broad peaks at 37.74 and 44.40°. These peaks lie between the standard peak position of β -W₂N

[37.74 2θ for (111) phase and 43.85 $^\circ 2\theta$ for (200) phase] and β -W₂C [36.98 2θ for (111) phase and 42.89 $^\circ 2\theta$ for (200) phase], indicating the presence of either the solid solution β -WN_xC_y or a physical mixture of β -W₂N and β -W₂C.¹⁷⁸ Films deposited at 550, 600, and 650 $^\circ\text{C}$ show evidence of increased crystallinity with four peaks observed at approximately 37.50, 43.70, 63.55 and 75.05 $^\circ$, corresponding to the (111), (200), (220) and (311) phases of β -WN_xC_y, respectively. The (111) peaks become sharper at higher deposition temperature, suggesting an increase in grain size. The XRD spectra for films deposited at 700 and 750 $^\circ\text{C}$ show convoluted peaks, which are deconvoluted as shown in Figures 5-6 and 5-7, respectively. Deconvolution of XRD peaks for film deposited at 700 $^\circ\text{C}$ affords 5 peaks at 35.40, 37.60, 38.20, 40.00 and 43.10 $^\circ$. The two peaks at 37.60 and 43.10 $^\circ$ match the standard β -W₂N (111) and β -W₂N (200) peaks at 37.75 and 43.85 $^\circ$, respectively. The three peaks at 35.40, 38.20 and 40.00 $^\circ$ are close to the peaks of the binary compounds α -W₂C (100), α -W₂C (002) and α -W₂C (101) with reference values of 34.52, 38.03 and 39.57 $^\circ$, respectively.¹⁷⁸ The deconvolution of XRD spectra for films deposited at 700 $^\circ\text{C}$ indicates the presence of a physical mixture of β -W₂N and α -W₂C phases.

Deconvolution of XRD spectra for films deposited at 750 $^\circ\text{C}$ also show 5 peaks at 34.90, 37.60, 38.80, 39.80 and 43.10 $^\circ$. The peaks at 37.60 and 43.10 $^\circ$ match the standard β -W₂N (111) and β -W₂N (200) peaks reasonably well. The other three peaks at 34.90, 38.80, and 39.80 again match reasonably well with the standard α -W₂C (100), α -W₂C (002), and α -W₂C (101) peaks values, respectively. Thus the film deposited at 750 $^\circ\text{C}$ is a binary mixture of β -W₂N and α -W₂C phases with neither of the two phases showing any preferred orientation.

As discussed in Chapter 4, GIXD is more sensitive in detecting crystalline phases in thin films because of its larger interaction volume. As discussed in Chapter 4, XRD measurements for films grown with **3a,b** and ammonia showed no peaks while the GIXD spectra showed peaks

corresponding to β -W₂N or β -W₂C. Hence, to ascertain crystallinity of films grown from **4** with greater accuracy, GIXD measurements were done (Figure 5-8). Grazing incidence XRD measurements confirmed that the films deposited by **4** at 400 and 450 °C are X-ray amorphous as no peaks corresponding to the thin film were observed. The films deposited between 500 and 650 °C are polycrystalline with the peak position indicating the presence of a solid solution of β -WN_xC_y or a mixture of β -W₂N and β -W₂C. For deposition at 700 and 750 °C, the GIXD spectra show peak convolution similar to that observed in XRD spectra. Hence the GIXD results reaffirmed the results obtained from XRD.

For XRD measurements, the X-rays penetrate completely through the thin film and into the substrate as indicated by the large Si peak observed in the XRD spectra. The intensity of the diffracted beam would depend on both the crystallinity of the film as well as the thickness of the film assuming all other parameters such as film density are constant. Since the film thickness is different for deposition at different temperature, XRD measurements cannot be used to compare crystallinity for films deposited at different growth temperature. But for GIXD measurement, X-rays penetrate only the top 1 - 2 nm of the film because of the shallow angle of incidence. Hence, even if the films are of varying thickness, GIXD would have a constant interaction volume if all the films are thicker than 2 nm and the depth of penetration of X-rays is same for films deposited at different growth temperature. Since the smallest film thickness for growth from **4** is 45 nm, GIXD measurements can be used to compare film crystallinity of films for deposition at different temperature assuming film density is constant. Figure 5-8 shows that the intensity of the WN_xC_y peak increases as deposition temperature is increased from 500 to 600 °C, indicating that the film crystallinity increases. This increase in crystallinity is probably because increased energy is available for crystallite formation and surface diffusion with an

increase in deposition temperature. As deposition temperature is increased from 600 to 650°C, the WN_xC_y peak intensity decreases, suggesting a decrease in film crystallinity. As shown from XPS analysis (*vide infra*), additional C deposited at 700 °C segregates to form both graphitic and diamond-like C. It is possible that the C segregation starts at 650 °C resulting in a decrease in surface diffusivity of the adsorbed species during film growth. The decrease in surface diffusivity causes a decrease in film crystallinity for deposition at 650 °C. The film crystallinity decreases further at 700 °C deposition temperature as suggested by a decrease in peak intensity of convoluted W_2N and W_2C peaks. The XPS spectrum for deposition at 700 °C shows that there is large amount of elemental C (diamond-like and graphitic) present in the films, further supporting the assertion that C segregation results in a decrease in film crystallinity. At 750 °C growth temperature, the peak intensity increases again but the increase is observed for the peak corresponding to W_2C suggesting that the crystallinity increase is due to the growth of W_2C crystalline phase (Figure 5-7).

5.5 Lattice Parameter

Since β - W_2N and β - W_2C have the same crystal structure with only a 2.7% lattice mismatch, it is possible that a solid solution of significant extent is formed. As described elsewhere, XRD peak shifts can be used to estimate the combined extent of the solid solution and residual strain.¹⁵⁷ The (111) peak of β - WN_xC_y or β - W_2N and β - W_2C has the highest intensity and thus was used for calculating the lattice parameter. Figure 5-9 shows the change in lattice parameter with deposition temperature for films deposited with **4** and **2a,b**. For films deposited with **4**, the lattice parameter is 4.12 Å for deposition at 500 °C, which is nearly identical to the literature value of 4.126 Å for β - W_2N .¹⁷⁸ As the deposition temperature increases from 500 to 650 °C, there is a concomitant increase in the estimated lattice parameter. Changes in the lattice parameter can result from an increase in uniform strain in the film or a change in film

composition. Uniform strain can be introduced by differential thermal expansion. Since the films grown from **4** are highly disordered and have small grains ($< 50 \text{ \AA}$, *vide post*), minimal uniform strain is expected to exist in these films. Thus, the increase in lattice parameter between 500 and 650 °C is attributed to the increase in C content and decrease in N content. For film deposited with **4** at 700 and 750 °C, the measured lattice parameter for the $\beta\text{-W}_2\text{N}$ peak is 4.13 and 4.14 Å, respectively. The lattice parameters of $\alpha\text{-W}_2\text{C}$ for film grown at 700 °C are: $a = 2.97 \text{ \AA}$ and $c = 4.68 \text{ \AA}$, while the values are: $a = 2.92 \text{ \AA}$ and $c = 5.18 \text{ \AA}$ for the film grown at 750 °C.

Comparison of films deposited with **4** and **2a,b** shows that for films grown between 500 and 600 °C, those deposited with **4** have a slightly larger lattice parameter than those deposited with **2a,b**. This is consistent with the higher C content in the films deposited from **4**. The lattice parameter for films deposited from **4** and **2a,b** increases with deposition temperature between 500 and 650 °C. This increase in lattice parameter value with deposition temperature is due to an increase in C content with temperature for films deposited with both **4** and **2a,b**.

5.6 Grain Size

As discussed in Chapter 3, the average grain size for polycrystalline materials can be estimated using the Scherrer equation if it is assumed that XRD peak broadening is due to the crystallite size distribution. Again, since the (111) reflection was most intense, it was used to determine FWHM and estimate the change in grain size with temperature for films deposited with **4** (Figure 5-10).

For films grown at 500 °C, the average grain size of crystallites for material deposited from **4** is 25 Å. Between 500 and 650 °C, the average grain size gradually increases from 25 Å to 34 Å. Higher surface diffusivity of atoms at higher deposition temperature facilitates nucleation and grain growth. At 700 and 750 °C, a two phase mixture of $\alpha\text{-W}_2\text{C}$ and $\beta\text{-W}_2\text{N}$ phases is formed. The average grain size for the $\alpha\text{-W}_2\text{C}$ phase, calculated from the (101) peak, is

30 and 42 Å for deposition at 700 and 750 °C, respectively. The average grain size for β -W₂N phase, calculated from (111) reflection, is 39 and 47 Å for deposition at 700 and 750 °C, respectively. The comparison of grain size for **4** and **2a,b** shows that the average grain size for films deposited with **4** is lower than that for films deposited by **2a,b** over the entire deposition temperature range.

5.7 Film Growth Rate

The growth rate for films grown from **4** was calculated from the measured film thickness (X-SEM) and deposition time. Figure 5-11 shows X-SEM images for films grown between 400 and 750 °C in 50 °C intervals. The growth rate varied from 3 Å/min to 24 Å/min, with the lowest growth rate observed at 400 °C and highest growth rate observed at 700 °C. There is an exponential increase in film thickness between 400 and 600 °C. As the deposition temperature is increased from 600 to 700 °C, there is a small increase in growth rate from 21 Å to 24 Å. The growth rate decreases to 17 Å/min as the deposition temperature is increased to 750 °C. To determine whether a further decrease in growth rate is observed at higher temperature, growth was attempted at 800 °C. There was no hard film deposited at 800 °C, however there was a carbon-like deposit observed on the substrate surface, which could easily be removed from the Si substrate by a cotton swab.

Figure 5-12 shows Arrhenius plots of growth rate for deposition from **4** and **2a,b** in the presence of hydrogen. The growth rate for films deposited with **4** is lower than that for films deposited with **2a,b** between 400 and 650 °C. The Arrhenius plot for **4** is consistent with film growth between 400 and 600 °C being surface reaction limited with a change to mass transfer limited between 600 and 700 °C. The decrease in growth rate at 750 °C and no film growth at 800 °C is possibly because of homogenous decomposition of the precursor above 750 °C. While the transition from surface reaction limited growth to mass transfer limited growth occurs

between 550 and 600 °C for **2a,b, 4** shows the same transition at 600 °C. The activation energy for **4** calculated from the Arrhenius relationship for film growth using **4** is 0.54 eV, which is significantly lower than 0.84 eV activation energy reported for **2a,b**. The value of activation energy for **4** is within the typical values between 0.5 and 1.0 eV observed for CVD growth in surface reaction limited regime.

5.9 Atomic Bonding from XPS Measurement

Figure 5-13 shows the XPS measurements for films deposited from **4** at 400, 500, 600, and 700 °C and Table 3-7 (Chapter 3) summarizes the reference peaks of elemental C, elemental W and different compounds of W, N, C and O obtained from the literature. Table 5-2 and 5-3 summarizes the peak parameters from peak fitting analysis done for the XPS peaks of W, C, N and O. The deconvolution of W $4f_{7/2}$ and $4f_{5/3}$ peaks was done by using the peak separation between $4f_{7/2}$ and $4f_{5/2}$ peaks of 2.1 eV and peak area ratio $4f_{7/2}$: $4f_{5/2}$ of 4:3. The deconvolution of W 4f and 4p peaks for film deposited at 400 °C indicates the presence of three different binding states of W. The first W $4f_{7/2}$ peak at 31.9 eV lies between the reference W peaks of W_2N (~33.0 eV) and W_2C (~ 31.5 eV), indicating that the W atom is bonded to both C and N. The second $4f_{7/2}$ peak at 34.0 eV lies between the reference WO_2 peak at 32.9 eV and W_2O_5 peak at 34.6 eV, suggesting that the phase of tungsten oxide is WO_x with the value of x between 2.0 and 2.5. The third W $4f_{7/2}$ peak at 35.7 eV corresponds to the W present in WO_3 . As the deposition temperature is increased from 400 to 700 °C, the intensity of the W peak corresponding to WN_xC_y increases whereas the intensity of W peak corresponding to both WO_x and WO_3 decreases.

For deposition at 400 °C, the N 1s peak is at 397.8 eV and corresponds well with the reference N 1s peak for WN_x film.¹¹⁹ As the temperature is increased to 500 °C, a broad shoulder which is centered at 399.2 eV develops. This broad peak indicates that a small amount

of N is present in amorphous state most probably at grain boundaries.¹¹⁹ The relative intensity of the amorphous N peak around 399.5 eV increases as the deposition temperature is increased from 500 to 600 °C. This indicates that although the overall N content of film decreases as deposition temperature is increased from 500 to 600 °C, the relative % of N present in the amorphous state increases with respect to that bonded to W. The XPS spectra at 700 °C shows no N 1s peak even though the AES measurements indicate the presence of N because of the poor detection limit of XPS for detecting light elements (N) in a heavy element matrix (W).

For deposition at 400 °C, a small broad C 1s peak at 283.8 eV is observed in the XPS spectrum. This peak position is slightly higher than the reference C 1s peak for W₂C at ~ 283.5 eV. At 500 °C, the C 1s peak can be deconvoluted into two different peaks at 283.5 eV and 284.9 eV. The former peak corresponds to C bonded to W and the latter peak reflects C present in amorphous phase. As the deposition temperature is increased from 500 to 600 °C, the peak intensity of both carbidic and amorphous C increases. The C 1s spectrum for deposition at 700 °C can be deconvoluted into three distinct peaks at 283.6 eV, 284.5 eV, and 285.5 eV. The first peak at 283.6 corresponds to carbidic carbon bonded to W. The second and third peaks at 284.5 and 285.5 eV reflect the presence of graphitic carbon (sp² bonded C) and diamond-like C (sp³ bonded C). Previous studies on diamond-like C films have shown the presence of C as both graphitic C with a peak at ca. 284.5 eV and diamond-like C with a broad peak at ca. 285.3 eV.^{192,193} The presence of graphitic and diamond-like C for films deposited at 700 °C shows that besides phase separation of α -W₂C, C separates from the WN_xC_y as graphitic and diamond-like C.

The O 1s peak for deposition at 400 °C can be deconvoluted into two peaks at 530.8 and 531.8 eV. The peak at 530.8 eV corresponds to O bonded to W in WO_x or WO₃. Since O is

present as O^{2-} , the O peak does not show peak separation between the two different bonding states in WO_x and WO_3 . The other peak at 531.8 eV corresponds to O present in WN_xC_y . Previous study on tungsten oxynitride has shown that XPS spectra for O 1s show a peak at 531.7 eV for O present in WN_x matrix.²⁰³ The O 1s peaks for films deposited at 500, 600 and 700 °C can be similarly deconvoluted to two peaks corresponding to O present as WO_x or WO_3 and O present in the WN_xC_y matrix.

To summarize the XPS results, film deposited at 400 °C shows presence of the WN_xC_y with a significant amount of WO_x and WO_3 . At 500 °C, the bulk of the film is WN_xC_y with small amounts of WO_x and WO_3 . Additionally, film deposited at 500 °C shows the presence of both C and N in an amorphous state probably at grain boundaries. Incidentally, the lowest temperature at which the presence of amorphous C and N is observed is 500 °C, which is also the temperature at which crystallinity is first observed. The film deposited at 600 °C consists of WN_xC_y , a small amount of WO_x/WO_3 together with amorphous N and C. At 700 °C, the film shows the presence of WN_xC_y , graphitic and diamond-like C and a small amount of WO_x/WO_3 .

5.8 Film Resistivity

Figure 5-14 shows the film resistivity at different deposition temperature for films grown with precursors **4** and **2a,b**. For depositions with **4** at 400 °C, the resistivity is 1150 $\mu\Omega$ -cm. The resistivity decreases to 980 $\mu\Omega$ -cm for deposition at 450 °C due to higher W content and lower C and N content of the film. Between 450 and 600 °C deposition temperature, the film resistivity gradually increases from 980 to 6857 $\mu\Omega$ -cm. This increase is attributed to a decrease in W content of the film. The resistivity of films deposited at 700 and 750 °C is ca. 2400 $\mu\Omega$ -cm. The XRD spectra indicate the formation of a two phase mixture of β - W_2N and α - W_2C at these temperatures and XPS measurement shows the separation of C to form graphitic C and diamond-like C. The phase separation at 700 and 750 °C results in segregation of excess amorphous C as

α -W₂C, graphitic C and diamond-like C resulting in decrease of film resistivity. The decrease in resistivity as deposition temperature is increased from 600 to 650 °C could result from the onset of phase separation at 650 °C, even though the phase separation is not clearly seen in the XRD spectrum at 650 °C.

Comparison of resistivity for films deposited with **4** and **2a,b** reveals that while the lowest resistivity obtained with **2a,b** is 750 $\mu\Omega$ -cm at 450 °C, the lowest resistivity obtained with **4** is 980 $\mu\Omega$ -cm at 450 °C. The resistivity of films deposited with **2a,b** increases throughout the deposition temperature, whereas the resistivity of films deposited with **4** show a steep increase between 450 and 600 °C followed by a decrease in resistivity between 600 and 750 °C because of the phase separation of W₂N and W₂C.

5.9 Diffusion Barrier Testing

To determine the effectiveness of diffusion barrier deposited with **4**, barrier films deposited at 450 and 500 °C were coated with 100 nm PVD Cu. The thickness of films deposited at 450 and 500 was 45 and 55 nm, respectively. The Cu/barrier/Si stack was annealed in vacuum at temperature ranging from 200 to 600 °C for 30 min to determine the temperature at which Cu diffuses through the barrier film into the Si substrate. After annealing, three-point AES depth profile and XRD measurements were done to detect copper diffusion through the barrier film.

Figure 5-16 shows the depth profile for a post-anneal Cu/WN_xC_y/Si stack for WN_xC_y films deposited from **4** at 450 °C. For anneal at 200 °C for 30 min, the AES depth profile shows that the Cu/WN_xC_y interface is similar to that for films that were not annealed (Figure 5-15), suggesting that no bulk copper diffusion had occurred. As the anneal temperature is increased to 400 °C, there is slight mixing of the Cu/WN_xC_y interface, however, the copper has not diffused through the barrier film. For 500 °C anneal, there is further diffusion of Cu in the WN_xC_y film, but the barrier film is able to prevent complete diffusion of Cu through it. After annealing at 600

°C, the AES profile shows that there is complete diffusion of copper through the barrier film. Intermixing is also observed for the WN_xC_y/Si interface. The depth profiling shows that 45 nm barrier film of WN_xC_y deposited from **4** at 450 °C is able to prevent bulk Cu diffusion when annealed at 500 °C for 30 min.

Figure 5-17 shows the XRD plots for films deposited from **4** at 450 °C before annealing and after annealing at 200, 400, 500 and 600 °C. No peak(s) corresponding to WN_xC_y is observed because film deposited at 450 °C is X-ray amorphous. As discussed in the literature review chapter, the recrystallization temperature is important for diffusion barrier film because diffusion along grain boundaries is believed to be the primary cause for barrier failure. Amorphous W_2N film deposited by PVD recrystallizes after annealing at 600 °C.¹⁸² However, for WN_xC_y film deposited by **4**, the film does not recrystallize even after annealing at 600 °C as seen from the XRD pattern. This is expected since ternary compounds tend to have higher recrystallization temperature as compared to binary compounds.

The pre-anneal XRD profile shows peaks at 31.1, 50.75 and 74.55 2 θ degrees and these peaks correspond to Cu (111), Cu (200) and Cu (220) reflections, respectively. After annealing at 200 °C, the intensity of Cu peaks increases because of grain growth in the Cu film. No peak corresponding to $CuSi_x$ compound is observed indicating that there is no bulk diffusion of copper after annealing at 200 °C. As the annealing temperature is increased, the intensity of Cu peaks further increases because of grain growth, however, no other peaks is observed besides peaks corresponding to Cu and Si substrate suggesting that bulk phase copper diffusion did not occur even after annealing at 600 °C. This result contradicts the AES measurement which shows that Cu has diffused through the barrier film and into Si substrate after annealing at 600 °C. This apparent contradiction occurs because XRD can detect $CuSi_x$ compound formation only after

sufficient amount of the silicide has formed. If a small amount of Cu has diffused through the barrier at the onset of barrier failure, XRD is not able to detect small quantities of CuSi_x whereas AES can detect Cu in barrier film or Si even if the Cu content is ca. 1 at. % because of the higher sensitivity of AES. As discussed in the Chapter 2, XRD and four point probe are the least sensitive techniques for detecting copper diffusion through the barrier. Previous studies have also shown that even though the barrier film has failed at lower annealing temperature, XRD only detects the barrier failure at much higher anneal temperature.⁶³

Figure 5-18 shows the 3 point AES depth profile for a post-anneal Cu/ WN_xC_y /Si stack for WN_xC_y films deposited from **4** at 500 °C. After annealing at 200 °C and 400 °C for 30 min, the Cu- WN_xC_y interface is similar to that for films that were not annealed, suggesting that no bulk diffusion of copper has occurred. For 500 °C annealing, slight mixing of Cu- WN_xC_y interface is evident in the AES depth profile. Copper diffuses through the barrier film after annealing at 600 °C and significant intermixing of Cu and WN_xC_y is observed in AES depth profile. The AES depth profiling shows that 55 nm barrier film of WN_xC_y deposited with **4** at 500 °C is also able to prevent Cu diffusion when annealed at 500 °C for 30 min. Figure 5-19 shows the XRD measurements on a Cu/ WN_xC_y /Si stack before annealing and after annealing at 200, 400, 500 and 600 °C. Similar to film deposited at 450 °C, the film deposited at 500 °C do not show recrystallization of the barrier film. The XRD spectra do not indicate formation of CuSi_x even after annealing at 600 °C for the reason discussed above, even though the barrier film has failed.

5-10 Conclusions

It has been demonstrated that the mixed imido guanidinato complex $\text{W}(\text{N}^i\text{Pr})\text{Cl}_3[\text{}^i\text{PrNC}(\text{NMe}_2)\text{N}^i\text{Pr}]$ (**4**) can be used in an aerosol assisted CVD system to deposit WN_xC_y thin films. A comparison of effect of $\text{Cl}_4(\text{CH}_3\text{CN})$ and $\text{Cl}_3(\text{}^i\text{Pr}(\text{NMe}_2)\text{N}^i\text{Pr})$ ligands on film properties is presented by comparing the film composition, crystallinity, lattice parameter,

grain size, growth rate and resistivity of films deposited with **4** and **2a,b**. The AES spectra showed the presence of W, N, C and O in this material. When compared with films grown with **2a,b**, the films grown with **4** have a higher C/W ratio and a similar N/W ratio. The O content of films deposited with **4** is also significantly lower than that for films deposited with **2a,b**, especially at lower deposition temperature. The lowest growth temperature for **4** is 400 °C, which is 50 °C lower than that for **2a,b**. For both **4** and **2a,b**, films grown at and above 500 °C are crystalline. From the diffusion barrier application standpoint, films deposited with **4** at 450 and 500 °C were able to prevent copper diffusion after annealing at 500 °C for 30 min in vacuum. Since the film deposited from **4** at 450 °C is amorphous, has the lowest resistivity of 980 $\mu\Omega\text{-cm}$ and can prevent Cu diffusion after annealing at 500 °C, films deposited from **4** at 450 °C are candidates for diffusion barrier application.

Table 5-1. Selected bond distances (Å) and bond angles (°) for **4**

Bond Length (Å)		Bond Angle (degree)	
W-N1	2.247(4)	N1-W-N3	163.23(18)
W-N2	1.961(4)	N2-W-C13	155.81(13)
W-N3	1.702(4)	C11-W-C12	167.30(5)
W-C11	2.3752(15)	N2-W-N3	101.44(19)
W-C12	2.3819(16)	N1-W-N2	61.88(16)
W-C13	2.3833(14)	W-N1-C1	90.3(3)
C1-N2	1.399(6)	N1-C1-N2	107.8(4)
C1-N1	1.294(6)	W-N2-C1	100.0(3)
C1-N4	1.373(6)	W-N3-C10	168.4(8)

Table 5-2. Analysis results from the deconvolution of the XPS peak of W for films deposited from **4** on Si(100) substrate at 400, 500, 600 and 700 °C

Deposition temperature		WN _x C _y			WO _x (2.0 < x < 2.5)			WO ₃		
		Peak Position (eV)	% Area	FWHM (eV)	Peak Position (eV)	% Area	FWHM (eV)	Peak Position (eV)	% Area	FWHM (eV)
400	W4f _{7/2}	31.95	20.4	1.61	34.01	17.0	1.84	35.74	15.9	2.00
	W4f _{5/2}	33.90	15.3	1.94	36.01	11.1	1.97	37.94	11.9	1.81
	W4p _{3/2}	37.10	3.8	2.15	39.27	2.8	1.64	41.04	1.8	1.20
500	W4f _{7/2}	31.89	40.4	1.36	33.51	8.7	1.52	37.61	4.8	1.96
	W4f _{5/2}	34.06	30.3	1.48	35.61	6.6	2.17	37.49	1.0	1.75
	W4p _{3/2}	35.51	6.3	2.02	38.81	1.3	1.27	41.11	0.6	2.16
600	W4f _{7/2}	32.01	38.2	1.30	33.72	7.8	1.61	35.31	7.4	1.78
	W4f _{5/2}	34.10	29.8	1.50	35.59	5.9	2.01	37.41	5.6	2.44
	W4p _{3/2}	37.40	3.0	1.98	38.89	0.9	1.41	40.71	1.4	3.45
700	W4f _{7/2}	32.05	36.3	1.28	33.54	9.9	1.61	35.33	7.5	2.14
	W4f _{5/2}	34.15	27.2	1.33	35.64	7.4	1.86	37.53	5.6	2.15
	W4p _{3/2}	37.45	2.7	2.04	38.94	2.0	1.22	40.83	1.4	2.10

Table 5-3. Analysis results from the deconvolution of XPS peaks of C, N and O for films deposited from **4** on Si(100) substrate at 400, 500, 600 and 700 °C

Deposition temperature	C 1s				N1s			O1s		
	Peak Position	% Area	FWHM	Peak Position	% Area	FWHM	Peak Position	% Area	FWHM	
	(eV)		(eV)	(eV)		(eV)	(eV)		(eV)	
400	Peak 1	283.83	100.0	2.29	397.81	100.0	1.83	530.85	15.9	2.00
	Peak 2	--	--	--	--	--	--	531.85	11.9	1.81
500	Peak 1	283.51	73.7	1.48	397.71	84.1	1.50	530.77	66.2	1.59
	Peak 2	284.95	26.3	2.19	399.25	15.9	1.77	532.11	33.8	2.03
600	Peak 1	283.59	72.3	1.54	397.73	64.6	1.73	530.57	49.4	1.46
	Peak 2	285.06	27.7	1.98	399.49	35.4	2.87	531.69	50.6	2.02
700	Peak 1	283.60	19.2	1.53	--	--	--	530.77	52.4	1.81
	Peak 2	284.50	44.2	1.64	--	--	--	531.91	47.6	2.48
	Peak 3	285.50	36.6	2.43	--	--	--	--	--	--

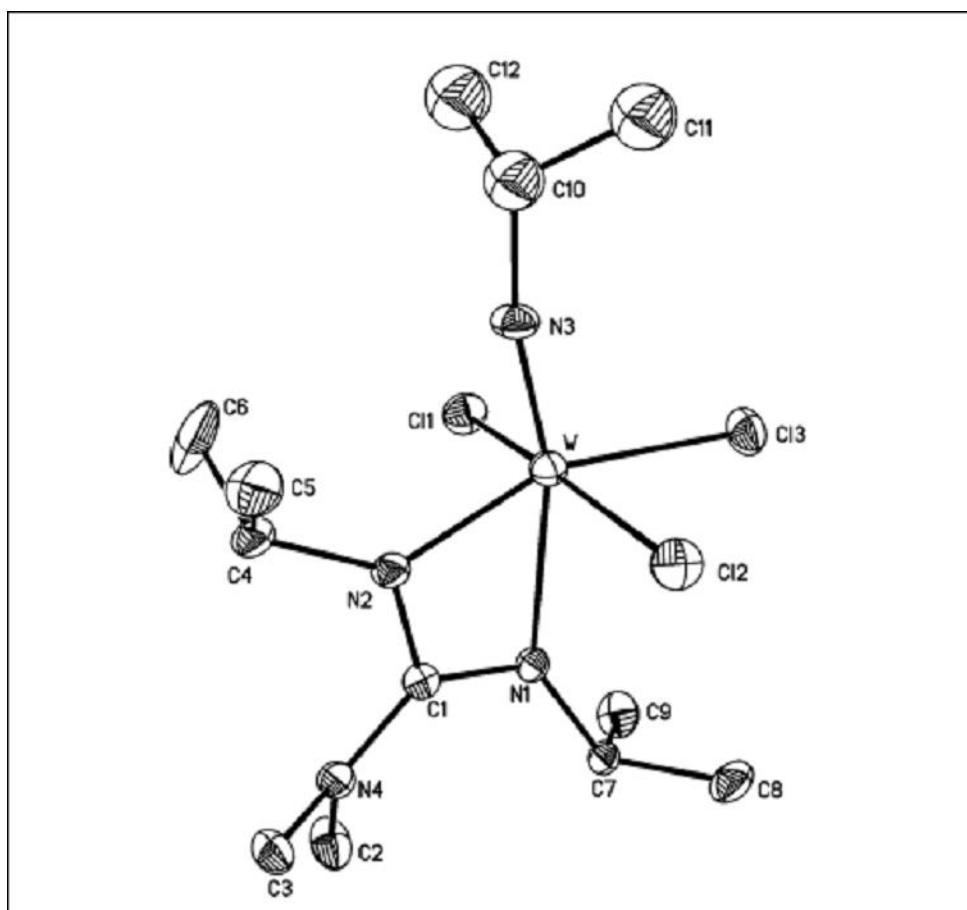


Figure 5-1. Thermal ellipsoids diagram of the molecular structure of $W(N^iPr)Cl_3[{}^iPr(NMe_2)N^iPr]$. Thermal ellipsoids are drawn at 40 % probability, and the hydrogen atoms have been omitted for clarity.²⁰²

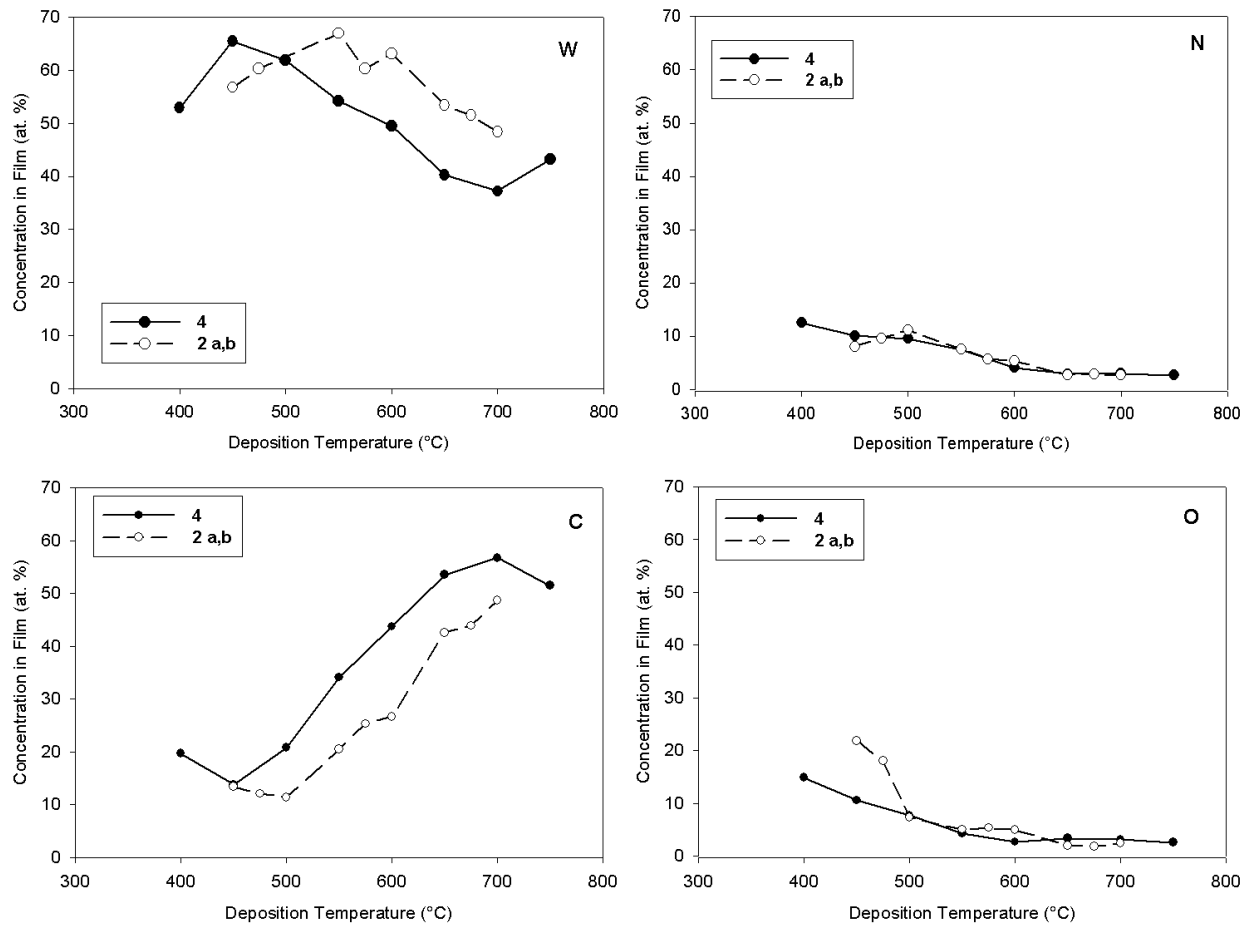


Figure 5-2. Composition of films deposited from **4** and **2a,b** on Si (100) substrate at different deposition temperature as determined by AES after 0.5 min of sputtering

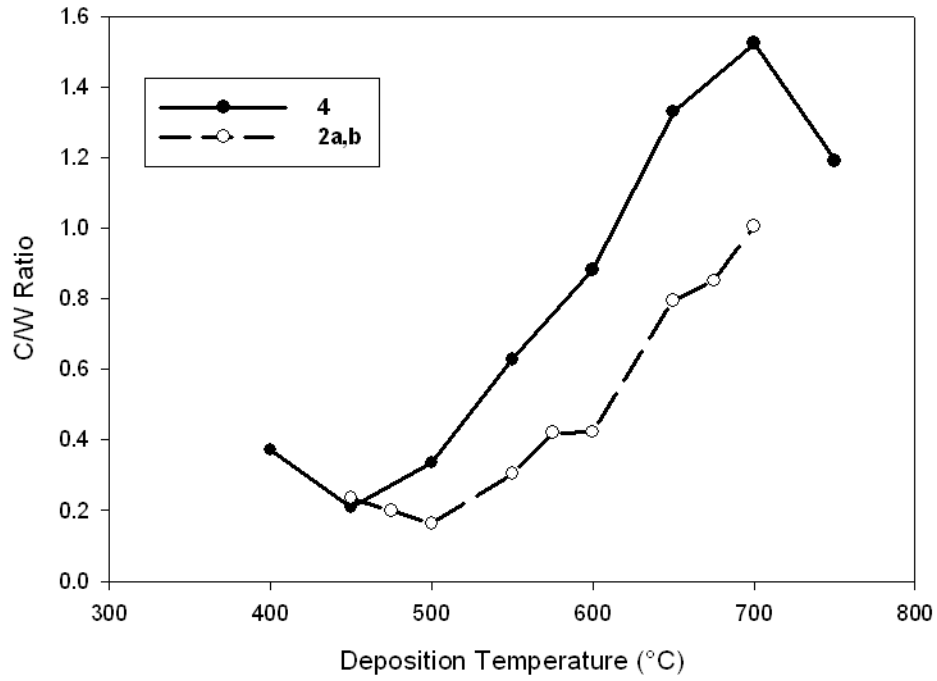
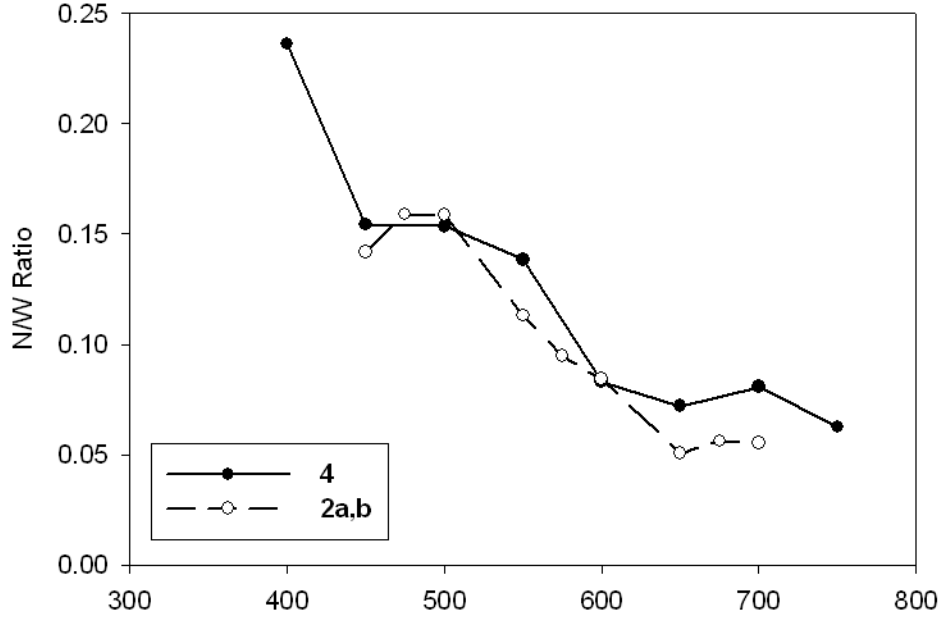


Figure 5-3. N/W and C/W atomic ratios for films deposited from **4** and **2a,b** on Si (100) substrate at different deposition temperature as determined by AES after 0.5 min of sputtering

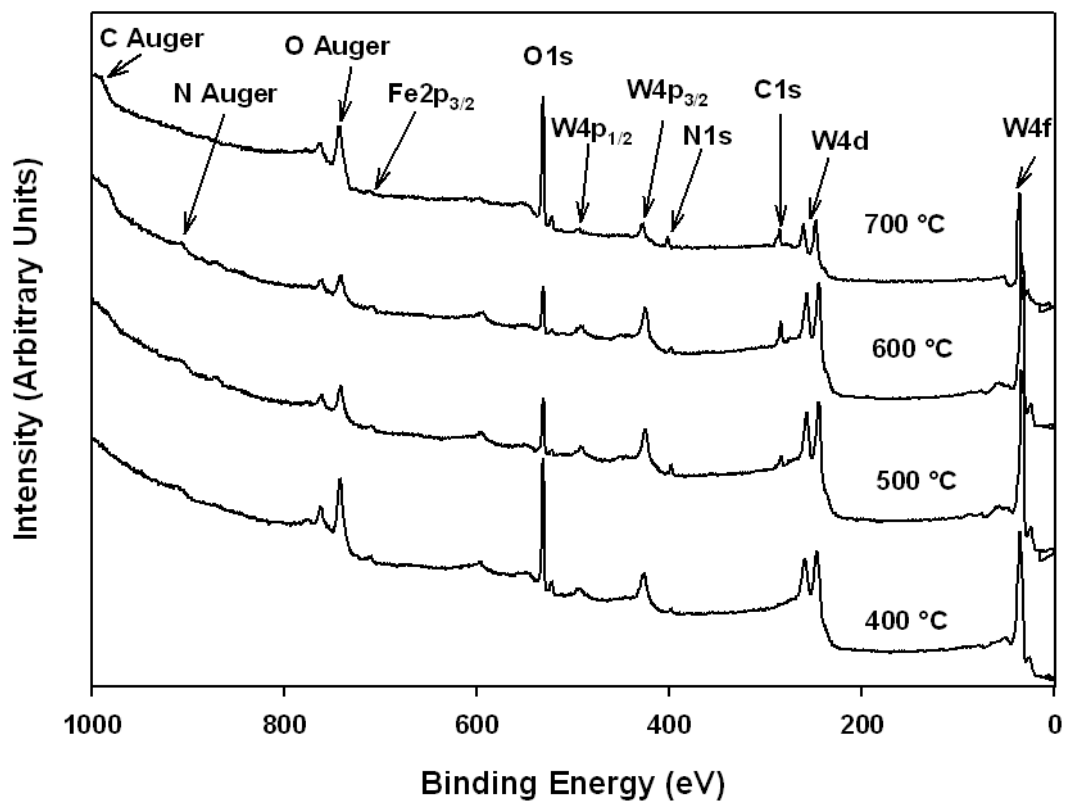


Figure 5-4. X-ray photoelectron spectroscopy patterns for films deposited from **4** at 400, 500, 600 and 700 °C on Si(100) surface

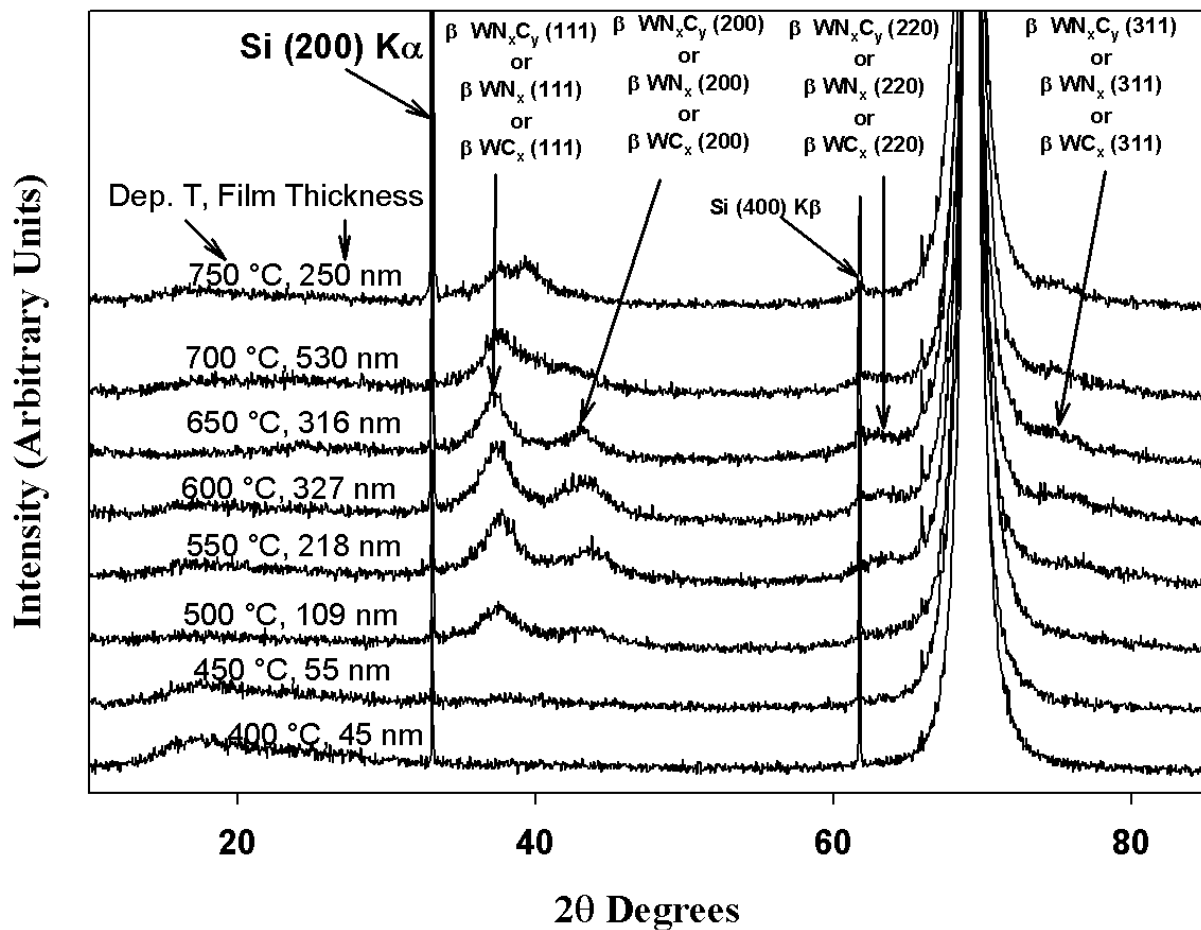


Figure 5-5. X-ray diffraction patterns for films deposited from 4 on Si (100) substrate

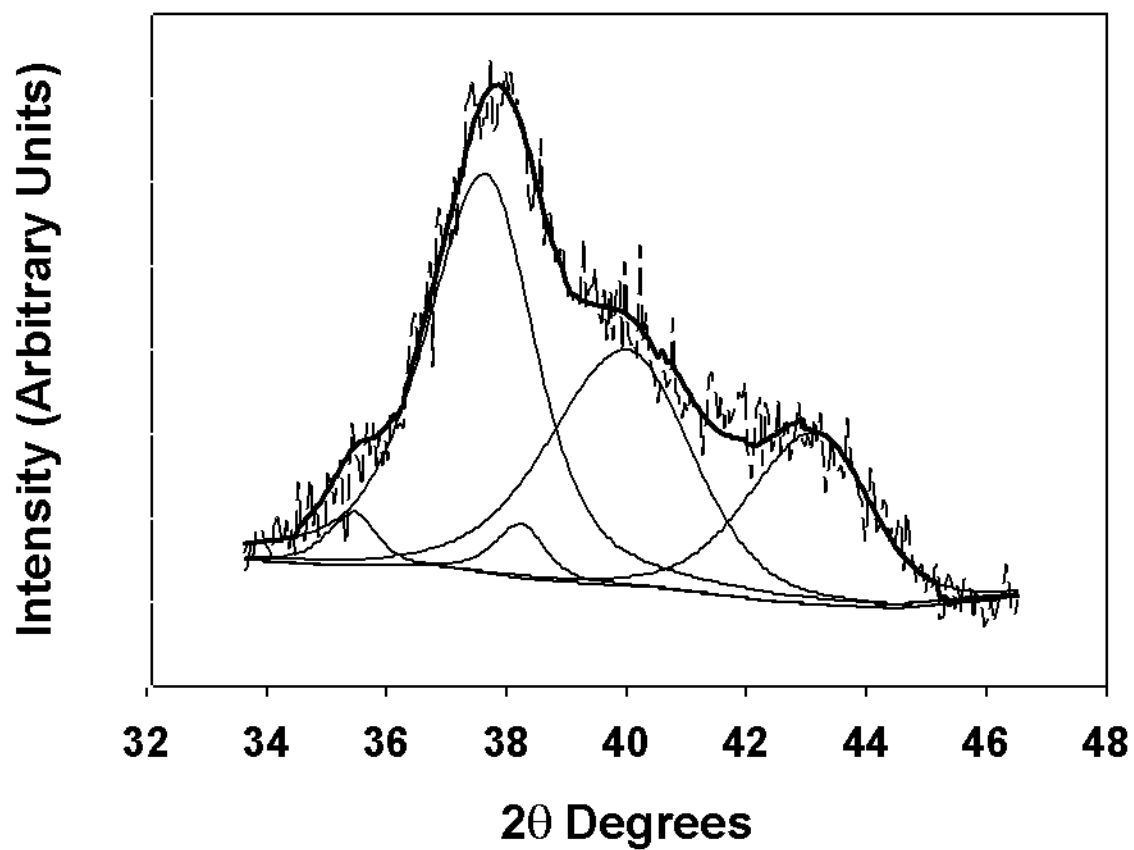


Figure 5-6. Deconvolution of XRD peaks for films deposited from **4** at 700 °C on a Si (100) substrate. The dashed line represents raw data, solid lines represent individual peaks of β -W₂N and α -W₂C used for deconvolution and the bold solid line represents the profile calculated from individual peaks.

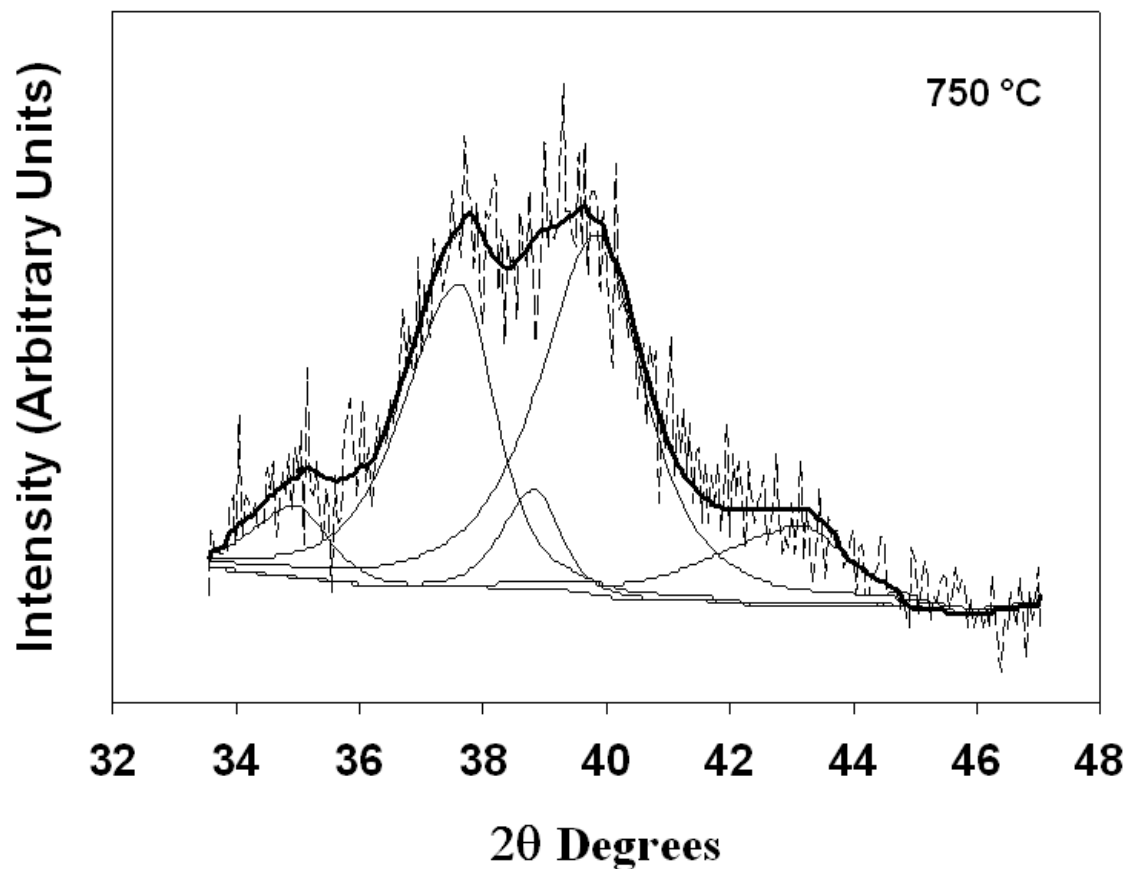


Figure 5-7. Deconvolution of XRD peaks for films deposited from **4** at 750 °C on a Si (100) substrate. The dashed line represents raw data, solid lines represent individual peaks of β -W₂N and α -W₂C used for deconvolution and the bold solid line represents the profile calculated from individual peaks.

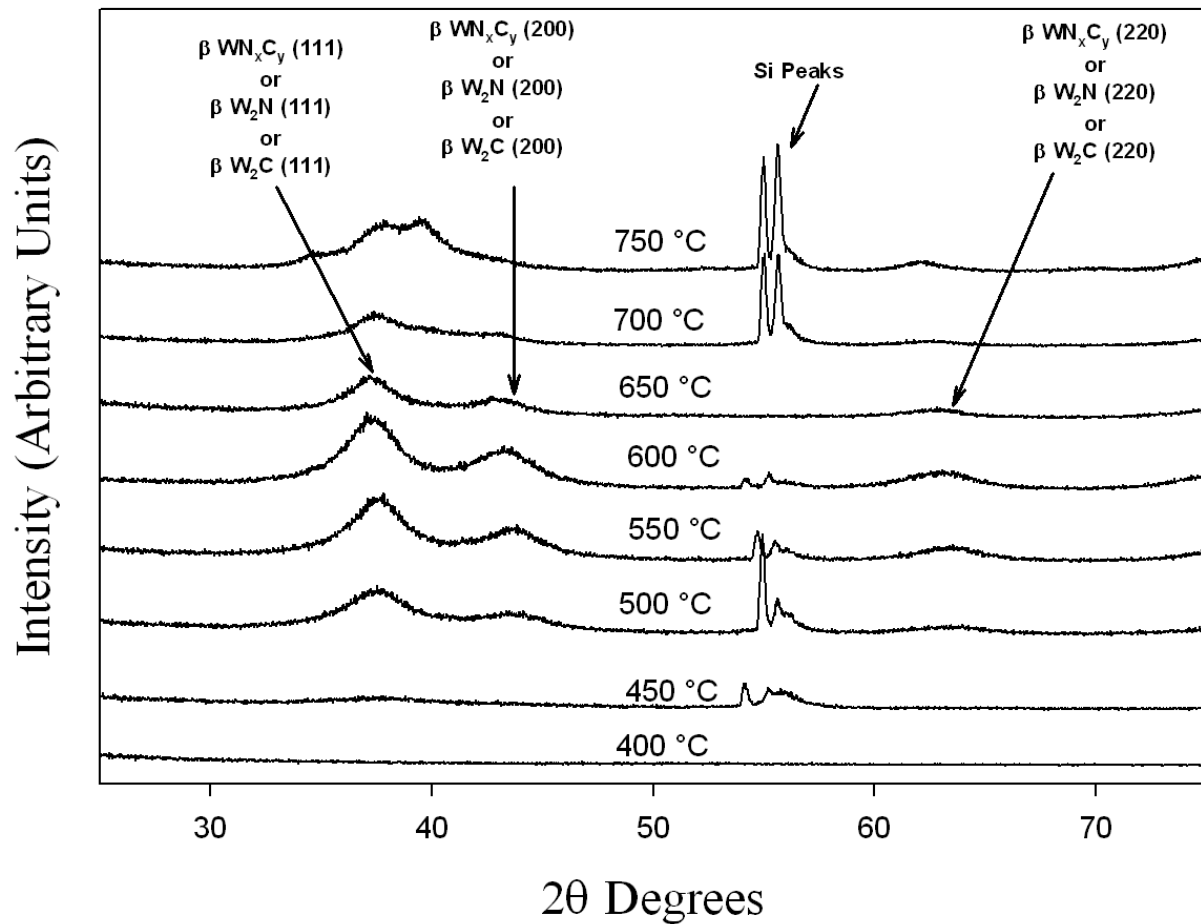


Figure 5-8. Grazing incidence X-ray diffraction spectra for films deposited from 4 on Si (100) substrate

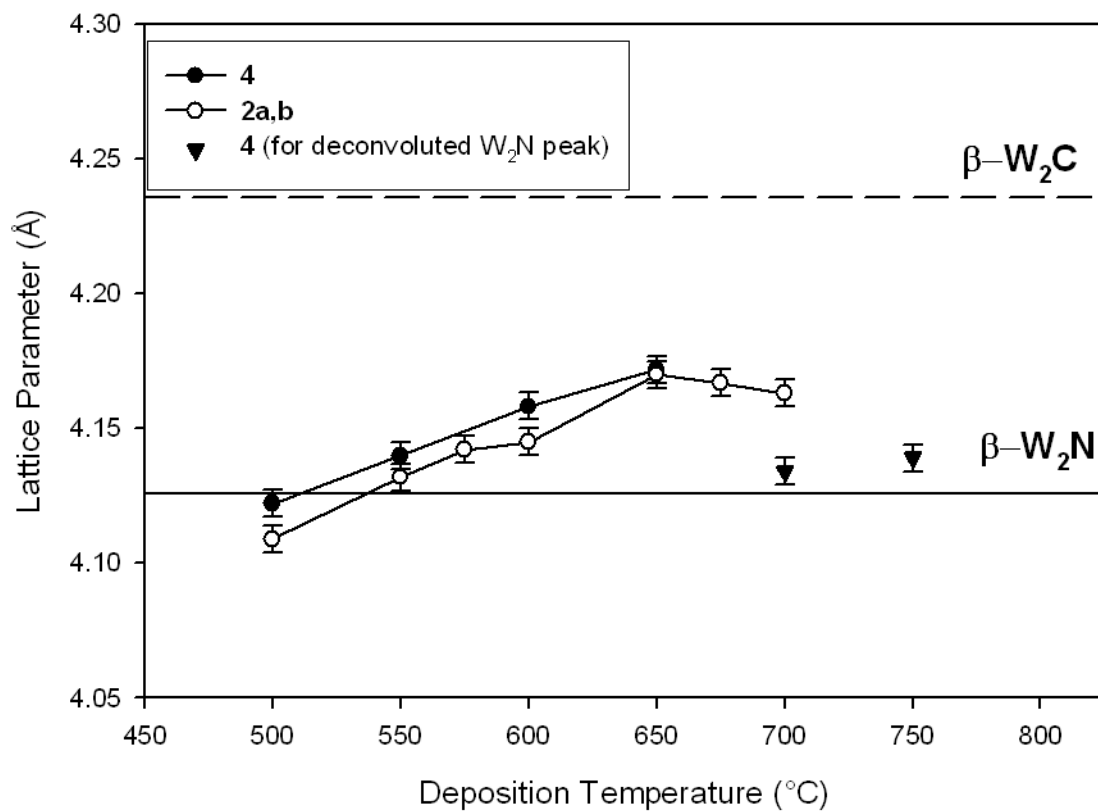


Figure 5-9. Lattice parameters for films grown from **4** and **2a,b** on Si (100) substrate. The solid line at 4.126 Å corresponds to the standard lattice parameter for β-W₂N. The dotted line at 4.236 Å corresponds to standard lattice parameter for β-W₂C (111). Error bars indicate uncertainty in determination of peak position for lattice parameter calculation.

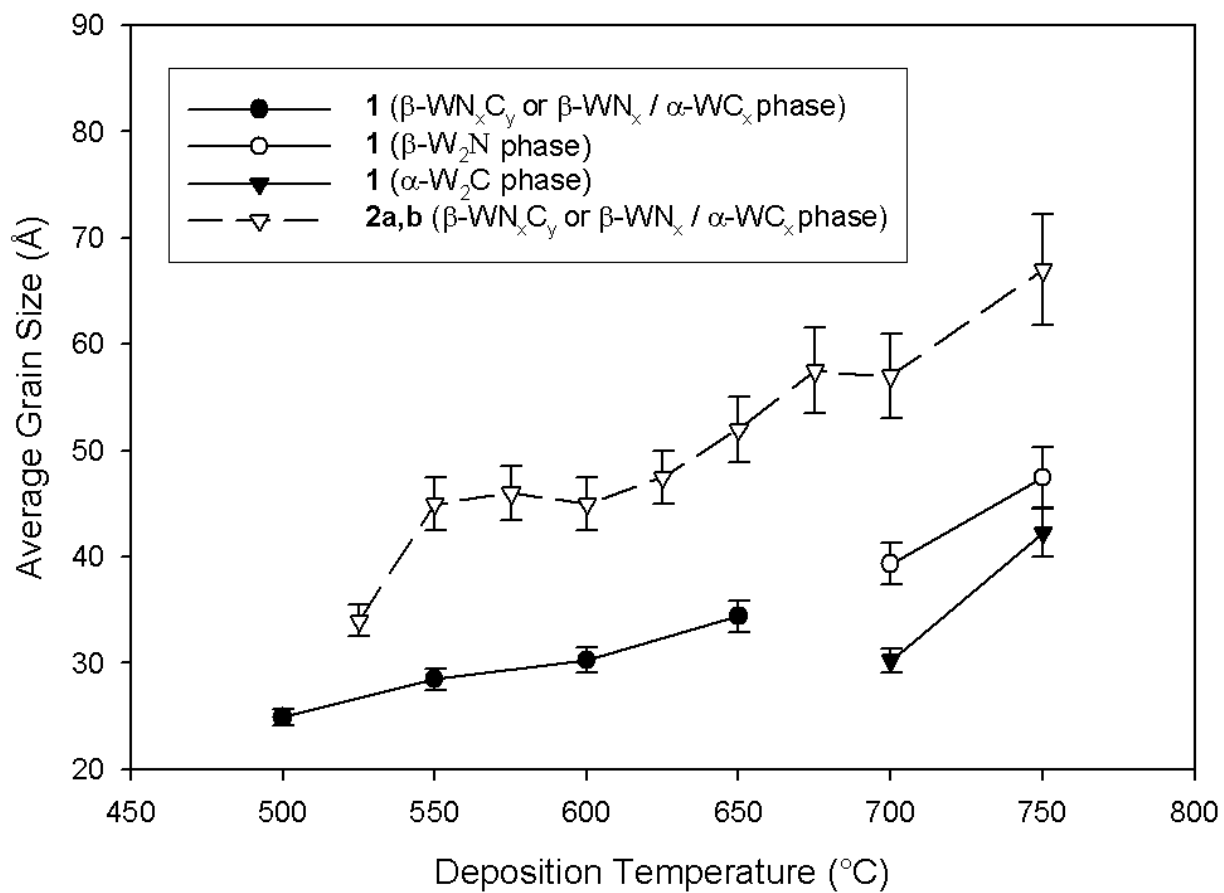


Figure 5-10. Average grain size at different deposition temperature for films grown from **4** and **2a,b** on Si (100) substrate

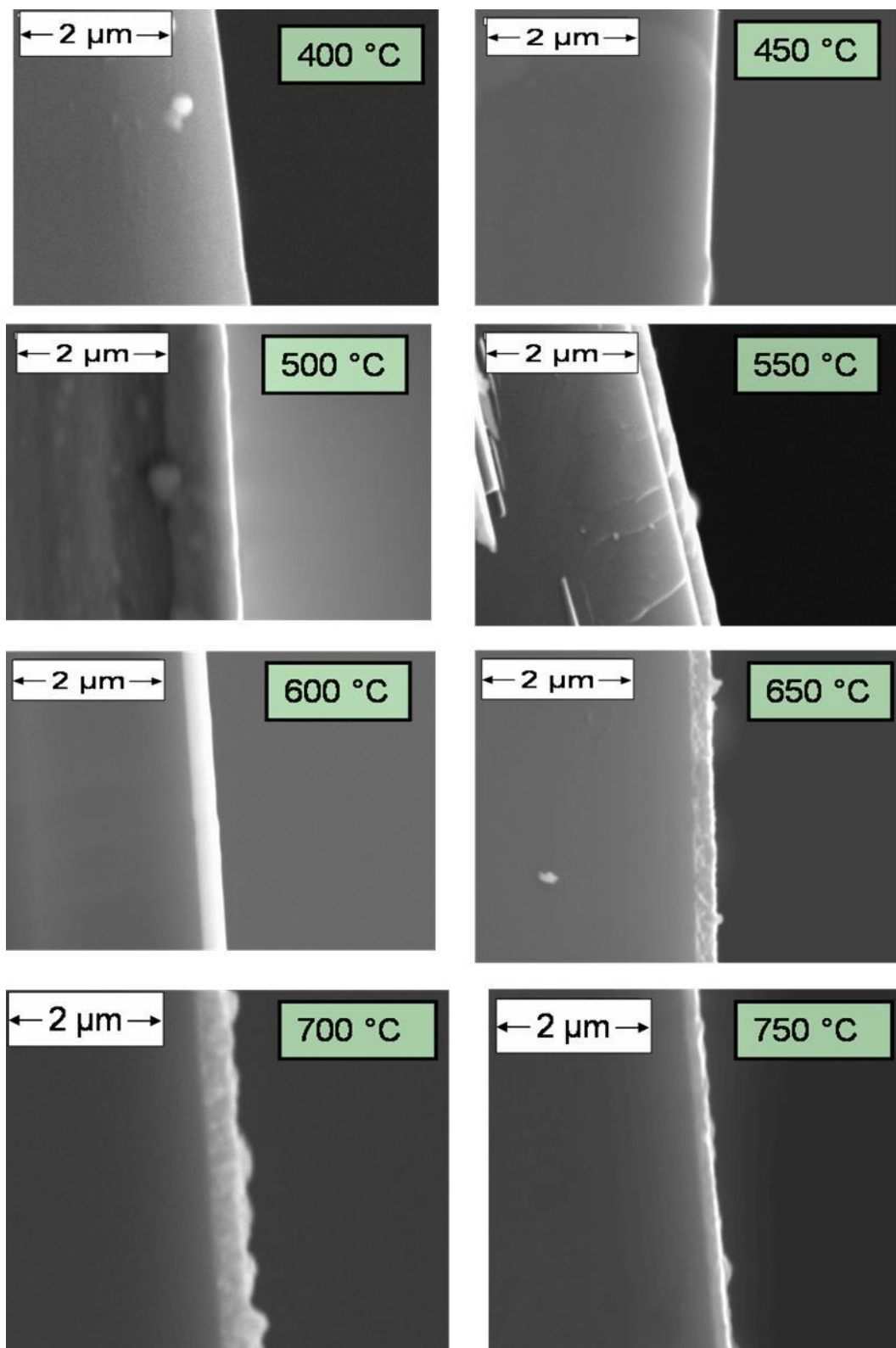


Figure 5-11. Scanning electron microscope images for films grown from **4** on Si (100) substrate between 400 and 750 °C in 50 °C increments

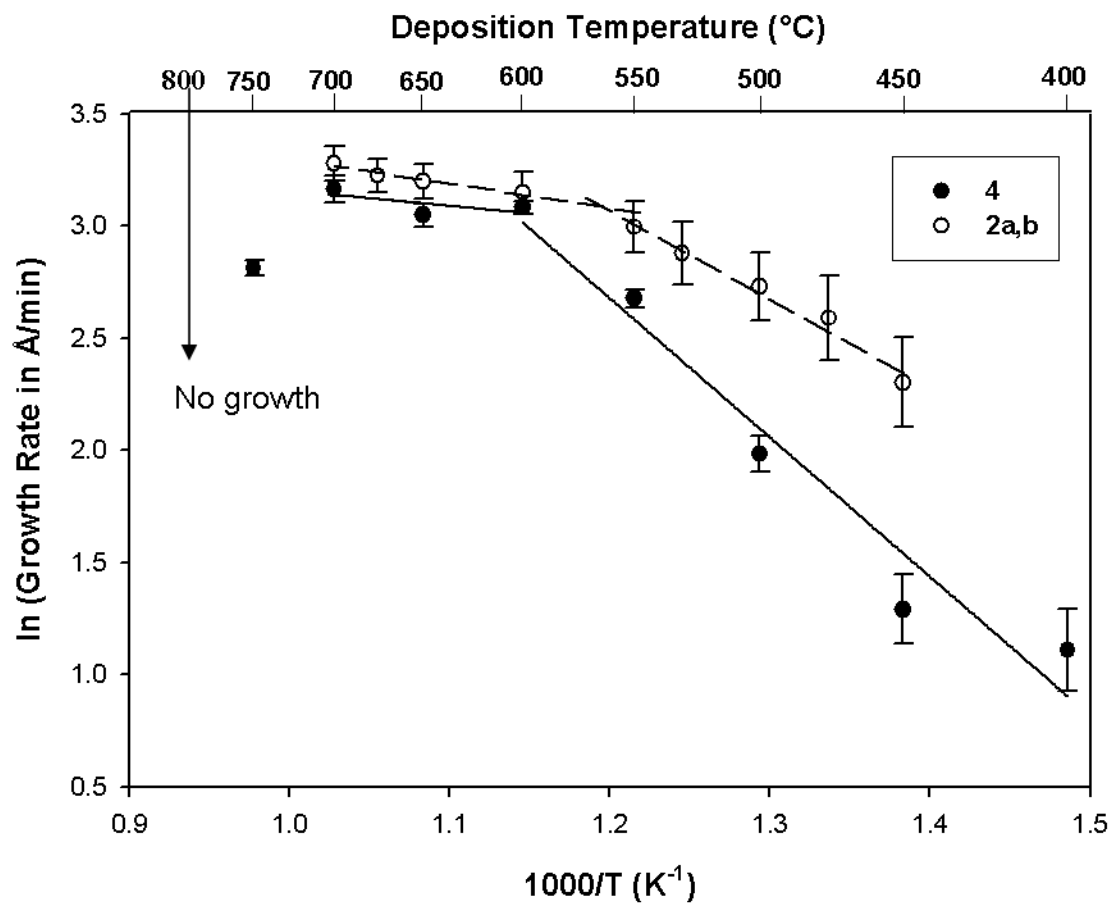


Figure 5-12. Arrhenius plot of log of film growth rate vs. inverse temperature for deposition from **4** and **2a,b** on a Si(100) substrate

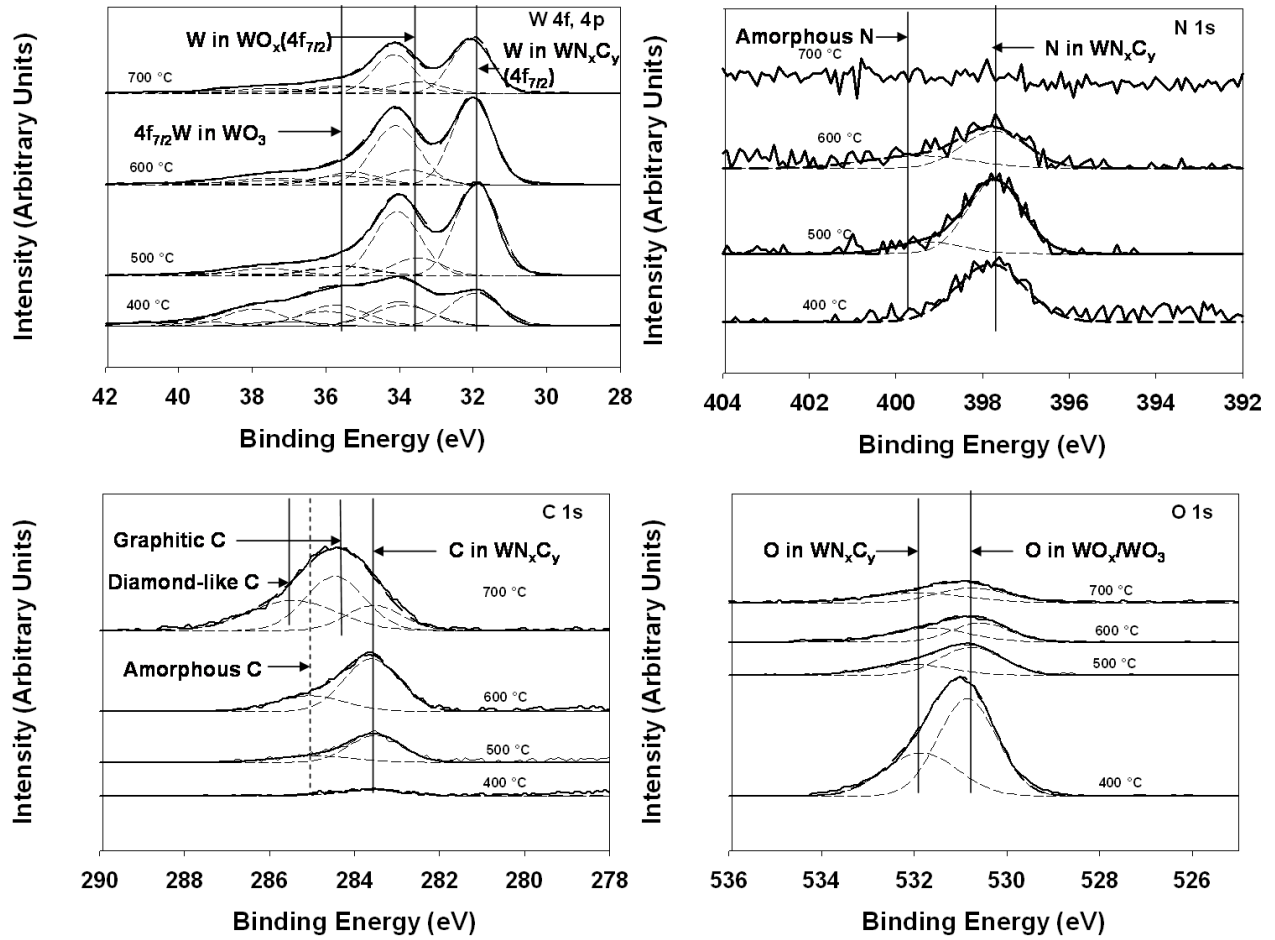


Figure 5-13. Deconvolution of the XPS peaks of W, N, C and O for film deposited from **4** at 400, 500, 600 and 700 °C on Si (100) substrate

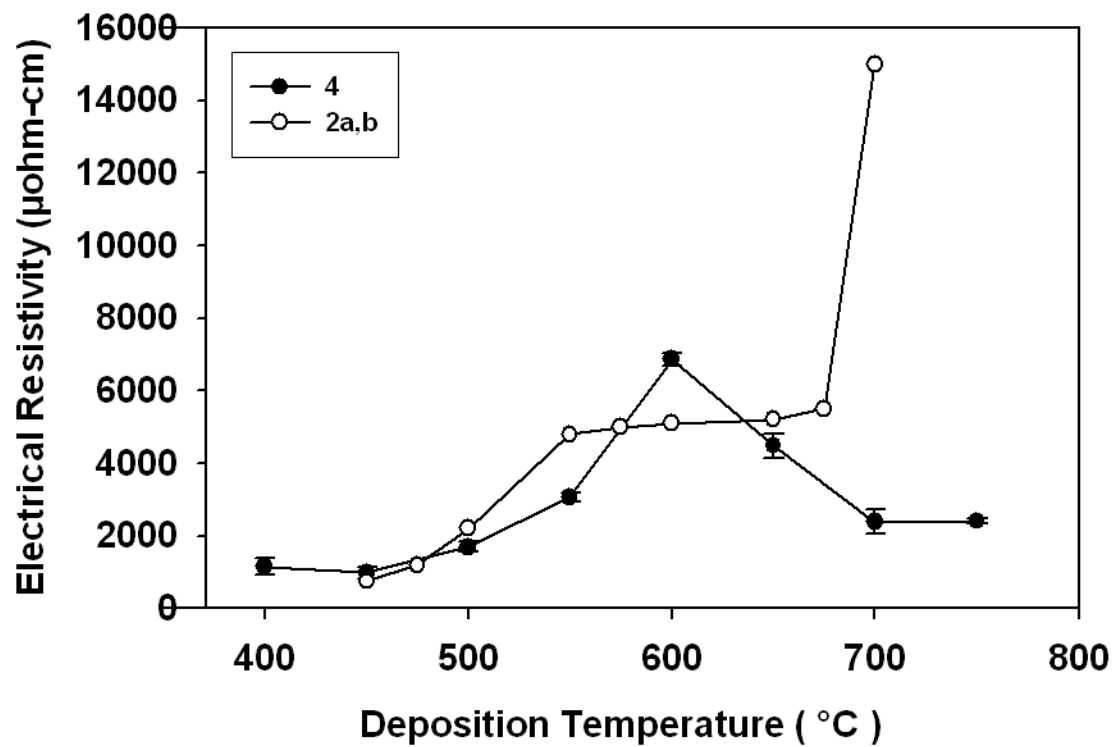


Figure 5-14. Change in film resistivity with deposition temperature for films grown on Si (100) from **4** and **2a,b**

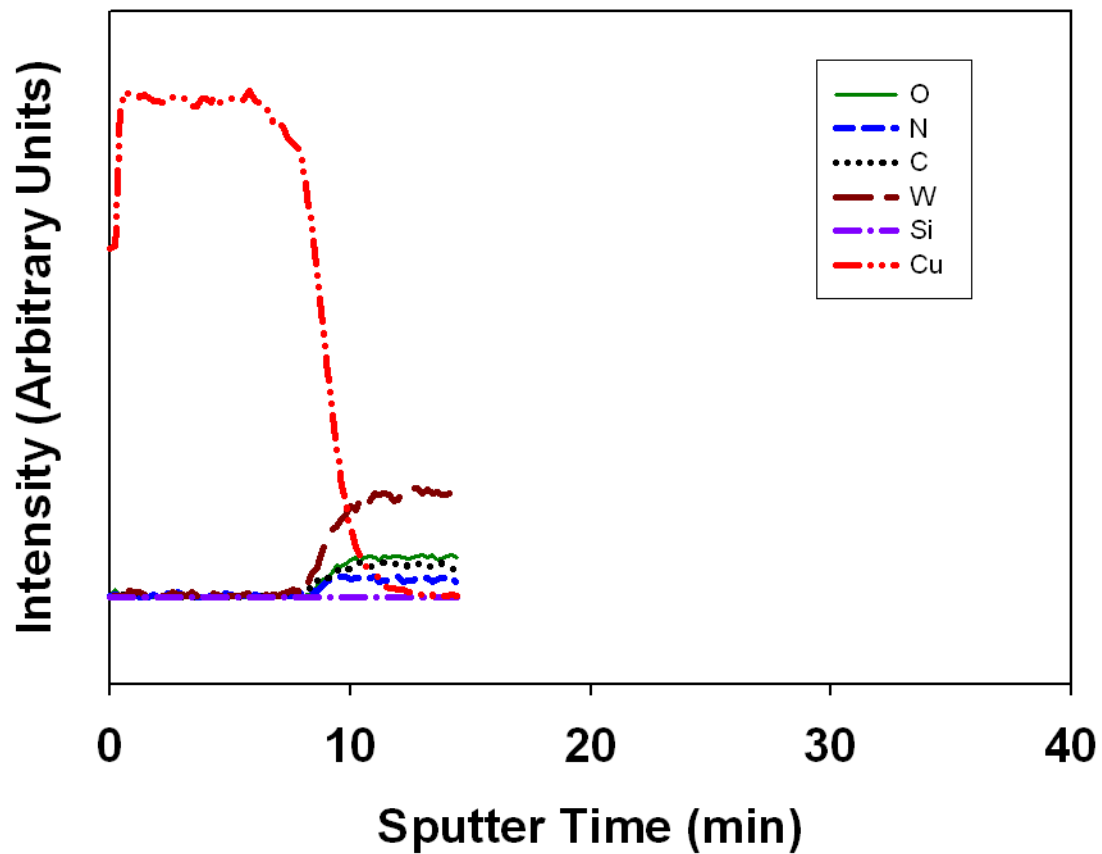


Figure 5-15. Pre-anneal AES depth profile of Cu (100 nm)/ WN_xC_y (45 nm)/Si (substrate) stack for WN_xC_y film deposited at 450 °C (using precursor **4**) showing the Cu-barrier interface.

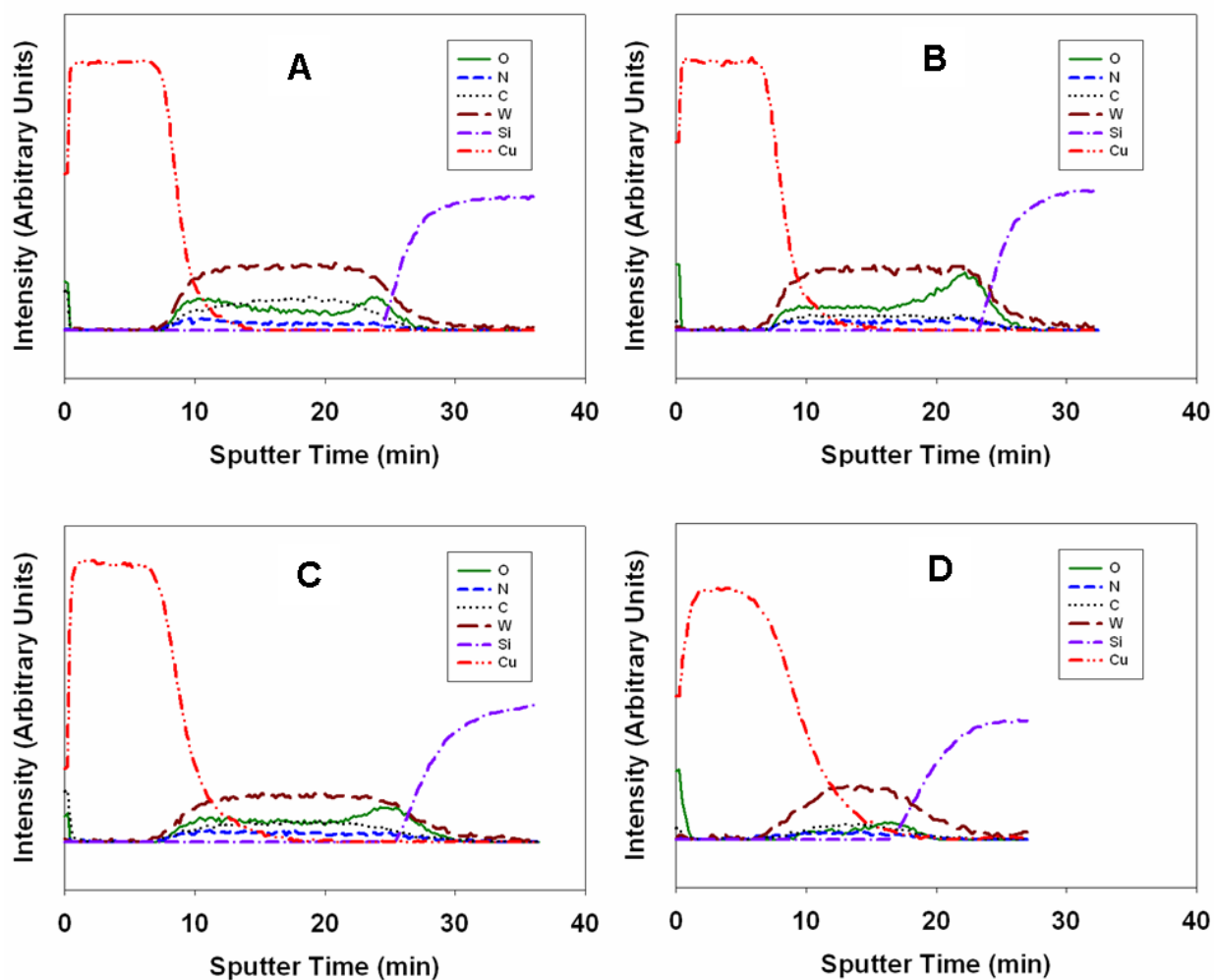


Figure 5-16. Auger electron spectroscopy depth profiles of Cu (100 nm)/ WN_xC_y (45 nm)/Si (100) stack for WN_xC_y film deposited at 450 °C (using precursor **4**) and annealed in vacuum for 30 min at A) 200 °C B) 400 °C C) 500 °C D) 600 °C.

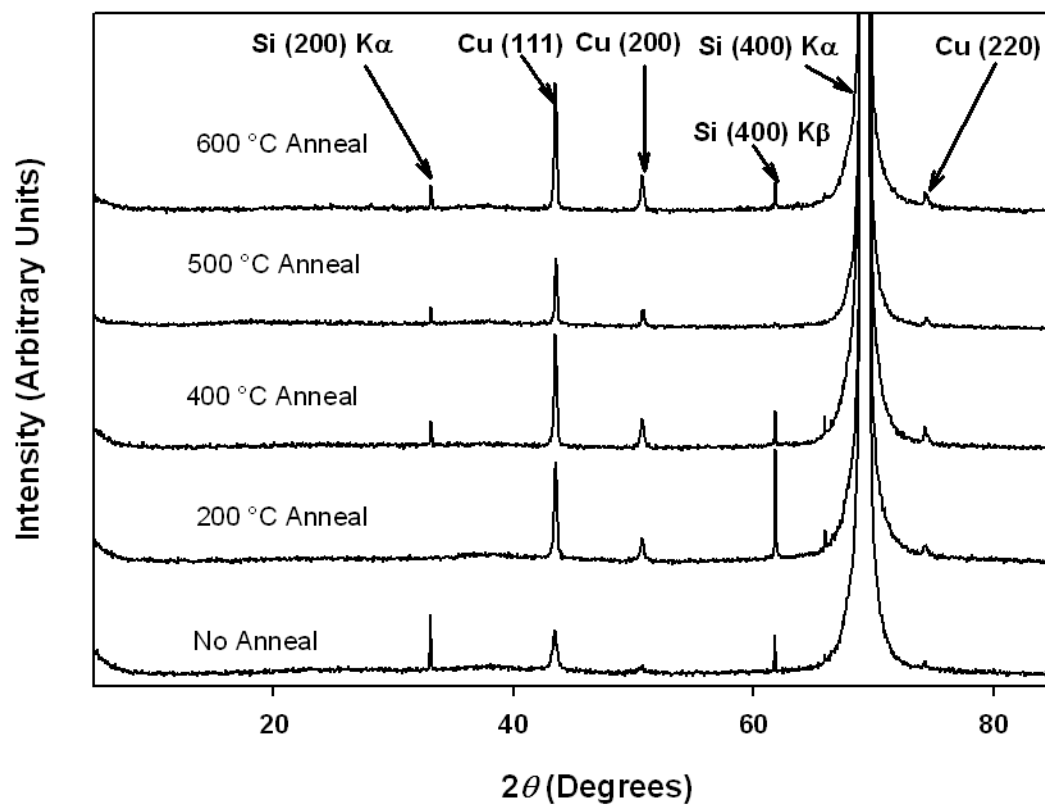


Figure 5-17. X-ray diffraction plots for Cu/WN_xC_y/Si stack (WN_xC_y films deposited from 4 at 450 °C) before annealing and after annealing at 200, 400, 500 and 600 °C

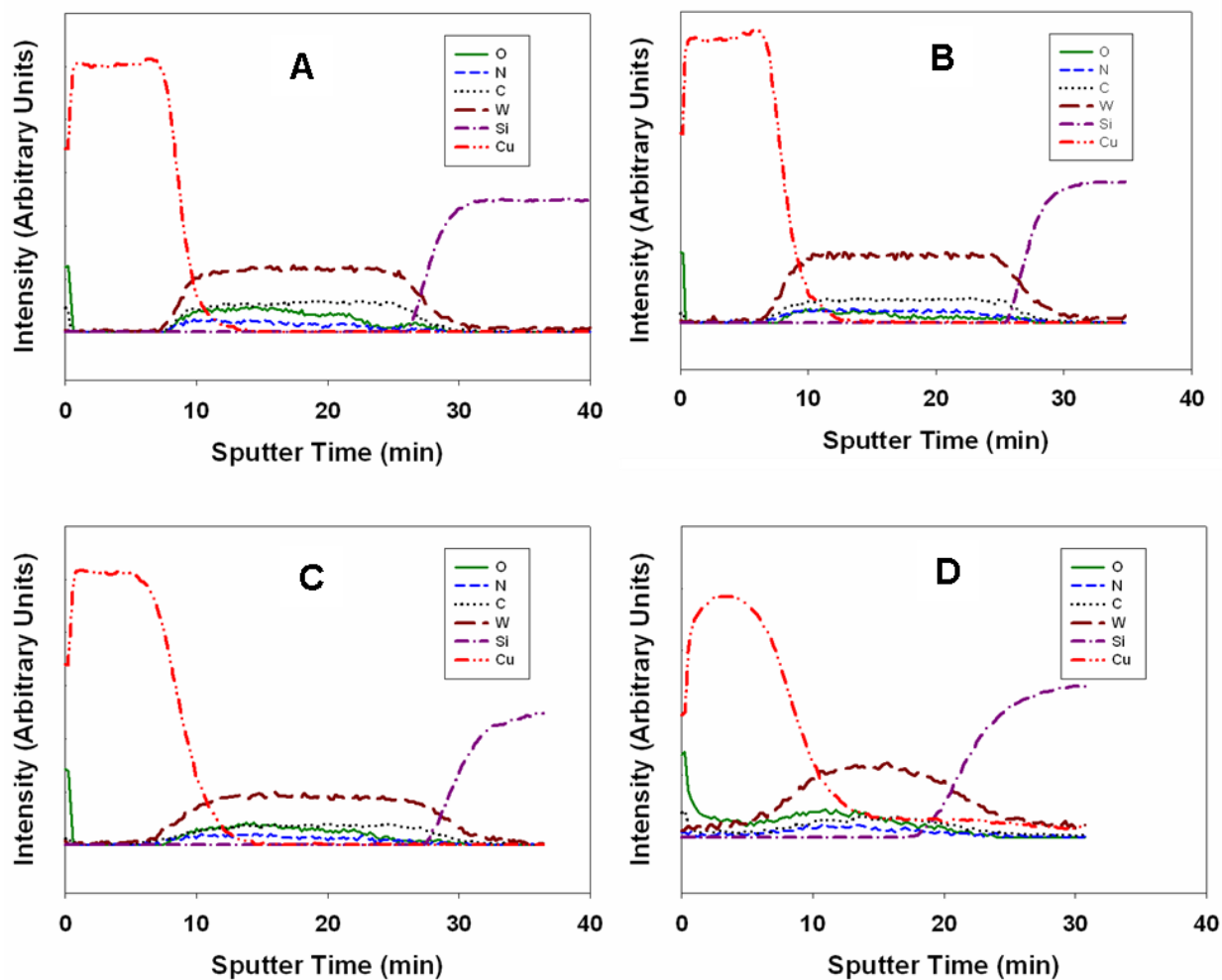


Figure 5-18. Auger electron spectroscopy depth profiles of Cu (100 nm)/ WN_xC_y (55 nm)/Si (100) stack for WN_xC_y film deposited at 500 °C (using precursor **4**) and annealed in vacuum for 30 min at A) 200 °C B) 400 °C C) 500 °C D) 600 °C.

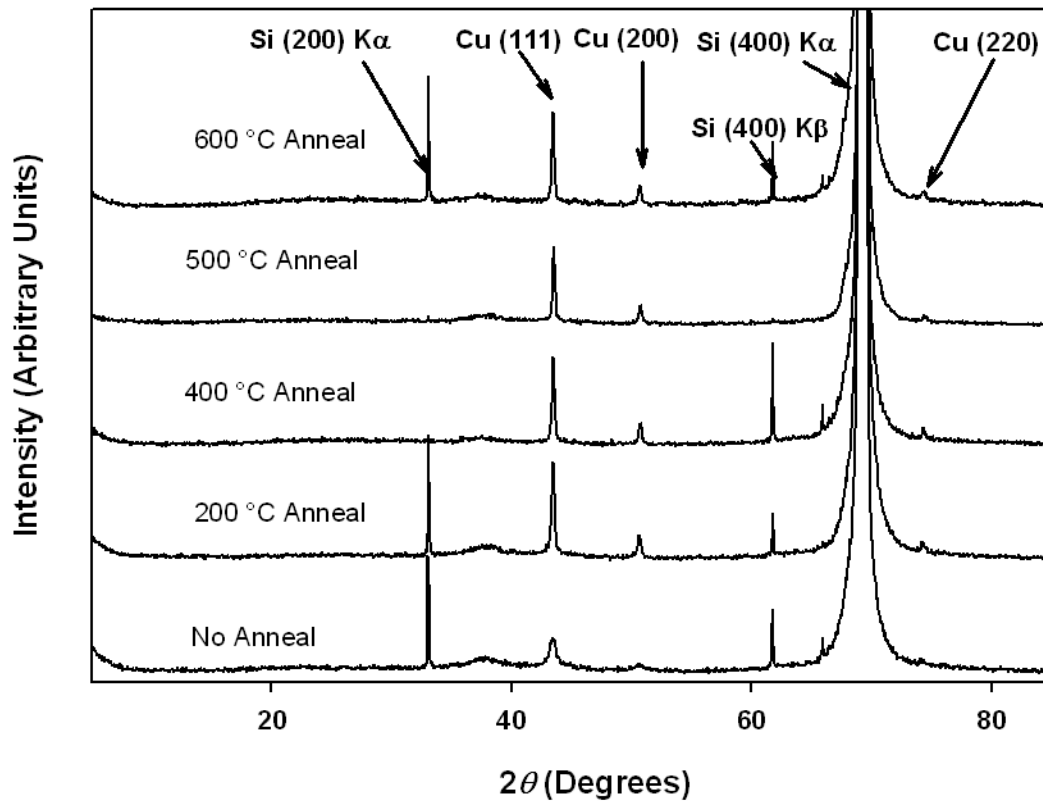


Figure 5-19. X-ray diffraction plots for Cu/WN_xC_y/Si stack (WN_xC_y films deposited with 4 at 500 °C) before annealing and after annealing at 200, 400, 500 and 600 °C

CHAPTER 6
DEPOSITION OF WN_xC_y FROM $W(N^iPr)Cl_3[iPrNC(NMe_2)N^iPr]$: EFFECT OF NH_3 CO-
REACTANT ON FILM PROPERTIES

Chapter 5 discussed the growth of WN_xC_y films from **4** and H_2 co-reactant. When **4** is used with H_2 as co-reactant, the films deposited by CVD are W rich and deficient in N. The highest N content of 12 at. % is observed for deposition from **4** at 400 °C. To increase the film N content, the effect of NH_3 co-reactant on deposition of WN_xC_y using **4** was investigated. The effect of NH_3 co-reactant on lowest deposition temperature, film crystallinity, growth rate and resistivity was also studied. Two different experiments were done, one using a mixture of NH_3 and H_2 as co-reactants (designated as 1A) and other using a mixture of NH_3 and N_2 as co-reactants (designated as 1B). Table 6-1 shows the molar flow rate of reactants for 1A and 1B. Films deposited for 1A and 1B are compared to those deposited with only H_2 as co-reactant (designated as 1C) to understand the effect of NH_3 (with or without H_2) on film properties.

6.1 Film Growth Studies

Films grown by procedures 1A and 1B were generally smooth and had a shiny metallic surface with film color varying from golden to shiny black. The lowest temperature at which appreciable film growth was observed for 1A and 1B was 300 °C. The use of NH_3 (with or without H_2) lowers the deposition temperature by 100 °C (two experimental increments). Addition of NH_3 as co-reactant lowers the energy barrier for film growth resulting in film deposition at lower temperature.

6.2 Film Composition

Figure 6-1 shows AES results for 1A, 1B and 1C. For films deposited with co-reactants $NH_3 + H_2$ (procedure 1A), the W content varies between 51 and 59 at. % between 300 and 650 °C. The N content in the film is relatively constant at ca. 18 at. % between 300 and 400 °C with the highest value of 21 at. % observed for deposition at 450 °C. Between 450 and 750 °C, the N

content gradually decreases from 21 at. % to 10 at. %. The sources of N in the film are **4**, NH₃ and benzonitrile. The decrease in N content with increase in deposition temperature could result from cleavage of N containing ligands from the precursor, lower incorporation of N from NH₃ and benzonitrile or volatilization of N from the film at higher deposition temperature.

Volatilization of N from WN_xC_y films has been reported to occur at 700 °C,⁸⁹ hence the decrease in N content between 450 and 700 °C is due to decrease in N incorporation from precursor and/or NH₃. The C content of the film monotonically increases from 11 at. % at 350 °C to 43 at. % at 750 °C deposition temperature. The increased C content of the film is due to incorporation of C from the precursor and/or benzonitrile into the film. The O content of the film decreases from 17 at. % at 350 °C to 4 at. % at 500 °C and remains constant at ca. 4 at. % between 500 and 750 °C. Oxygen can be incorporated into the film during growth or post-growth. The sources of O during film growth are residual gases (oxygen and water vapor) in the reactor and O impurity in the precursor (usually in the ppm levels). Oxygen can also be incorporated into the film due to post-growth exposure to air. The XPS results (*vide infra*) show that O in the film is incorporated both during growth and post-growth. The O incorporated during film growth forms WO_x (2 < x < 2.5)/WO₃ whereas the O incorporated due to post-growth exposure to air is incorporated in the WN_xC_y lattice.

For films deposited with only NH₃ co-reactant (procedure 1B), the W and O content of film decreases and N and C content of film increases between 300 and 500 °C. Between 500 and 750 °C, the W and O content of the film remains relatively unchanged at ca. 39 at. % and 3 at. % respectively, the N content of film decreases from 30 at. % to 15 at. % and the C content of the film increases from 30 to 49 at. %. This observation suggests that at 500 °C deposition temperature, there is a major change in mechanism of reaction for 1B. Deposition temperature

higher than 500 °C triggers decrease in N content possibly due to cleavage of N containing ligand(s) in the precursor or lower N incorporation from NH₃.

Comparison of composition of films deposited for 1A, 1B and 1C shows that the most prominent effect of using NH₃ as co-reactant (with or without H₂) is the significant increase in film N content throughout the deposition temperature range. In general, the film N content shows a twofold increase for 1A and a threefold increase for 1B as compared to 1C. While previous studies on **2a,b** and **3a,b** have shown an increase in film N content when NH₃ + H₂ is used as co-reactant, the work on precursor **4** shows that the film N content can be further increased by using only NH₃ as co-reactant.

6.3 Film Crystallinity

Figure 6-2 shows the XRD patterns for films deposited for 1A between 300 and 750 °C. The XRD spectra for films deposited between 300 and 450 °C show no peaks attributable to the film, but only peaks associated with the substrate (Si(200) K α , Si(400) K β , and Si(400) K α reflections at 33.10, 61.75 and 69.20° 2 θ , respectively). The absence of other peaks in these two spectra suggests that films deposited for 1A below 500 °C are X-ray amorphous. The XRD pattern for the film deposited at 500 °C shows the emergence of crystallinity as evidenced by the two broad peaks at 37.26 and 43.69°. These peaks lie between the standard peak position of β -W₂N [37.74 2 θ for (111) phase and 43.85 ° 2 θ for (200) phase and β -W₂C [36.98 2 θ for (111) phase and 42.89 ° 2 θ for (200) phase¹⁷⁸, indicating the presence of either the solid solution β -WN_xC_y or a physical mixture of β -W₂N and β -W₂C. Since the intensity of the most intense reflection (111) is small, the other peaks corresponding to (220) and (311) reflections at 63.55 and 75.05° are not clearly visible in the XRD spectra. Figure 6-3 shows the XRD patterns for films deposited for 1B between 300 and 750 °C. The XRD spectra for 1B show no peaks

attributable to the film, but only peaks associated with the Si substrate suggesting that films deposited are X-ray amorphous throughout the deposition temperature range.

The comparison of films deposited for 1A, 1B and 1C shows that the films are amorphous for deposition below 500 °C irrespective of the co-reactant used. But at and above 500 °C, 1A and 1C result in formation of polycrystalline phases while 1B films are amorphous. This suggests that when H₂ is used as co-reactant for 1A and 1C, the reaction mechanism at temperature above 450 °C encourages the formation of crystallites, resulting in formation of polycrystalline thin films. When only NH₃ is used as co-reactant for 1B, the reaction mechanism hinders the formation of crystallites resulting in deposition of amorphous films throughout the deposition temperature range.

6.4 Lattice Parameter

Figure 6-4 shows the change in lattice parameter with deposition temperature for 1A and 1C. The (111) peak of β -WN_xC_y has the highest intensity and thus was used for calculating the lattice parameter. For 1A, the lattice parameter is 4.17 Å for deposition at 500 °C, which is between the literature value of lattice parameter for β -W₂N (4.126 Å) and β -W₂C (4.236 Å). As the deposition temperature is increased from 500 to 550 °C, the lattice parameter decreases to 4.15 Å. Since the lattice mismatch between β -W₂N and β -W₂C is only 2.7 %, it is possible that W, N and C form a solid solution. For a WN_xC_y solid solution, an increase in interstitial concentration (C, N and/or O) in the non-metal sublattice would result in an increase in lattice parameter while an increase in vacancy concentration in the non-metal sublattice would result in a decrease in lattice parameter. Transition metal nitrides and carbides are known to have appreciable vacancy concentration on both non-metal and metal sublattices.³⁹ Since the (C+N+O)/W ratio remains unchanged between 500 and 550 °C, the decrease in lattice parameter suggests an increase in vacancy concentration for deposition at 550 °C. Between 550 and 700

°C, the lattice parameter gradually increases from 4.15 to 4.19 Å. In the same temperature range, the (C+N+O)/W ratio increases primarily because of an increase in C content while the N and O content of the film decreases. The additional C can be incorporated into the W sublattice in carbidic form or outside the W sublattice in amorphous form. The increase in lattice parameter between 550 and 700 °C suggests that there is a net increase in the amount of C present in the W sublattice as the temperature is increased from 550 to 700 °C. As the deposition temperature is increased from 700 to 750 °C, the lattice parameter decreases from 4.19 to 4.15 Å even though the C content of the film increases suggesting either a net decrease in amount of C present in W sublattice because of phase separation of C to form graphitic/ diamond-like C (*vide infra*) or an increase in vacancy concentration.

Comparison of films deposited with procedures 1A and 1C shows that for films grown at 500 °C, 1A results in a higher lattice parameter than 1C because of the higher (C+N+O)/W ratio. For deposition between 550 and 650 °C, 1A results in a higher lattice parameter than 1C even though the (C+N+O)/W ratio for 1A is smaller than that by procedure 1C indicating that films deposited for 1C have a higher vacancy concentration in that temperature range. For deposition between 700 and 750 °C, 1C affords a lower lattice parameter than 1A because 1C results in phase separation of α -W₂C causing a decrease in C content in the W sublattice of WN_xC_y phase.

6.5 Grain Size

For polycrystalline materials, the XRD peak broadening could be due to crystallite size distribution, instrumental broadening or uniform strain in the film. Line profile analysis can be used to deconvolute the effect of crystallite size distribution from the effect of uniform strain on XRD peak broadening. Line profile analysis of XRD spectra for 1A indicated that the peak broadening was primarily due to crystallite size distribution and the effect of uniform strain on peak broadening was negligible. If the XRD peak broadening is entirely due to crystallite size

distribution, Scherrer's equation can be used to calculate the average crystallite size. Since the (111) reflection was most intense, it was used to determine FWHM and estimate grain size for 1A and 1C. Figure 6-5 shows the average crystallite size for 1A and 1C using Scherrer's equation. For 1A, the average grain size is approx. 48 Å for deposition between 500 and 650 °C. Average grain size increases slightly to 55 Å for deposition at 700 °C and drops again to 50 Å for deposition at 750 °C. Overall, the average grain size measurement indicates that the films deposited by 1A at and above 500 °C are nanocrystalline and the effect of deposition temperature on average grain size is minimal. Comparison of films deposited using 1A and 1C shows that films deposited for 1A have a larger average grain size than those deposited for 1C over the entire deposition temperature range.

6.6 Film Growth Rate

The growth rate for 1A and 1B was calculated from film thickness measurement using X-SEM. Figures 6-6 and 6-7 show X-SEM images for films grown at different deposition temperature for 1A and 1B respectively. For 1A, the growth rate varied from 3 to 14 Å/min between 300 and 750 °C. Figure 6-8 shows the Arrhenius plot for films grown for 1A, 1B and 1C. For films grown between 300 and 550 °C by 1A, the growth rate increases logarithmically with inverse of temperature, indicating that the growth is in the kinetic controlled growth regime and surface reaction is the rate limiting step. As discussed earlier, the slope of an Arrhenius plot can be used to calculate the value of E_a . For 1A, the apparent activation energy is 0.45 eV. Between 550 and 750 °C, the Arrhenius plot for 1A shows a small negative slope. Growth for 1A between 550 and 750 °C is in the diffusion limited growth regime and the negative slope is probably because of homogenous gas phase decomposition of the precursor, which leads to decrease in growth rate with increase in deposition temperature. For 1B, the Arrhenius plot shows that film growth between 300 and 400 °C is in the kinetically controlled growth regime

and the apparent activation energy for film growth is 0.27 eV. Between 400 and 750 °C, the film growth rate for 1B is almost constant indicating that the growth is in the diffusion limited growth regime.

Comparison of film growth for 1A, 1B and 1C shows that the rates of films growth by 1C have the highest value for E_a of 0.54 eV while the growth for 1A has the lowest value of E_a of 0.27 eV. While the E_a value for 1B is higher than 1A, the growth rate for 1B is significantly higher than that for 1A suggesting that the addition of H_2 to NH_3 significantly increases the film growth rate. Overall, the selection of co-reactant(s) has a significant impact on the film growth rate and the lowest deposition temperature for precursor **4**. The temperature at which the growth mechanism changes from kinetically controlled to diffusion limited is also different for 1A, 1B and 1C because of difference in mechanisms of film growth and the changes in hydrodynamic properties for different co-reactant mixtures.

6.7 Atomic Bonding

Figure 6-9 shows the results of XPS peak deconvolution and Tables 6-2 and 6-3 show the peak fit parameters obtained from deconvolution for films deposited by 1A. The reference peaks for elemental C, elemental W and different compounds of W, N, C and O are listed in Table 3-7 (Chapter 3). The deconvolution of W $4f_{7/2}$ and $4f_{5/3}$ peaks was done by using the peak separation between the $4f_{7/2}$ and $4f_{5/2}$ peaks of 2.1 eV and peak area ratio $4f_{7/2}: 4f_{5/2}$ of 4:3. The deconvolution of W 4f and 4p peaks for film deposited by 1A at 300 °C indicates the presence of three different bonding states of W. The first W $4f_{7/2}$ peak at 32.1 eV lies between the reference W peaks of W_2N (~33.0 eV) and W_2C (~ 31.5 eV), indicating that the W atom is bonded to both C and N. The second $4f_{7/2}$ peak at 33.7 eV lies between the WO_2 peak at 32.9 eV and W_2O_5 peak at 34.6 eV, suggesting that the phase of tungsten oxide is WO_x ($2 < x < 2.5$). The third W $4f_{7/2}$ peak at 35.7 eV corresponds to W present in WO_3 . As the deposition temperature is increased

from 300 to 400 °C, the W peak corresponding to WN_xC_y increases whereas the intensity of W peak corresponding to WO_x and WO_3 decreases, which is consistent with the AES results that shows a decrease in O content of the film in the same deposition temperature range. For deposition at 500 °C and above for 1A, the W peaks can be deconvoluted into only WN_xC_y and WO_x peaks and there is no evidence of the presence of WO_3 . Comparison of W peaks for 1A and 1C shows that while 1C shows evidence of WO_3 throughout the deposition temperature range, 1A shows the presence of WO_3 only below 500 °C suggesting that use of NH_3 as co-reactant suppresses the formation of WO_3 phase.

The N peak for 1A at 300 °C can be deconvoluted into two peaks. The first N 1s peak at 397.7 eV corresponds well with the reference N 1s peak for WN_x film.¹¹⁹ The second peak at 399.9 eV suggests that N is also present as amorphous N.¹¹⁹ Between 300 and 700 °C, the N peak can be similarly deconvoluted into a dominant peak around 397.5 eV and a broad shallow peak around 399.5 eV implying that the bulk of the N is bonded to W and a small amount of N is present in amorphous phase.

Between 300 and 500 °C, the C 1s peak for 1A can be deconvoluted into two peaks around 283.6 eV and 285.4 eV. The former peak corresponds to C bonded to W (reference peak at 283.5 eV) and the latter peak reflect C present as amorphous carbon (reference peak between 284.5 and 285.2 eV). For deposition at 600 and 700 °C, the C 1s spectra can be deconvoluted into three distinct peaks at 283.5 eV, 284.5 and 285.8 eV. The first peak corresponds to carbidic carbon bonded to W. The second and third peaks at 284.5 and 285.5 eV reflect the presence of graphitic carbon (sp^2 bonded C) and diamond-like C (sp^3 bonded C) respectively. Previous reports have indicated that the XPS peaks for graphitic C and diamond-like C appear at ca. 284.5 eV and ca. 285.3 eV respectively.^{192,193} The presence of graphitic and diamond-like C for films

deposited at 600 and 700 °C shows that C separates from the WN_xC_y phase as has been reported previously for 1C. While films deposited by 1C show evidence of phase separation of C to form graphitic and diamond-like C only at 700 °C, films deposited for 1A and 1B show the initiation of similar process at 600 °C suggesting that the use of NH_3 co-reactant (with or without H_2) lowers the initiation temperature for C phase separation.

The O 1s peak for deposition between 300 and 700 °C can be deconvoluted into two peaks at ca. 530.7 and ca. 532.0 eV. The peak at 530.7 eV corresponds to O bonded as WO_x or WO_3 . The other peak at 532.0 eV corresponds to O present in WN_xC_y . As discussed Chapter 6, O could be incorporated into the film either during film growth because of oxygen and water vapor impurity in the reactor or after the film growth because of exposure to atmosphere. The presence of WO_x/WO_3 phase suggests that residual gas in reactor and/or O impurity in the precursor react(s) with the precursor to form WO_x/WO_3 during the film growth. The source of O bound to W in WN_xC_y is most likely atmospheric O that diffuses through the film when the film is exposed to atmosphere. In summary, deconvolution of the O 1s peak suggests that O is incorporated in the film during growth as WO_x/WO_3 and post growth as O loosely bound to W in WN_xC_y .

XPS results for 1A show that films deposited between 300 and 400 °C are WN_xC_y with significant amount of WO_x and WO_3 along with small amounts of amorphous N and C. For deposition between 400 and 500 °C, the bulk of the film is WN_xC_y with a small amount of WO_x and increased amounts of amorphous C and N. The film deposited at 600 and 700 °C consists of WN_xC_y , a small amount of WO_x along with graphitic and diamond-like C.

XPS measurements for 1B (Figure 6-10, Tables 6-4 and 6-5) show that there is no major difference in the bonding states of W, N and O for 1A and 1B. The only major difference is seen

for the bonding state of C, especially for deposition below 500 °C. For deposition at 300, 350 and 400 °C, the C 1s peak for 1A shows that C is present in both carbidic and amorphous phases, whereas the C 1s peak for 1B shows that C is present in only carbidic form. For 1B, the broad amorphous C peak at 284.8 eV appears only at 500 °C deposition temperature. This observation suggests that the use of only NH₃ as co-reactant favors the deposition of carbidic C, particularly at low deposition temperatures.

6.8 Film Resistivity

Figure 6-11 shows the variation of film resistivity with deposition temperature for films grown using procedures 1A, 1B and 1C. For 1A at 300 °C, the resistivity is 4182 μΩ-cm. As the deposition temperature is increased from 300 to 600 °C, the film resistivity gradually increases to 8395 μΩ-cm possibly due to increase in C content of the film. Film resistivity peaks for deposition at 650 °C and decreases thereafter. Deposition for 1B shows that low resistivity (393 μΩ-cm) films are deposited at 300 °C. For growth between 350 and 400 °C, there is a sharp increase in film resistivity because of the decrease in W content of the film. Between 400 and 550 °C resistivity increases due to the increase in C and N content of the film. Above 500 °C, resistivity decreases for 1B because of a decrease in N content of the film.

Comparison of film resistivity for 1A, 1B and 1C shows that the co-reactant used for deposition of WN_xC_y from **4** can have a significant effect on resistivity. When either only H₂ or only NH₃ are used as co-reactants, low resistivity films are deposited at low deposition temperature. However, when both H₂ and NH₃ are used together for deposition, high resistivity films are deposited throughout the deposition temperature range. A number of factors could affect the film resistivity including metal to non-metal ratio, crystallinity, grain size, density and bonding state of non-metals; the choice of co-reactants affect each of these factors due to different reaction mechanisms for each co-reactant mixture.

6.9 Diffusion Barrier Testing

To determine the effectiveness of diffusion barrier film deposited by procedures 1A and 1B, barrier films deposited at 300, 350 and 400 °C were coated with 100 nm PVD Cu. Prior to the deposition of Cu thin film, the barrier film was exposed to atmosphere for approximately 1-2 hour(s). The Cu/barrier/Si stack was annealed in vacuum at 500 °C for 30 min. After annealing, three-point AES depth profile and XRD measurements were done to detect copper diffusion through the barrier film.

6.9.1 Barrier Testing for 1A

Figure 6-12 shows the depth profile of pre- and post-anneal Cu/WN_xC_y (1A)/Si stacks for WN_xC_y films deposited at 300, 350 and 400 °C. The thickness of the film deposited at 300, 350 and 400 °C was 37, 75 and 75 nm respectively. For deposition at 300 °C, the pre-anneal depth profile (Figure 6-12 A) indicates that the copper has already penetrated through the barrier into the Si substrate. This is an artifact resulting from the ‘knock-on’ effect of sputtering (*vide supra*). The post-anneal profile (Figure 6-12 B) for deposition at 300 °C shows that the Cu has penetrated deeper into the barrier film, indicating that the barrier film was unable to prevent Cu diffusion. For deposition at 350 °C, the comparison of pre- and post-anneal depth profile (Figure 6-12 C and D) shows that copper diffuses through the barrier film after annealing. For deposition at 400 °C, the pre-anneal depth profile shows sharp interfaces between Cu/ barrier and barrier/Si. After annealing at 500 °C for 30 min, Cu has further penetrated into the barrier but not completely, indicating that 75 nm WN_xC_y film (1A) was able to prevent Cu diffusion through the barrier film after vacuum annealing at 500 °C. Intermixing is seen in the depth profile for both Cu/ barrier interface and the barrier/ Si interface.

A number of factors could influence the diffusion barrier performance of WN_xC_y including film density and composition. For 1A, the film composition is relatively constant for deposition

at 300, 350 and 400 °C. To determine the density of the films for different deposition temperature, an indirect method is the comparison of their relative sputter rate. For films with similar composition, denser films would have a lower sputter rate as compared to less dense films and vice versa. Table 6-6 shows the sputter rate for the barrier film deposited by procedure 1A at 300, 350 and 400 °C. Comparison of the relative sputter rate for 1A shows that film deposited at 300 and 350 °C have a higher sputter rate and hence lower density as compared to film deposited at 400 °C. So, the better diffusion barrier performance of film deposited at 400 °C is primarily because of higher film density.

Figure 6-13 shows the pre- and post-anneal XRD measurements for films deposited by procedure 1A. For 300 °C, the pre-anneal depth profile shows five peaks at 43.50, 50.70, 61.75, 69.30 and 74.60 2- θ degrees. The peaks at 43.50, 50.70 and 69.30 degrees correspond to Cu(111), Cu(220) and Cu(220) phases whereas the peaks at 61.75 and 69.30 degrees corresponds to Si(400) $k\alpha$ and Si(400) $k\beta$ respectively. The XRD profile also indicates that PVD copper deposition on WN_xC_y shows a preferential orientation of (111). This is highly desirable because the Cu(111) phase has a better electromigration resistance as compared to other crystalline phases. The post anneal XRD profile shows an increase in the intensity of peaks corresponding to copper suggesting grain growth of Cu crystallites due to annealing. No peaks corresponding to Cu_3Si are observed in the post-anneal XRD profile even though the AES depth profile shows that copper has diffused through the barrier film. This apparent contradiction is due to the poor sensitivity of XRD in detecting small amount of Cu_3Si crystallites. The pre- and post-anneal XRD spectra for barrier film deposited for 1A at 350 and 400 °C show results similar to those of film deposited at 300 °C. No evidence of Cu_3Si is seen in post-anneal XRD spectra for barrier

film deposited at 350 and 400 °C suggesting that no bulk diffusion of Cu has occurred after annealing.

6.9.2 Barrier Testing for 1B

Figure 6-14 shows the depth profile for pre- and post-anneal Cu/WN_xC_y/Si stacks for WN_xC_y films deposited by procedures 1B at 300, 350 and 400 °C. The thickness of WN_xC_y film from deposition at 300, 350 and 400 °C was 12, 23 and 45 nm respectively. Since the films deposited by 1B are much thinner than those deposited by 1A, the ‘knock-on’ effect of sputtering was anticipated to be worse. Etching off the Cu layer prior to AES depth profiling can eliminate the artifact arising from the ‘knock-on’ effect. The Cu layer was etched-off using 50 % HNO₃ solution before AES depth profiling. For deposition by procedure 1B at 300 °C, the post-anneal profile shows that Cu has diffused through the barrier layer into the Si. Comparison of the barrier/ Si interfaces for the pre- and post-anneal depth profiles shows no evidence of intermixing at this interface. For deposition at 350 °C, a trace amount of copper can be seen in the post-anneal depth profile indicating that the barrier film was not effective in preventing copper diffusion. For deposition at 400 °C, the post-anneal AES depth profile shows that there is no copper diffusion through the barrier film suggesting that the barrier film was able to prevent Cu diffusion after annealing at 500 °C. No intermixing at the barrier/ Si interface is observed. Overall, for both 1A and 1B films, barrier films deposited at 300 °C are not able to prevent Cu diffusion whereas barrier films deposited at 400 °C are able to prevent Cu diffusion after annealing at 500 °C. To identify the factor(s) that make film deposited at 400 °C effective as diffusion barriers, the sputter rate of films deposited at 300, 350 and 400 °C by procedure 1B was calculated from the AES depth profile as discussed above (Table 6-6). The sputter rate for films deposited by 1B is expected to be higher than that for films deposited for 1A because of lower W content in the films deposited for 1B. Unlike films deposited for 1A, films deposited

for 1B show variation in W content for deposition at 300, 350 and 400 °C, hence the sputter rates for these films cannot be directly correlated to film density because film composition influences sputter rates. As expected, the sputter rate for film deposited at 400 °C is lower than that for film deposited at 300 and 350 °C because of the higher non-metal (N+C+O) to W ratio for film deposited at 400 °C. Hence, no conclusive evidence of effect of density on diffusion barrier performance could be obtained from sputter rates for films deposited for 1B. Another important factor that influences diffusion barrier performance is the film composition. Film deposited at 400 °C has significantly higher N content as compared to films deposited at 300 and 350 °C. One of the reasons for the better diffusion barrier performance of film deposited at 400 °C for 1B could be its higher N content.

Figure 6-15 shows the pre- and post-anneal XRD measurements for barrier films deposited by procedure 1B. Similar to Figure 6-13 for 1A, Figure 6-15 for 1B shows no evidence of copper diffusion for films deposited at 300, 350 and 400 °C. The only peaks observed correspond to copper and Si, suggesting that no bulk diffusion of copper has occurred through the barrier film after annealing. Similar to films deposited by 1A, films deposited by 1B also show preferential deposition of Cu(111) phase when copper is deposited by PVD.

6-10 Film Conformality

As discussed in Chapter 2, the conformality of barrier film is of utmost importance for deposition in high aspect ratio features. Since the film deposited by procedure 1B at 400 °C showed good diffusion barrier performance and high N content, conformality test was done for deposition at 400 °C with only NH₃ as co-reactant. Deposition was done on patterned chips provided by Samsung. The dielectric material in the test chip was FSG and the feature size was 0.2 μm with aspect ratio of 2:1. Figure 6-16 shows the X-SEM image of the feature after diffusion barrier deposition using **4** and only NH₃ co-reactant. The film thickness for deposition

at 400 °C on FSG dielectric is 5 nm, which is significantly lower than the 45 nm thick films deposited on Si substrate at the same deposition temperature. This implies that nucleation on FSG substrate for 1B takes longer time than on Si substrate. The film is highly conformal visually, however, a precise number for conformality could not be calculated because of the insufficient resolution of the SEM images.

6-11 Conclusions

It has been demonstrated that the mixed imido guanidinato complex $W(N^iPr)Cl_3[{}^iPrNC(NMe_2)N^iPr]$ (**4**) can be used with $NH_3 + H_2$ (procedure 1A) and $NH_3 + N_2$ (procedure 1B) to deposit WN_xC_y thin films in an aerosol assisted CVD system. The use of NH_3 lowers the minimum growth temperature for **4** by 100 °C. The use of NH_3 with or without H_2 as co-reactant has significant effect on film composition, growth rate, crystallinity, grain size and resistivity. Comparison of films deposited with procedures 1A, 1B and 1C shows that the best films in terms are deposited by 1B because of the lower resistivity of films at low deposition temperature, amorphous film deposition throughout the deposition temperature range and higher N content. Diffusion barrier testing shows that films deposited at 400 °C for both 1A and 1B are able to prevent Cu diffusion after annealing at 500 °C for 30 min in vacuum. Films deposited for 1B at 400 °C also show good conformality in a 0.2 μm 2:1 aspect ratio feature.

Table 6-1. Molar flow rates used for deposition of WN_xC_y thin film from precursor **4**.

Reactant	Molar flow rate (mol/min)	
	1A	1B
4	1.16×10^{-6}	1.16×10^{-6}
Benzonitrile	6.47×10^{-4}	6.47×10^{-4}
H ₂	4.09×10^{-2}	--
NH ₃	1.02×10^{-3}	1.02×10^{-3}
N ₂	--	4.09×10^{-2}

Table 6-2. Analysis results from deconvolution of XPS peaks of W for films deposited by procedure 1A on Si(100) substrate between 300 and 700 °C.

Deposition temperature		WN _x C _y			WO _x (2 < x < 2.5)			WO ₃		
		Peak position (eV)	% Area	FWHM (eV)	Peak position (eV)	% Area	FWHM (eV)	Peak position (eV)	% Area	FWHM (eV)
300	W4f _{7/2}	32.12	10.50%	1.51	33.71	15.20%	1.78	35.75	26.90%	2.29
	W4f _{5/2}	34.22	7.90%	1.70	35.81	11.40%	1.95	37.95	20.10%	2.23
	W4p _{3/2}	37.52	1.60%	1.52	39.11	2.30%	2.20	41.15	4.00%	2.57
350	W4f _{7/2}	31.91	18.70%	1.46	33.79	17.90%	1.99	35.61	15.60%	2.01
	W4f _{5/2}	33.91	14.00%	1.67	35.89	13.40%	2.21	37.75	11.70%	1.85
	W4p _{3/2}	37.31	2.80%	2.60	39.19	3.60%	1.72	41.01	2.30%	2.26
450	W4f _{7/2}	32.05	33.90%	1.39	33.88	14.60%	1.97	35.36	3.30%	1.51
	W4f _{5/2}	34.15	27.10%	1.68	35.98	10.90%	2.24	37.46	2.50%	1.71
	W4p _{3/2}	37.45	5.10%	2.34	39.28	2.20%	1.67	40.76	0.50%	1.53
550	W4f _{7/2}	32.00	41.40%	1.39	34.06	13.00%	1.97	--	--	--
	W4f _{5/2}	34.20	31.10%	1.56	36.06	9.10%	2.44	--	--	--
	W4p _{3/2}	37.40	4.10%	2.26	39.46	1.30%	2.49	--	--	--
650	W4f _{7/2}	31.99	32.60%	1.25	33.38	18.70%	2.05	--	--	--
	W4f _{5/2}	34.19	23.50%	1.28	35.48	15.00%	2.02	--	--	--
	W4p _{3/2}	37.39	6.50%	1.72	38.78	3.70%	1.96	--	--	--
750	W4f _{7/2}	31.98	33.10%	1.32	33.48	17.40%	1.84	--	--	--
	W4f _{5/2}	34.27	24.80%	1.48	35.58	13.90%	2.05	--	--	--
	W4p _{3/2}	37.38	8.30%	1.95	38.88	2.60%	1.50	--	--	--

Table 6-3. Analysis results from deconvolution of XPS peaks of C, N and O for films deposited by procedure 1A on Si(100) substrate between 300 and 700 °C

Deposition temperature		C 1s			N1s			O1s		
		Peak position (eV)	% Area	FWHM (eV)	Peak position (eV)	% Area	FWHM (eV)	Peak position (eV)	% Area	FWHM (eV)
300	Peak 1	283.59	58.30%	1.7	397.69	60.40%	1.64	530.9	64.00%	1.51
	Peak 2	285.35	41.70%	2.22	399.97	39.60%	2.1	531.93	36.00%	2.12
350	Peak 1	283.43	59.50%	1.21	397.79	82.90%	1.56	530.65	64.80%	1.48
	Peak 2	284.82	40.50%	1.42	399.77	17.10%	1.25	531.9	35.20%	1.71
400	Peak 1	283.54	73.30%	1.26	397.64	80.10%	1.58	530.65	64.80%	1.48
	Peak 2	285	26.70%	1.64	399.39	19.90%	2.26	531.9	35.20%	1.71
500	Peak 1	283.48	73.20%	1.36	397.68	75.60%	1.63	530.61	63.40%	1.53
	Peak 2	284.81	26.80%	1.67	399.75	24.40%	2.1	532.17	36.60%	1.98
600	Peak 1	283.43	55.50%	1.41	397.64	75.20%	1.69	530.63	62.60%	1.66
	Peak 2	284.57	28.20%	1.61	399.42	24.80%	1.95	531.98	37.40%	2.05
	Peak 3	286.19	16.30%	2.28	--	--	--	--	--	--
700	Peak 1	283.55	44.70%	1.63	397.73	79.30%	1.59	530.78	64.10%	1.62
	Peak 2	284.6	28.50%	1.73	399.04	20.70%	2.1	532.06	35.90%	1.94
	Peak 3	285.73	26.80%	2.3	--	--	--	--	--	--

Table 6-4. Analysis results from deconvolution of XPS peaks of W for films deposited by procedure 1B on Si(100) substrate between 300 and 700 °C.

Deposition temperature		WN _x C _y			WO _x (2 < x < 2.5)			WO ₃		
		Peak position (eV)	% Area	FWHM (eV)	Peak position (eV)	% Area	FWHM (eV)	Peak position (eV)	% Area	FWHM (eV)
300	W4f _{7/2}	31.82	17.40%	1.5	33.44	20.20%	2.17	35.4	14.10%	2.04
	W4f _{5/2}	33.92	13.10%	1.55	35.54	15.10%	2.17	37.55	11.30%	1.96
	W4p _{3/2}	37.22	2.60%	1.52	38.84	4.00%	1.46	40.7	2.10%	1.91
350	W4f _{7/2}	32.01	36.50%	1.59	33.71	9.40%	1.6	35.2	7.00%	1.72
	W4f _{5/2}	34.11	26.30%	1.51	35.81	7.10%	1.64	37.3	5.30%	1.88
	W4p _{3/2}	37.41	5.50%	2.19	39.11	1.90%	1.22	40.6	1.10%	2.02
400	W4f _{7/2}	31.89	38.50%	1.47	33.56	9.80%	1.95	35.5	4.30%	1.57
	W4f _{5/2}	34.04	28.90%	1.47	35.66	7.40%	1.94	37.6	3.20%	1.88
	W4p _{3/2}	37.29	5.80%	2.31	38.96	1.50%	1.15	40.9	0.60%	1.8
500	W4f _{7/2}	31.91	37.00%	1.28	33.41	15.70%	2.1	--	--	--
	W4f _{5/2}	34.11	27.70%	1.4	35.51	11.80%	1.98	--	--	--
	W4p _{3/2}	37.31	5.50%	1.68	38.81	2.40%	2.18	--	--	--
600	W4f _{7/2}	31.94	36.10%	1.29	33.39	16.50%	2.12	--	--	--
	W4f _{5/2}	34.14	27.10%	1.36	35.49	12.40%	2.01	--	--	--
	W4p _{3/2}	37.34	5.40%	1.84	38.79	2.50%	2.39	--	--	--
700	W4f _{7/2}	31.93	34.50%	1.22	33.24	18.20%	1.97	--	--	--
	W4f _{5/2}	34.13	25.80%	1.26	35.34	13.60%	1.84	--	--	--
	W4p _{3/2}	37.33	5.20%	1.81	38.64	2.70%	2.11	--	--	--

Table 6-5. Analysis results from deconvolution of XPS peaks of C, N and O for films deposited by procedure 1B on Si(100) substrate between 300 and 700 °C

Deposition temperature		C 1s			N1s			O1s		
		Peak position (eV)	% Area	FWHM (eV)	Peak position (eV)	% Area	FWHM (eV)	Peak position (eV)	% Area	FWHM (eV)
300	Peak 1	283.54	100.00%	1.53	397.55	71.50%	1.43	530.75	71.10%	1.5
	Peak 2	--	--	--	398.96	28.50%	1.96	531.97	28.90%	1.84
350	Peak 1	283.46	100.00%	1.57	397.58	83.30%	1.5	530.57	67.40%	1.48
	Peak 2	--	--	--	399.2	16.70%	1.52	531.85	32.60%	1.93
400	Peak 1	283.39	85.70%	1.55	397.5	87.20%	1.58	530.46	70.20%	1.58
	Peak 2	284.85	14.30%	1.62	399.25	12.80%	1.73	531.85	29.80%	1.96
500	Peak 1	283.32	64.60%	1.33	397.5	82.70%	1.48	530.39	64.20%	1.56
	Peak 2	284.72	35.40%	2.08	398.91	17.30%	1.58	531.64	35.80%	1.93
600	Peak 1	283.42	61.80%	1.5	397.49	69.00%	1.53	530.45	64.40%	1.54
	Peak 2	284.5	25.80%	1.77	398.99	31.00%	2	531.89	35.60%	1.81
	Peak 3	286	12.40%	1.5	--	--	--	--	--	--
700	Peak 1	283.33	45.70%	1.29	397.54	70.30%	1.39	530.33	57.50%	1.55
	Peak 2	284.42	31.40%	1.57	398.82	29.70%	1.56	531.66	42.50%	1.86
	Peak 3	285.93	23.00%	2.46	--	--	--	--	--	--

Table 6-6. Apparent sputter rate of barrier film measured by dividing barrier film thickness by the time required to sputter the film during AES depth profiling

Deposition Temperature (°C)		1A	1B
300	pre-anneal	74	80
	post-anneal	82	68
350	pre-anneal	93	74
	post-anneal	150	70
400	pre-anneal	65	94
	post-anneal	60	88

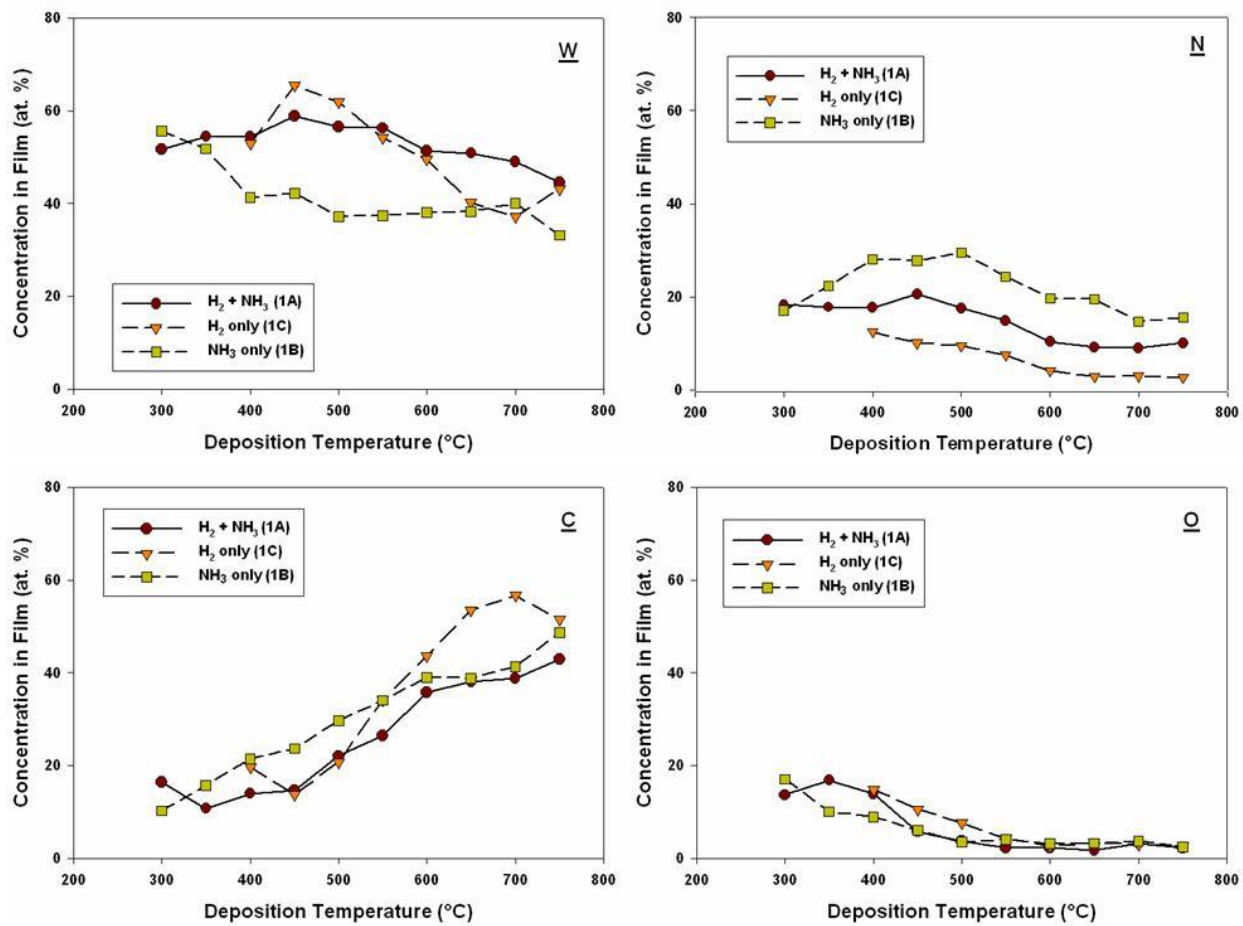


Figure 6-1. Composition of films deposited by procedures 1A, 1B and 1C on Si (100) substrate at different deposition temperature as determined by AES after 0.5 min of sputtering

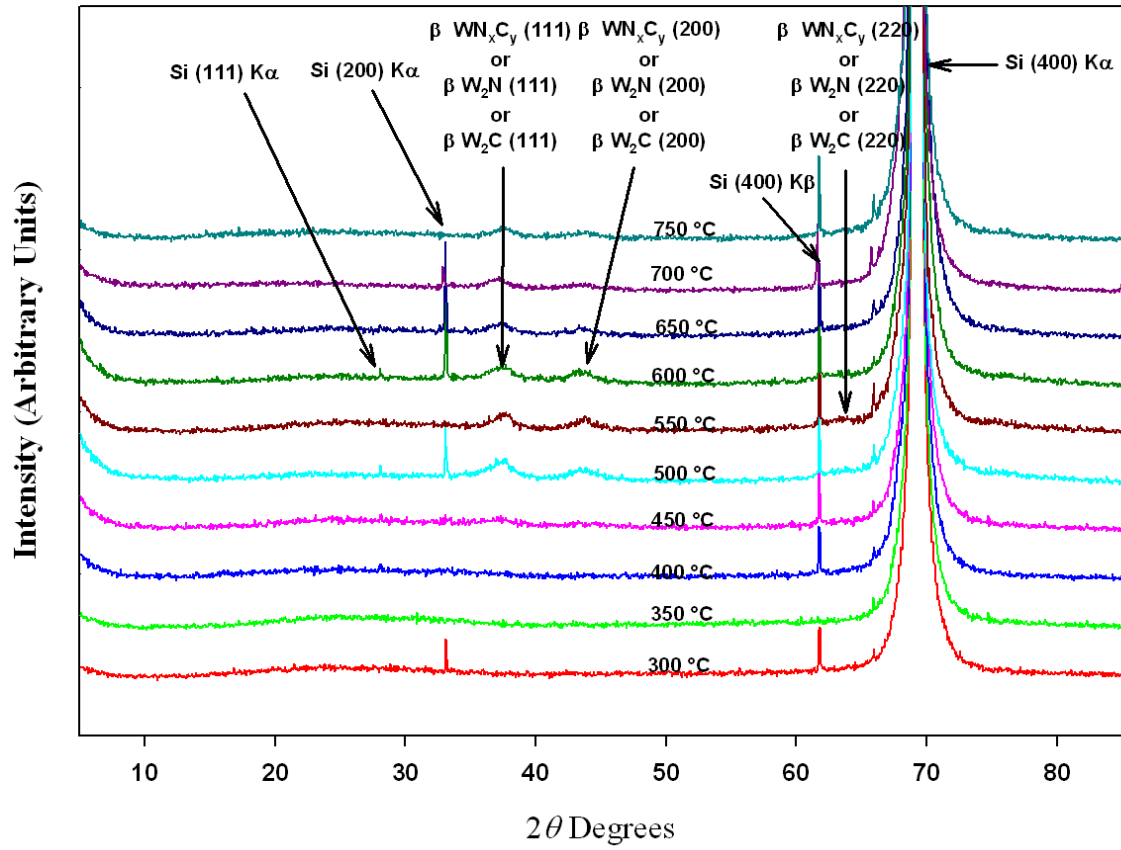


Figure 6-2. X-ray diffraction patterns for films deposited on Si (100) substrate by procedure 1A

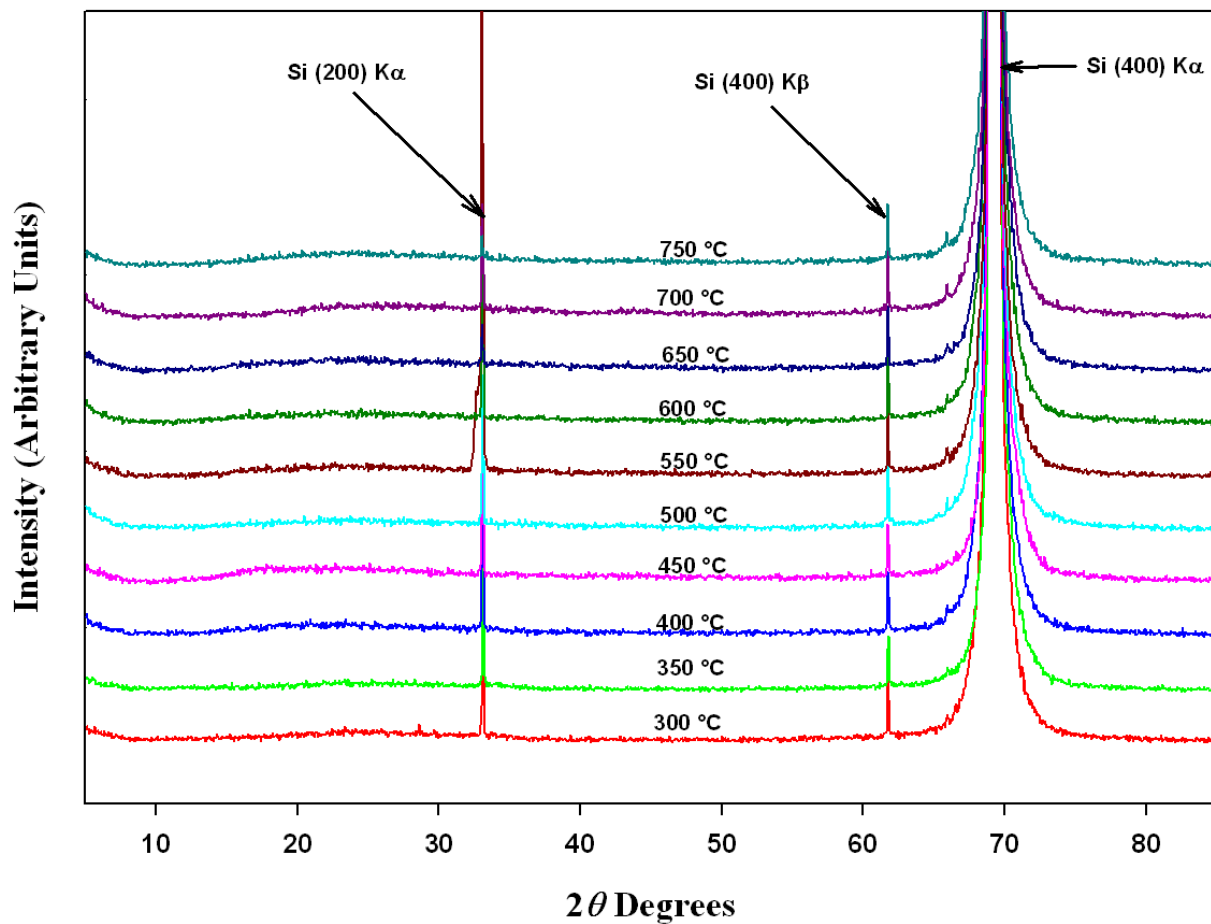


Figure 6-3. X-ray diffraction patterns for films deposited on Si (100) substrate by procedure 1B

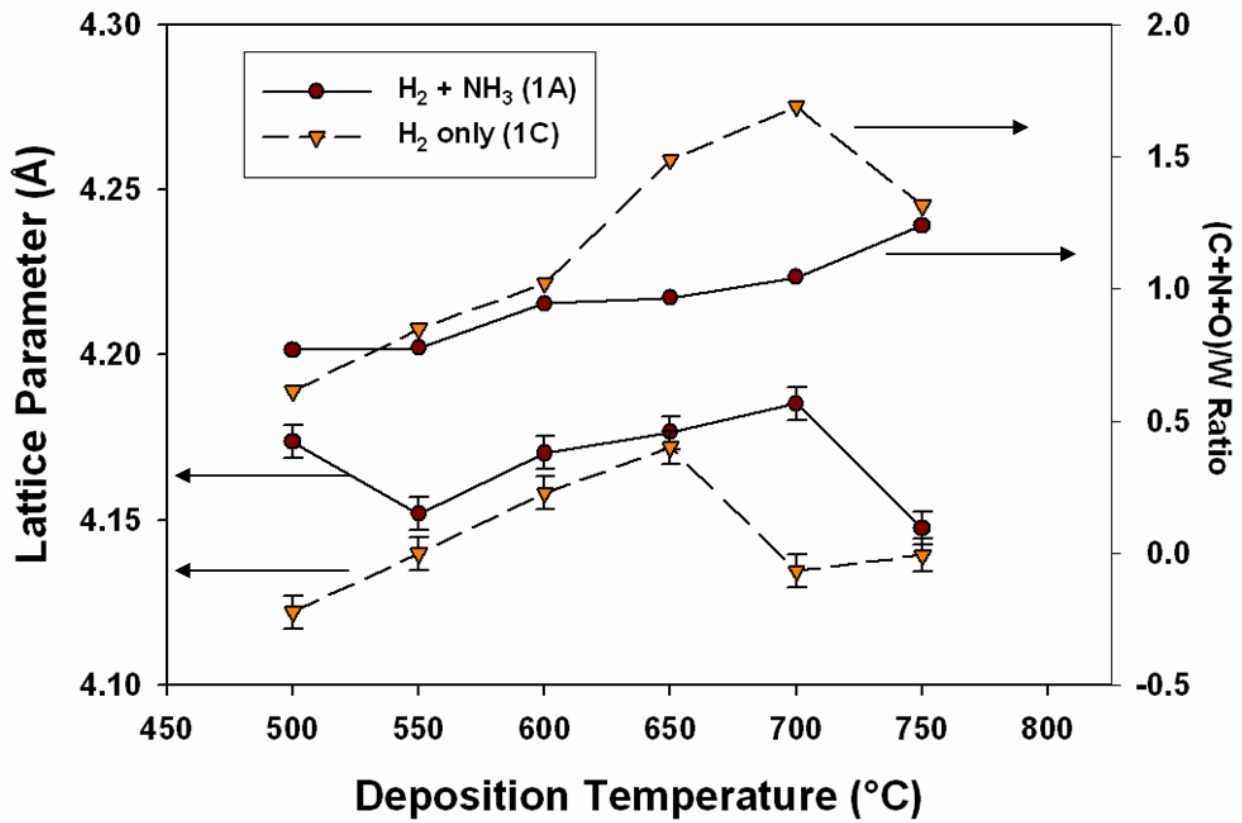


Figure 6-4. Lattice parameters for films grown by procedures 1A and 1C on Si (100) substrate. Error bars indicate uncertainty in determination of peak position for lattice parameter calculation.

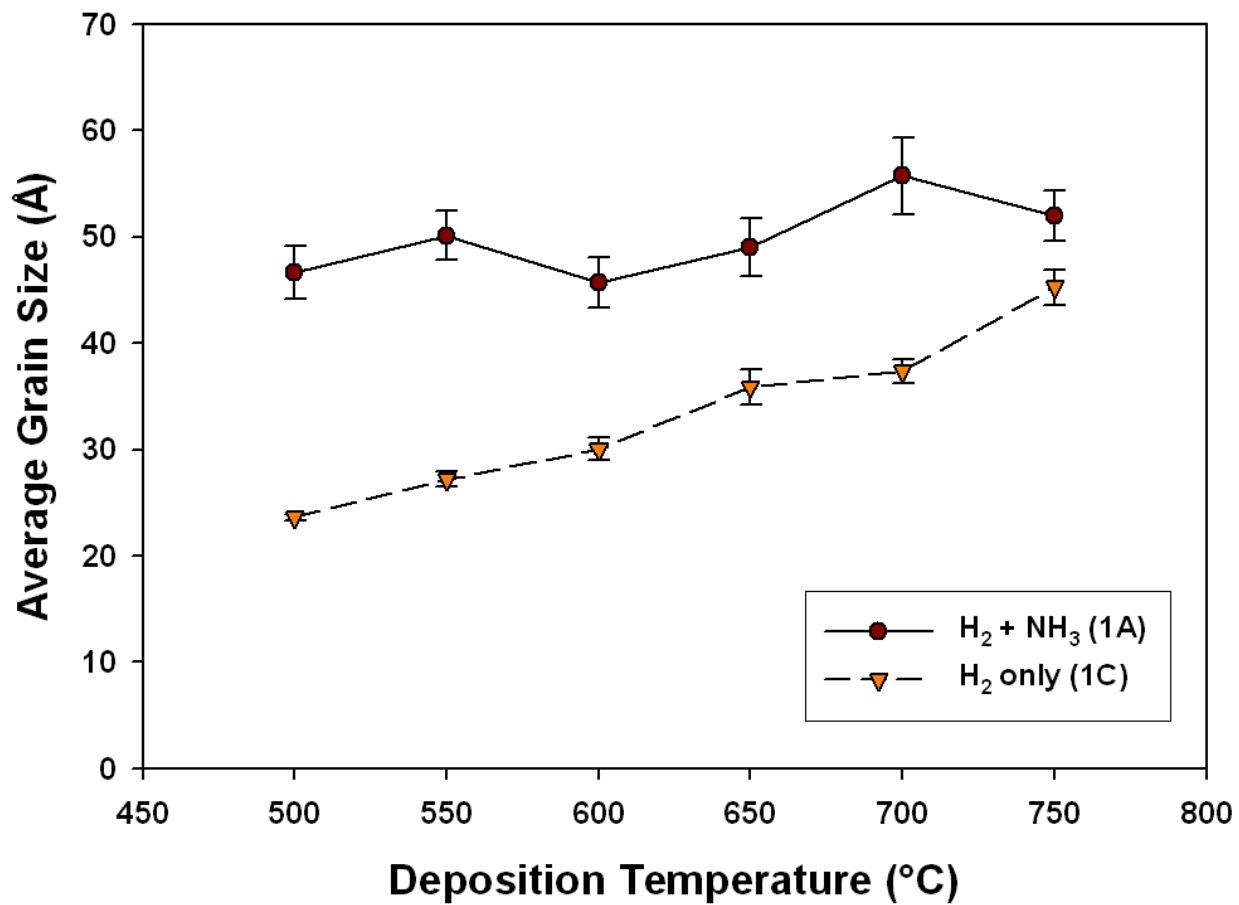


Figure 6-5. Average grain size at different deposition temperature for films grown by procedures 1A and 1B on Si (100) substrate.

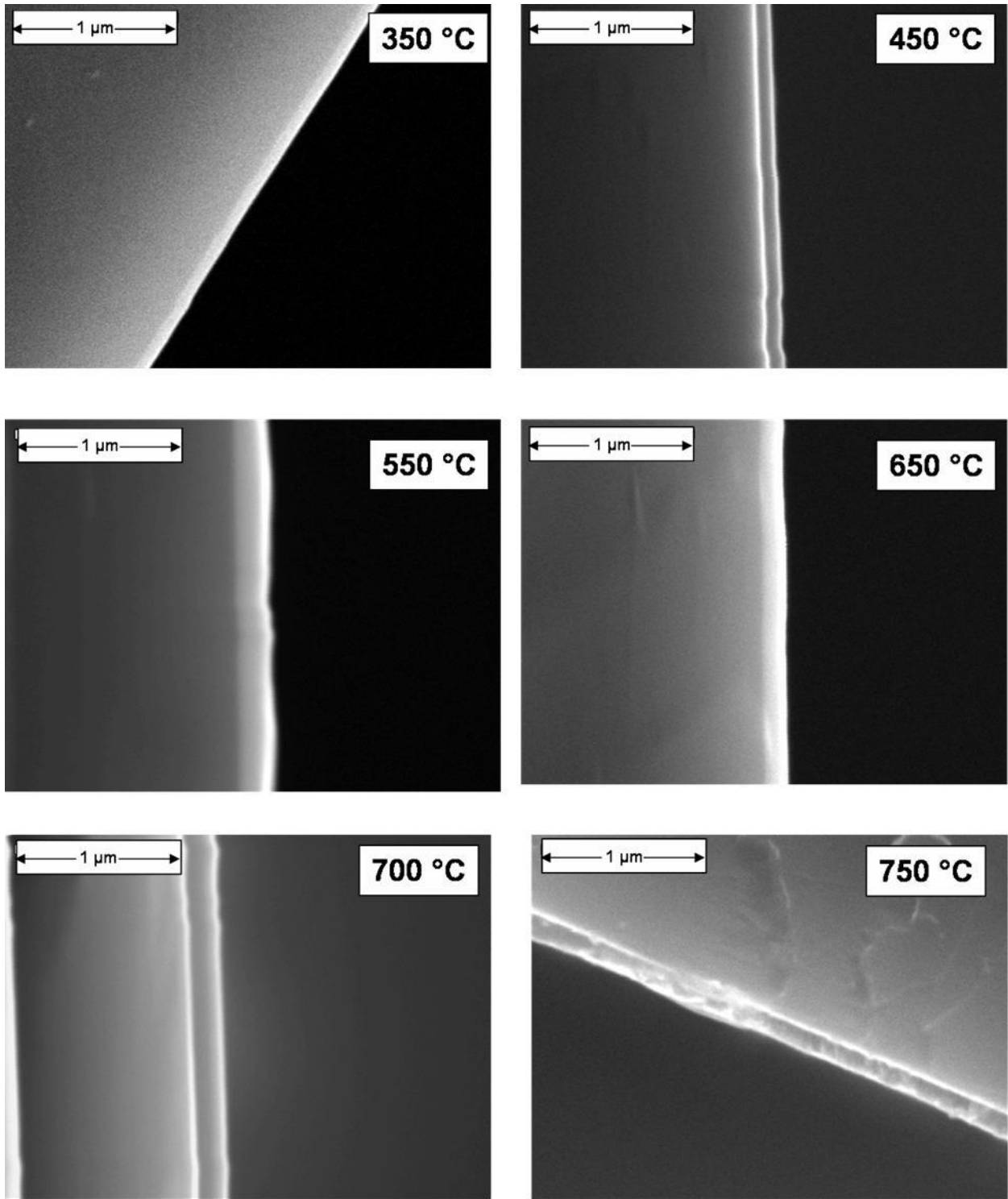


Figure 6-6. Scanning electron microscope images for films grown by procedure 1A at different deposition temperature on Si (100) substrate

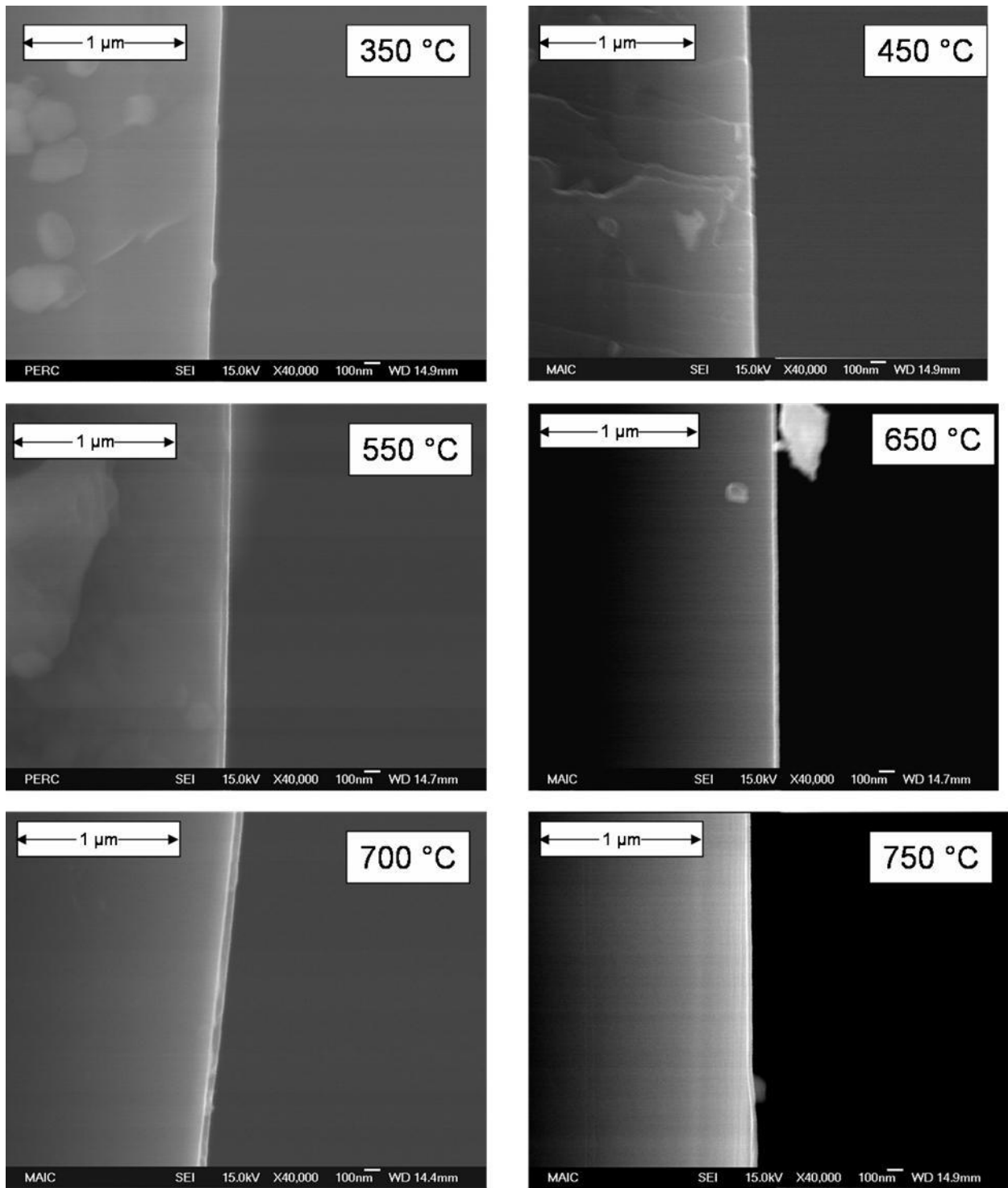


Figure 6-7. Scanning electron microscope images for films grown by procedure 1B at different deposition temperature on Si (100) substrate

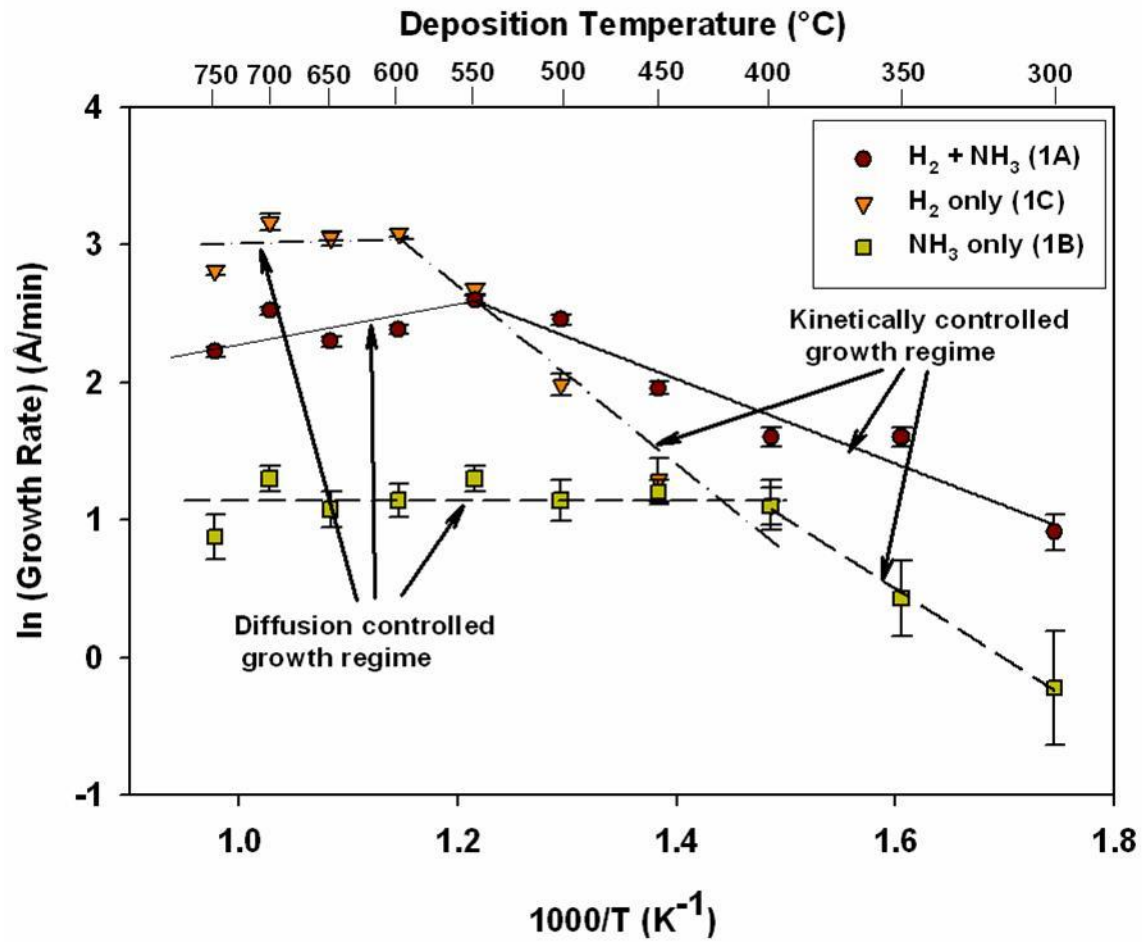


Figure 6-8. Arrhenius plot for growth using procedures 1A, 1B and 1C for growth on a Si(100) substrate

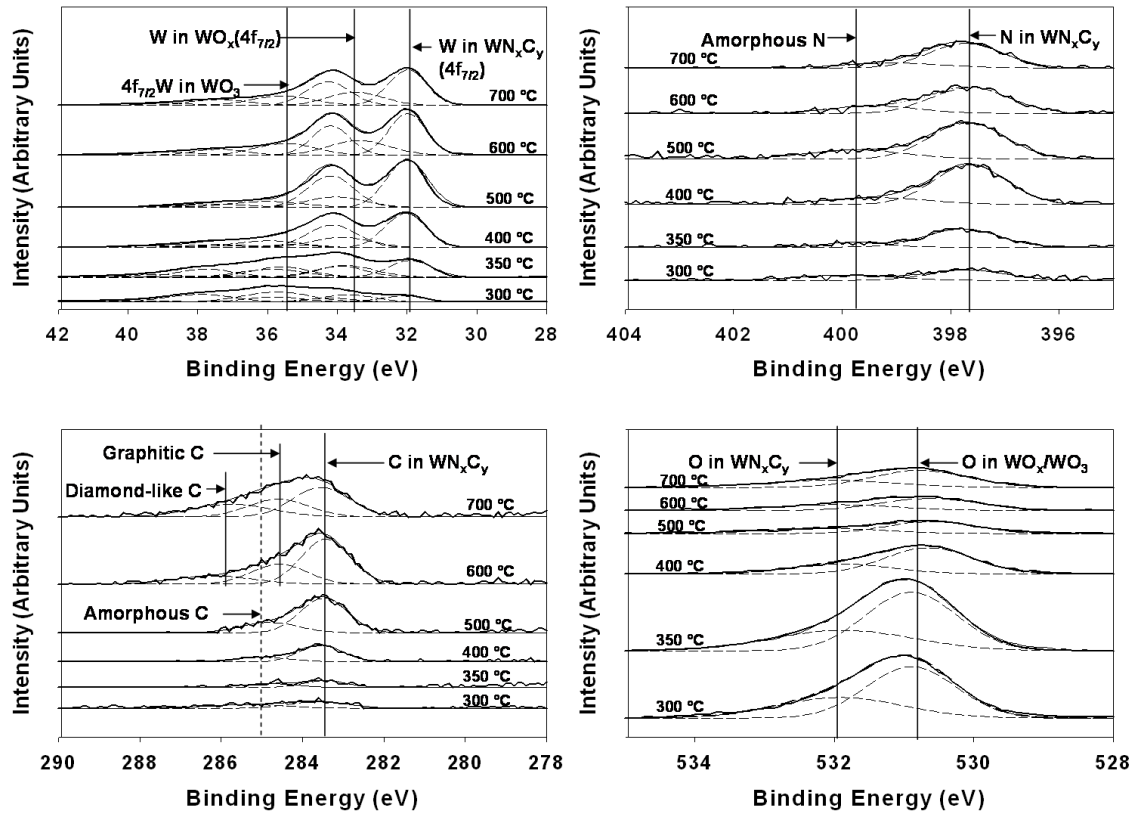


Figure 6-9. X-ray photoelectron spectroscopy measurements for films deposited by procedure 1A between 300 and 700 °C on Si (100) substrate

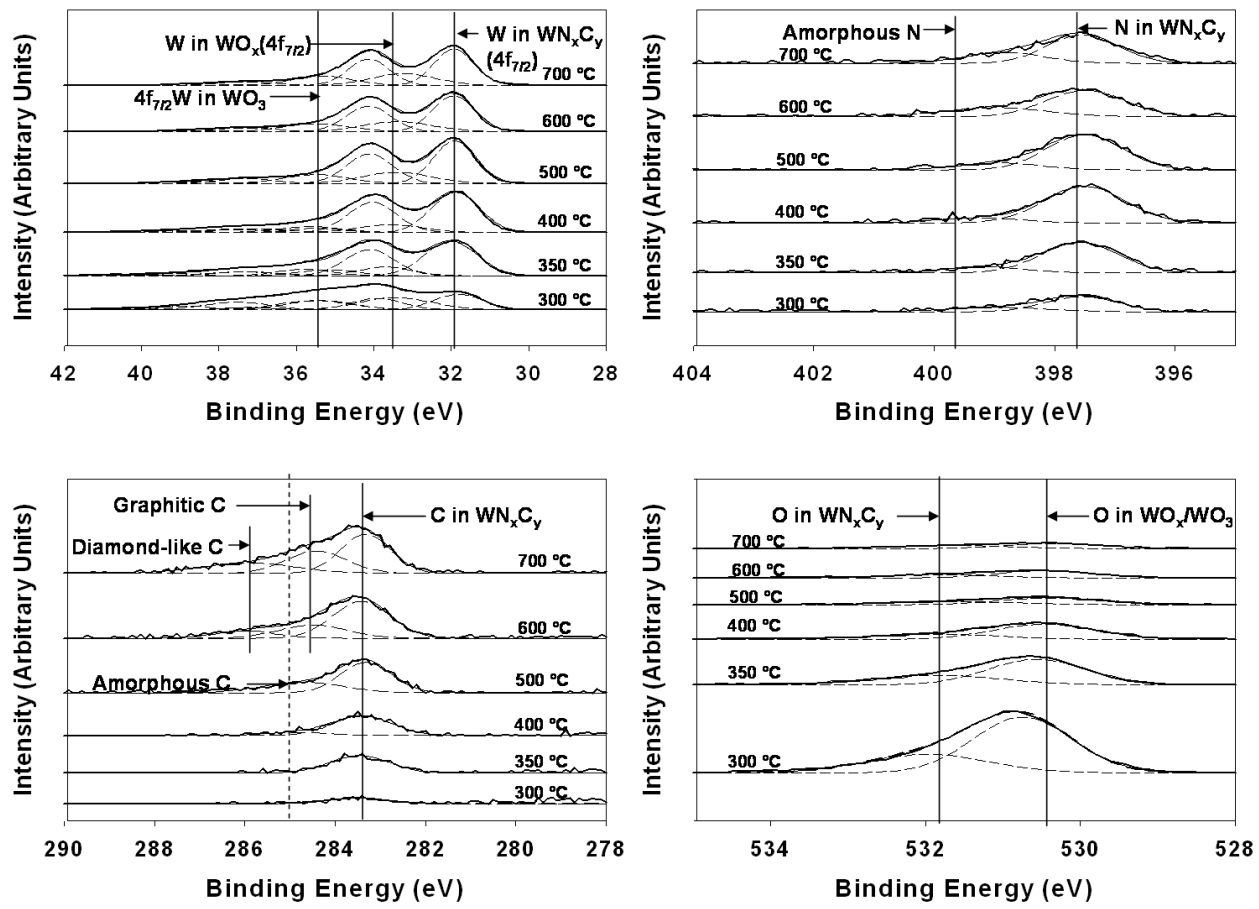


Figure 6-10. X-ray photoelectron spectroscopy measurements for films deposited for between 300 and 700 °C by procedure 1B on Si (100) substrate

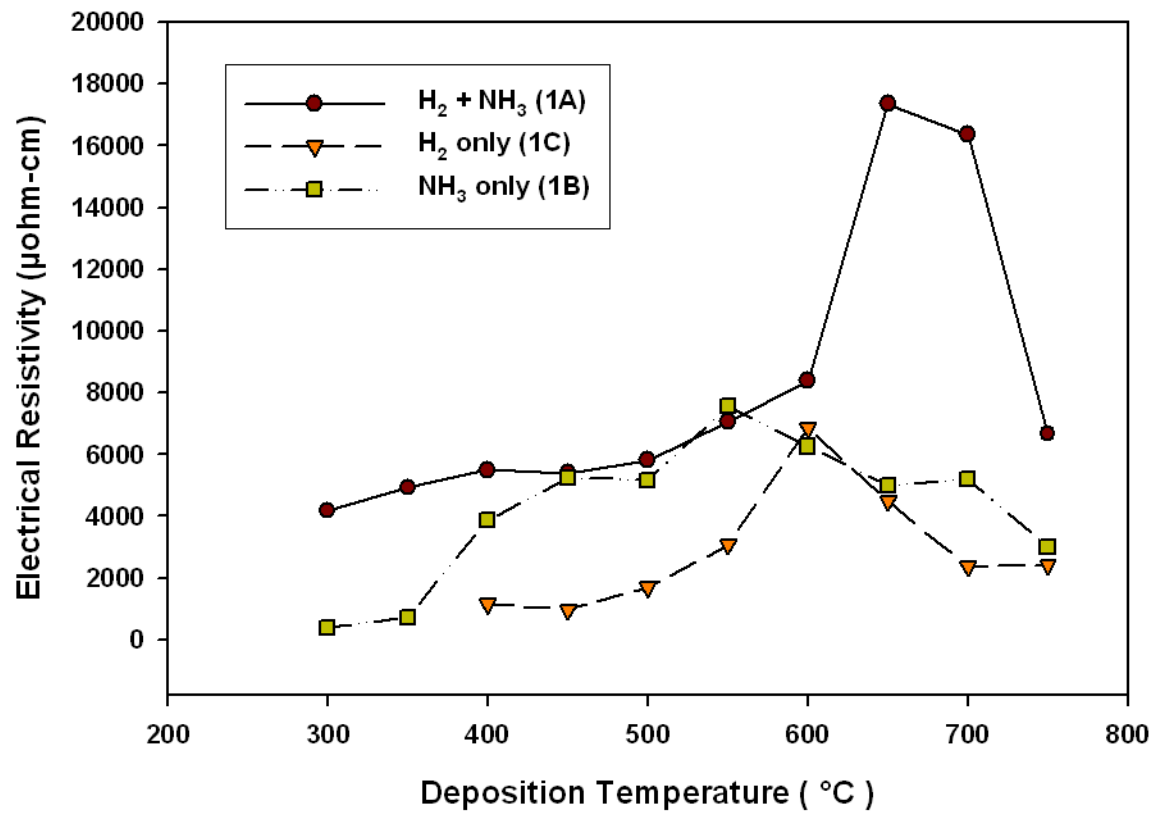


Figure 6-11. Change in film resistivity with deposition temperature for films deposited by procedures 1A, 1B and 1C on Si (100) substrate

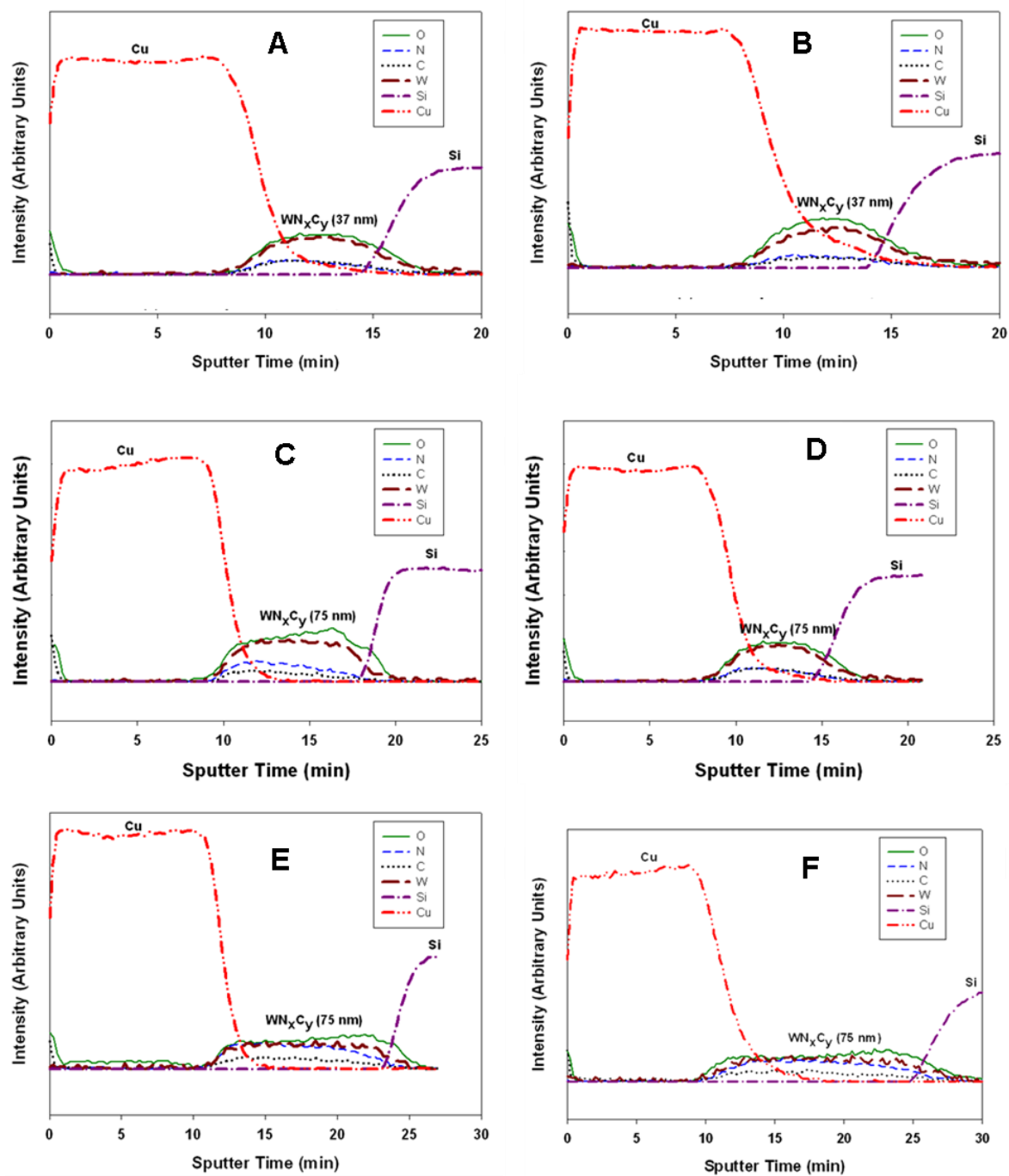


Figure 6-12. Pre- and post-anneal AES depth profiles of Cu (100 nm)/ WN_xC_y /Si (substrate) stacks for WN_xC_y films deposited by procedure 1A. A) Barrier deposition at 300 °C, no annealing. B) Barrier deposition at 300 °C, annealing at 500 °C. C) Barrier deposition at 350 °C, no annealing. D) Barrier deposition at 350 °C, annealing at 500 °C. E) Barrier deposition at 400 °C, no annealing. F) Barrier deposition at 400 °C, annealing at 500 °C.

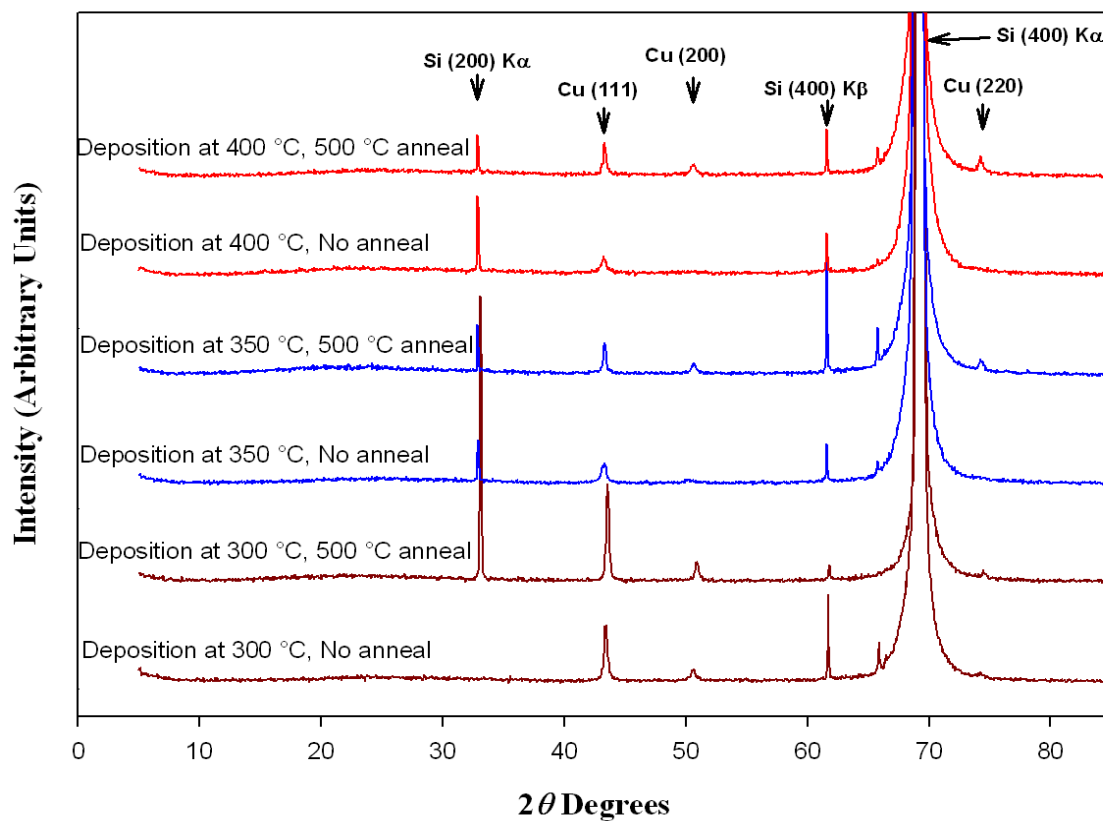


Figure 6-13. Pre- and post-anneal XRD measurements of Cu (100 nm)/ WN_xC_y /Si (substrate) stacks for WN_xC_y film deposited by procedure 1A at 300, 350 and 400 °C

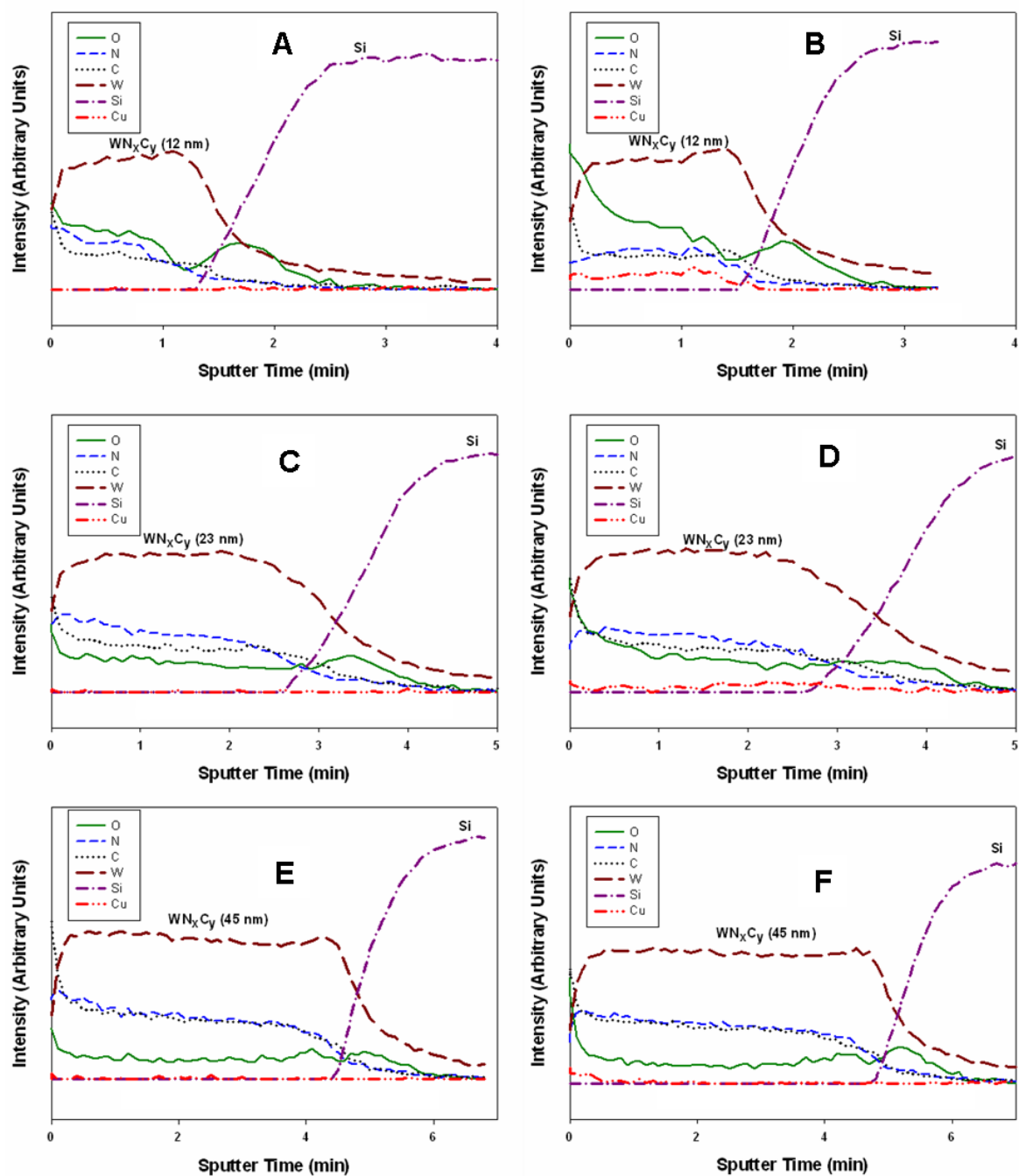


Figure 6-14. Pre- and post-anneal AES depth profiles of Cu (100 nm)/ WN_xC_y /Si (substrate) stacks for WN_xC_y film deposited by procedure 1B. After vacuum annealing and prior to AES depth profiling, the Cu layer in the Cu/WN_xC_y /Si stack was etched-off. A) Barrier deposition at 300 °C, no annealing. B) Barrier deposition at 300 °C, annealing at 500 °C. C) Barrier deposition at 350 °C, no annealing. D) Barrier deposition at 350 °C, annealing at 500 °C. E) Barrier deposition at 400 °C, no annealing. F) Barrier deposition at 400 °C, annealing at 500 °C.

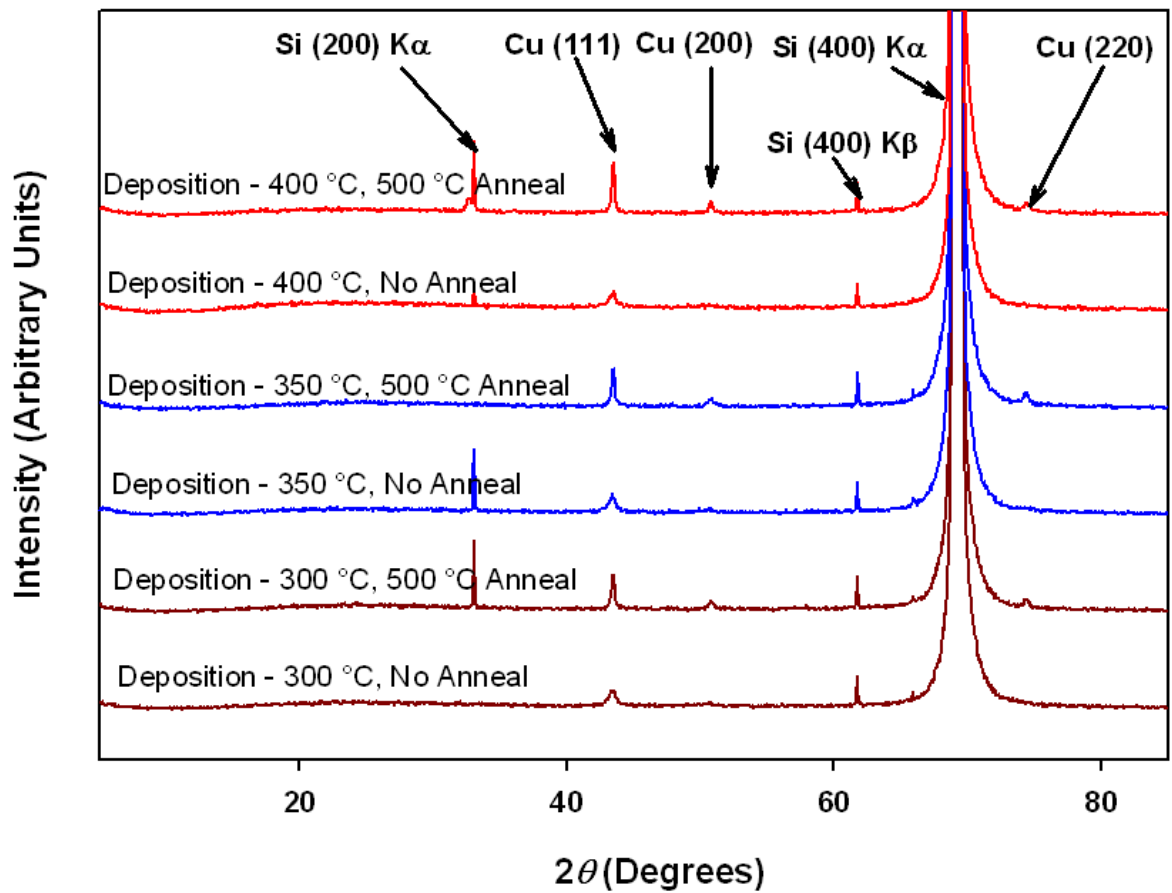


Figure 6-15. Pre- and post-anneal XRD measurements of Cu (100 nm)/ WN_xC_y /Si (substrate) stack for WN_xC_y film deposited by procedure 1B at 300, 350 and 400 °C

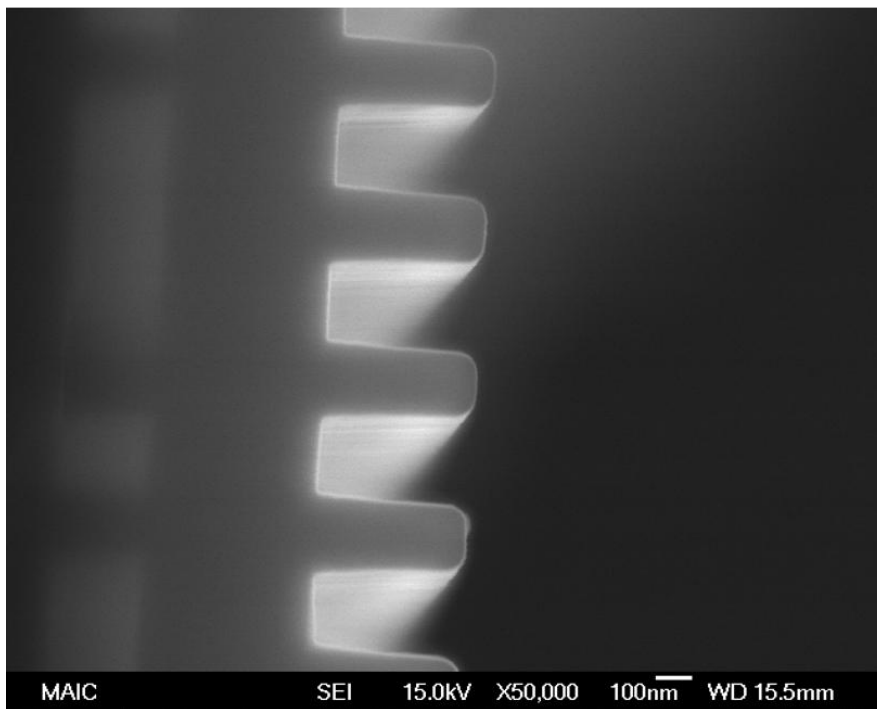
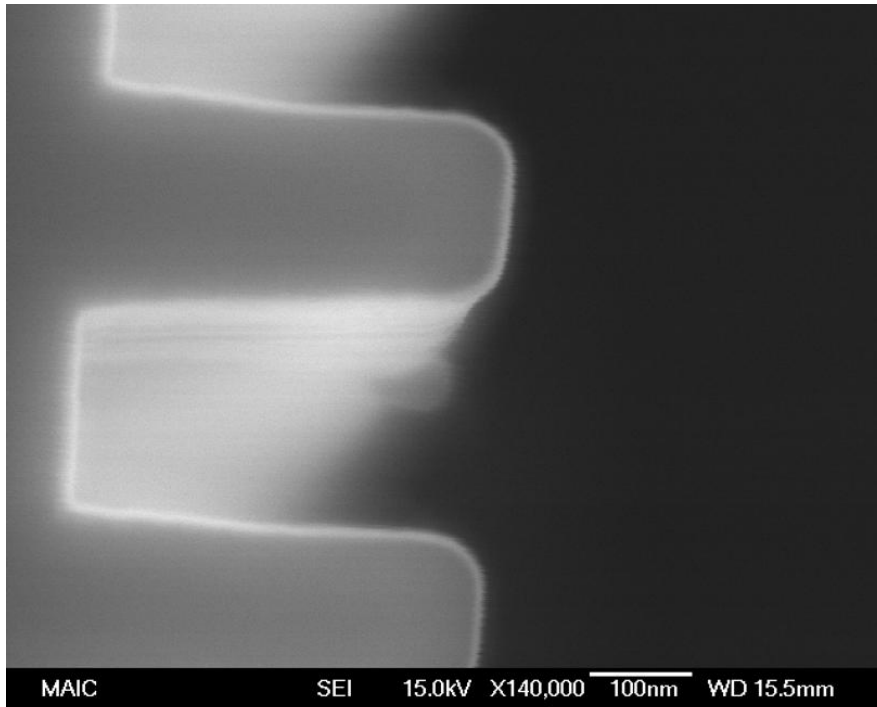


Figure 6-16. Scanning electron microscope images of WN_xC_y thin films deposited on FSG dielectric. The feature size is $0.2\ \mu\text{m}$ with aspect ratio of 2:1

CHAPTER 7

DEPOSITION OF $W_N{}_x C_y$ FROM $(CH_3CN)Cl_4W(NNMe_2)$ FOR DIFFUSION BARRIER APPLICATION

Chapters 4, 5 and 6 discussed two different approaches for increasing film N content. The first approach used NH_3 as a co-reactant with precursor **3** and **4** to increase the film N content. The second approach used metal-organic precursor **4** which contains more N atoms per W atom (Chapter 5). Following the same approach, $(CH_3CN)Cl_4W(NNMe_2)$ (**5**) has been used to deposit $W_N{}_x C_y$ thin films for diffusion barrier application. Scheper et al.²⁰⁴ have demonstrated that diorganohydrazido(2-) titanium complexes can be used for the deposition of titanium nitride thin films by CVD. This chapter discusses the characterization of the films deposited from **5** using CVD and evaluates the effectiveness of the deposited films in preventing diffusion of copper.

7.1 Precursor Synthesis

A Schlenk flask was charged with WCl_6 (2.10 g, 5.30 mmol) and methylene chloride (40 ml). 1,1-Dimethylhydrazine (0.4 ml, 5.3 mmol) was added to the flask under vigorous stirring at $-78\text{ }^\circ\text{C}$. After 10 min, the solvent was removed *in vacuo* while warming to room temperature. After removing the solvent, acetonitrile (15 mL) was added to the flask and the mixture was stirred for 30 min. The solvent was removed *in vacuo* and solids from the reaction were extracted with 2x15 mL of methylene chloride. The combined extracts were filtered and the volume reduced to 10 mL. The product was precipitated from the mixture by adding vigorously stirred pentane (200 mL) maintained at $0\text{ }^\circ\text{C}$. The orange product **5** was filtered off as a microcrystalline powder and dried *in vacuo*.

7.2 Film Growth by CVD

When CVD growth was attempted at $400\text{ }^\circ\text{C}$ from **5** in an inert atmosphere with N_2 as carrier gas, the resulting film contained W and O while no C or N was detected by AES.

However, when H₂ was used as carrier gas at the same deposition temperature, the deposited film contained W, N, C and O as determined by AES. Hence, the H₂ co-reactant is essential for deposition of WN_xC_y thin film from **5**. Appreciable film growth was observed for **5** at deposition temperature as low as 300 °C when H₂ was used as co-reactant. This temperature is the lowest growth temperature among all the precursors **1 - 5** when only H₂ is used as co-reactant. The film characterization and testing reported in this chapter were performed on films deposited using **5** and H₂ as co-reactant. Table 7-1 provides the molar flow rate of reactants used in the MOCVD reactor. The molar flow rate of **5** was same as that used for deposition using precursor **4**. The color of the deposited film varied from golden brown at low deposition temperature to grayish at higher deposition temperature.

7.3 Film Composition

Figure 7-1 shows AES results for films deposited using **5** between 300 and 700 °C. The AES results showed that films deposited from **5** contained W, N, C and O in varying concentration for deposition between 300 and 650 °C. The films deposited between 300 and 650 °C are W rich, with W content varying between 51 and 63 at. %. The W content of film decreases to 34 at. % for deposition at 700 °C because of excessive incorporation of C in the film. The N content in the film is 11 at. % for deposition at 300 °C. As the deposition temperature is increased from 300 to 350 °C, the film N content increases dramatically to 24 at. %, which is also the highest value of N content obtained for deposition from **5** throughout the deposition temperature range. For deposition between 350 and 750 °C, the film N content decreases from 24 at. % to 5 at. %. The sources of N in the film are precursor **5** and/or benzonitrile. The decrease in N content between 350 and 650 °C is due to a decrease in N incorporation from the precursor and benzonitrile. For deposition at 700 °C, the AES measurement shows that the film N content is below the detection limit of AES. This indicates

that deposition temperature higher than 650 °C leads to cleavage of N containing ligand from the precursor, resulting in deposition of WC_x thin film.

The C content of the film remains constant at ca. 9 at. % for deposition between 300 and 400 °C. Between 400 and 600 °C, the C content of film monotonically increases from 9 at. % to 41 at. % and remains unchanged at 650 °C. The increased C content of the film is due to increased incorporation of C from the precursor and/or benzonitrile into the film with an increase in deposition temperature.¹⁵⁵ Increasing the deposition temperature further to 700 °C causes a sharp increase in film C content to 63 at. %. The O content of the film decreases from 19 at. % at 300 °C to 15 at. % at 350 °C. In Chapter 6, it has been argued that the O in the film is incorporated during growth as well as post-growth. The XPS results (*vide infra*) show that O in the film is incorporated both during growth and post-growth. For growth between 450 and 600 °C, the O content of the film decreases from 9 at. % to 2 at. % and remains constant at 2 at. % between 600 and 700 °C.

Due to the presence of chlorine in **5**, the possible presence of chlorine in the films was of interest. As discussed earlier, XPS was used to detect the presence of Cl in the film because the W NNN peak in AES spectra overlaps with the Cl LMM peak at ca. 180 eV. Figure 7-2 shows the XPS data for films deposited using **5** between 300 and 700 °C. No peaks were observed for either Cl 2s or Cl 2p_{3/2} at 270eV and 199 eV, respectively, confirming that the chlorine level in the films was lower than the detection limit of XPS (ca. 1 at. %).

7.4 Film Crystallinity

Figure 7-3 shows the XRD patterns for films deposited from **5** between 300 and 700 °C. The XRD spectra for films deposited between 300 and 500 °C show no peaks attributable to the film, but only peaks associated with the substrate (Si(200) K α , Si(400) K β , and Si(400) K α reflections at 33.10, 61.75 and 69.20° 2 θ , respectively). The absence of other peaks in these

spectra suggests that films deposited up to 500 °C are X-ray amorphous. The XRD pattern for the film deposited between 550 and 650 °C shows the emergence of crystallinity as evidenced by the two broad peaks that lie between the standard peak positions of β -W₂N [37.74 2 θ for (111) phase and 43.85 ° 2 θ for (200) phase] and β -W₂C [36.98 2 θ for (111) phase and 42.89 ° 2 θ for (200) phase],¹⁷⁸ indicating the presence of either the solid solution β -WN_xC_y or a physical mixture of β -W₂N and β -W₂C. Since the intensity of most the intense (111) reflection is small, the other peaks corresponding to (220) and (311) reflections at 63.55 and 75.05° are not clearly visible in the XRD spectra. For deposition at 700 °C, the two peaks at 37.20 and 42.55 ° 2 θ correspond to β -W₂C because the films contain only W, C and O as indicated by AES measurement.

7.5 Lattice Parameter

Figure 7-4 shows the change in lattice parameter with deposition temperature for films deposited from **5**. The (111) peak of β -WN_xC_y or β -W₂N and β -W₂C has the highest intensity and thus was used for calculating the lattice parameter. For film deposited at 550 °C, the lattice parameter has a value of 4.13 Å, which is similar to the literature value of lattice parameter for β -W₂N (4.126 Å). As the deposition temperature is increased from 550 to 600 °C, the lattice parameter value remains almost unchanged at 4.12 Å even though the C content of the film increases by 9 at. % in the same temperature range. If the additional C were incorporated in the W sublattice, the lattice parameter value would have increased. An observation to the contrary suggests that the additional C is incorporated outside the W sublattice in amorphous state. Between 600 and 650 °C, the lattice parameter increases from 4.12 to 4.16 Å. In the same temperature range, the film composition remains relatively unchanged. The increase in lattice parameter could be due to increase in interstitials (C, N and/or O) or a decrease in vacancies in the W sublattice. As deposition temperature is increased to 700 °C, the lattice parameter

increases further to 4.18 Å. At 700 °C, the film is β -W₂C but the lattice parameter of 4.18 Å is much lower than the standard lattice parameter of 4.236 Å for β -W₂C possibly due to strain in the film.

7.6 Grain Size

As discussed earlier, XRD peak broadening could be used to determine average crystallite size for polycrystalline films using Scherrer's equation. Since the (111) reflection was most intense, it was used to determine FWHM and estimate average grain size. Figure 7-5 shows the average crystallite size for films deposited from **5**. The average grain size is 45 Å for deposition at 550 °C. Between 550 and 650 °C, the average grain size increases with an increase in deposition temperature. With an increase in deposition temperature, the surface diffusivity of adsorbed species increases resulting in an increase in grain growth. The average grain size decreases to 30 Å at 700 °C because of the formation of β -W₂C instead of β -WN_xC_y. Overall, the average grain size measurement indicates that the films deposited from **5** at and above 550 °C are nanocrystalline with average grain size varying between 30 and 66 Å.

7.7 Film Growth Rate

The growth rate for films deposited from **5** was determined by dividing the film thickness measured using X-SEM by deposition time. Figure 7-6 shows X-SEM images for films grown at different deposition temperature from **5**. The growth rate increased from 1 Å/min at 300 °C to 4 Å/min for deposition at 400 °C. Between 450 and 650 °C, the growth rate gradually decreases from 13 Å/min to 10 Å/min. For deposition at 700 °C, the growth rate increased significantly to 38 Å/min suggesting a change in growth mechanism at this temperature. Figure 7-7 shows the Arrhenius plot for films grown for deposition from **5**. Film growth rate increased exponentially with temperature between 300 and 450 °C, indicating that the growth is in the kinetically controlled growth regime and that surface reaction is the rate limiting step. Using the Arrhenius

equation, the apparent activation energy calculated for the kinetically controlled growth regime is 0.52 eV. For film deposited between 450 and 650 °C, growth is in the diffusion limited growth regime. Typically, growth in the diffusion limited growth regime shows a small positive slope. The small negative slope in the Arrhenius plot for growth from **5** suggests that some precursor is decomposed via homogenous reactions resulting in a decrease in growth rate in the diffusion limited growth regime. The transition from kinetically controlled to diffusion limited growth occurs between 450 and 500 °C.

7.8 Atomic Bonding from XPS

Figure 7-8 shows the deconvolution for the XPS peaks of W, N, C and O for films deposited from **5** between 300 and 700 °C. The corresponding peak fitting parameters obtained from deconvolution are listed in Table 7-2 and Table 7-3. The reference peaks of elemental C, elemental W and different compounds of W, N, C and O are listed in Table 3-7 (Chapter 3). The deconvolution of the W 4f and 4p peaks at 300 °C indicates the presence of three different binding states of W. The first W 4f_{7/2} peak at 31.8 eV lies between the reference W peaks of W₂C (ca. 31.5 eV) and W₂N (ca. 33.0 eV), indicating that the W atom is bonded to both C and N. The second 4f_{7/2} peak at 33.4 eV lies between the reference WO₂ peak at 32.9 eV and reference W₂O₅ peak at 34.6 eV, suggesting that the stoichiometry of tungsten oxide is WO_x (2 < x < 2.5). The third W 4f_{7/2} peak at 35.2 eV corresponds to W present in WO₃. These results are similar to those obtained for films deposited from **4** by procedures 1A, 1B and 1C (Chapter 6). With a increase in deposition temperature, intensity of the W peak corresponding to WO_x and WO₃ decreases, which is consistent with the AES results that shows a decrease in O content of the film in the same deposition temperature range. For deposition at 700 °C, the W peaks can be deconvoluted into WN_xC_y and WO_x peaks without a contribution from WO₃. The N peak for deposition at 300 °C can be deconvoluted into two peaks. The first N 1s peak at 397.5 eV

corresponds well with the reference N 1s peak for N in WN_x film.¹¹⁹ The second peak at 398.8 eV suggests that N is also present in amorphous state.¹¹⁹ Between 300 and 600 °C, the N peak can be similarly deconvoluted to a dominant peak around 397.5 eV and a broad shallow peak around 398.5 eV implying that the bulk of N is bonded to W and a small amount of N present in amorphous phase. The film deposited at 700 °C shows no N 1s peak confirming that the film is WC_x .

Between 300 and 700 °C, the C 1s peak can be deconvoluted into two peaks around 283.4 eV and 285.0 eV. The former peak corresponds to C bonded to W (reference peak at 283.5 eV) and the latter peak reflects C present in amorphous phase (reference peak between 284.5 and 285.2 eV). Between 300 and 500 °C, the C 1s peak deconvolution shows that the C in the film is predominantly bonded to W with some C present in amorphous state. However, for deposition at 600 and 700 °C, the ratio of amorphous C to carbidic C increases dramatically suggesting an increase in ligand and/ or benzonitrile decomposition and subsequent incorporation of amorphous C in the film.

The O 1s peak for deposition between 300 and 700 °C can be deconvoluted into two peaks at 530.5 and 531.7 eV. The peak at 530.5 eV corresponds to O bonded to W in WO_x or WO_3 . The other peak at 531.7 eV corresponds to O bonded to W in WN_xC_y . As discussed earlier, O could be incorporated into the film either during film growth because of O and water vapor impurity in the reactor or after the film growth because of exposure of film to atmosphere. The presence of WO_x/WO_3 suggests that residual gas (oxygen, water vapor) in reactor and/or O impurity in the precursor react with the precursor on the film surface during film growth. The source of O bound to W in WN_xC_y is most likely atmospheric O that diffuses through the film when the film is exposed to atmosphere. With an increase in deposition temperature, the peak

intensity of O decreases for both O present in WO_x/WO_3 and O loosely bound to W in WN_xC_y . The O present in WO_x/WO_3 decreases with an increase in deposition temperature because of the increase in film thickness with deposition temperature or densification of film. The peak intensity of O loosely bound to W in WN_xC_y decreases with increase in deposition temperature because of decreased O diffusion in the film from atmosphere as a result of denser and thicker films deposited at higher temperatures. In summary, deconvolution of 1s peak of O suggests that O is incorporated in the film during growth as WO_x/WO_3 and post growth as O loosely bound to W in WN_xC_y .

XPS results indicate that films deposited at 300 and 400 °C are WN_xC_y with significant amount of WO_x and WO_3 along with presence of small amounts of amorphous N and C. For deposition at 500 and 600 °C, the bulk of the film is WN_xC_y with a small amount of WO_x and increased amount of amorphous C. The film deposited at 700 °C consists of WC_x along with a small amount of WO_x and a significantly higher amount of amorphous C.

7.9 Film Resistivity

Figure 7-9 shows the variation of film resistivity with deposition temperature for films deposited from **5**. Films with the lowest resistivity of 844 $\mu\Omega$ -cm are obtained for deposition at 300 °C. This value is considerably higher than bulk resistivities of pure W_2N and W_2C . Previous study on ALD WN_xC_y has also shown that films with a low resistivity of 300 – 400 $\mu\Omega$ -cm can be deposited at low deposition temperature (300 – 350 °C).¹⁴⁵ A number of factors influence the resistivity of transition metal nitrides and carbides including metal to non-metal ratio, vacancies in metal and non-metal sublattice, bonding states of C and N, presence of contaminants such as O, film crystallinity and porosity. The high film resistivity for film deposited from **5** could be because of interplay between some or all of these factors. As the deposition temperature is increased from 300 to 350 °C, the film resistivity increases sharply to

2250 $\mu\Omega\text{-cm}$ possibly due to the increase in N content of the film. Between 350 and 400 °C, there is a sharp increase in film resistivity because of the decrease in W content of the film. Between 450 and 600 °C, film resistivity gradually decreases from 2800 to 1200 $\mu\Omega\text{-cm}$. The film deposited at 700 °C shows the highest resistivity of 4400 $\mu\Omega\text{-cm}$ even though AES results indicate that the film is WC_x , which has low bulk resistivity. The film deposited at 700 °C is C rich and high resistivity of the film is believed to be due to the presence of excessive amorphous C in the film as indicated by the XPS spectrum.

7.10 Diffusion Barrier Testing

To determine the effectiveness of diffusion barrier film deposited from **5**, barrier films deposited at 350 and 400 °C were coated with 100 nm PVD Cu. Prior to the deposition of Cu thin film, the barrier film was exposed to atmosphere for approximately 1 - 2 hour(s). The Cu/barrier/Si stack was annealed in vacuum at 500 °C for 30 min. After annealing, three-point AES depth profile and XRD measurements were done to detect copper diffusion through the barrier film. While XRD measurements were done on the Cu/barrier/Si stack, the AES measurements were done on a barrier/Si stack obtained after removing the Cu layer by etching with dilute HNO_3 . The Cu layer was removed to prevent the knock-on effect of sputtering (*vide supra*).

Figure 7-10 shows the depth profile of pre- and post-anneal $\text{Cu}/\text{WN}_x\text{C}_y/\text{Si}$ stacks for WN_xC_y films deposited at 350 and 400 °C. The thickness of the film deposited at 350 and 400 °C was 50 and 60 nm respectively. For deposition at 350 °C, the pre-anneal depth profile (Figure 7-10 A) shows the background signal for Cu when there is no Cu diffusion. The pre-annealed stack has a sharp barrier/Si interface. The post-anneal AES depth profile (Figure 7-10 B) shows that the Cu signal is similar to that observed in the pre-anneal depth profile suggesting that the barrier film was able to prevent Cu diffusion into the Si. The barrier/Si interface is sharp

in the post-anneal AES depth profile with no indication of mixing at this interface. The XRD measurement of the pre- and post-annealed film stack shown in Figure 7-11 shows peaks corresponding to Cu and Si with no indication of presence of Cu₃Si. Thus, both AES and XRD measurements indicate that 50 nm barrier film deposited at 350 °C was able to prevent Cu diffusion after annealing at 500 °C in vacuum for 30 min. Furthermore, the XRD profile shows that PVD copper deposition on WN_xC_y has a preferred orientation of (111). This is highly desirable because the Cu(111) phase has a better electromigration resistance as compared to other crystalline phases of Cu.

For deposition at 400 °C, the comparison of pre- and post-anneal depth profile (Figures 7-10 C and D) shows that copper has not diffused through the barrier film after annealing. The post-anneal depth profile shows a sharp barrier/Si interface indicating that no intermixing has occurred at this interface. The XRD profile shown in Figure 7-11 also indicates that the post-anneal film stack exhibits no peaks corresponding to Cu₃Si. Thus, barrier film deposited at 400 °C is able to prevent Cu diffusion after annealing at 500 °C in vacuum. As with film deposited at 350 °C, WN_xC_y film deposited at 400 °C also favors deposition of (111) oriented Cu film for deposition by PVD.

7-11 Conclusions

It has been demonstrated that the tungsten hydrazido complex (CH₃CN)Cl₄W(NNMe₂) (**5**) can be used with H₂ in an aerosol assisted CVD system to deposit WN_xC_y thin films. The H₂ co-reactant is essential for deposition of WN_xC_y films as deposition with **5** in inert atmosphere (N₂ carrier gas) resulted in deposition of WO_x films. The lowest growth temperature for **5** was 300 °C, which is the lowest among precursors **1 - 5**. Films deposited with **5** consisted of W, N, C and O as determined by AES and no Cl impurity was detected by XPS. The film N content was significantly higher for films deposited from **5** as compared to films deposited from **1 - 4**.

Amorphous film deposition was observed for deposition below 550 °C. Films were quite resistive as compared to bulk resistivity of pure W_2N and W_2C . Diffusion barrier testing shows that films deposited at 350 and 400 °C were able to prevent bulk Cu diffusion after annealing at 500 °C in vacuum for 30 min.

Table 7-1. Molar flow rates of reactants in CVD reactor for deposition from precursor **5**

Reactant	Molar flow rate (mol/min)
Precursor (5)	1.16×10^{-6}
H ₂	4.09×10^{-2}
Benzonitrile (solvent)	6.47×10^{-4}

Table 7-2. Analysis results from deconvolution of XPS peak of W for films deposited from **5** on Si(100) substrate between 300 and 700 °C.

Deposition temperature		WN _x C _y			WO _x (2 < x < 2.5)			WO ₃		
		Peak position (eV)	% Area	FWHM (eV)	Peak position (eV)	% Area	FWHM (eV)	Peak position (eV)	% Area	FWHM (eV)
300	W4f _{7/2}	31.76	27.70%	1.49	33.36	14.10%	1.53	35.18	10.80%	1.96
	W4f _{5/2}	33.86	20.80%	1.64	35.51	10.60%	1.8	37.28	8.10%	2.09
	W4p _{3/2}	37.16	4.20%	2.49	38.76	2.10%	1.26	40.58	1.60%	1.82
400	W4f _{7/2}	31.67	35.10%	1.49	33.63	13.90%	2.74	35.09	3.60%	1.55
	W4f _{5/2}	33.77	26.30%	1.51	35.73	10.40%	2.35	37.19	2.70%	1.62
	W4p _{3/2}	37.07	5.30%	3.31	39.03	2.10%	1.7	40.49	0.50%	1.69
500	W4f _{7/2}	31.6	41.50%	1.38	33.4	7.50%	1.93	34.87	5.30%	1.52
	W4f _{5/2}	33.7	31.10%	1.36	35.5	5.70%	1.88	36.97	4.00%	2.32
	W4p _{3/2}	37	4.10%	2.78	38.8	0.80%	1.32	40.27	0.50%	1.5
600	W4f _{7/2}	31.92	42.00%	1.35	34.18	5.70%	1.71	35.4	5.20%	1.3
	W4f _{5/2}	33.98	33.60%	1.39	36.28	4.30%	2.09	37.5	3.90%	3.33
	W4p _{3/2}	37.32	4.20%	2	39.58	0.60%	1.19	40.8	0.50%	1.5
700	W4f _{7/2}	31.76	39.50%	1.24	33.4	12.50%	2.38	--	--	--
	W4f _{5/2}	33.92	29.60%	1.34	35.5	9.40%	2.05	--	--	--
	W4p _{3/2}	37.16	7.10%	2.22	38.8	1.90%	1.68	--	--	--

Table 7-3. Analysis results from deconvolution of XPS peaks of C, N and O for films deposited from **5** on Si(100) substrate between 300 and 700 °C.

Deposition temperature		C 1s			N1s			O1s		
		Peak position (eV)	% Area	FWHM (eV)	Peak position (eV)	% Area	FWHM (eV)	Peak position (eV)	% Area	FWHM (eV)
300	Peak 1	283.44	77.40	1.78	397.50	79.40	1.40	530.63	73.00	1.43
	Peak 2	285.16	22.60	2.10	398.75	20.60	1.73	531.72	27.00	1.65
400	Peak 1	283.35	75.80	1.20	397.50	77.70	1.38	530.54	65.70	1.32
	Peak 2	284.81	24.20	1.68	398.79	22.30	2.10	531.62	34.30	1.55
500	Peak 1	283.33	84.30	1.35	397.52	79.50	1.29	530.49	68.10	1.34
	Peak 2	285.09	15.70	1.54	398.89	20.50	1.87	531.61	31.90	1.54
600	Peak 1	283.45	57.80	1.43	397.62	83.20	1.64	530.45	59.20	1.45
	Peak 2	284.76	42.20	2.49	399.28	16.80	2.10	531.77	40.80	1.81
700	Peak 1	283.47	73.30	1.98	--	--	--	530.57	63.30	1.66
	Peak 2	285.11	26.70	2.70	--	--	--	531.76	36.70	1.54

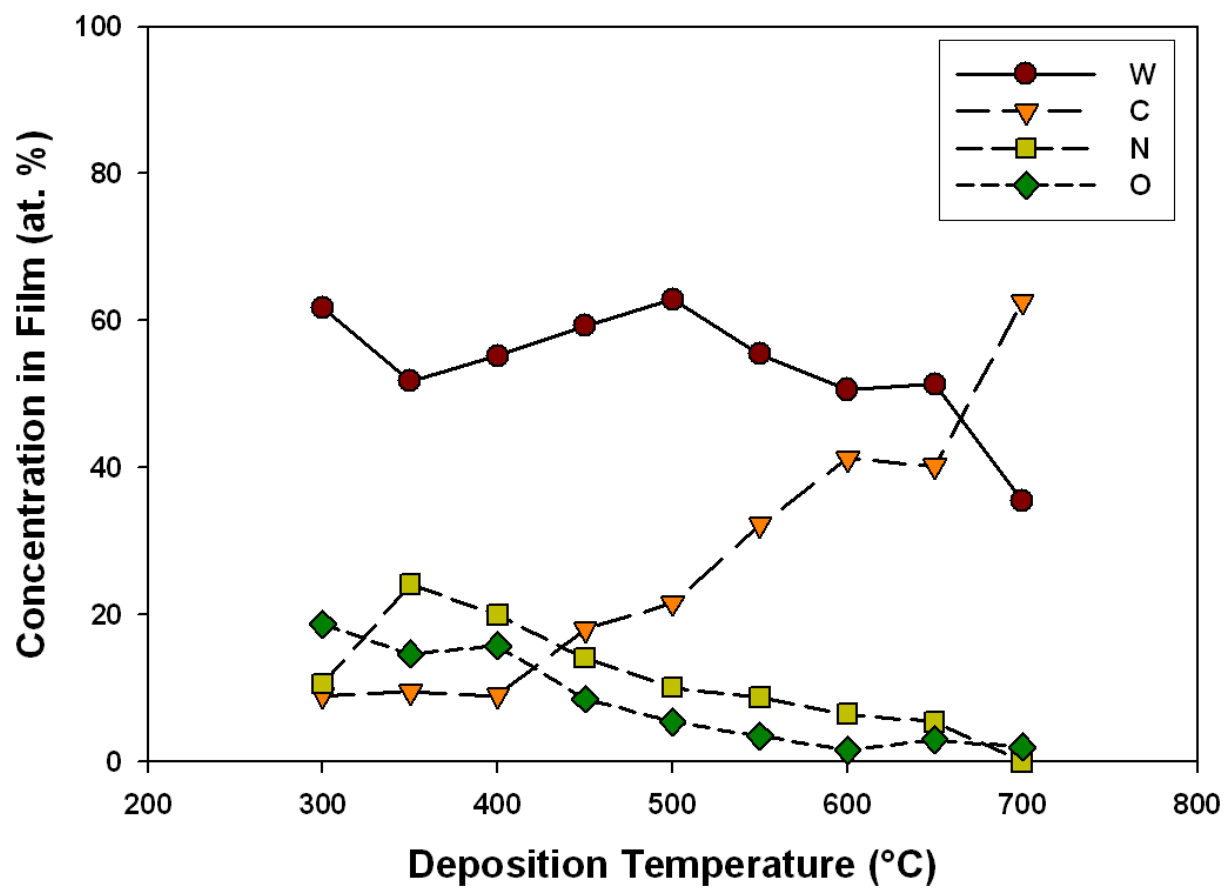


Figure 7-1. Composition of films deposited from **5** on Si (100) substrate at different deposition temperature as determined by AES after 0.5 min of sputtering

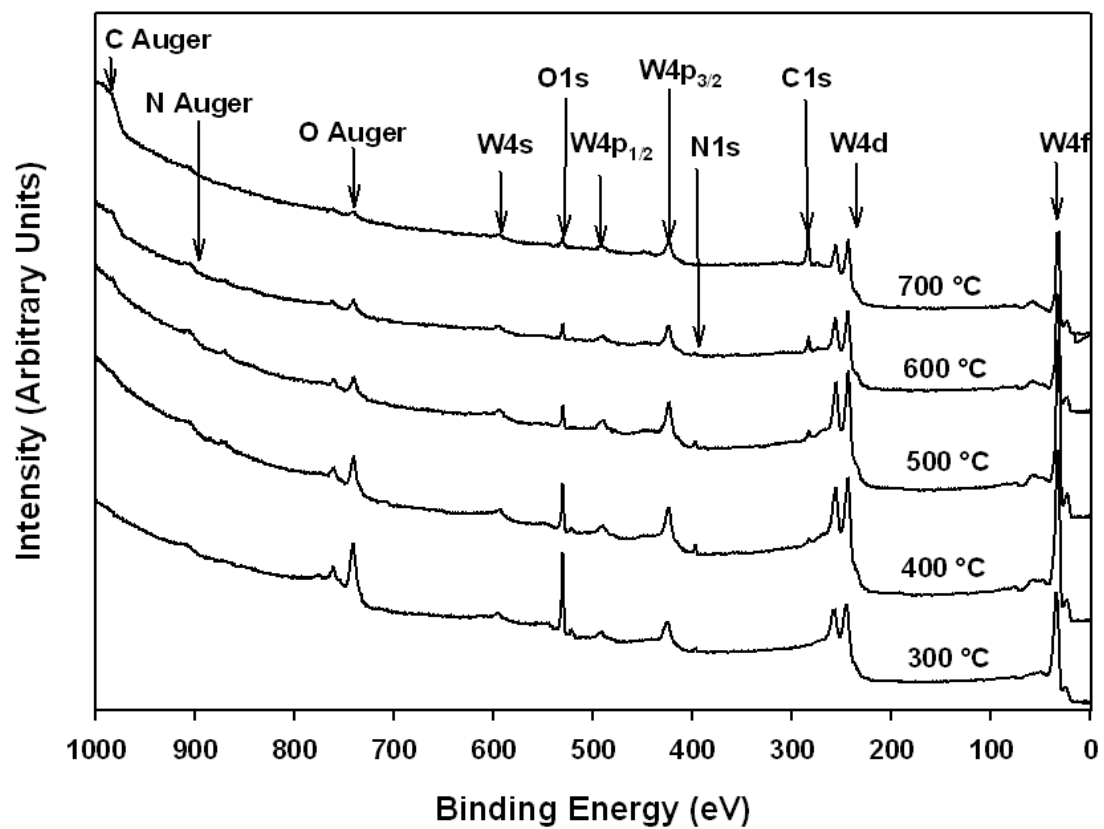


Figure 7-2. X-ray photoelectron spectroscopy measurements for films deposited from **5** on Si (100) substrate at different deposition temperature

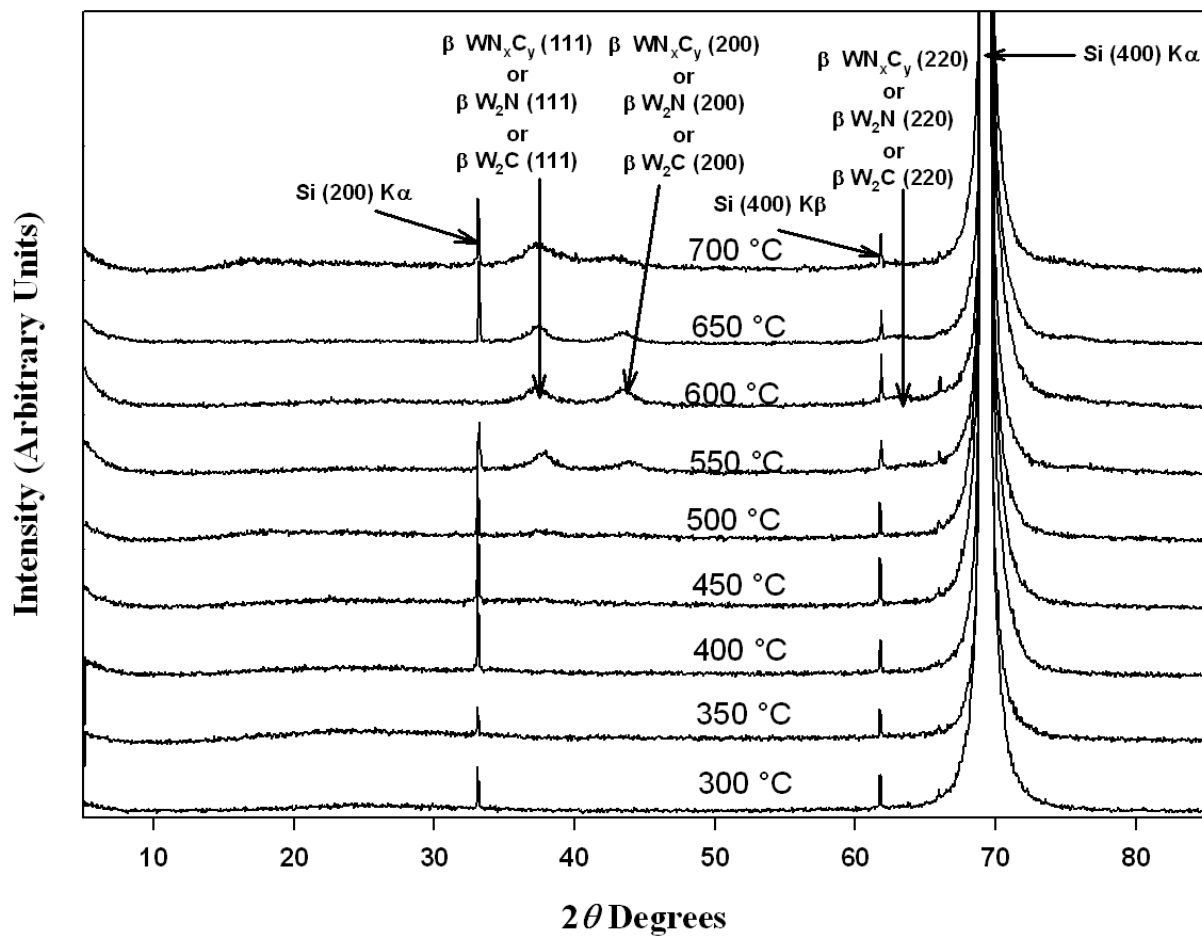


Figure 7-3. X-ray diffraction patterns for films deposited from 5 between 300 and 700 °C on Si (100) substrate

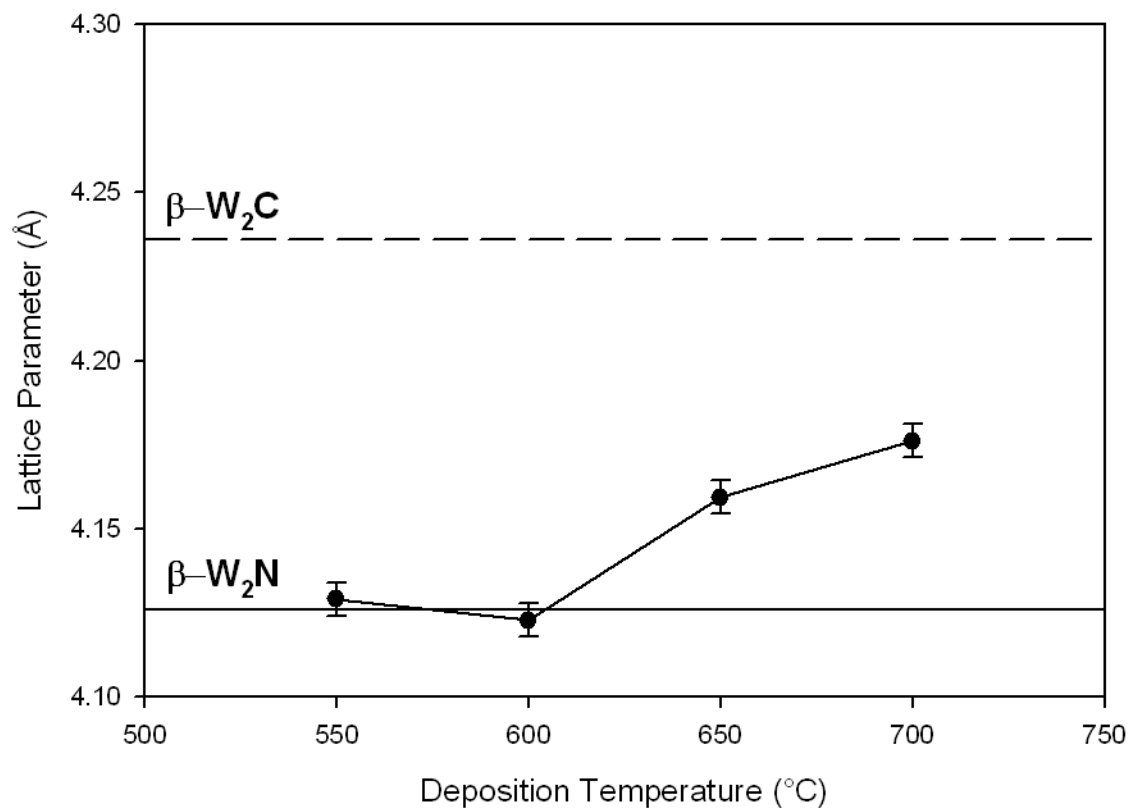


Figure 7-4. Lattice parameters for films grown from **5** on Si (100) substrate. Error bars indicate uncertainty in determination of peak position for lattice parameter calculation.

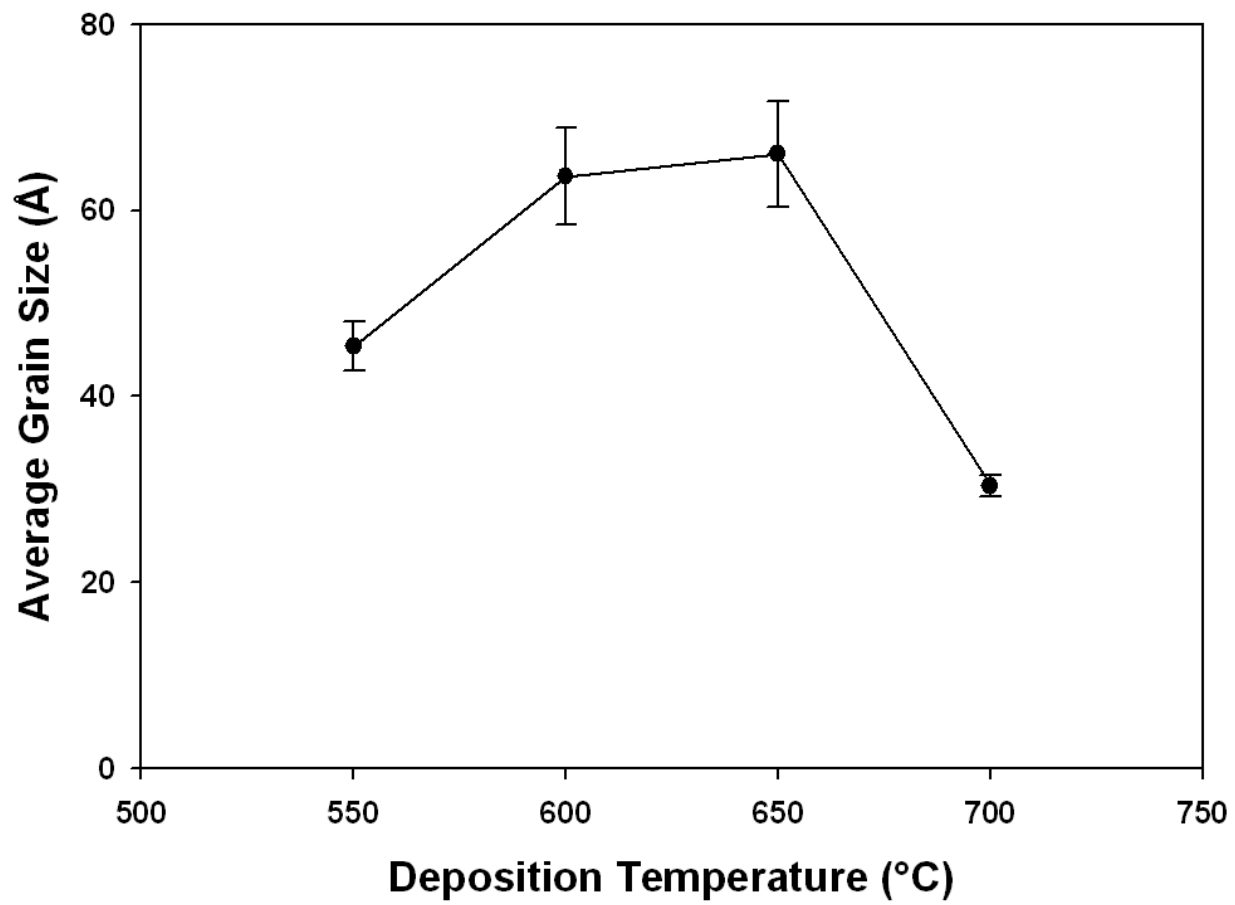


Figure 7-5. Average grain size for films grown from **5** at different deposition temperature on Si (100) substrate.

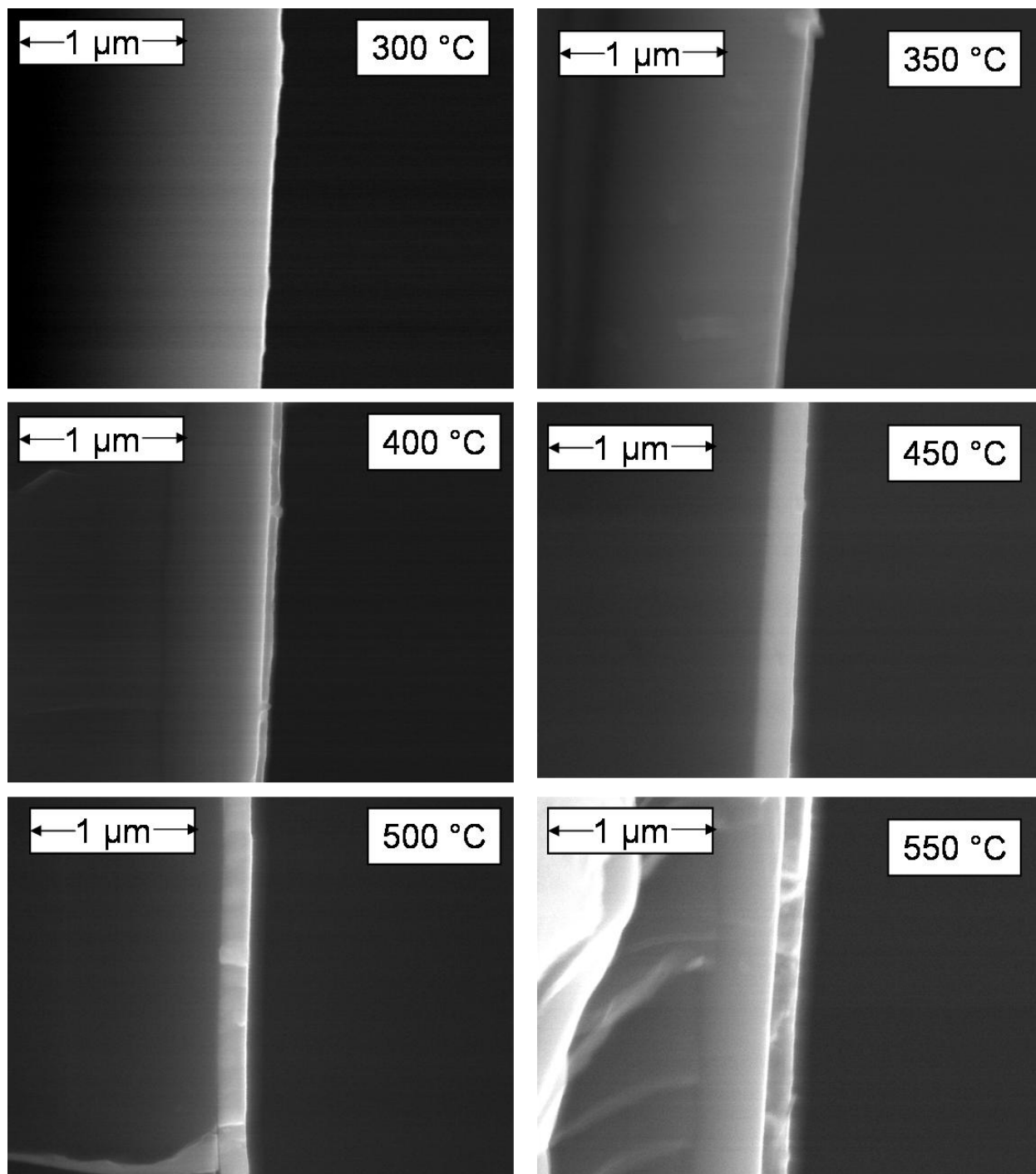


Figure 7-6. Scanning electron microscope images for films deposited from **5** between 300 and 700 °C on Si (100) substrate

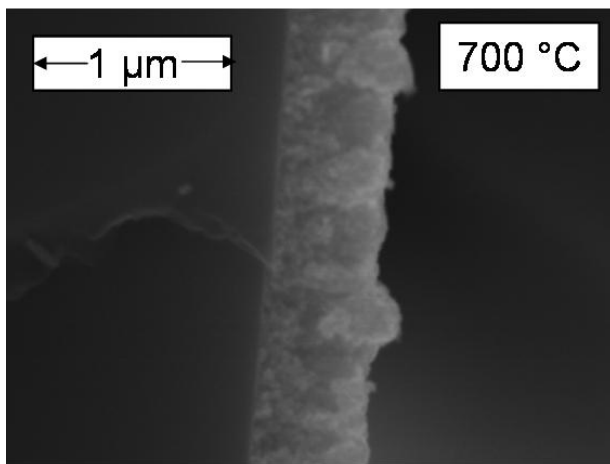
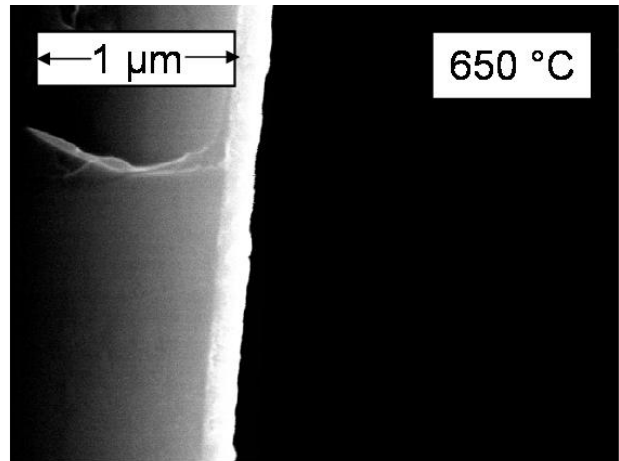
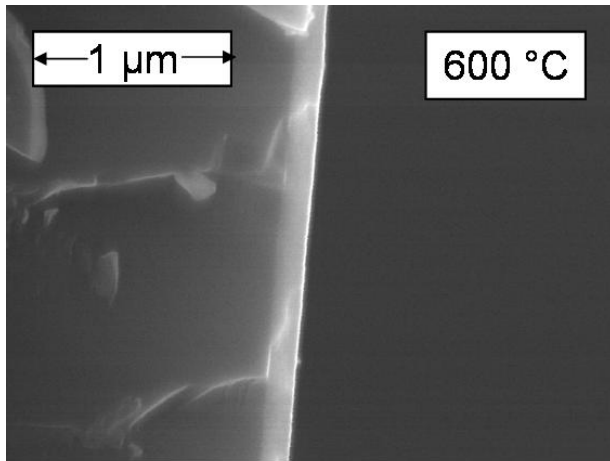


Figure 7-6. Continued...

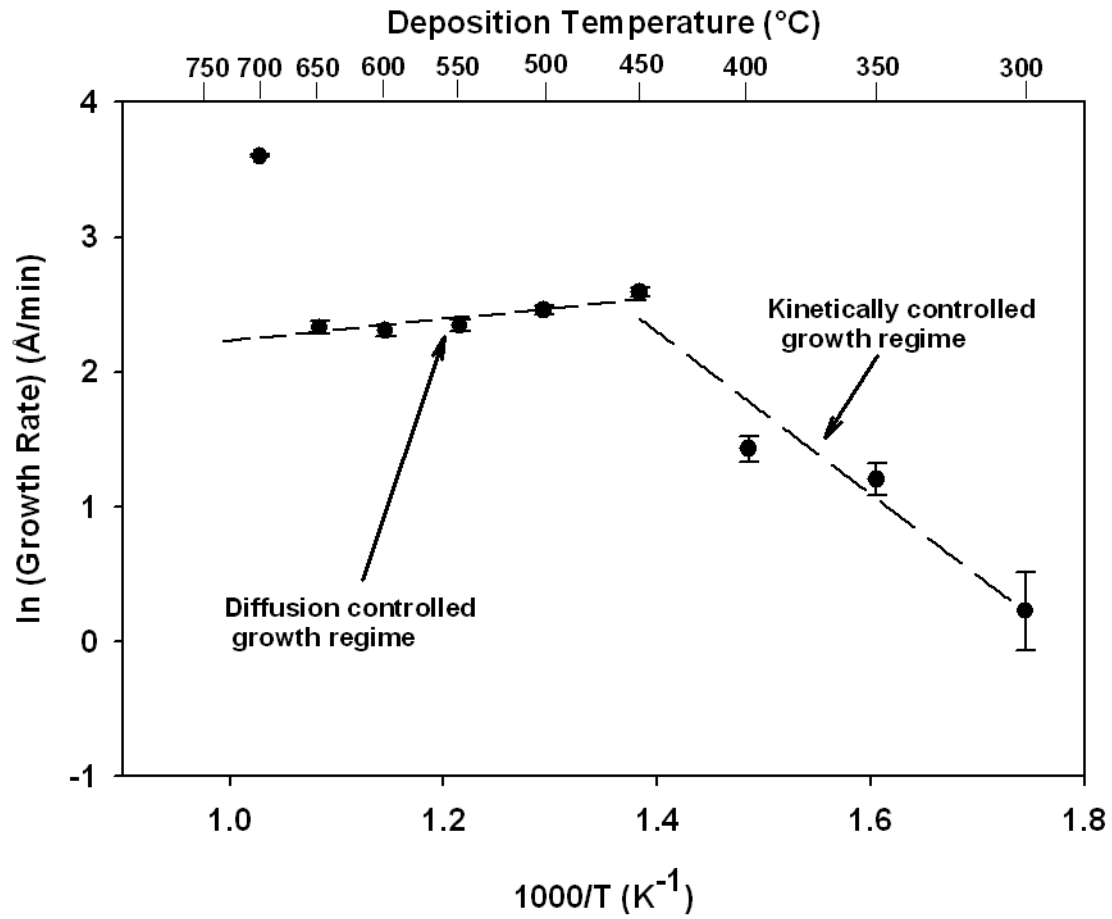


Figure 7-7. Arrhenius plot for deposition from 5 on a Si(100) substrate

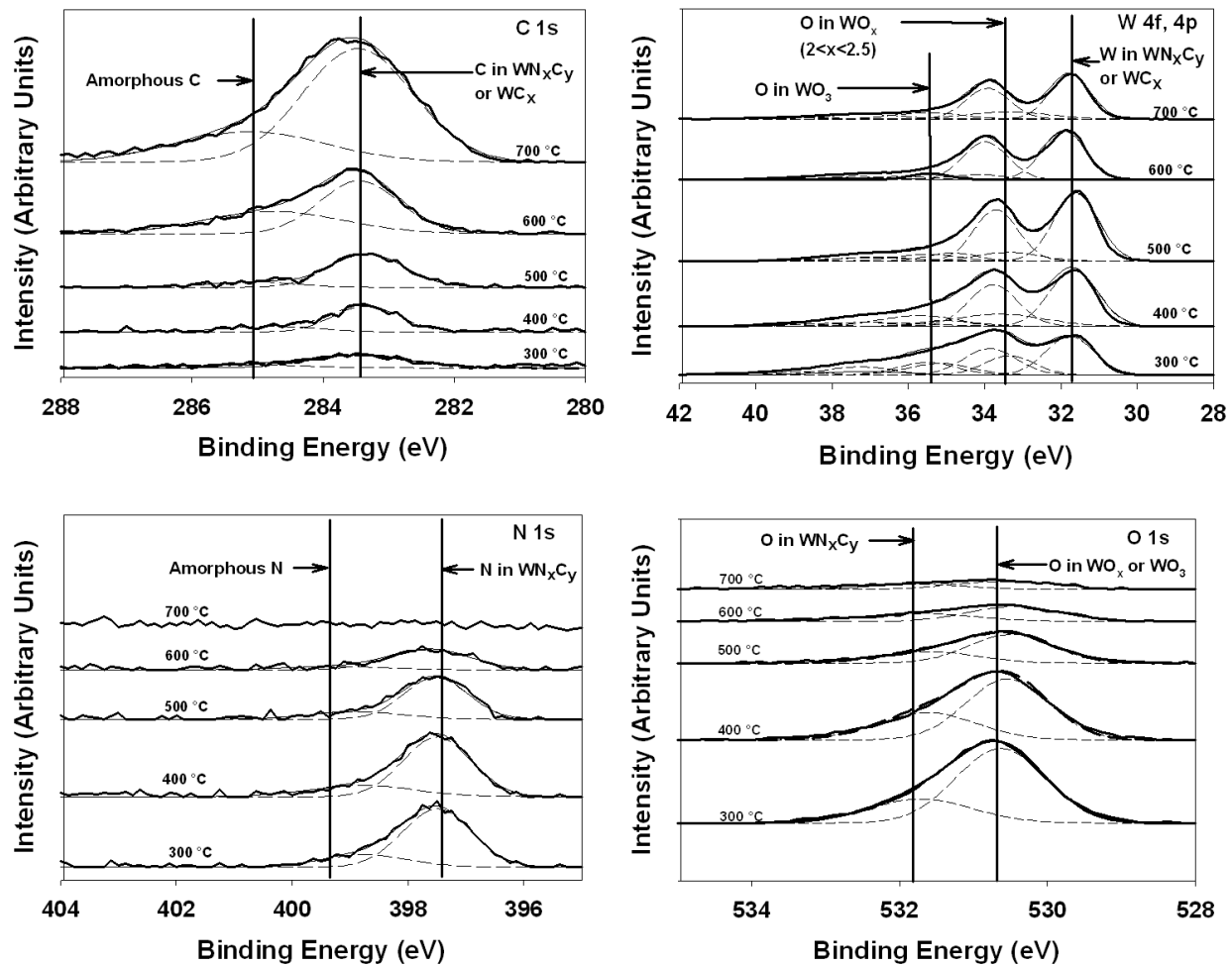


Figure 7-8. X-ray photoelectron spectroscopy measurements for films deposited from **5** between 300 and 700 °C on Si (100) substrate

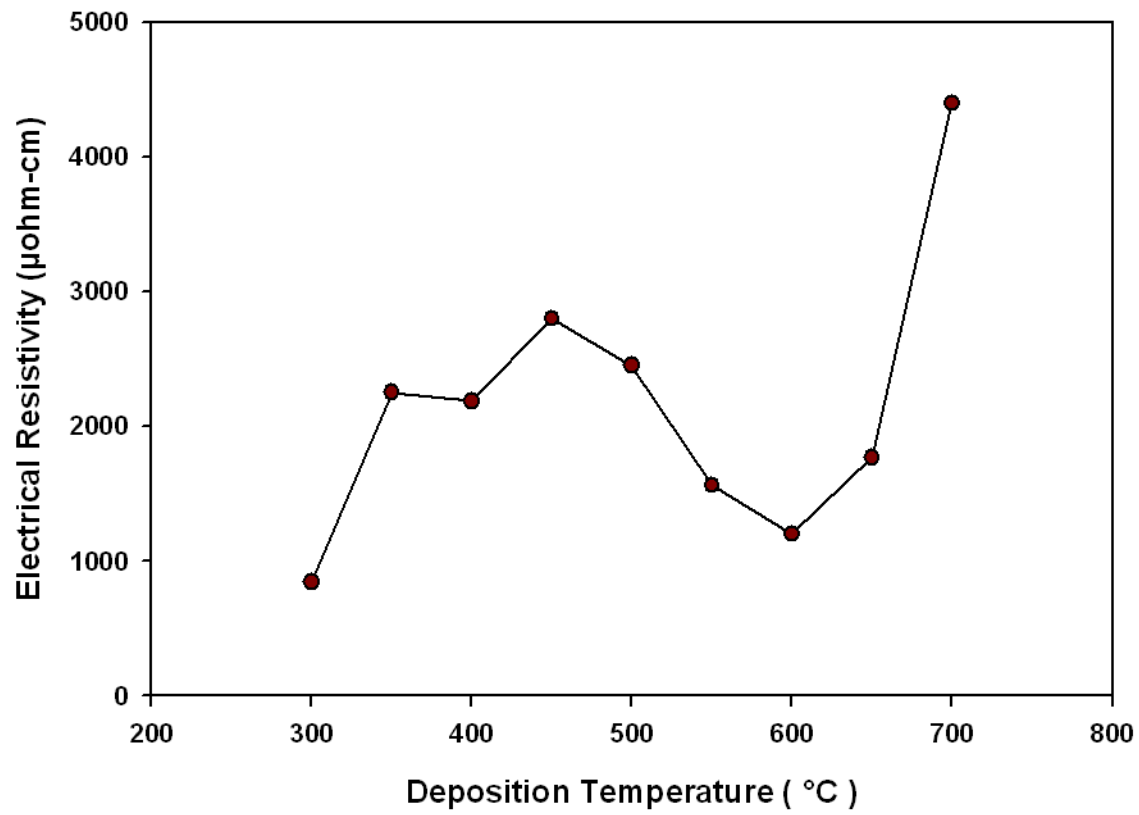


Figure 7-9. Change in film resistivity with deposition temperature for films deposited from **5** on Si (100) substrate

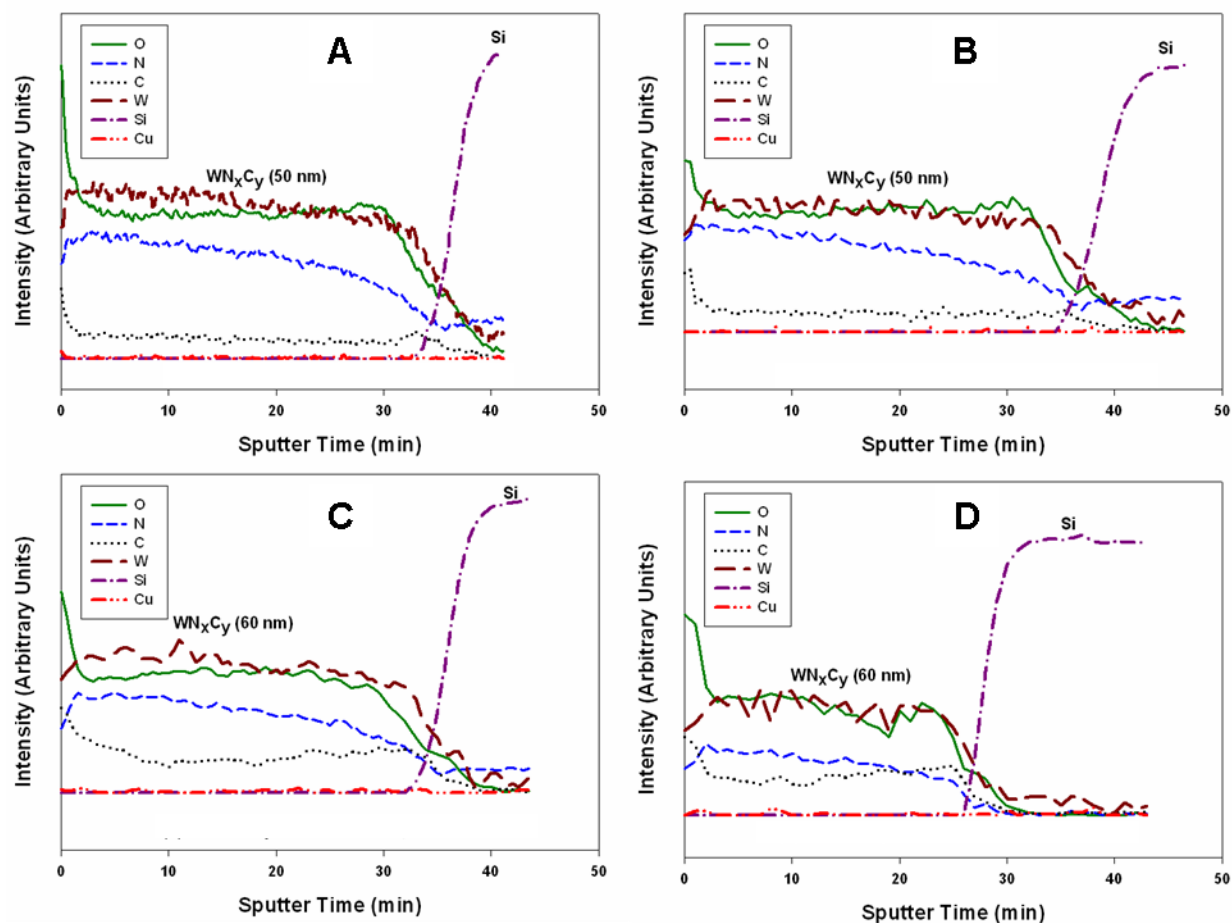


Figure 7-10. Pre- and post-anneal AES depth profile of Cu/WN_xC_y/Si (substrate) stack for WN_xC_y film deposited from **5**. After vacuum annealing and prior to AES depth profiling, the Cu layer in the Cu/WN_xC_y/Si stack was removed by etching. A) Barrier deposition at 350 °C, no annealing. B) Barrier deposition at 350 °C, annealing at 500 °C. C) Barrier deposition at 400 °C, no annealing. D) Barrier deposition at 400 °C, annealing at 500 °C.

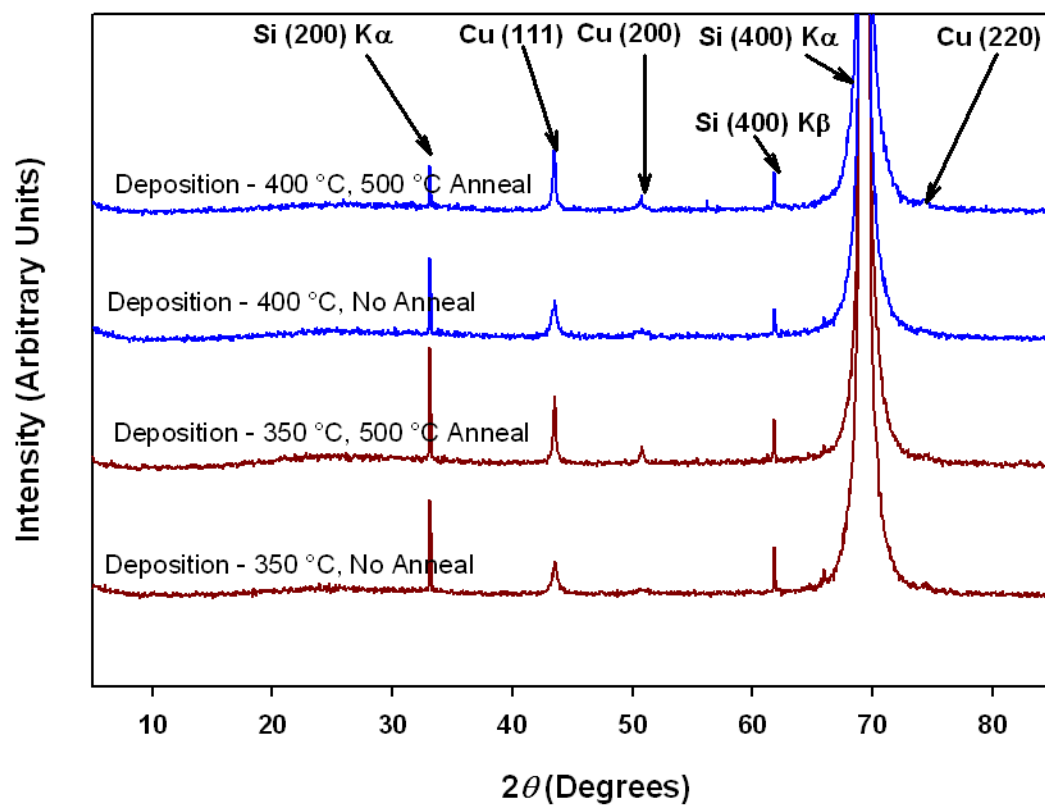


Figure 7-11. Pre- and post-anneal XRD measurement of Cu (100 nm)/ WN_xC_y /Si (substrate) stack for WN_xC_y film deposited from 5 at 350 and 400 °C

CHAPTER 8

QUANTUM MECHANICAL CALCULATIONS FOR PREDICTING PRECURSOR FRAGMENTATION

Chemical vapor deposition is a very complex process to model because it is not an equilibrium process. Moreover, the numerous reaction pathways accessible to the precursor molecule both in gas phase as well as on the substrate surface make fundamental understanding of CVD processes all the more challenging. Computational chemistry can be used to study possible reaction pathway(s) for metal-organic precursors. In this chapter, homogenous decomposition of precursor **5** has been investigated using density functional theory (DFT) and statistical mechanics. Based on the calculation results, possible reaction pathways for precursor **5** have been proposed.

8.1 Computational Methodology

A brief description of density functional theory is presented in Appendix A. All the calculations were done using Gaussian 03W software. For calculating binding energy of transition metal compounds such as hydrides, the Hartree Fock theory is not very accurate until quite high levels of theory are used to account for the electron correlation. In contrast, DFT has been shown to predict geometries and binding energies in transition metal compounds more accurately.²⁰⁵ The B3LYP functional, which has been quite accurate in predicting structure and energy of transition metal compounds, was used for geometry optimization and energy calculations. The calculations were done using a split basis set (LanL2DZ for W and 6-31G(d) for all other elements). To reduce the computational time, the effective core potential LanL2DZ was used for W.²⁰⁶ The molecular structures were visualized using Molden and gOpenMol.^{207,208} Thermodynamic properties were calculated using the statistical mechanics package in the Gaussian 03W software.

8.2 Geometry Optimization

Figure 8.1 shows the structure of **5** obtained from X-ray crystallographic determination and the computationally optimized geometry. As expected, the experimental and calculated geometries of **5** are quite similar. Table 8.1 shows the comparison of selected bond lengths and bond angles obtained from X-ray crystallographic measurement and computational geometry optimization. The calculated structure of **5** shows octahedral coordination at the W center. Comparison of experimentally obtained and calculated bond lengths listed in Table 8-1 show that except for the W-N1 bond length, the bond lengths obtained from calculation are larger than those obtained experimentally. The DFT calculations are done for gas phase species whereas the experimentally obtained structure is for solid precursor. The differences in bond angles could arise because of crystal packing forces that are not accounted for in gas phase DFT calculations.

8.3 Acetonitrile Cleavage

Previous study on **1a,b**, **2a,b** and **3a,b** has shown that dissociation of the acetonitrile ligand from the precursors is facile at growth temperature ($> 450\text{ }^{\circ}\text{C}$).²⁰⁹ To study the cleavage of acetonitrile ligand from precursor **5**, ΔG_f° and ΔH_f° were calculated for **5**, CH_3CN and $\text{Cl}_4\text{W}(\text{NNMe}_2)$ (**5a**). The ΔG° and ΔH° values for cleavage of acetonitrile from **5** were then calculated using Equations 8-1 and 8-2.

$$\Delta G^{\circ} = \Delta G_f^{\circ}(\mathbf{5a}) + \Delta G_f^{\circ}(\text{CH}_3\text{CN}) - \Delta G_f^{\circ}(\mathbf{5}) \quad (8-1)$$

$$\Delta H^{\circ} = \Delta H_f^{\circ}(\mathbf{5a}) + \Delta H_f^{\circ}(\text{CH}_3\text{CN}) - \Delta H_f^{\circ}(\mathbf{5}) \quad (8-2)$$

Figure 8-2 shows the optimized structures for **5a** and CH_3CN and Table 8-2 lists selected bond lengths and bond angles for **5a**. The calculated values for ΔG° and ΔH° can be assumed to be approximately equal to ΔG^{\ddagger} and ΔH^{\ddagger} because the transition states for endothermic reactions

should be product-like. The values for ΔG° and ΔH° for acetonitrile cleavage are 6.68 and 14.92 kcal/mol respectively. These values are slightly higher than those obtained for **1a - 3a** reported previously,²⁰⁹ suggesting that the acetonitrile cleavage reaction for precursor **5** has a higher energy barrier as compared to the other precursors.

8.4 Chlorine Cleavage

One of the important findings from film growth characterization discussed in Chapter 7 is that even though precursor **5** contains four Cl atoms per W atom, the film deposited using **5** showed no evidence of Cl in the XPS measurement indicating that Cl incorporation in the film is below the detection limit of XPS (ca. 1 at. %). Hence, possible reaction pathways that can lead to Cl cleavage have been explored computationally. It should be noted that these calculations are done for homogeneous gas phase reactions and the thermodynamic properties are calculated at 298.15 K and 1 atm.

8.4.1 Reaction of **5a** with H₂

Two mechanistic pathways for the removal of Cl from **5a** have been explored. The first pathway involves loss of Cl₂ from **5a** by reductive elimination. The ΔH^\ddagger value for reductive elimination of Cl₂ from **5a** is 95.92 kcal/mol (Figure 8-3). The magnitude of this value suggests that the reductive elimination pathway is not accessible to **5a**. It should also be noted that the calculated values of ΔG° for reductive elimination product (RI-1) indicated that the triplet was more stable than the singlet, a possible indication of spin crossover problems with reductive elimination. The second pathway involved reaction of transition metal complex with H₂. Possible pathways for reaction of H₂ with transition metals include oxidative addition, coordination of H₂ followed by transfer of an acidic proton and σ -bond metathesis. However, neither oxidative addition nor coordination of H₂ is available for a d⁰ complex such as **5**.

Previous work has shown that a transition state could be found for σ -bond metathesis of H_2 with the $Cl_4W(N^iPr)$.²⁰⁹ The calculated ΔH^\ddagger value for the σ bond metathesis of H_2 with **5a** was 35.55 kcal/mol, indicating that this pathway should be accessible under the growth conditions. The ΔH^\ddagger calculated for **5a** is very similar to the values reported previously for $Cl_4W(N^iPr)$.²⁰⁹

8.4.2 Reaction Pathways for Removal of a Chloride from MI-1

Figure 8-4 shows reaction pathways for reductive elimination and σ -bond metathesis of MI-1 to replace a second chloride ligand with hydride. For reductive elimination of HCl from MI-1, the value of ΔH^\ddagger is 37.26 kcal/mol. This value is quite low as compared to those previously reported for calculations on **2a**.²⁰⁹ For σ -bond metathesis, the reaction can proceed to replace the chloride atom at either a *cis* or the *trans* position. The search for transition states for both *cis* and *trans* configurations and subsequent calculation of ΔH^\ddagger showed that the values of activation energy for both these reaction pathways are quite similar. The formation of *cis* isomer MT-2 *cis* is slightly more favorable energetically as compared to the *trans* isomer MT-2 *trans*. Overall, the ΔH^\ddagger values for reductive elimination and σ -bond metathesis for both *cis* and *trans* configurations are quite similar. This result is different from that for **2a**, which showed that the reductive elimination was energetically less favorable as compared to σ -bond metathesis for second chloride cleavage.

8.4.3 Reaction Pathways for Removal of Chloride from MI-2 and RI-2

Since the second chloride reaction discussed above could form MI-2 *cis*, MI-2 *trans* or RI-2, possible reaction pathways for these intermediates have been explored. Figure 8-5 shows the different reductive elimination and σ -bond metathesis pathways for MI-2 *cis* and *trans* isomers. Figure 8-6 shows the reductive elimination of HCl from RI-2. Similar to RI-2, the RI-3 structure is more stable as a triplet than a singlet. The ΔH^\ddagger value for reductive elimination of HCl from RI-2 was 43.07 kcal/mol. To get a better idea of reaction surface for pathways involving MI-2

cis, MI-2 *trans* and RI-2, the reactions that lead to the fourth chloride cleavage needs to be studied.

8.4.4 Reaction Pathways for Removal of the Fourth Chloride from 5a

Possible reaction pathways for MI-3 and RI-3 are shown in Figure 8-7. The reductive elimination of HCl from MI-3 has an energy barrier of 74.64 kcal/mol. The σ -bond metathesis from MI-3 has a smaller energy barrier ($\Delta H^\ddagger = 38.09$ kcal/mol). The σ -bond metathesis reaction for RI-3 has a ΔH^\ddagger value of 48.26 kcal/mol.

Since the energy barriers for second chloride cleavage by σ -bond metathesis and reductive elimination are quite similar (*vide supra*), a comparative study of the energy barriers for third and fourth chloride cleavage reactions is required to ascertain which of these pathways would be more favorable if the reaction were to proceed by sequentially removing all chlorides. Figures 8-8, 8-9 and 8-10 shows the ΔH values with respect to the ΔH (**5a**) for different reaction pathways for intermediates MI2-*cis*, MI2-*trans* and RT2. Benchmarking the ΔH values to ΔH (**5a**) allows the comparison of different reaction pathways corresponding to MI2-*cis*, MI2-*trans* and RT2 intermediates. The comparison of different reaction pathways passing through intermediates MI2-*cis*, MI2-*trans* and RI2 shows that the removal of second chloride at the *trans* position by σ bond metathesis to form MI2-*trans* intermediate is most favorable energetically, followed by removal of third and fourth chloride also by σ bond metathesis to form MI4. The difference between the energy values for third and fourth chloride cleavage for reaction pathways through intermediates MI2-*cis* and MI2-*trans* is small (ca. 5 kcal/mol), hence it is possible that reaction pathway involving intermediate MI2-*cis* would also be accessible to **5a** if the reaction were to proceed via sequential elimination of all four chlorines in the gas phase.

The above mentioned calculation gives relative comparison of different pathways that can lead to sequential removal of all Cl from the precursor via either σ bond metathesis or reductive

elimination. Realistically, the values of activation energy for the removal of third and fourth Cl atoms from **5a** are high enough to preclude the availability of these pathways under the reaction conditions (deposition temperature of 300 °C or higher).

8.5 Conclusion

Computational chemistry has been used to assess the reaction pathways for precursor **5**. The facile dissociation of acetonitrile ligand from **5**, which has been observed experimentally for reaction in solution, is also observed for calculations done for gas phase reaction. Various reaction pathways for Cl cleavage from **5a** have also been explored. For the first Cl cleavage from **5a**, σ -bond metathesis is energetically favored and the activation energy value suggests that this pathway would be accessible to **5a**. For the second Cl cleavage, both σ -bond metathesis and reductive elimination pathways have similar energy barriers. However the high activation energy (ca. 50 kcal/mol) for the second Cl cleavage for both σ -bond metathesis and reductive elimination pathways indicates that these pathways may or may not be accessible to intermediate MI-1. Because of very high energy barriers for the third and fourth Cl cleavages, these pathways would not be accessible to **5a** in the gas phase.

While the present work focuses on homogenous reactions for acetonitrile dissociation from **5** and sequential Cl cleavage from **5a**, further work is needed to understand heterogeneous reaction pathways of **5**, **5a** and other reaction intermediates. The investigation of heterogeneous reactions requires computationally intensive calculations and is a topic for future research.

Table 8-1. Selected bond lengths (Å) and bond angles (°) for precursor **5** obtained from X-ray crystallographic measurement and DFT calculation

Bond	Calculated	Experimental
W1 - Cl ^a	2.388	2.347(16)
W1 - N1	1.749	1.769(5)
N1 - N2	1.289	1.271(8)
W1 - N3	2.268	2.224(7)
N2 - C1	1.467	1.438(7)
N1 - W1 - Cl ^a	96.8	95.9(4)
N3 - W1 - Cl ^a	83.24	84.07(4)
W1 - N1 - N2	178.0	180.0

^a Average value for four equivalent chlorides.

Table 8-2. Selected bond lengths (Å) and bond angles (°) for **5a** obtained from DFT calculation

Bond	Calculated
W1 - Cl ^a	2.351
W1 - N1	1.734
N1 - N2	1.293
Cl - W1 - N1 ^a	102.1
W1 - N1 - N2	177.5

^a Average value for four equivalent chlorides.

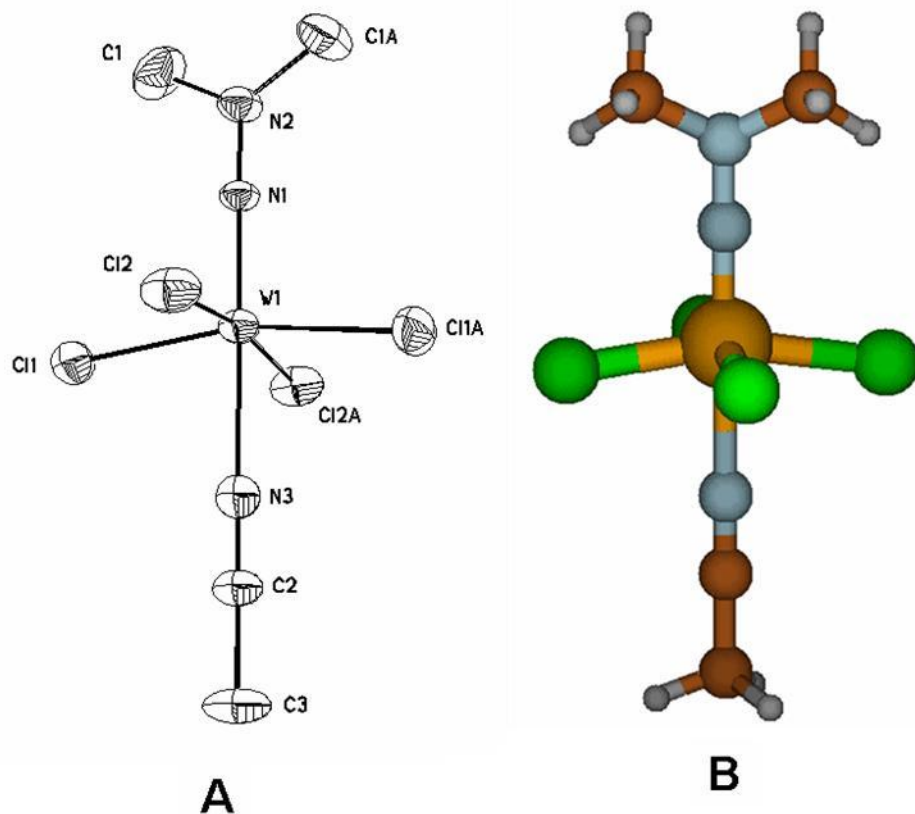


Figure 8-1. Geometry of **5**. A) X-ray crystallographic determination. The thermal ellipsoids diagram are drawn at 50 % probability. Hydrogen atoms are omitted for clarity. B) Geometry optimization by DFT calculation

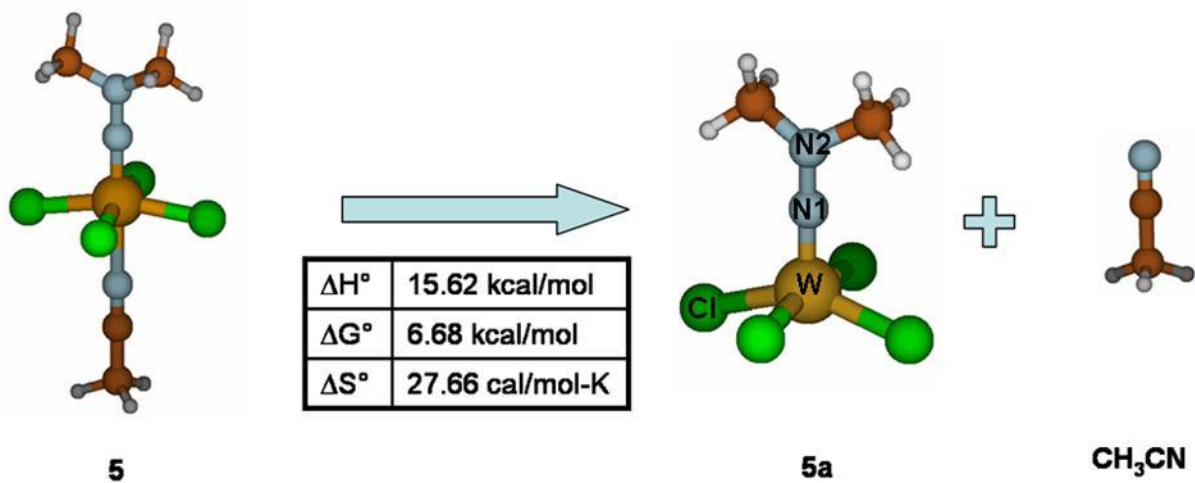


Figure 8-2. Cleavage of acetonitrile ligand from precursor **5**. The figure shows optimized geometries for **5a** and CH_3CN

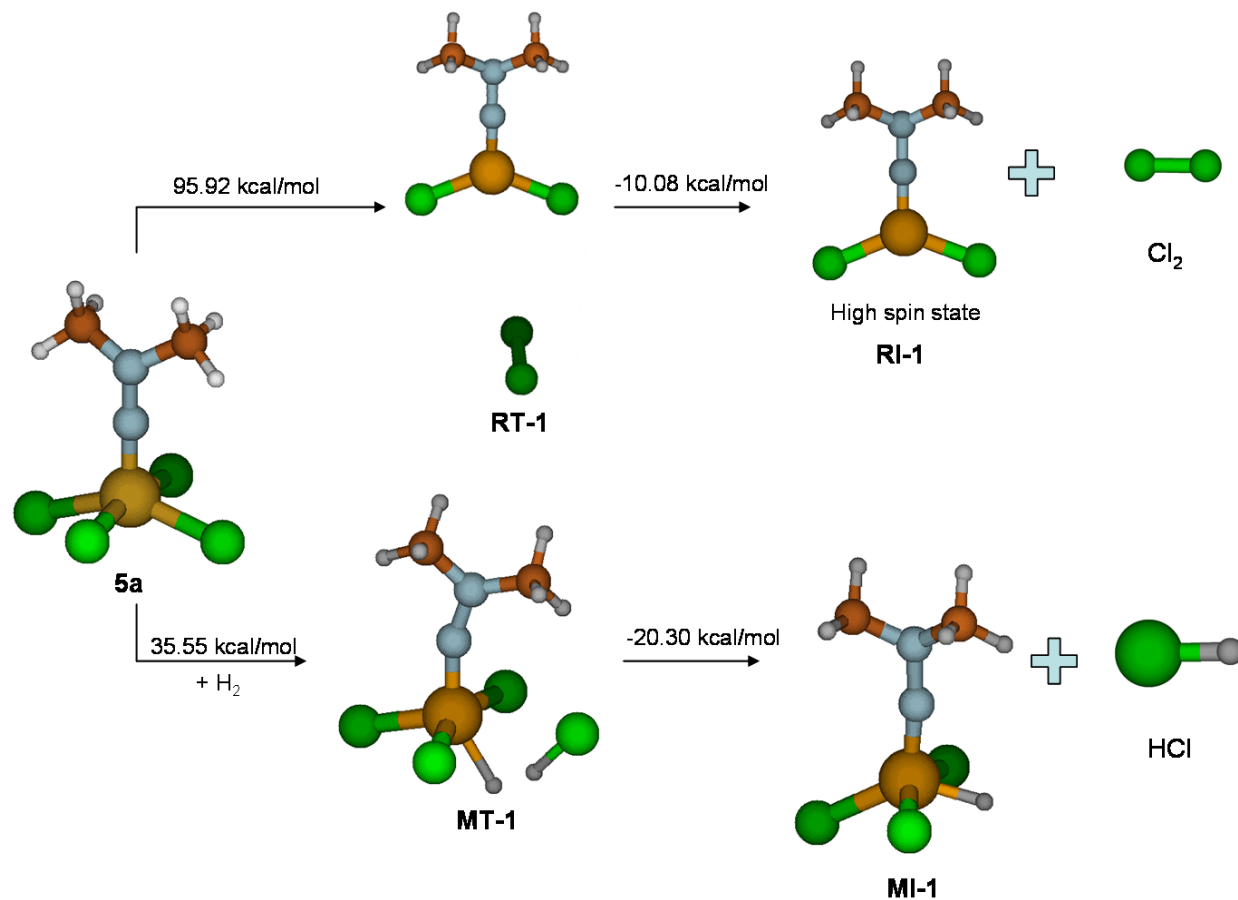


Figure 8-3. Calculated transition state and products for reductive elimination and σ -bond metathesis from **5a**. M = metathesis, R = reductive elimination, T = transition state and I = reaction intermediate

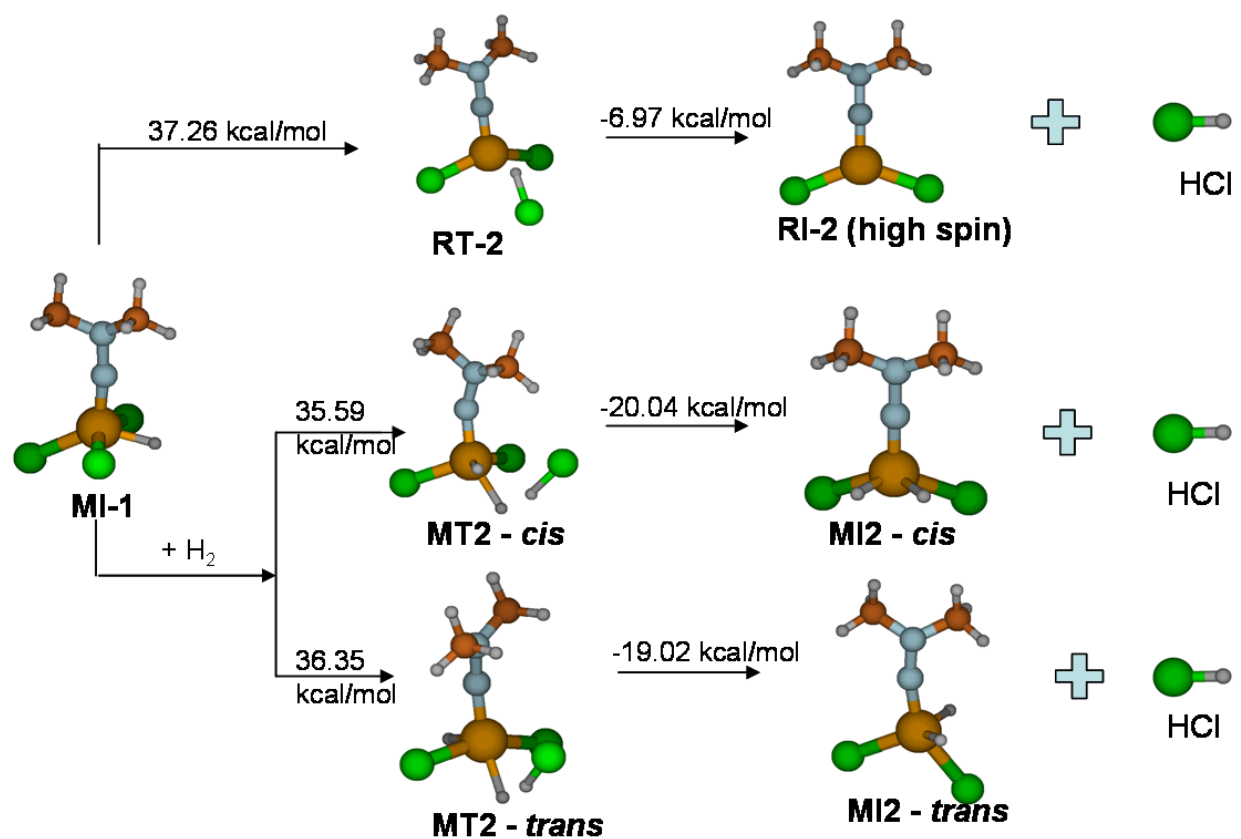


Figure 8-4. Possible reaction pathways for chloride cleavage by reductive elimination and σ -bond metathesis from MI-1 intermediate. M = metathesis, R = reductive elimination, T = transition state and I = reaction intermediate

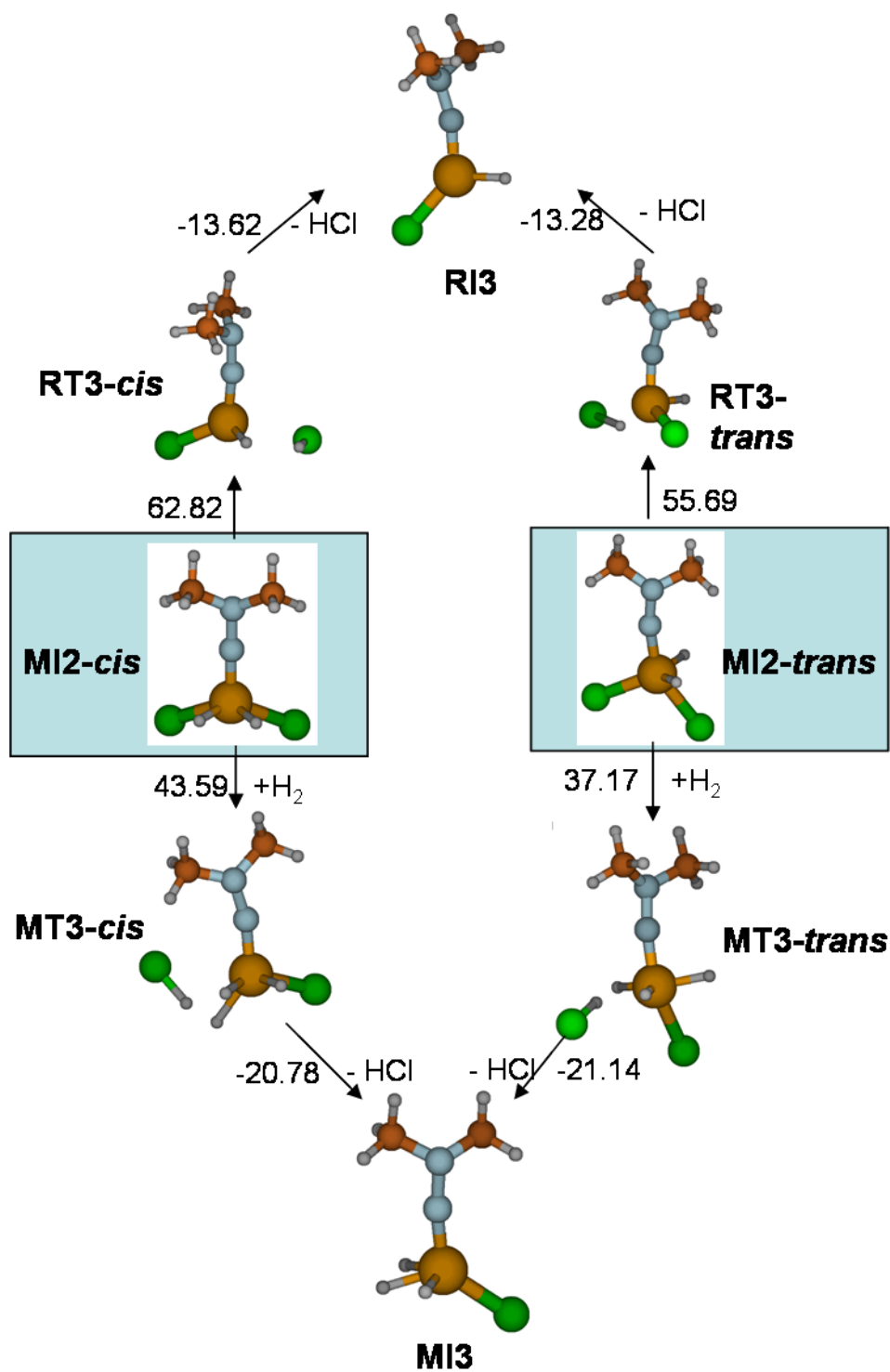


Figure 8-5. Possible reaction pathways for reductive elimination and σ -bond metathesis from MI-2 (*cis* and *trans*). M = metathesis, R = reductive elimination, T = transition state and I = reaction intermediate

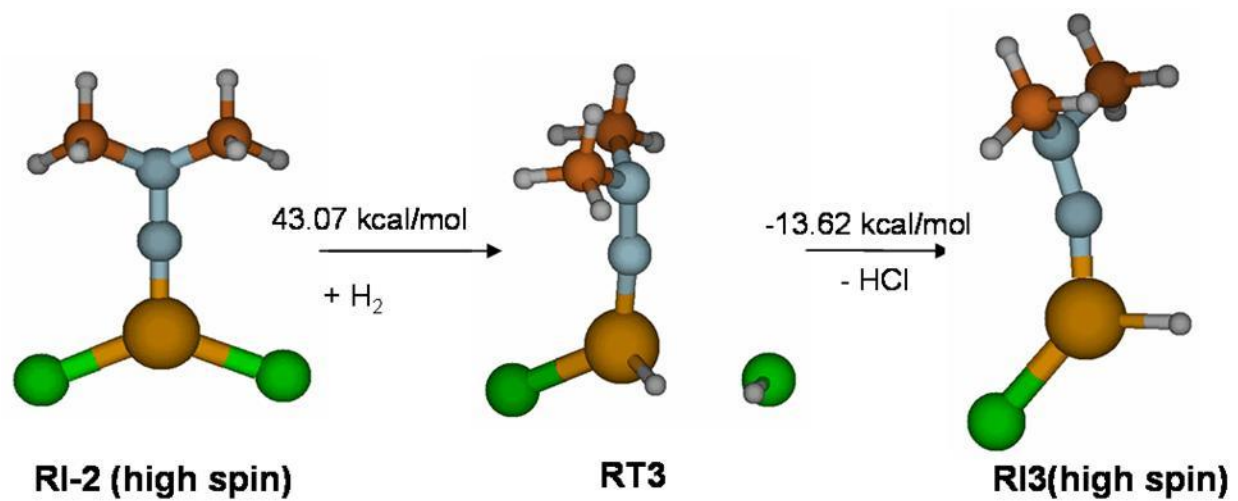


Figure 8-6. Possible reaction pathway for reductive elimination from RI-2. R = reductive elimination, T = transition state and I = reaction intermediate

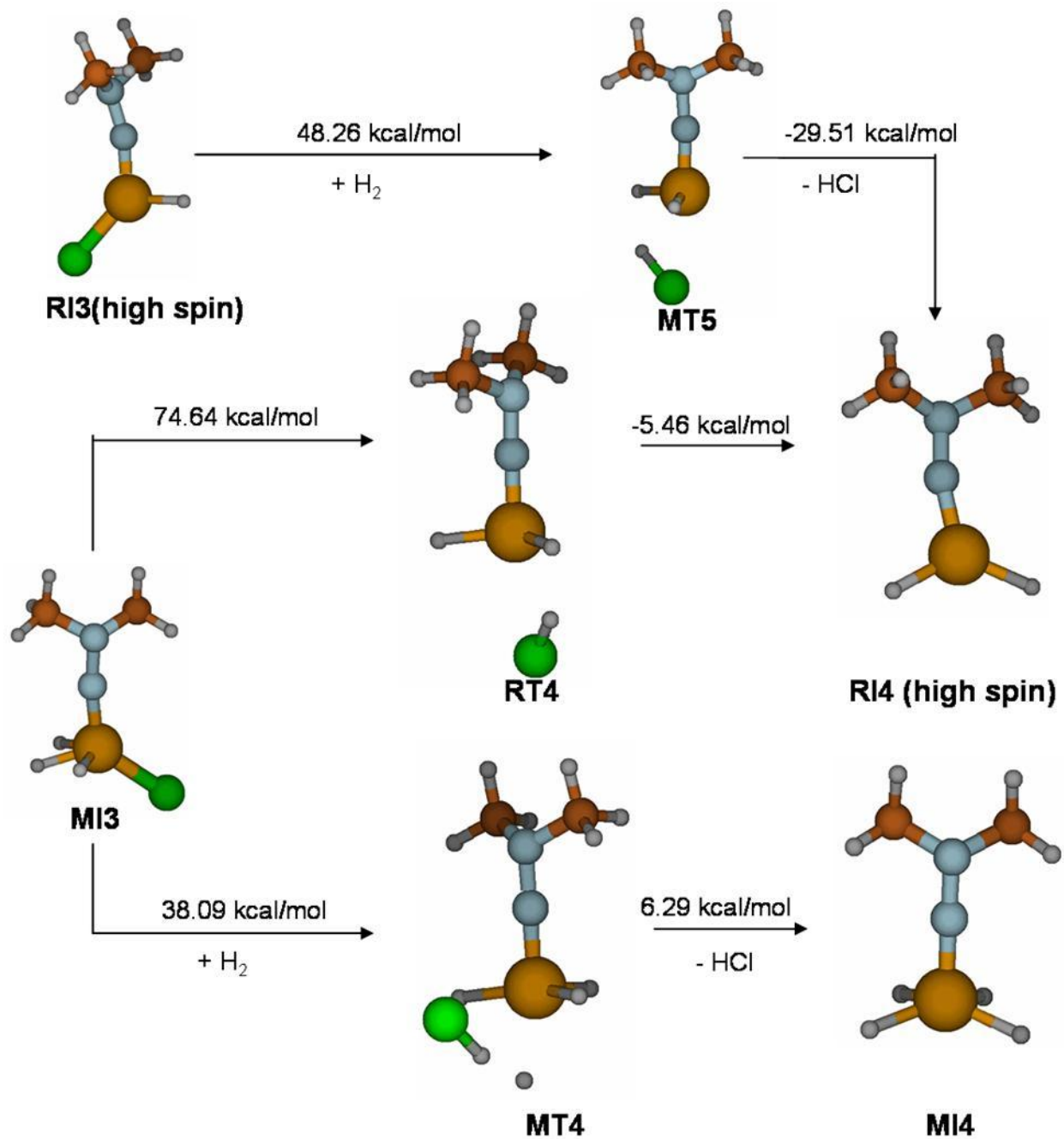
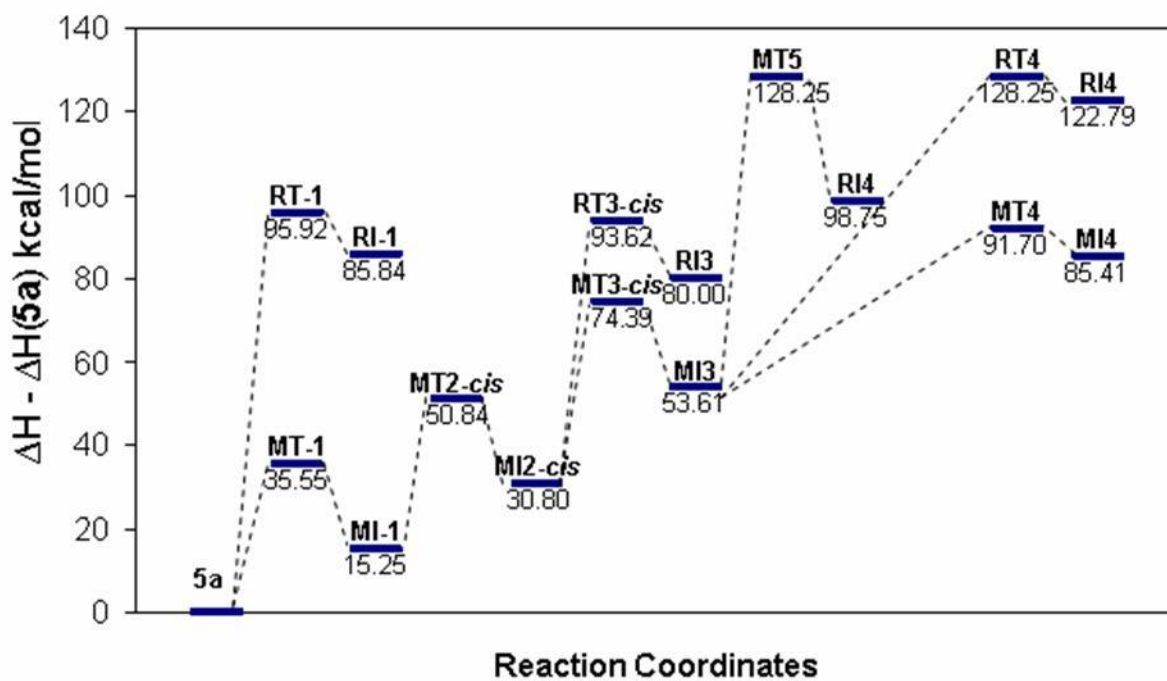
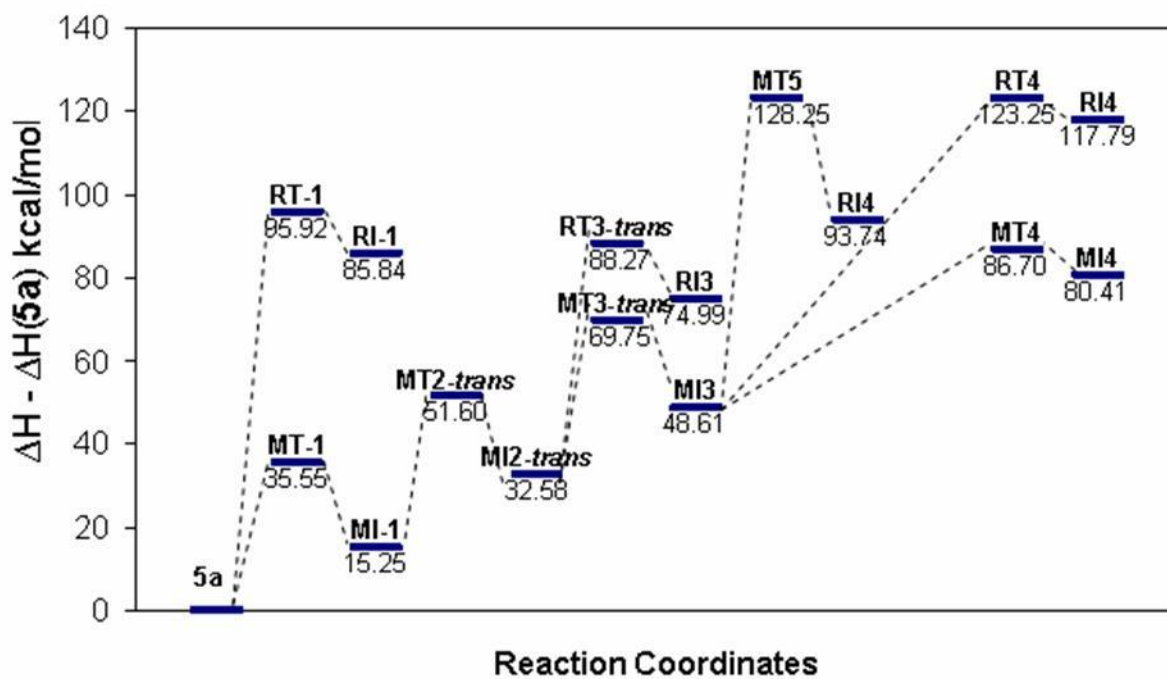


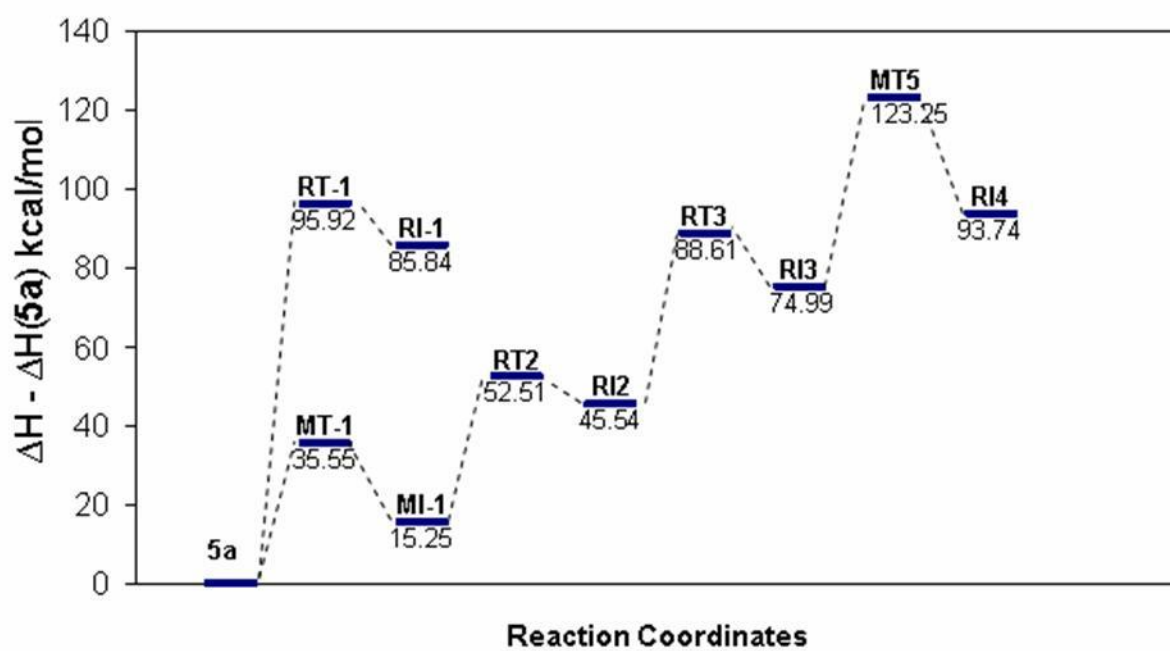
Figure 8-7. Possible reaction pathways for reductive elimination and/or σ -bond metathesis from MI-3 and RI-3. M = metathesis, R = reductive elimination, T = transition state and I = reaction intermediate



Figures 8-8. The ΔH values with respect to the ΔH (**5a**) for reaction pathway through intermediate *MI2-cis*. The energy values are in kcal/mol



Figures 8-9. The ΔH values with respect to the ΔH (**5a**) for reaction pathway through intermediate **MI2-trans**. The energy values are in kcal/mol



Figures 8-10. The ΔH values with respect to the ΔH (**5a**) for reaction pathway through intermediate RI2. The energy values are in kcal/mol

CHAPTER 9 CONCLUSION AND FUTURE WORK

The films deposited using **3a,b**, **4** and **5** show many properties that are essential for diffusion barrier application. First and foremost, the work demonstrates that WN_xC_y can be effective in preventing Cu diffusion. Films deposited at low temperature from **4** and **5a,b** are able to prevent bulk Cu deposition after annealing at 500 °C for 30 min in vacuum. Secondly, precursor **5** could be used to deposit films at temperatures as low as 300 °C indicating that MOCVD is capable of depositing films at temperature acceptable for diffusion barrier application. Third, the films showed good adhesion and were thermally and mechanically stable after annealing upto 500 °C. Fourth, WN_xC_y film promotes the growth of (111) oriented PVD Cu, which is important to obtain Cu films with high electromigration resistance.

This chapter discusses the additional experiments needed to evaluate the potential of WN_xC_y deposition from metal organic precursors for diffusion barrier application.

9.1 Diffusion Barrier Testing

The diffusion barrier testing reported in the present work gives preliminary results on the effectiveness of barrier film in preventing bulk Cu diffusion. However, these tests need further refinement in three critical areas: film thickness control, contamination control and trace copper detection under realistic testing conditions.

9.1.1 Film Thickness Control

The barrier films tested in present work used relatively thick films (20 - 80 nm) for evaluating their efficacy as diffusion barriers. Future copper metallization would require barrier films that are thinner than 10 nm. Atomic layer deposition shows the most promise for deposition of ultra thin barrier films with excellent conformality. Since **4** and **5** have shown promising results for films deposited by MOCVD, these precursors should be used in ALD mode

to meet the thickness and conformality requirements for future barrier films. Actual barrier testing on these ultra-thin films is essential for providing accurate evaluation of the barrier material as well as the deposition process.

There are a number of challenges that need to be addressed to deposit ALD films using precursors **4** and **5**. Since precursors **4** and **5** are solids with low vapor pressure, their delivery in the reactor requires dissolution of the precursor in a suitable solvent such as benzonitrile. For MOCVD growth, the precursor solvent mixture was delivered to the reactor using a nebulizer system. The ALD system needs to be modified so that it can use the nebulizer system for delivery of the precursor solution. For ALD, the nebulizer system should be capable of withstanding 1 Torr operating pressure. The nebulizer system used in present work requires relatively high pressure of 350 Torr. However such high pressures are not suitable for ALD, so the nebulizer system also needs to be redesigned so that it is capable of operating at lower pressures (~ 1 Torr).

9.1.2 Contamination Control

AES studies done on films deposited from **4** and **5** have shown that films deposited at low deposition temperature (< 500 °C) contain a significant amount of O contamination. In the presence of a high level of contamination, the diffusion barrier performance of the film could be significantly altered. The XPS studies have shown that the source of O is not only the residual O in the reactor, but also post-growth O incorporated during exposure of the film to the atmosphere. To reduce the O incorporated during film growth, it is essential to grow film in a clean system. This might be possible in the new ALD reactor system, which could be purged and kept under inert atmosphere so that the reactor is not exposed to atmosphere after every experiment. The transfer chamber attached to the ALD reactor could then be used to load the samples into the ALD system. To reduce the O incorporated due to post-growth exposure to

atmosphere, the barrier films need to be coated with Cu *in situ*. *In situ* Cu deposition would eliminate or at least minimize the O contamination from atmosphere. The CVD reactor has been connected to the ALD reactor through the transfer chamber so that *in situ* deposition of Cu is now possible. Future experiments should be performed using this new system to ascertain the ‘true’ properties and diffusion barrier capabilities of the barrier film.

9.1.3 Realistic Diffusion Barrier Testing

The diffusion barrier testing reported in present work accelerated the diffusion process by annealing the Cu/barrier/Si stack in vacuum at 500 °C. However, the driving force for diffusion in actual ICs is not just temperature but also bias. Hence, a more realistic test to access the diffusion barrier efficacy would be bias temperature stress. To detect Cu diffusion, the present work used AES depth profiling and XRD measurements. These techniques are good for detecting bulk Cu diffusion but not trace Cu diffusion. The detection of Cu should be done using electrical characterization such as p⁺n junction diode because electrical characterization is able to detect trace Cu diffusion through the barrier film.

9.2 Diffusion Barrier Integration

At present, numerous processes and materials have shown good promise for fulfilling the future requirements of diffusion barrier thin film. However, significant work needs to be done on integration of these barrier films into actual interconnect. While a barrier film might be excellent in preventing Cu diffusion, there are additional requirements on the barrier film and deposition process. The barrier film needs to have good adhesion to adjacent layers and that include Cu, low-*k* dielectric and etch stop layers. While the present work reported film growth only on Si substrate, additional work needs to be done to determine adhesion of the WN_xC_y film to Cu, low-*k* dielectric and etch stop layers. The four point bend test is an excellent technique to ascertain the adhesion of thin films quantitatively. These tests need to be performed on the

barrier film deposited on different substrates. The barrier deposition process also needs to be compatible with the overall metallization deposition scheme. This includes low deposition temperature and pin-hole free film deposition. Lastly, the barrier deposition process which employs gaseous reactants should be compatible with ultra low- k dielectrics. Since ultra low- k dielectric films are highly porous, the gaseous reactants used in CVD and ALD process could diffuse through the dielectric film, thereby increasing its the dielectric constant and negating any benefits obtained from adoption of ultra low- k dielectric film. The integration of CVD or ALD with ultra low- k dielectric films is a challenge for future metallization schemes and pore sealing techniques for ultra low- k films like plasma exposure need to be explored.

APPENDIX DENSITY FUNCTIONAL THEORY

The energy of a multi-particle system, E , is given by the Schrödinger equation (Eq. A-1).

$$E\Psi = H\Psi \tag{A-1}$$

Ψ is the wave function and H is the Hamiltonian operator. The Hamiltonian operator in the Schrödinger equation depends on the positions and atomic number of the nuclei and the total number of electrons. The dependence of the Hamiltonian on the total number of electrons suggests that a useful physical observable would be the electron density ρ , since, integrated over all space, it gives the total number of electrons N .

$$N = \int \rho(r) dr \tag{A-2}$$

The assignment of nuclear atomic numbers is also available from the density, since for each nucleus A located at an electron density maximum r_A ,

$$\left. \frac{\partial \bar{\rho}}{\partial r_A} \right|_{r_A=0} = -2Z_A \rho(r_A) \tag{A-3}$$

Given a known density, one could form the Hamiltonian operator, solve the Schrödinger equation, and determine the wave functions and energy eigenvalues. Hohenberg and Kohn proposed two theorems that revolutionized the DFT methodology.²¹⁰

- Hohenberg-Kohn existence theorem: the non-degenerate ground state density must determine the external potential (the charges and positions of the nuclei), and thus the Hamiltonian and the wave function.
- Hohenberg-Kohn Variational Theorem: the density obeys the variational principle.

Kohn-Sham self-consistent field methodology takes as a starting point a fictitious system of non-interacting electrons that have for their overall ground state density the same density as some real system of interest where electrons do interact. Since the electron density determines

the position and atomic numbers of nuclei, these quantities are necessarily identical in the non-interacting and in the real systems. The energy functional is then divided into specific components to facilitate further analysis.

$$E(\rho) = T_{\text{ni}}[\rho(r)] + V_{\text{ne}}[\rho(r)] + V_{\text{ee}}[\rho(r)] + \Delta T[\rho(r)] + \Delta V_{\text{ee}}[\rho(r)] \quad (\text{A-4})$$

T_{ni} is the kinetic energy of non-interacting electrons, V_{ne} is the nuclear-electron interaction, V_{ee} is electron-electron repulsion, ΔT is the correction to the kinetic energy deriving from the interacting nature of electrons and ΔV_{ee} includes all non-classical corrections to electron-electron repulsion energy. The above equation can be rewritten as Equation A-5.

$$E[\rho(r)] = \sum_i^N \left(\langle \chi_i | -\frac{1}{2} \nabla_i^2 | \chi_i \rangle - \langle \chi_i | \sum_k^{\text{nuclei}} \frac{Z_k}{|r_i - r_k|} | \chi_i \rangle \right) + \left(\sum_i^N \langle \chi_i | \frac{1}{2} \int \frac{\rho(r')}{|r_i - r'|} dr' | \chi_i \rangle \right) + E_{\text{xc}}[\rho(r)] \quad (\text{A-5})$$

N is the number of electrons in the system and E_{xc} is the exchange-correlation energy (a parameter that accounts for the terms ΔT and ΔV_{ee}). The density is given by Equation A-6.

$$\rho = \sum_{i=1}^N \langle \chi_i | \chi_i \rangle \quad (\text{A-6})$$

If orbitals χ minimize E , then Equation A-7 can be used to calculate E .

$$h_i^{\text{KS}} \chi_i = \varepsilon_i \chi_i \quad (\text{A-7})$$

The Kohn-Sham one electron operator is defined by Equation A-8.

$$h_i^{\text{KS}} = -\frac{1}{2} \nabla_i^2 - \sum_k^{\text{nuclei}} \frac{Z_k}{|r_i - r_k|} + \int \frac{\rho(r')}{|r_i - r'|} dr' + V_{\text{xc}} \quad (\text{A-8})$$

$$V_{\text{xc}} = \frac{\delta E_{\text{xc}}}{\delta \rho} \quad (\text{A-9})$$

V_{xc} is the so-called functional derivative. For the determination of Kohn-Sham (KS) orbitals, a basis set is used, similar to the Hartree Fock method. The KS orbitals are expressed within a

basis set of functions $\{\Phi_i\}$. The individual orbital coefficients are determined by solution of a secular equation (as in the Hartree Fock method).

Spin correction is made in DFT by using individual functionals of α and β densities. The spin densities at any position are expressed in terms of ζ , the normalized spin polarization.

$$\zeta(r) = \frac{\rho^\alpha(r) - \rho^\beta(r)}{\rho(r)} \quad (\text{A-10})$$

A.1 Exchange-Correlation Functional (E_{xc})

The exchange-correlation functional accounts for:

- coulombic correlation energy associated with electron-electron repulsion
- quantum mechanical exchange which arises from antisymmetry requirement
- correction for classical self-interaction energy
- difference in kinetic energy between a fictitious non-interacting system and a real system.

In practice, most modern functionals do not try to compute (4) explicitly. The effect of (4) is either ignored completely or it is incorporated using ‘hole function’ with kinetic energy correction.

A.1.1 Exchange Energy Density

Hohenberg and Kohn showed that if the electron density varies extremely slowly with position, then $E_{xc}(\rho)$ is accurately given by Equation A-11.

$$E_{xc}^{LDA} = \int \rho(r) \varepsilon_{xc}(\rho) dr \quad (\text{A-11})$$

ε_{xc} ($= \varepsilon_x + \varepsilon_c$) is the exchange plus correlation energy per electron in a homogenous electron gas. Slater proposed that the exchange hole about any position could be approximated as a sphere of constant potential with a radius depending on the magnitude of the density at that position. With this approximation, the ε_x is determined by Equation A-12.

$$\varepsilon_x(\rho) = -\frac{9\alpha}{8} \left(\frac{3}{\pi}\right)^{1/3} \int \rho^{4/3}(r) dr \quad (\text{A-12})$$

The Slater approach takes the value of $\alpha = 1$. The LDA (local density approximation) approach takes a value of $\alpha = 2/3$ while the X_α model most typically uses $\alpha = 3/4$. The LDA, Slater and X_α methods can be extended to account for spin polarization using the equation A-13.

$$\varepsilon_x[\rho(r), \zeta] = \varepsilon_x^0[\rho(r)] + \{\varepsilon_x^1[\rho(r)] - \varepsilon_x^0[\rho(r)]\} \left[\frac{(1+\zeta)^{4/3} + (1-\zeta)^{4/3} - 2}{2(2^{1/3} - 1)} \right] \quad (\text{A-13})$$

ε_x^1 is the exchange energy for system of uniform electron gas with electrons of like spin and ε_x^0 is the exchange energy calculated using equation derived by Slater. Systems that have spin polarization (e.g. open shell systems) must use the spin polarized formalism and it is generally referred to as ‘local spin density approximation’ (LSDA).

A.1.2 Correlation Energy Density

Even for a simple uniform electron gas, no analytical derivation has been reported. However, by using Monte Carlo techniques, the total energy of uniform electron gases of several different densities have been calculated to a very high accuracy.²¹¹ By subtracting the exchange energy density for each case, the correlation energy density can then be calculated. The functional is given by Equation A-15.

$$\varepsilon_c^i(r_s) = \frac{A}{2} \left\{ \begin{array}{l} \ln \frac{r_s}{r_s + b\sqrt{r_s} + c} + \frac{2b}{\sqrt{4c - b^2}} \tan^{-1} \left(\frac{\sqrt{4c - b^2}}{2\sqrt{r_s} + b} \right) \\ - \frac{bx_0}{x_0^2 + bx_0 + c} \left\{ \ln \left[\frac{(\sqrt{r_s} - x_0)^2}{r_s + b\sqrt{r_s} + c} \right] + \frac{2(b + x_0)}{\sqrt{4c - b^2}} \tan^{-1} \left(\frac{\sqrt{4c - b^2}}{2\sqrt{r_s} + b} \right) \right\} \end{array} \right\} \quad (\text{A-14})$$

$$r_s(r) = \left(\frac{3}{4\pi\rho(r)} \right)^{1/3} \quad (\text{A-15})$$

A, x_0 , b, c are different empirical constants for $i = 0$ and $i = 1$. Vosko *et al.* proposed several different fitting schemes, and two functional forms (VWN and VWN5) have been widely

used.²¹² LSDA calculations that employ a combination of Slater exchange and the VWN correlation energy expression are referred to as using SVWN method.

A.2 Density Gradient Correction

The LSDA approximation assumes a uniform electron gas as the source of energy expression. It is assumed that the exchange-correlation energy density at every position in space for the molecule is the same as it would be for the uniform electron gas having the same density as is found at that position. However, in a molecule, this approximation is not true. A plausible way to increase the accuracy of the correlation functional for molecular calculations is to make it depend not only on the local value of density but also on the gradient of density. This approach is referred to as ‘gradient corrected’ or ‘generalized gradient approximation’ (GGA). The correction term is added to the LDA functional.

$$\varepsilon_{x/c}^{GGA} [\rho(r)] = \varepsilon_{x/c}^{LSD} [\rho(r)] + \Delta\varepsilon_{x/c} \left[\frac{\nabla\rho(r)}{\rho^{4/3}(r)} \right] \quad (\text{A-16})$$

The subscript x/c indicates that the same functional holds for either exchange or correlation.

A.2.1 Correction to Exchange Functional:

The most popular GGA exchange functional has been developed by Becke (usually abbreviated by ‘B’).²¹³ The ‘B’ functional has a single empirical parameter which is optimized by fitting to the exactly known exchange energies of the six noble gas atoms He through Rn. Several other exchange functionals that have been reported are CAM(B), FT9 and mPW.²¹⁴⁻²¹⁶ There is very little data available in literature on the comparison of these different functionals for actual molecules.

A.2.2 Correction to Correlation Functional

Various functionals developed by researchers for GGA correction to the correlation functional include PW86, PW91, B95 and LYP.²¹⁷⁻²²⁰ The PW86 functional includes one

empirical parameter fitted for the neon gas atom. The PW91 and B95 functionals use a different expression from the general expression described above and do not contain any empirical parameter. LYP does not correct the LDA expression but computes the full correlation energy. It contains four empirical parameters fitted to the He atom. Of all the correlation functionals, LYP is the only one that provides an exact cancellation of the self-interaction error in one-electron systems. The LYP functional has proved more robust for systems that are more prone to over delocalization because of its effective cancellation of self-interaction error.

The common nomenclature of expressing the functionals used in calculation is combining the acronyms for correlation and exchange functionals. For instance, BLYP calculation combines Becke's GGA exchange with the GGA correlation functional of Lee, Yang and Parr. In literature, the most widely used combinations are BP86, B3LYP and BPW91. Results from these three levels of theory are fairly comparable.

A.3 Similarity Between Hartree-Fock (HF) and DFT Methodologies

The two main similarities between HF and DFT techniques are:

- Mathematically, both use basis sets to obtain orbitals
- The kinetic energy and nuclear attraction components of matrix elements are identical.

There is a key difference between HF and DFT methodologies. Density functional theory contains no approximations, it is exact. It is only required to know E_{xc} as a function of ρ . Since the exact nature of E_{xc} is not known, the relevant equations are solved approximately. In contrast, HF is a deliberately approximate theory.

A.4 Comparison of DFT to Molecular Orbital Theory²⁰⁵

A.4.1 Computational Efficiency

The formal scaling of DFT has been noted to be in principle no worse than N^3 , where N is the number of basis functions used to represent KS (Kohn-Sham) orbitals. This is better than HF

which scales by a factor of N^4 . The scaling factor refers to how computational time increases with the number of basis functions. For programs that use the same algorithms to carry out HF and DFT calculations, the cost of a DFT calculation on a moderately sized molecule (~ 15 atoms) is double that of the HF calculations with the same basis set. However, if the program is optimized for DFT, the calculation cost is much lower for DFT as compared to HF method.

A.4.2 Energetics

For a given average level of accuracy, hybrid DFT methods are the most efficient in predicting atomization energies as compared to more expensive methods. Of the currently available DFT models, GGA models offer a major improvement over the older LSDA model. Moreover, the P86 functional should be avoided. There is no clear preference amongst the remaining functionals, other than noting that the hybrid functional tends to perform better than pure functionals.

In calculating binding energies in transition metal compounds such as hydrides, the molecular orbital method is not very accurate until quite high levels are used to account for the electron correlation. In contrast, DFT has been shown to predict binding energies in transition metal compounds more accurately.

A.4.3 Geometries

Analytical first derivatives are available for almost all density functionals, and as a result geometry optimization can be carried out with facility. The performance of most functionals is usually quite good when it comes to predicting minimum energy structures. Accuracies in bond angles for DFT average about 1 degree, the same as is found for HF and MP2.

For transition metals, DFT has proven to be a tremendous improvement over HF and post-HF methods, particularly when the metal atom is coordinatively unsaturated. The narrow separation between filled and empty d-block orbitals typically leads to enormous non-dynamical

correlation problems with an HF treatment, and DFT is much less prone to analogous problems. Even in cases of a saturated coordination sphere, DFT methods typically significantly outperform HF and MP2.

Density functional theory has shown weakness in predicting geometries for van der Waals complexes and ionic complexes. Hydrogen bonds are somewhat too short as a rule, and most charge transfer complexes have their polarities overestimated.

A.5 The Future of DFT

The DFT methodology has become very popular for various calculations in quantum chemistry. Density functional theory has the advantage of allowing for correlation effects to be included in a calculation that takes roughly the same time as a HF calculation, which does not include correlation. However there are some drawbacks of the DFT method and these are the areas that are currently being actively investigated. There is no systematic way of improving the DFT calculations. There is no clear roadmap for the systematic improvement of the E_{xc} functionals. It is certain that a lot of research effort in the future is going to be on the formulation of these functionals.

Density functional theory also has not been widely accepted as the method of choice for excited states. The development of DFT formalisms to handle excited states remains a subject of active research. Since DFT uses approximate functionals, KS DFT is not variational and can yield an energy below the true ground state energy. Calculations with gradient corrected functionals are size consistent. The currently used KS DFT functionals often do not give good results for activation energies of reactions. Although KS DFT yields good results for most molecular properties with the presently available functionals, KS DFT cannot match the accuracy that methods like CCSD(T) and QCISD(T) can achieve. Of course, CCSD(T) and QCISD(T) are limited to dealing with small molecules, whereas DFT can handle rather large

molecules. In summary, DFT has emerged as one of the promising fields in the field of quantum calculations. It is most certainly going to be an area of active research in the years to come.

LIST OF REFERENCES

- ¹ P. Van Zant, *Microchip Fabrication: A Practical Guide to Semiconductor Processing*, (McGraw-Hill, 2000).
- ² M. T. Bohr, "Interconnect Scaling - The real limiter to high performance ULSI," Proceedings of IEEE International Electron Devices Meeting, 241 (1995).
- ³ S. P. Murarka, I. V. Verner, and R. J. Gutmann, *Copper-Fundamental Mechanisms for Microelectronic Applications* (John Wiley and Sons, New York, NY, 2000).
- ⁴ R. I. M. Dang, and N. Shigyo, IEEE Electron Devices Lett. **EDL-2**, 196 (1981).
- ⁵ S. P. Jeng, R. H. Havemann, and M. C. Chang, Mat. Res. Soc. Symp. **337**, 24 (1994).
- ⁶ G. H. Schnable, and R. S. Keen, Proceedings of the IEEE **57**, 1570 (1969).
- ⁷ R. V. Penny, Physics and Chemistry of Solids **25**, 335 (1964).
- ⁸ K. N. Tu, J. Appl. Phys. **94**, 5451 (2003).
- ⁹ I. Ames, F. M. d'Heurle, and R. E. Horstmann, IBM J. Research and Development **14**, 461 (1970).
- ¹⁰ M. Sakimoto, T. Fujii, H. Yamaguchi, and K. Eguchi, Proceedings of the IEEE Reliability Physics Symposium, Las Vegas, NV, 333, April (1995).
- ¹¹ K. Maex, M. R. Baklanov, S. H. Brongersma, and Z. S. Yanovitskaya, J. Appl. Phys. **93**, 8793 (2003).
- ¹² M. Michael, R. E. Todd, J. -H. Zhao, C. Hu, T. Cho, and P. S. Ho, Annual Review of Materials Science **30**, 645 (2000).
- ¹³ F. Iacopi, C. Zistl, C. Jehoul, Z. S. Tokei, Q. T. Le, A. Das, C. Sullivan, G. Prokopowicz, D. Gronbeck, M. Gallagher, J. Calvert, and K. Maex, Microelectron. Eng. **64**, 351 (2002).
- ¹⁴ A. A. Istratov, C. Flink, and E. R. Weber, Physica Status Solidi B: Basic Research **222**, 261 (2000).
- ¹⁵ E. R. Weber, Appl. Phys. **A30**, 1 (1983).
- ¹⁶ A. A. Istratov, H. Hedemann, M. Seibt, O. F. Vyvenko, W. Schroter, T. Heiser, C. Flink, H. Hieslmair, and E. R. Weber, J. Electrochem. Soc., **145**, 3889 (1998).

- ¹⁷ C. Flink, H. Feick, S. A. McHugo, W. Seifert, H. Hieslmair, T. Heiser, A. A. Istratov, and E. R. Weber, *Physical Rev. Lett.* **85**, 4900 (2000).
- ¹⁸ B. J. Howard, and C. Steinbruchel, *Appl. Phys. Lett.* **59**, 914 (1991).
- ¹⁹ D. Shamiryan, T. Abell, F. Iacopi, and K. Maex, *Mater. Today* **7**, 34 (2004).
- ²⁰ L. Peters, 'Alers visits interconnect reliability concerns', *Semiconductor International* Sept. (2005), <http://www.reed-electronics.com/semiconductor/article/CA6252222?pubdate=9%2F1%2F2005>, last accessed May (2007).
- ²¹ C. L. Gan, C. V. Thompson, K. L. Pey, W. K. Choi, H. L. Tay, B. Yu, and M. K. Radhakrishnan, *Appl. Phys. Lett.* **79**, 4592 (2001).
- ²² C. -K. Hu, K. L. Lee, D. Gupta, and P. Blauner, *Mat. Res. Soc. Symp. Proc.* **428**, 43 (1996).
- ²³ C. -K. Hu, L. Gignac, E. Liniger, B. Herbst, D. L. Rath, S. T. Chen, S. Kaldor, A. Simon, and W. -T. Tseng, *Appl. Phys. Lett.* **83**, 869 (2003).
- ²⁴ C. -K. Hu, L. Gignac, and R. Rosenberg, *Microelectron. Reliability* **46**, 213 (2005).
- ²⁵ E. G. Liniger, and C. Dziobkowski, *Thin Solid Films* **513**, 295 (2006).
- ²⁶ A. V. Vairagar, Z. Gan, V. Shao, S. G. Mhaisalkar, H. Li, K. N. Tu, Z. Chen, E. Zschech, H. J. Engelmann, and S. Zhang, *J. Electrochem. Soc.* **153**, G840 (2006).
- ²⁷ International Technology Roadmap for Semiconductors, www.itrs.net, (2005), last accessed May (2007).
- ²⁸ S. M. Rosnagel, and J. Hopwood, *Appl. Phys. Lett.* **63**, 3285 (1993).
- ²⁹ A. Paranjpe, R. Bubber, L. Velo, G. Shang, S. Gopinath, J. Dalton, and M. Moslehi, *Proceedings of IEEE International Interconnect Technology Conference*, San Francisco, CA, 119, May (1999).
- ³⁰ A. E. Kaloyeros, and E. Eisenbraun, *Annual Rev. in Material Science* **30**, 363 (2000).
- ³¹ M. H. Tsai, S. C. Sun, H. T. Chiu, and S. H. Chuang, *Appl. Phys. Lett.* **68**, 1412 (1996).
- ³² R. Ecke, S. E. Schulz, M. Hecker, and T. Gessner, *Microelectron. Eng.* **64**, 261 (2002).
- ³³ S. Bystrova, A. A. I. Aarnink, J. Holleman, and R. A. M. Wolters, *J. Electrochem. Soc.* **152**, G522 (2005).
- ³⁴ K. Wetzig and C. M. Schneider, *Metal Based Thin Films for Electronics*, 2nd Edition, figure 4.1(b) page 231 (Wiley-VCH, 2006).

- ³⁵ D. T. Price, R. J. Gutmann, and S. P. Murarka, *Thin Solid Films* **308–309**, 525 (1997).
- ³⁶ N. A. Gjostein, *Diffusion* (American Society for Metals, Metal Park, Ohio 1973).
- ³⁷ M. A. Nicolet, *Thin Solid Films* **52**, 415 (1978).
- ³⁸ B. Movchan, and A. Demchishin, *Fiz. Metal. Metalloved.* **28**, 653 (1969).
- ³⁹ L. E. Toth, *Transition Metal Carbides and Nitrides*, (Academic Press, New York and London, 1971).
- ⁴⁰ J. A. Thornton, and D. W. Hoffman, *Thin Solid Films* **171**, 5 (1989).
- ⁴¹ N. Hellgren, K. Maca, E. Broitman, M. P. Johansson, L. Hultman, and J-E. Sundgren, *J. Appl. Phys.* **88**, 524 (2000).
- ⁴² M. Uekubo, T. Oku, K. Nii, M. Murakami, K. Takahiro, S. Yamaguchi, T. Nakano, and T. Ohta, *Thin Solid Films* **286**, 170 (1996).
- ⁴³ D. Mao and J. Hopwood, *J. Appl. Phys.* **96**, 820 (2004).
- ⁴⁴ J. A. T. Norman, *J. Phys. IV France* **11**, 497 (2001).
- ⁴⁵ J. S. Becker, S. Suh, S. Wang, and R. G. Gordon, *Chem. Mater.* **15**, 2969 (2003).
- ⁴⁶ M. Ritala, M. Leskelä, *Handbook of Thin Film Materials, vol. 1*, 103, (Academic Press 2001).
- ⁴⁷ G. W. Book, K. Pfeifer, and S. Smith, *Microelectron. Eng.* **64**, 255 (2002).
- ⁴⁸ H. Kizil, and C. Steinbruchel, *Thin Solid Films* **449**, 158 (2004).
- ⁴⁹ T. Heiser, C. Brochard, and M. Swaaneen, *Mat. Res. Soc. Symp. Proc.* **612**, D7.3.1 (2000).
- ⁵⁰ T. Heisner, S. McHugo, H. Hieslmair, and E. R. Weber, *Appl. Phys. Lett.* **70**, 3576 (1997).
- ⁵¹ S. R. Kurtz, and R. G. Gordon, *Thin Solid Films* **140**, 277 (1986).
- ⁵² A. Sherman, *J. Electrochem. Soc.* **137**, 1892 (1990).
- ⁵³ N. Yokoyama, K. Hinode, and Y. Homma, *J. Electrochem. Soc.* **138**, 190 (1991).
- ⁵⁴ J. C. Hu, T. C. Chang, L. J. Chen, Y. L. Yang, S. Y. Chen, and C. Y. Chang, *J. Vac. Sci. Technol. A* **17**, 2389 (1999).

- ⁵⁵ M. J. Buiting, A. F. Otterloo, and A. H. Montree, *J. Electrochem. Soc.* **138**, 500 (1991).
- ⁵⁶ C. Faltermeier, C. Goldberg, M. Jones, A. Upham, D. Manger, G. Peterson, J. Lau, and A. E. Kaloyeros, *J. Electrochem. Soc.* **144**, 1002 (1997).
- ⁵⁷ C. Faltermeier, C. Goldberg, M. Jones, A. Upham, A. Knorr, A. Ivanova, G. Peterson, and A. E. Kaloyeros, *J. Electrochem. Soc.* **145**, 676 (1998).
- ⁵⁸ N. J. Archer, *Thin Solid Films* **80**, 221 (1981).
- ⁵⁹ N. J. Ianno, U. Ahmed, and D. E. Englebert, *J. Electrochem. Soc.* **136**, 276 (1989).
- ⁶⁰ A. Intemann, H. Koerner, and F. Koch, *J. Electrochem. Soc.* **140**, 3215 (1993).
- ⁶¹ K. Sugiyama, S. Pac, Y. Takahashi, and S. Motojima, *J. Electrochem. Soc.* **122**, 1545 (1975).
- ⁶² R. M. Fix, R. G. Gordon, and D. M. Hoffman, *Chem. Mater.* **2**, 235 (1990).
- ⁶³ K. -C. Park, K. -B. Kim, I. J. M. M. Raaijmakers, and K. Ngan, *J. Appl. Phys.* **80**, 5674, (1996).
- ⁶⁴ S. C. Sun, and M. H. Tsai, *Thin Solid Films* **253**, 440 (1994).
- ⁶⁵ R. M. Fix, R. G. Gordon, and D. M. Hoffman, *Chem. Mater.* **3**, 1138 (1991).
- ⁶⁶ I. J. Raaijmakers, *Thin Solid Films* **247**, 85 (1994).
- ⁶⁷ C. Amato-Wierda, and D. A. Wierda, *J. Mater. Res.* **15**, 2414 (2000).
- ⁶⁸ C. -K. Wang, L. -M. Liu, M. Liao, H. -C. Cheng, and M. -S. Lin, *Jpn. J. Appl. Phys.* **35**, 4274 (1996).
- ⁶⁹ S. -H. Kim, D. -S. Chung, K. -C. Park, K. -B. Kim, and S. -H. Min, *J. Electrochem. Soc.* **146**, 1455 (1999).
- ⁷⁰ I. J. Raaijmakers, and J. Yang, *Appl. Surf. Sci.* **73**, 31 (1993).
- ⁷¹ J. M. Bulger, C. S. Whelan, A. Dumont, M. Kuhn, and J. Clark, *J. Vac. Sci. Technol. B* **17**, 410 (1999).
- ⁷² J. -Y. Yun, and S. -W. Rhee, *Thin Solid Films* **312**, 24 (1998).
- ⁷³ W. Besling, A. Satta, J. Schumacher, T. Abell, V. Sutcliffe, A. -M. Hoyas, G. Beyer, D. Gravesteijn, and K. Maex, *Proceedings of IEEE International Interconnect Technology Conference*, Burlingame, CA, 288, June (2002).

- ⁷⁴ K. -E. Elers, V. Saanila, P. J. Soininen, W. -M. Li, J. T. Kostamo, S. Haukka, J. Juhanaja, and W. F. A. Besling, *Chem. Vap. Deposition* **8**, 149 (2002).
- ⁷⁵ M. Ritala, M. Leskelä, E. Rauhala, and P. Haussalo, *J. Electrochem. Soc.* **142**, 2731 (1995).
- ⁷⁶ S. Smith, G. Book, W. M. Li, Y. M. Sun, P. Gillespie, M. Tuominen, and K. Pfeifer, *Proceedings of the IEEE International Interconnect Technology Conference*, San Francisco, CA, 135, June (2003).
- ⁷⁷ S. Smith, W. -M. Li, K. -E. Elers, and K. Pfeifer, *Microelect. Eng.* **64**, 247 (2002).
- ⁷⁸ K. -E. Elers, J. Winkler, K. Weeks, and S. Marcus, *J. Electrochem. Soc.* **152**, G589 (2005).
- ⁷⁹ P. Mårtensson, M. Juppo, M. Ritala, M. Leskelä, and J. -O. Carlsson, *J. Vac. Sci. Technol. B* **17**, 2122 (1999).
- ⁸⁰ M. Juppo, M. Ritala, and M. Leskelä, *J. Electrochem. Soc.* **147**, 3377 (2000).
- ⁸¹ M. Juppo, P. Alén, M. Ritala, T. Sajavaara, J. Keinonen, and M. Leskelä, *Electrochem. Solid State Lett.* **5**, C4 (2002).
- ⁸² M. Juppo, A. Rahtu, and M. Ritala, *Chem. Mater.* **14**, 281 (2002).
- ⁸³ M. Ritala, M. Leskelä, E. Rauhala, and J. Jokinen, *J. Electrochem. Soc.* **145**, 2915 (1998).
- ⁸⁴ J. -S. Min, Y. -W. Son, W. -G. Kang, S. -S. Chun, and S. -K. Kang, *Jpn. J. Appl. Phys.* **37**, 4999 (1998).
- ⁸⁵ D. -J. Kim, Y. -B. Jung, M. -B. Lee, Y. -H. Lee, J. -H. Lee, and J. -H. Lee, *Thin Solid Films* **372**, 276 (2000).
- ⁸⁶ J. W. Elam, M. Schuisky, J. D. Ferguson, and S. M. George, *Thin Solid Films* **436**, 145 (2003).
- ⁸⁷ J. -H. Yun, E. -S. Choi, C. -M. Jang, and C. -S. Lee, *Jpn. J. Appl. Phys.* **41**, L418 (2002).
- ⁸⁸ J. Y. Kim, Y. Kim, and H. Jeon, *Jpn. J. Appl. Phys.* **42**, L414 (2003).
- ⁸⁹ J. Y. Kim, S. Seo, D. Y. Kim, H. Jeon, and Y. Kim, *J. Vac. Sci. Technol. A* **22**, 8 (2004).
- ⁹⁰ J. Hillman, J. Hautala, and S. Caliendo, *Proceedings of Advanced Metallization Conference*, San Diego, CA, 313, Oct. (2000).

- ⁹¹ X. Chen, G. G. Peterson, C. Goldberg, G. Nuesca, H. L. Frisch, and A. E. Kaloyeros, *J. Mater. Res.* **14**, 2043 (1999).
- ⁹² A. E. Kaloyeros, X. Chen, T. Stark, K. Kumar, S. -C. Seo, G. G. Peterson, H. L. Frisch, B. Arkles, and J. Sullivan, *J. Electrochem. Soc.* **146**, 170 (1999).
- ⁹³ A. Y. Ganin, L. Kienle, and G. V. Vajenine, *Eur. J. Inorg. Chem.* **16**, 3233 (2004).
- ⁹⁴ X. Chen, H. L. Frisch, A. E. Kaloyeros, B. Arkles, and J. Sullivan, *J. Vac. Sci. Technol. B* **17**, 182 (1999).
- ⁹⁵ M. H. Tsai, S. C. Sun, H. T. Chiu, C. E. Tsai, and S. H. Chuang, *Appl. Phys. Lett.* **67**, 1128 (1995).
- ⁹⁶ M. H. Tsai, S. C. Sun, C. P. Lee, H. T. Chiu, C. E. Tsai, S. H. Chuang, and S. C. Wu, *Thin Solid Films* **270**, 531 (1995).
- ⁹⁷ M. H. Tsai, S. C. Sun, C. E. Tsai, S. H. Chuang, and H. T. Chiu, *J. Appl. Phys.* **79**, 6932 (1996).
- ⁹⁸ R. M. Fix, R. G. Gordon, and D. M. Hoffman, *Chem. Mater.* **5**, 614 (1993).
- ⁹⁹ G. C. Jun, S. L. Cho, and K. B. Kim, *Jpn. J. Appl. Phys.* **37**, L30 (1998).
- ¹⁰⁰ S. -L. Cho, K. -B. Kim, S. -H. Min, and H. -K. Shin, *Mat. Res. Soc. Symp. Proc.* **514**, 531 (1998).
- ¹⁰¹ H. Machida, A. Hoshino, T. Suzuki, A. Ogura, and Y. Shshita, *J. Cryst. Growth* **237-239**, 586 (2002).
- ¹⁰² H. T. Chiu, and W. P. Chang, *J. Mater. Sci. Lett.* **11**, 96 (1992).
- ¹⁰³ J. W. Hong, M. L. Lee, K. I. Choi, Y. Chung, S. W. Lee, G. H. Choi, S. T. Kim, U. -I. Chung, J. T. Moon, and B. -I. Ryu, *Proceedings of the IEEE 2005 International* , 141, June (2005).
- ¹⁰⁴ L. Hiltunen, M. Leskelä, M. Mäkelä, L. Niinistö, E. Nykänen, and P. Soininen, *Thin Solid Films* **166**, 149 (1988).
- ¹⁰⁵ M. Ritala, P. Kalsi, D. Riihelä, K. Kukli, M. Leskelä, and J. Jokinen, *Chem. Mater.* **11**, 1712 (1999).
- ¹⁰⁶ P. Alén, M. Juppo, M. Ritala, and M. Leskelä, *J. Mater. Res* **17**, 107 (2002).
- ¹⁰⁷ H. Kim, A. J. Kellock, and S. M. Rossnagel, *J. Appl. Phys.* **92**, 7080 (2002).

- ¹⁰⁸ E. Eisenbraun, O. van der Straten, Y. Zhu, K. Dovidenko, and A. Kaloyeros, Proceedings of the IEEE International, Burlingame, CA, 207, June (2001).
- ¹⁰⁹ K. I. Choi, B. H. Kim, S. W. Lee, J. M. Lee, W. S. Song, G. H. Choi, U. -I. Chung, and J. T. Moon, Proceedings of the IEEE International Interconnect Technology Conference, 6th, Burlingame, CA, 129, June (2003).
- ¹¹⁰ J. -S. Park, H. -S. Park, and S. -W. Kang, J. Electrochem. Soc. **149**, C28 (2002).
- ¹¹¹ Y. Y. Wu, A. Kohn, and M. Eizenberg, J. Appl. Phys. **95**, 6167 (2004).
- ¹¹² A. Furuya, H. Tsuda, and S. Ogawa, J. Vac. Sci. Technol. B **23**, 979 (2005).
- ¹¹³ A. Furuya, N. Ohtsuka, N. Ohashi, S. Kondo, and S. Ogawa, J. Vac. Sci. Technol. A **24**, 103 (2006).
- ¹¹⁴ W. J. Maeng, S. -J. Park, and H. Kim, J. Vac. Sci. Technol. B **24**, 2276 (2006).
- ¹¹⁵ H. Kim, C. Detavenier, O. van der Straten, S. M. Rosnagel, A. J. Kellock, and D. -G. Park, J. Appl. Phys. **98**, 014308-1 (2005).
- ¹¹⁶ J. W. Hong, K. I. Choi, Y. K. Lee, S. G. Park, S. W. Lee, J. M. Lee, S. B. Kang, G. H. Choi, S. T. Kim, U. -I. Chung, and J. T. Moon, Proceedings of the IEEE International, 141, June (2005).
- ¹¹⁷ M. Nagai, and K. Kishida, Appl. Surf. Sci. **70/71**, 759 (1993).
- ¹¹⁸ M. Nagai, N. Hirano, and S. Omi, Jpn. J. Appl. Phys. **39**, 4558 (2000).
- ¹¹⁹ T. Nakajima, K. Watanabe, and N. Watanabe, J. Electrochem. Soc. **134**, 3175 (1987).
- ¹²⁰ N. Gonohe, Materials Transactions **43**, 1585 (2002).
- ¹²¹ S. D. Marcus, and R. F. Foster, Thin Solid Films **236**, 330 (1993).
- ¹²² C. Meinier, C. Monteil, C. Savall, F. Palmino, J. Weber, R. Berjoan, and J. Durand, Appl. Surf. Sci. **125**, 313 (1998).
- ¹²³ A. R. Ivanova, C. J. Galewski, C. A. Sans, T. E. Seidel, S. Grunow, K. Kumar, and A. E. Kaloveros, Mat. Res. Soc. Symp. **564**, 321 (1999).
- ¹²⁴ C. W. Lee, Y. T. Kim, and S. -K. Min, Appl. Phys. Lett. **62**, 3312 (1993).
- ¹²⁵ C. W. Lee, Y. T. Kim, C. Lee, J. Y. Lee, S. -K. Min, and Y. W. Park, J. Vac. Sci. Technol. B **12**, 69 (1994).

- ¹²⁶ C. W. Lee, Y. T. Kim, and J. Y. Lee, *Appl. Phys. Lett.* **64**, 619 (1994).
- ¹²⁷ Y. T. Kim, C. W. Lee, and S. -K. Min, *Jpn. J. Appl. Phys.* **32**, 6126 (1993).
- ¹²⁸ C. S. Kwon, D. J. Kim, C. W. Lee, Y. T. Kim, and I. -H. Choi, *Mat. Res. Soc. Symp. Proc.* **355**, 441 (1995).
- ¹²⁹ M. F. Bain, B. M. Armstrong, and H. S. Gamble, *J. Mat. Sci.* **14**, 329 (2003).
- ¹³⁰ J. Lin, A. Tsukune, T. Suzuki, and M. Yamada, *J. Vac. Sci. Technol. A* **16**, 611 (1998).
- ¹³¹ S. Ganguli, L. Chen, T. Levine, B. Zheng, and M. Chang, *J. Vac. Sci. Technol. B* **18**, 237 (2000).
- ¹³² H. -T. Chiu, S. -H. Chuang, *Mat. Res. Soc. Symp. Proc.* **250**, 317 (1992).
- ¹³³ H. -T. Chiu, S. -H. Chuang, *Mat. Res. Soc. Symp. Proc.* **8**, 1353 (1993).
- ¹³⁴ E. L. Crane, H. -T. Chiu, and R. G. Nuzzo, *J. Phy. Chem. B* **105**, 3549 (2001).
- ¹³⁵ J. E. Kelsey, C. Goldberg, G. Nuesca, G. Peterson, and B. Arkles, *J. Vac. Sci. Technol. B* **17**, 1101 (1999).
- ¹³⁶ B. H. Lee, and K. Yong, *J. Electrochem. Soc.* **151**, C594 (2004).
- ¹³⁷ S. Jeon, K. Yong, S. -G. Park, and S. -W. Rhee, *J. Vac. Sci. Technol B* **24**, 1428 (2006).
- ¹³⁸ R. G. Gordon, S. Barry, R. N. R. Broomhall-Dillard, V. A. Wagner, and Y. Wang, *Mat. Res. Soc. Symp. Proc.* **612**, D9121 (2000).
- ¹³⁹ J. W. Klaus, S. J. Ferro, and S. M. George, *Appl. Surf. Sci.* **162-163**, 479 (2000).
- ¹⁴⁰ J. W. Klaus, S. J. Ferro, and S. M. George, *J. Electrochem. Soc.* **147**, 1175 (2000).
- ¹⁴¹ S. -H. Kim, J. -K. Kim, N. Kwak, H. Sohn, J. Kim, S. -H. Jung, M. -R. Hong, S. H. Lee, and J. Colling, *Electrochem. Solid-State Lett.* **9**, C54 (2006).
- ¹⁴² H. S. Sim, S. Kim-II, and Y. T. Kim, *J. Vac. Sci. Technol. B* **21**, 1411 (2003).
- ¹⁴³ C. W. Lee, and Y. T. Kim, *J. Vac. Sci. Technol. B* **24**, 1432 (2006).
- ¹⁴⁴ J. S. Becker, and R. G. Gordon, *Appl. Phys. Lett.* **82**, 2239 (2003).
- ¹⁴⁵ W. -M. Li, K. Elers, J. Kostamo, S. Kaipio, S. Huotari, M. Soininen, P. J. Soininen, M. Tuominen, S. Haukka, S. Smith, and W. Besling, *Proceedings of the IEEE International Interconnect Technology Conference*, 191, June (2002).

- ¹⁴⁶ W. -M. Li, M. Tuominen, S. Haukka, H. Sprey, and I. J. Raaijmakers, *Solid State Technology* **106**, 103 (2003).
- ¹⁴⁷ S. -H. Kim, S. S. Oh, K. -B. Kim, D. -H. Kang, W. -M. Li, S. Haukka, and M. Tuominen, *Appl. Phys. Lett.* **82**, 4486 (2003).
- ¹⁴⁸ S. J. Wang, H. Y. Tsai, S. C. Sun, and M. H. Shiao, *J. Electrochem. Soc.* **148**, G500 (2001).
- ¹⁴⁹ A. M. Hoyas, Y. Travaly, J. Schumacher, T. Sajavaara, C. M. Whelan, B. Eyckens, O. Richard, S. Giangrandi, B. Brijs, W. Vandervorst, K. Maex, J. P. Celis, A. M. Jonas, and A. Vantomme, *J. Appl. Phys.* **99**, F64 (2006).
- ¹⁵⁰ K. -S. Kim, M. -S. Lee, S. -S. Yim, H. -M. Kim, K. -B. Kim, H. -S. Park, W. Koh, W. -M. Li, M. Stokhof, and H. Sprey, *Appl. Phys. Lett.* **89**, 081913-1 (2006).
- ¹⁵¹ A. M. Hoyas, J. Schumacher, C. M. Whelan, M. R. Baklanov, L. Carbonell, J. P. Celis, and K. Maex, *J. Vac. Sci. Technol. B* **23**, 1551 (2005).
- ¹⁵² D. Emur, V. Terzieva, J. Schumacher, V. Sutcliffe, C. M. Whelan, and K. Maex, *J. Electrochem. Soc.* **152**, B512 (2005).
- ¹⁵³ O. J. Bchir, K. M. Green, M. S. Hlad, T. J. Anderson, B. C. Brooks, C. B. Wilder, D. H. Powell, and L. McElwee-White, *J. Organomet. Chem.* **684**, 338 (2003).
- ¹⁵⁴ O. J. Bchir, S. W. Johnston, A. C. Cuadra, T. J. Anderson, C. G. Ortiz, B. C. Brooks, D. H. Powell, and L. McElwee-White, *J. Cryst. Growth* **249**, 262 (2003).
- ¹⁵⁵ O. J. Bchir, K. C. Kim, T. J. Anderson, V. Craciun, B. C. Brooks, and L. McElwee-White, *J. Electrochem. Soc.* **151**, G697 (2004).
- ¹⁵⁶ O. J. Bchir, K. M. Green, M. S. Hlad, T. J. Anderson, B. C. Brooks, and L. McElwee-White, *J. Cryst. Growth* **261**, 280 (2004).
- ¹⁵⁷ O. J. Bchir, K. M. Green, H. M. Ajmera, E. A. Zapp, T. J. Anderson, B. C. Brooks, L. L. Reitfort, D. H. Powell, K. A. Abboud, and L. McElwee-White, *J. Am. Chem. Soc.* **127**, 7825 (2005).
- ¹⁵⁸ R. I. Hegde, R. W. Fiordalice, E. O. Travis, and P. J. Tobin, *J. Vac. Sci. Technol. B* **11**, 1287 (1993).
- ¹⁵⁹ R. Leuterecker, B. Fröschle, U. Cao-Minh, and P. Ramm, *Thin Solid Films* **270**, 621 (1995).

- ¹⁶⁰ P. -T. Liu, T. -C. Chang, J. C. Hu, Y. L. Yang, and S. M. Sze, *J. Electrochem. Soc.* **147**, 368 (2000).
- ¹⁶¹ A. Paranjpe, and M. IslamRaja, *J. Vac. Sci. Technol. B* **13**, 2105 (1995).
- ¹⁶² M. Danek, M. Liao, J. Tseng, K. Littau, D. Saigal, H. Zhang, R. Mosley, and M. Eizenberg, *Appl. Phys. Lett.* **68**, 1015 (1996).
- ¹⁶³ D. -H. Kim, S. -L. Cho, K. -B. Kim, J. J. Kim, J. W. Park, and J. J. Kim, *Appl. Phys. Lett.* **69**, 4182, (1996).
- ¹⁶⁴ J. Bonitz, S. E. Schulz, and T. Gessner, *Microelectron. Eng.* **70**, 330 (2003).
- ¹⁶⁵ G. S. Sandhu, S. G. Meikle, and T. T. Doan, *Appl. Phys. Lett.* **62**, 240 (1993).
- ¹⁶⁶ J. -Y. Yun, M. -Y. Park, and S. -W. Rhee, *J. Electrochem. Soc.* **146**, 1804 (1999).
- ¹⁶⁷ J. Y. Kim, G. H. Choi, Y. D. Kim, Y. Kim, and H. Jeon, *Jpn. J. Appl. Phys.* **42**, 4245 (2003).
- ¹⁶⁸ J. W. Elam, C. A. Wilson, M. Schuisky, Z. A. Sechrist, and S. M. George, *J. Vac. Sci. Technol. B* **21**, 1099 (2003).
- ¹⁶⁹ K. Hieber, *Thin Solid Film* **24**, 157 (1974).
- ¹⁷⁰ D. W. Sloan, P. M. Blass, and J. M. White, *Appl. Surf. Sci.* **143**, 142 (1999).
- ¹⁷¹ X. Zhao, N. P. Magtoto, and J. A. Kelber, *Thin Solid Films* **478**, 188 (2005).
- ¹⁷² G. Beyer, A. Satta, J. Schuhmacher, K. Maex, W. Besling, O. Kilpela, H. Sprey, and G. Tempel, *Microelectron. Eng.* **64**, 233 (2002).
- ¹⁷³ O. J. Bchir, Dissertation, University of Florida (2005).
- ¹⁷⁴ R. C. Reid, J. M. Prausnitz, B. E. Poling, *The Properties of Gases and Liquids, 4th Edition*, (McGraw-Hill, New York, NY 1987).
- ¹⁷⁵ S. A. Gokoglu, PhD Thesis, Yale University (1982).
- ¹⁷⁶ R. B. Bird, W. E. Stewart, and E. N. Lightfoot, *Transport Phenomena*, (John Wiley and Sons, New York, NY 1960).
- ¹⁷⁷ M. A. Kuczarski, *J. Wide Bandgap Mater.* **7**, 192 (2000).
- ¹⁷⁸ Database of Joint Committee on Powder Diffraction Pattern (JCPDS), (2006).

- ¹⁷⁹ B. D. Cullity, and S. R. Stock, *Elements of X-ray Diffraction, 3rd Edition*, (Prentice Hall, Upper Saddle River, NJ, 2001).
- ¹⁸⁰ *Handbook of Auger Electron Spectroscopy*, edited by K. D. Childs, B. A. Carlson, L. A. LaVanier, J. F. Moulder, D. F. Paul, W. F. Stickle, and D. G. Watson, (Physical Electronics, Eden Prairie, 3rd Edition, 1995).
- ¹⁸¹ G. Soto, W. de la Cruz, and M. H. Farias, *J. Electron Spectroscopy and Related Phenomena* **135**, 27 (2004).
- ¹⁸² Y. G. Shen, and Y. W. Mai, *Material Sci. Eng. A* **288**, 47 (2000).
- ¹⁸³ J. Luthin, and C. Linsmeier, *J. Nuc. Mater.* **290**, 121 (2001).
- ¹⁸⁴ Y. M. Sun, S. Y. Lee, A. M. Lemonds, E. R. Engbrecht, S. Veldman, J. Lozano, J. M. White, J. G. Ekerdt, I. Emesh, and K. Pfeifer, *Thin Solid Films* **397(1-2)**, 109 (2005).
- ¹⁸⁵ M. B. Zellner, and J. G. G. Chen, *Catal. Today* **99(3-4)**, 299 (2005).
- ¹⁸⁶ A. Katrib, F. Hemming, P. Wehrer, L. Hilaire, and G. Maire, *J. Electron Spectroscopy and Related Phenomena* **76**, 195 (1995).
- ¹⁸⁷ D. Gogova, K. Gesheva, A. Kakanakova-Georgieva, and M. Surtchev, *Eur. Physical Journal Appl. Phys.* **11**, 167 (2000).
- ¹⁸⁸ G. E. McGuire, G. K. Schweitzer, and T. A. Carlson, *Inorg. Chem.* **12**, 2450 (1973).
- ¹⁸⁹ J. L. Alay, H. Bender, G. Brijs, A. Demesmaeker, and W. Vandervorst, *Surface and Interface Analysis* **17**, 373 (1991).
- ¹⁹⁰ J. -M. Giraudon, P. Devassine, J. -F. Lamonier, L. Delannoy, L. Leclercq, and G. Leclercq, *J. Solid State Chemistry* **154**, 412 (2000).
- ¹⁹¹ R. J. Colton, and J. W. Rabalais, *Inorg. Chem.* **15**, 236 (1976).
- ¹⁹² H. Nakazawa, T. Kawabata, M. Kudo, and M. Mashita, *Appl. Surf. Sci.* **253**, 4188 (2007).
- ¹⁹³ N. Yasui, H. Inaba, and S. Sasaki, *e-Journal of Surf. Sci. Nanotech.* **4**, 129 (2007).
- ¹⁹⁴ *Handbook of X-ray Photoelectron Spectroscopy*, edited by J. F. Moulder, W. F. Stickle, P. E. Sobol, and K. D. Bomber, (Physical Electronics Inc., 1995).
- ¹⁹⁵ S. F. Pedersen, and R. R. Schrock, *J. Am. Chem. Soc.* **104**, 7483 (1982).
- ¹⁹⁶ D. Briggs, and M. P. Seah, *Practical Surface Analysis Vol. 1*, (John Wiley & Sons, 1992).

- ¹⁹⁷ K. -E. Elers, V. Saanila, W. -M. Li, P. J. Soininen, J. T. Kostamo, S. Haukka, J. Juhanaja, and W. F. A. Besling, *Thin Solid Films* **434**, 94 (2003).
- ¹⁹⁸ C. J. Carmalt, A. C. Newport, S. A. O'Neill, I. P. Parkin, A. J. P. White, and D. J. Williams, *Inorg. Chem.* **44**, 615 (2005).
- ¹⁹⁹ B. S. Lim, A. Rahtu, and R. G. Gordon, *Nature Mater.* **2**, 749 (2003).
- ²⁰⁰ Z. W. Li, S. T. Barry, and R. G. Gordon, *Inorg. Chem.* **44**, 1728 (2005).
- ²⁰¹ A. Baunemann, D. Rische, A. Milanov, Y. Kim, M. Winter, C. Gemel, and R. A. Fischer, *Dalton Transactions* **18**, 3051 (2005).
- ²⁰² C. B. Wilder, L. L. Reitfort, K. A. Abboud, and L. McElwee-White, *Inorg. Chem.* **45**, 263 (2006).
- ²⁰³ P. Prieto, and R. E. Kirby, *J. Vac. Sci. Techno. A* **13**, 2819 (1995).
- ²⁰⁴ J. T. Scheper, P. J. McKarns, T. S. Lewkebandara, and C. H. Winter, *Mater. Sci. Semicond. Process* **2**, 149 (1999).
- ²⁰⁵ C. J. Cramer, *Essentials of Computational Chemistry*, (Wiley Interscience, 2004).
- ²⁰⁶ P. J. Hay, and W. R. Wadt, *J. Chem. Phys.* **82**, 270 (1985).
- ²⁰⁷ L. Laaksonen, *J. Mol. Graph.* **10**, 33 (1992).
- ²⁰⁸ G. Schaftenaar, and J. H. Noordik, *J. Computat. -Aided Mol. Design* **14**, 123 (2000).
- ²⁰⁹ Y. S. Won, Y. S. Kim, T. J. Anderson, L. L. Reitfort, I. Ghiviriga, and L. McElwee-White, *J. Am. Chem. Soc.* **128**, 13781 (2006).
- ²¹⁰ P. Hohenberg, and W. Kohn, *Phys. Rev.* **136**, B864 (1964).
- ²¹¹ D. M. Ceperley, and B. J. Alder, *J. Phys. Rev. Lett.* **45**, 566 (1980).
- ²¹² S. J. Vosko, L. Wilk, and M. Nusair, *Can. J. Phys.* **58**, 1200 (1980).
- ²¹³ A. D. Becke, *J. Chem. Phys.* **38**, 3098 (1988).
- ²¹⁴ G. J. Laming, and N. C. Handy, *J. Chem. Phys.* **99**, 8756 (1993).
- ²¹⁵ M. Filatov, and W. Thiel, *Mol. Phys.* **91**, 847 (1997).
- ²¹⁶ C. Adamo, and V. Barone, *J. Chem. Phys.* **108**, 664 (1998).

- ²¹⁷ J. P. Perdew, Phys. Rev. B **33**, 8822 (1986).
- ²¹⁸ J. P. Perdew, and Y. Wang, Phys. Rev. B **45**, 13244 (1992).
- ²¹⁹ A. D. Becke, J. Chem. Phys. **104**, 1040 (1996).
- ²²⁰ C. Lee, W. Wang, R. G. Parr, Phys. Rev. B **37**, 785 (1988).

BIOGRAPHICAL SKETCH

Hiral M. Ajmera was born in Mumbai, India. He is the son of Mahesh and Neela Ajmera, and has a brother, Abhijit. He is married to Kinjal Ajmera. He did his schooling from Kendriya Vidyalaya, Rajkot in 1995 and received his bachelor of engineering (chemical) degree from Maharaja Sayajirao University, Baroda, India in 1999. He attended Rensselaer Polytechnic Institute from 1999 to 2000 and received his MS degree in chemical engineering in 2001. Upon graduation, he worked for two years at Applied Materials Inc. as a process engineer. He joined NuTool in 2003 as a process engineer and worked there for 8 months. In August 2003, he joined the PhD program in Chemical Engineering at University of Florida. Upon graduation, he plans to work for Intel Corporation in Portland, Oregon.